Stromingsberekeningen voor het ontwerp van stoomkraakreactoren

Computational Fluid Dynamics-Based Design of Steam Cracking Reactors

Carl Schietekat

UNIVERSITEIT
GENT

Stromingsberekeningen voor het ontwerp van stoomkraakreactoren

Computational Fluid Dynamics-based Design of Steam Cracking Reactors

Carl Schietekat

Promotoren: prof. dr. ir. Kevin M. Van Geem en prof. dr. ir. Guy B. Marin
Proefschrift ingediend tot het behalen van de graad van
Doctor in de Ingenieurswetenschappen: Chemische Technologie

Vakgroep Chemische Proceskunde en Technische Chemie
Voorzitter: prof. dr. ir. Guy B. Marin
Faculteit Ingenieurswetenschappen en Architectuur
Academiejaar 2014 – 2015

UNIVERSITEIT
GENT

Promotoren:

prof. dr. ir. Guy B. Marin

Laboratorium voor Chemische Technologie

Vakgroep Chemische Proceskunde en Technische Chemie

Universiteit Gent

prof. dr. ir. Kevin M. Van Geem

Laboratorium voor Chemische Technologie

Vakgroep Chemische Proceskunde en Technische Chemie

Universiteit Gent

Decaan: Prof. dr. ir. Rik Van de Walle

Rector: Prof. dr. Anne De Paepe

Andere leden

Prof. dr. ir. Guy B. Marin [promotor]

Laboratorium voor Chemische Technologie

Vakgroep Chemische Proceskunde en Technische Chemie

Universiteit Gent

Prof. dr. Marie-Françoise Reyniers

Laboratorium voor Chemische Technologie

Vakgroep Chemische Proceskunde en Technische Chemie

Universiteit Gent

Prof. dr. ir. Geraldine Heynderickx

Laboratorium voor Chemische Technologie

Vakgroep Chemische Proceskunde en Technische Chemie

Universiteit Gent

Prof. dr. ir. Luc Taerwe [voorzitter]

Vakgroep Bouwkundige Constructies

Universiteit Gent

Voor mijn ouders en broer

Acknowledgements

Vooreerst wil ik mijn promotoren, prof. dr. ir. Guy B. Marin en prof. dr. ir. Kevin M. Van Geem bedanken voor de kansen die ze me geboden hebben tijdens dit doctoraat. Ook wens ik jullie te bedanken voor de constructieve revisies van mijn artikels en doctoraatsthesis. Zonder jullie hulp en advies was dit werk nooit tot stand gekomen.

Many thanks go out to prof. Fox and his colleagues, prof. Alberto Passalacqua and dr. Bo Kong, for giving me the opportunity to work 2 months at Iowa State University. Thanks for sharing your expertise in Computational Fluid Dynamics and helping me take my first steps in OpenFOAM®. Thanks also go out to prof. Qian for hosting me at the East China University of Science and Technology. For the resulting fruitful collaboration on the modeling of steam cracking furnaces, I thank dr. Hu and Yu.

During my research, I had the opportunity to participate in several collaborations with companies. Specifically, I wish to thank dr. Marco van Goethem for the collaboration on the Swirl Flow Tube® technology and dr. Larry Kool for the project on the YieldUp® coating. I wish you all the best with the further development and commercialization of these technologies.

Veel dank gaat ook uit naar mijn masterproefstudenten; David Van Cauwenberghe, Pieter Verhees en Pieter Reyniers voor hun rechtstreekse en onrechtstreekse bijdragen tot dit werk. Sommigen hebben zich zelfs na hun masterproef nog blijvend ingezet voor dit werk, waarvoor zeer veel dank!

Het experimentele luik van dit werk zou onmogelijk geweest zijn zonder de expertise en hulp van Michaël Lottin, Hans Heene, Erwin Turtelboom, Bert Depuydt en Brecht Vervust. Georges Verenghen wil ik bedanken voor het onderhouden van de servers en de hulp bij alle computer-

Contents

Notation

Roman symbols

A	pre-exponential factor in (modified) Arrhenius equation	[s,mol,m³]
b	temperature exponent in modified Arrhenius equation	[-]
C_i-	molecules with i or less carbon atoms	[-]
C_i+	molecules with i or more carbon atoms	[-]
C_j	concentration of species j	[mol/m³]
c_P	mass specific heat capacity at constant pressure	[J/kg/K]
C_P	molar specific heat capacity at constant pressure	[J/mol/K]
d	a feature representing the thermochemical state in a grid cell	[variable]
D	diffusion coefficient	[m²/s]
e	fin height	[m]
E_a	activation energy	[J/mol/K]
	surface roughness	[m]
F	molar flow rate	[mol/s]
f_f	Fanning friction factor	[-]
h	specific enthalpy	[J/mol]
H_i	Gauss-Hermite orthogonal polynomial of ith order	[-]

$\breve{H}_i$	alternative Gauss-Hermite orthonormnal polynomial of ith order	[-]
ΔH_i	reaction enthalpy of reaction i	[J/mol]
I	turbulence intensity	[-]
$\bar{J}_j$	diffusional flux of species j	[mol/m²/s]
k_B	Boltzmann constant, $1.3806\ 10^{-23}$	[m²/kg/s²/K]
k_i	reaction rate coefficient of reaction i	[mol/m³/s]
l	turbulence length scale	[m]
L	length	[m]
MM	molecular mass	[kg/mol]
N	Gaussian quadrature order	[-]
nreac	number of reactions	[-]
nspec	number of species	[-]
Nu	Nusselt number	[-]
OD	maximum tube inner diameter of a finned tube, i.e. between opposite fin valleys	[m]
Pr	Prandtl number	[-]
q	heat flux	[W/m²]
Q	heat	[W]
r	radial coordinate	[m]
r_b	bend radius	[m]
r_i	reaction rate of reaction i	[mol/m³/s]

R_j	rate of production of species j	[mol/m³/s]
Re	Reynolds number	[-]
$\overline{\overline{S}}$	strain rate tensor	[s⁻¹]
S_E	any additional energy source, e.g. by radiation	[W/m³]
S_h	heat of reaction	[W/m³]
$\boldsymbol{S_M}$	any additional momentum source, e.g. gravitational	[kg/m²/s]
Sc	Schmidt number	[-]
t	minimum wall thickness	[m]
T	temperature	[K]
U	global heat transfer coefficient	[W/m²/K]
w	fin width	[m]
y	distance to the wall	[m]
z	axial distance	[m]
E	specific total energy	[J/kg]
$P(T)$	probability density function of temperature	[-]
R	universal gas constant, 8.314	[J/mol/K]
k	turbulent kinetic energy	[m²/s²]
p	pressure	[Pa]
t	time	[s]
$\boldsymbol{u}$	velocity vector	[m/s]
w_i	Gaussian quadrature weight of order i	[-]
x_i	Gaussian quadrature abscissa of order i	[-]

x_j	molar fraction of species j	[-]
Y_i	mass fraction of species i	[-]

Greek Symbols

α_{ij}	stoichiometric coefficient of species j in reaction i	[-]
α	correction factor on friction coefficient or Nusselt number	[-]
λ	thermal conductivity	[J/m²/s]
ρ	density	[kg/m³]
ϕ_m	mass flow rate	[kg/s]
$\bar{\bar{\tau}}$	stress tensor	[Pa]
ε	turbulent kinetic energy dissipation rate	[m²/s³]
ε_i	threshold value for the variable i	[variable]
ε_{LJ}	Lennard-Jones well depth	[m²/kg/s²]
ε_T	Temperature variance dissipation	[K²/s]
ζ	Nekrasov additional resistance coefficient for bends	[-]
σ_{LJ}	Lennard-Jones distance at which the intermolecular potential between the two particles is zero	[m]
σ_T^2	Temperature variance	[K²]
θ	azimuthal coordinate	[rad]
μ	viscosity	[kg/m/s]

ω	specific turbulence dissipation rate $= \frac{\varepsilon}{0.09k}$	[1/s]
Ω	cross-sectional area	[m²]

Sub- and superscripts

$-$	mean
+	dimensionless
avg	mixing cup average
c	consumption
center	at the centerline
CFD	raw result from CFD simulation
corr	calculated from a correlation
eff	effective, i.e. sum of laminar and turbulent contributions
eq	equivalent
exp	calculated from experimental results
ext	external
f	fluid mixture
h	heated
i	reaction i
inlet	inlet
int	internal, inner
j	species j

l   laminar

LJ   Lennard-Jones

max   maximum

outlet   outlet

p   production

rms   root mean square

s   solid

sim   simulated value, after correction for tube roughness

t   turbulent

T   temperature

y   based on the distance to the wall

Acronyms

BFW	Boiler Feed Water
CFL	Courant-Friedrichs-Lewy number
CIP	Coil Inlet Pressure, i.e. the process gas pressure at the inlet of the reactor, just upstream the radiation section, just downstream the critical venturi nozzle
COP	Coil Outlet Pressure, i.e. the process gas pressure at the outlet of the reactor, just upstream the adiabatic volume
COT	Coil Outlet Temperature, i.e. the process gas temperature at the outlet of the reactor, just upstream the adiabatic volume
CPU	Central processing unit, i.e. the electronic circuitry that carries out the instructions of a computer program by performing the basic arithmetic, logical, control and input/output (I/O) operations.
CSP	Computational Singular Perturbation
CSTR	Continuously Stirred Tank Reactor
DMDS	DiMethyl DiSulfide
DNS	Direct Numerical Simulation
DRG	Directed Relation Graph
DS	Dilution Steam
EOR	End-Of-Run
ILDM	Intrinsic Lower Dimensional Manifold
LES	Large Eddy Simulation

LMTD   Log Mean Temperature Difference

LPG   Liquefied Petroleum Gas

P/E   Propene-to-Ethene ratio, a cracking severity index

PAH   PolyAromatic Hydrocarbons

PE   Partial Equilibrium

PFO   Pyrolysis Fuel Oil

PGC   Process Gas Compressor

PSS   Pseudo-Steady State

PSSA   Pseudo-Steady State Assumption

pygas   pyrolysis gasoline

QUICK   Quadratic Upstream Interpolation for Convective Kinematics

SIMPLE   Semi-Implicit Method for Pressure-Linked Equations

SOR   Start-Of-Run

SST   Shear-Stress Transport

TLE   Transfer-Line Exchanger, i.e. the heat exchanger of a steam cracking furnace downstream the adiabatic volume

TMT   external skin Tube Metal Temperature

tpy   metric tons per year, i.e. 1000 kg per year

Samenvatting

Stoomkraken van koolwaterstoffen is een petrochemisch proces dat een groot deel van de basischemicaliën van de chemische industrie produceert, met name olefinen en aromaten. Conventionele voedingen voor het proces zijn derivaten van aardgas en aardolie zoals lichte gassen (ethaan, propaan, butaan), nafta's en gasolies. Deze voedingen worden verwarmd tot 820-890 °C in tubulaire reactoren die in grote ovens hangen. Deze hoge temperaturen initiëren de thermochemische omzetting naar de producten van het proces, namelijk olefinen (etheen en propeen) en aromaten (benzeen, tolueen, xyleen en styreen) en verschillende bijproducten. De huidige globale productiecapaciteit is meer dan 150 miljoen ton etheen per jaar. Verwachtingen zijn dat deze over de komende jaren zal stijgen, gedreven door nieuwe installaties en uitbreidingen in China, het Midden-Oosten en de Verenigde Staten.

Ongewenste reacties zorgen voor de vorming van een cokeslaag op de binnenwand van de reactor. Deze groeiende cokeslaag heeft twee negatieve gevolgen. Ten eerste, stijgt de drukval over de reactor waardoor de selectiviteit naar het belangrijkste product etheen daalt. Ten tweede, stijgt de temperatuur van het reactormateriaal gedurende de afzetting van de cokeslaag doordat cokes sterk isolerende eigenschappen heeft. Wanneer de drukval over de reactor of de temperatuur van het reactormateriaal vooraf gedefinieerde waarden overstijgt, wordt de oven uit dienst genomen om de cokeslaag van de reactoren af te branden met een lucht/stoom mengsel. De duur van één zo'n productiecyclus wordt de runlengte van de oven genoemd en is uiteraard sterk afhankelijk van de procescondities zoals temperatuur en voeding. De cyclische operatie tussen kraken en ontkolen van de ovens heeft een negatieve invloed op de beschikbaarheid en rendabiliteit van kraakeenheden. Om deze reden, hebben vele onderzoeksprogramma's geleid tot de ontwikkeling

van een uitgebreid gamma aan technologieën om de vorming van cokes te reduceren. Twee technologieën werden in dit werk onderzocht, namelijk driedimensionale reactorgeometrieën en een katalytische coating.

Bij de driedimensionale reactorgeometrieën, wordt de geometrie van de binnenwand van de reactor aangepast om een hogere convectieve warmteoverdracht te verkrijgen en/of om de warmte uitwisselende oppervlakte te vergroten. Door de betere warmteoverdracht, is de temperatuur van het reactormateriaal lager en is de runlengte langer. De aanpassingen van de reactorgeometrie zorgen echter voor een verhoogde drukval die de selectiviteit naar de gewenste producten beïnvloedt. Kwantificatie van dit effect aan de hand van industriële of pilootplant resultaten is om verschillende redenen onnauwkeurig. Daarom was het hoofddoel van dit werk de ontwikkeling en toepassing van numerieke simulatiecodes om het effect van deze driedimensionale reactortechnologieën op product selectiviteiten en cokesvormingssnelheid te kwantificeren.

In hoofdstuk 2, wordt een recent ontwikkelde driedimensionale reactor technologie genaamd Swirl Flow Tube® onderzocht op basis van experimenten en simulaties. De dwarsdoorsnede van een Swirl Flow Tube® is nog steeds schijfvormig zoals deze van een conventionele rechte reactorbuis, maar de middellijn volgt een helicoïdaal pad in plaats van een rechte lijn om een betere menging te verkrijgen. De experimentele resultaten tonen aan dat de globale warmteoverdrachtscoëfficiënt 1.2 tot 1.5 keer hoger is in vergelijking met een rechte buis. De ongewenste drukval is beperkt tot 1.4 tot 2.2 keer die van een rechte buis. Een numeriek stromingsmodel werd gebruikt om de experimenten te simuleren en toonde een goede overeenkomst met de experimentele resultaten. Het model geeft aan dat de verhoogde

warmteoverdracht en drukval te verklaren zijn door een hogere schuifspanning. De resultaten bevestigen het potentieel van de applicatie van de SFT$^{®}$ technologie in stoomkraakreactoren.

De kwantificatie van het effect van de verhoogde warmteoverdracht en drukval op product opbrengsten en cokesvorming vereist het implementeren van een gasfase reactie model en een cokesmodel in het stromingsmodel. In hoofdstuk 3 worden dergelijke driedimensionale stromingssimulaties besproken voor de evaluatie van gevinde reactorbuizen. Het wordt aangetoond dat voor een bepaald industrieel reactorontwerp de maximale temperatuur van het reactormateriaal met 50 K verlaagd kan worden wanneer optimale geometrische parameters voor de vinnen gebruikt worden. Hierdoor daalt de cokesvormingssnelheid met 50 %. De drukval over de reactor stijgt echter met ongeveer 50 % en resulteert in kleine, maar significante veranderingen in de selectiviteiten van de lichte olefinen.

Het gebruik van gedetailleerde chemie in stromingssimulaties geeft aanleiding tot zeer lange simulatietijden. Daarom werd in hoofdstuk 4 een methode ontwikkeld om gedetailleerde, fundamentele reactiemodellen te gebruiken in stromingssimulaties door toepassing van de pseudo-stationaire toestandshypothese (PSSH). Naargelang de grootte van het reactiemodel, werd een reductie van de simulatietijd met een factor van 7 tot 54 verkregen. Een industriële reactor werd gesimuleerd voor zowel een standaard, rechte buis als voor een geoptimaliseerde gevinde buis. Vergelijking van de resultaten van het 3D model met een meer gebruikelijk 1D reactor model toonde aan dat een significante fout gemaakt wordt in het 1D model door de verhoogde reactiesnelheden in de laminaire film aan de binnenwand van de reactor te verwaarlozen. Daarom werd het 1D model uitgebreid om rekening te houden met deze laminaire film.

Het hierboven vermelde onderzoek werd uitgevoerd met behulp van het commerciële programma FLUENT$^{®}$. Aangezien er geen toegang tot de broncode van dit programma beschikbaar is, zijn de

mogelijkheden van de gebruiker om de code aan te passen naar de specifieke noden van het beschouwde probleem beperkt. Verder, is parallellisatie van de simulaties over vele honderden CPU's moeilijk doordat per CPU een licentie nodig is. Daarom werd in hoofdstuk 5 een code ontwikkeld voor de driedimensionale simulatie van stoomkraakreactoren op basis van het gratis, open source pakket OpenFOAM®. Het effect van turbulente temperatuurschommelingen op de reactiesnelheden werd gekwantificeerd door het gebruik van een waarschijnlijkheidsdichtheid voor de temperatuur. Het effect of de opbrengst van de verschillende producten is bij gebruikelijke procescondities beperkt tot 0.1 wt%. Om de simulatietijd verder te beperken, werd een dynamische zoningsmethode geïmplementeerd. Tenslotte, werd de code succesvol aangewend voor de simulatie van een industriële reactor voor het kraken van butaan.

Zoals eerder vermeld, werd naast driedimensionale reactoren, ook een katalytische coating bestudeerd. Bij deze technologie wordt een katalysator als een coating op de binnenwand van de reactor aangebracht. Deze katalysator zet cokes om tot koolstofoxides en waterstof door reactie met de verdunningsstoom tijdens het kraken van de voeding. Op deze manier wordt minder cokes afgezet in de reactor en wordt de runlengte verlengd. In hoofdstuk 6, werd een dergelijke katalytische coating, genaamd YieldUp® experimenteel getest en werd de opschaling naar een industriële eenheid gemaakt met numerieke simulaties. Drie verschillende formulaties van de coating werden getest in een jet-geroerde reactor en vertoonden alle een verlaagde cokesvormingssnelheid over meerdere kraken/ontkolen cycli in vergelijking met een referentie reactormateriaal. De meest performante formulatie werd verder getest in een pilootplant. De totale cokesvorming werd met 76 % verminderd door toepassing van de coating. Opschaling van de coating naar een industriële ethaankraker werd gesimuleerd met gekoppelde oven-reactor simulaties. Toepassing van de coating resulteerde in een verlenging van de runlengte met meer

dan 400 % en een verhoging van de ongewenste CO en CO_2 opbrengsten tot 216 ppmw en 344 ppmw. Deze relatief hoge CO_2 opbrengst is een potentieel probleem voor de downstream eenheden.

Summary

Steam cracking of hydrocarbons is a petrochemical process that provides the bulk share of base chemicals for the chemical industry, i.e. olefins and aromatics. The hydrocarboneous feedstocks conventionally used in the process, originate from natural gas and crude oil and range from light gasses such as ethane, propane and butane to liquids such as naphthas and gas oils. These feedstocks are heated to 820-890 °C in tubular reactors suspended in large fired furnaces. These high temperatures initiate the thermochemical conversion to the process products, i.e. olefins (mainly ethene and propene) and aromatics (mainly benzene, toluene, xylenes and styrene). Current global production capacity of ethene is over 150 million metric tons per year and is projected to grow over the next years with main additions in China, the Middle East and the United States.

Undesired side reactions result in the formation of a coke layer on the reactor tube inner wall. This growing layer has two negative effects. Firstly, the reactor pressure drop increases which results in a loss of selectivity to ethene, the process' main product. Secondly, as coke is highly insulating, the reactor tube metal temperature increases over time during the growth of the coke layer. When the reactor pressure drop or the tube metal temperatures are higher than predefined maximum values, the furnace is take out of service and the coke layer is burned off using an air/steam mixture. The duration of one cracking cycle is referred to as the furnace run length. This cyclic operation of cracking/decoking of the furnaces has a negative influence on the cracker economics. Therefore, many research efforts have led to the development of technologies to mitigate the formation of coke. The two technologies investigated in this work, are three-dimensional reactor technologies and a catalytic coating.

In three-dimensional reactor technologies, the reactor tube inner geometry is altered from the conventional bare, straight tube to a more complex geometry to enhance convective heat transfer and/or increase heat transfer area. By the increased heat transfer, the tube metal temperature is lowered and the run length is increased. As these geometrical modifications result in an increased pressure drop compared to conventional bare tubes, the selectivity towards light olefins is affected. It is difficult to quantify the selectivity effect experimentally in an industrial or pilot plant. Hence, the main goal of this work was to develop and use numerical simulation tools to quantify the impact of three dimensional reactor technologies on product selectivities and coking rate.

In Chapter 2, a recently developed three-dimensional reactor technology called Swirl Flow Tube® (SFT®) is evaluated experimentally and numerically. The cross section of the SFT® remains circular like a conventional, straight tube but the centerline follows a helicoidal path providing enhanced mixing. The experimental results show that the heat transfer coefficient increases with a factor of 1.2 to 1.5 compared to a straight tube. The undesired pressure drop increase factor is only 1.4 to 2.2 which is moderate compared to other technologies. A computational fluid dynamic (CFD) model was adopted that showed satisfactory agreement to the experimental results. The increased heat transfer and pressure drop can be attributed to a higher wall shear stress. The results show the potential for the application of the SFT® technology in steam cracking reactor designs.

The effect of the increased heat transfer and pressure drop on product yields and coke formation can be accounted for by implementing a gas-phase reaction model and a coking model. In Chapter 3, such three-dimensional CFD simulations are discussed for the evaluation of finned reactor tubes. It was shown that the reactor tube metal temperatures can be reduced by up to 50 K

when applying optimal fin parameters compared to the equivalent bare tubes and that coking rates are reduced by up to 50 %. However, the increased friction and inner surface area lead to a pressure drop increase of about 50 % which causes small but significant shifts in light olefin selectivity.

Implementation of detailed chemistry in computational fluid dynamics results in very high simulation times. Therefore, in Chapter 4 a methodology is developed to use detailed single-event microkinetic reaction networks by on the fly application of the pseudo-steady state assumption (PSSA). Depending on the reaction network size, a speedup factor from 7 to 54 was obtained compared to standard routines. An industrial propane cracking reactor was simulated using both a conventional bare reactor and a helicoidally finned reactor. Comparison of the simulation results using the developed 3D model and a more conventionally used 1D reactor model shows that a significant error is made by neglecting the increased reaction rates in the laminar film near the reactor inner wall. Therefore the 1D plug flow reactor model was extended to account for the non-uniform radial temperature profile which resulted in a closer agreement between the 1D and 3D model.

All previously discussed work was performed using the commercial CFD package FLUENT$^{®}$. As there is no access to the source code, the possibilities to adjust the code to the specific needs of simulating a steam cracking reactor are limited. Furthermore, massive parallelization of a simulation over hundreds or thousands of CPU's is very expensive because of license limitations. Hence, in Chapter 5, a code was developed for the three-dimensional simulation of steam cracking reactors based on the free, open source CFD software package OpenFOAM$^{®}$. The effect of turbulent temperature fluctuations on the reaction rates was quantified by a probability density function for temperature. The effect on product yields under typical steam cracking conditions

was seen to be limited to about 0.1 wt%. To further reduce the computational time, a dynamic zoning method was implemented besides the application of PSSA. Finally, the code was successfully applied for the simulation of an industrial butane cracking reactor.

As mentioned previously, a catalytic coating to reduce coke formation was also studied in this work. This technology comprises the coating of the reactor inner wall with a catalyst that converts coke to carbon oxides and hydrogen by reaction with the dilution steam. In Chapter 6, a catalytic coating called YieldUp$^®$ was tested experimentally and the scale up to an industrial unit was simulated. Three different formulations of the coating were tested in a jet-stirred reactor setup and showed reduced coking rates over multiple coking/decoking cycles compared to a reference alloy. The best coating was further tested in a pilot plant. The overall coke formation was reduced by 76 % compared to a reference alloy reactor. Scale-up was assessed by simulating an industrial ethane cracking reactor. Application of the coating resulted in a simulated increase of the reactor runlength by a factor of five while the CO and CO_2 yields were limited to 216 ppmw and 344 ppmw respectively. This relatively high CO_2 yield can be higher than the specifications of downstream units depending on the design of the caustic tower.

Glossary

µ-radical	A radical for which bimolecular reactions can be neglected.
µ-radical hypothesis	The hypothesis that radicals with more than 5 carbon atoms are µ-radicals
3D reactor technology	A reactor technology that enhances heat transfer by geometrical modifications to the traditional straight, bare tube used as tubular reactors.
Ab initio	Latin term for "from first principles". It refers to the fact that the results are obtained by applying the established laws of nature without assumptions, special models or experimental input. Ab initio methods determine the energy of a molecule or transition state by solving the Schrödinger equation.
Arrhenius activation energy	The coefficient E_a describing the temperature dependency of the rate coefficient $k = A \exp(-E_a/RT)$ with A the temperature independent pre-exponential factor.
Arrhenius pre-exponential factor	See Arrhenius activation energy.
Catalytic coking mechanism	Mechanism that explains the formation of coke by action of a catalyst (typically Fe or Ni) during steam cracking processes.
COILSIM1D	Fundamental model for the simulation of steam cracking units developed at the Laboratory for Chemical Technology of Ghent University.

Coke	Solid carbonaceous residue that deposits inside the reactor and downstream equipment.
Computational fluid dynamics	A branch of fluid mechanics that uses numerical methods and algorithms to solve and analyze problems that involve fluid flows.
Condensation coking mechanism	Mechanism that explains the formation of coke when heavy polynuclear aromatics condense either directly on the wall or in the bulk gas phase and subsequently collect on the wall.
CRACKSIM	Single-event microkinetic model developed at the Laboratory for Chemical Technology describing the gas-phase reactions during steam cracking of hydrocarbons.
Energy dispersive X-ray analysis	Analytical technique that determines the elemental chemical composition of a sample by aiming a beam of high energy electrons to it and then quantifying the X-ray spectra emitted by the sample.
Enthalpy	The enthalpy H is a thermodynamic quantity and is calculated from the internal energy U as $H = U + pV$, with p the pressure and V the volume of the system
Entropy	The entropy S is a thermodynamic property that is related to the disorder of the system. A system with a larger number of states that can be occupied, will therefore have a higher entropy.
Feedstock reconstruction	Deriving the detailed composition of a complex feedstock (or in

fact any other mixture) from limited macroscopic information.

Gas phase heterogeneous coking mechanism	Mechanism that explains the formation of coke due to the interaction of precursors in the gas phase with active sites in the surface of previously deposited coke.
Gas phase homogeneous coking mechanism	See condensation coking mechanism.
Group additivity method	Technique that allows to predict properties from molecular structures. For example, within Benson's group additivity method a property can be written as a sum of contributions arising from its constituent groups.
Jet stirred reactor	Type of ideal continuously stirred tank reactor where ideal mixing is achieved by introduction of the feedstock to the reactor via jets.
Lumping	Grouping of species which are generally isomers or homologous species with similar reactivity in order to reduce the total number of species in a kinetic model.
one-dimensional reactor simulation	A reactor simulation using a model with one independent variable, e.g. a batch reactor or a plug flow reactor (PFR) model.
Pseudo-steady state approximation	An approximation made that the rate of production and consumption of a species are equal. Can be applied to multiple species in a reaction mechanism.
Pyrolysis	The uncatalyzed decomposition of organic components resulting from exposure to high temperature, in the absence of molecular

oxygen.

Radical coking mechanism	See gas phase heterogeneous coking mechanism.
Reaction family	A class of reactions that are characterized by the same pattern of electron rearrangement steps.
Reaction path degeneracy	The number of energetically equivalent paths that reactants can follow to be converted into products.
Run length	Time of operation between two decoke operations.
Scanning electron microscope	Type of electron microscope that produces images of a sample by scanning it with a focused beam of electrons.
Shale gas	Natural gas trapped in shale formations.
Single-event microkinetic model	A kinetic model that consists of elementary reactions and accounts for all energetically equivalent reaction paths, i.e. single-events, to determine each reaction rate.
Single-event pre-exponential factor	The pre-exponential factor excluding the number of single-events of the reaction.
Steam cracking	A petrochemical process in which saturated hydrocarbons are converted into small unsaturated hydrocarbons by exposure to high temperature in the presence of steam.
Swirl flow	A whirling or eddying flow of fluid.
Turbulence model	A model to predict the effects of turbulence. The continuity equations are often simplified by averaging, but models are needed to represent the scales of the flow that are not resolved.

Wall shear stress   Component of stress coplanar with the wall. It is the product of the viscosity and the derivative of axial speed to radial coordinate.

zero-dimensional reactor simulation   A reactor simulation using a model without any independent variable, e.g. a continuously stirred tank reactor (CSTR) model.

β-radical   A radical that undergoes both mono- and bimolecular reactions.

Chapter 1: Introduction and outline

1.1 Introduction

Global energy consumption has dramatically increased over the last 15 years with China being the main culprit as shown in Figure 1-1. The energy demand is projected to grow by 37% to 2040, an average annual growth rate of 1.1% per year. The slowdown in growth compared to previous decades is mainly due to energy efficiency gains and governmental changes in favor of less energy-intensive activities. China will still have the largest share in the energy demand growth until mid-2020's, when its population levels off and its economic growth will slow down. At that time, India, Southeast Asia, the Middle East and parts of Africa and Latin America are projected to take over as the leading regions for energy demand [1]. Crude oil, natural gas and coal are currently the main resources for energy with oil providing about 33 % of the world's energy usage.

The world oil supply will increase by 14 million barrels/day to 104 million barrels/day in 2040 as shown in Figure 1-2. While oil production in the United States, Brazil, Canada and the Middle East will grow, the rest of the world will face a net reduction in oil production. Indeed, by mid-2020, the non-OPEC oil supply will start to fall back and the world reliance on major resource-holding countries in the Middle East will increase [1]. Crude oil is mostly used for transportation purposes with gasoline, diesel and jet fuel making up more than three-quarters of current oil usage. Only about 10% of global oil production is used for the production of chemicals. The main

petroleum cuts used for chemicals production are petroleum gasses and naphtha, a petroleum cut

with a boiling range between 300 and 470 K.
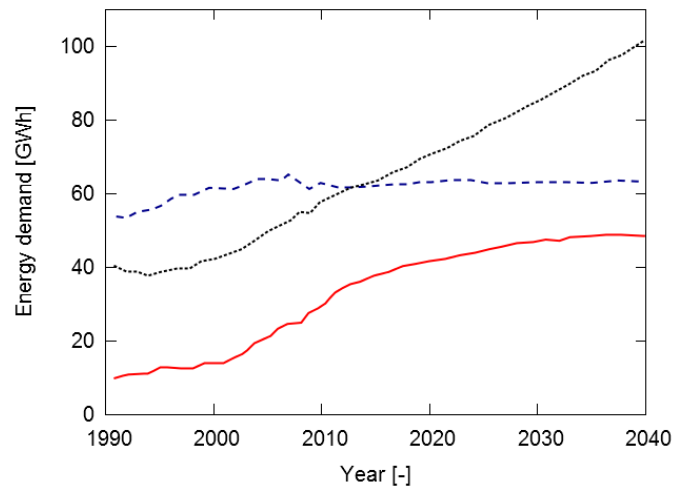
Figure 1-1: Global energy demand [GWh] as a function of time: ▬▬ - China; – – – - -OECD; ⋯⋯⋯ - Rest

of world [1].
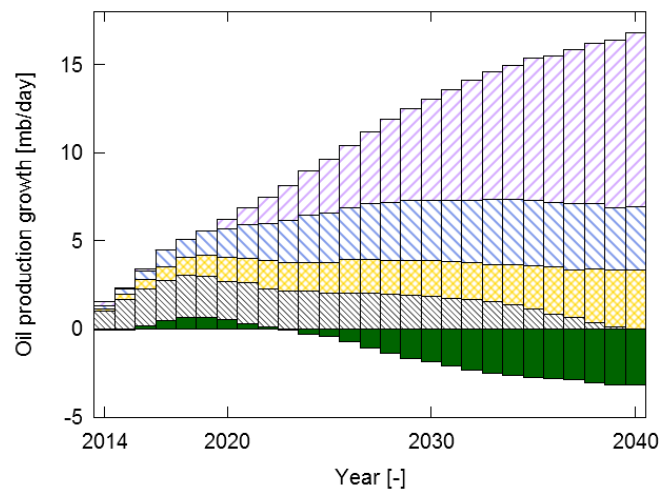
Figure 1-2: Cumulative oil production growth [mb/day] as a function of time: ▨ - United States; ▨ -

Canada; ▨ - Brazil; ▨ - Middle East; ▮ - Other producers [1].

All major regions, except Europe, will contribute to a more than 50% rise in natural gas output to 2040 [1]. Currently the third largest energy contributor, natural gas, will be the world's fastest growing major energy source through 2040 and is expected to surpass coal as second most important energy source. The share of unconventional gas will increase from 17% to 31% in the total natural gas output. Purified natural gas is mainly used for electricity production, residential heating and as an industrial fuel. Natural gas liquids, e.g. ethane, propane and butanes, and gas condensates obtained during natural gas treatment, are often used for the production of base chemicals. With the rise of new technologies such as hydraulic fracking, the production of natural gas trapped in shale formations, i.e. shale gas, has boomed over recent years. As shale gas can contain more than 20 mol% of C_2+ molecules, it is expected to increase natural gas liquids production by more than 40 % [2].

Although the fraction of natural gas and oil consumption used for the production of chemicals and materials is relatively small compared to the fraction used for transportation, heating and electricity production, the economic importance is significant due to the higher added value of chemicals compared to fuels and electricity. Most of these high-value chemicals and materials are derived from a limited number of base chemicals. These main base chemicals comprise hydrogen, olefins such as ethene, propene and 1,3-butadiene, and aromatics such as benzene, toluene and xylenes, supplemented with some heteroatom-containing chemicals such as ammonia, chlorine and sulfuric acid. The bulk of the olefins production and a large part of the aromatics production proceeds through the steam cracking process with ethene being the main product of the process. Ethene is the raw material used in the manufacture of poly(ethene), oxirane, 1,2-dichloroethane, poly(ethene terephthalate), poly(1-chloroethene) and polystyrene as well as fibers and other organic chemicals. Figure 1-3A shows the global ethene production,

production capacity and the resulting operating rate [3]. Global ethene capacity in 2012 was nearly 150 million metric tons per year (tpy). The capacity is expected to increase to 185 million tpy in 2017 with production surpassing 160 million tpy. Demand in 2008 was affected by the economic crisis, but it picked up in and after 2010 and continues to grow over the medium term. Notwithstanding the strong growth in production, the operating rate is expected to remain around 90 % due to new additions of capacity as shown in Figure 1-3B. In total 33 Mtpy capacity is to be added by 2017. China will lead the growth with 13.7 Mtpy. More than 6 Mtpy of capacity, i.e. 1/5th of global capacity addition is projected to be added in the Middle East. The Middle East has plentiful cheap feedstock and this is the main reason for the considerable growth of the ethene market in this region. The North American share of additions grows to 40% in 2017 driven by cheap ethane from shale gas exploitation.
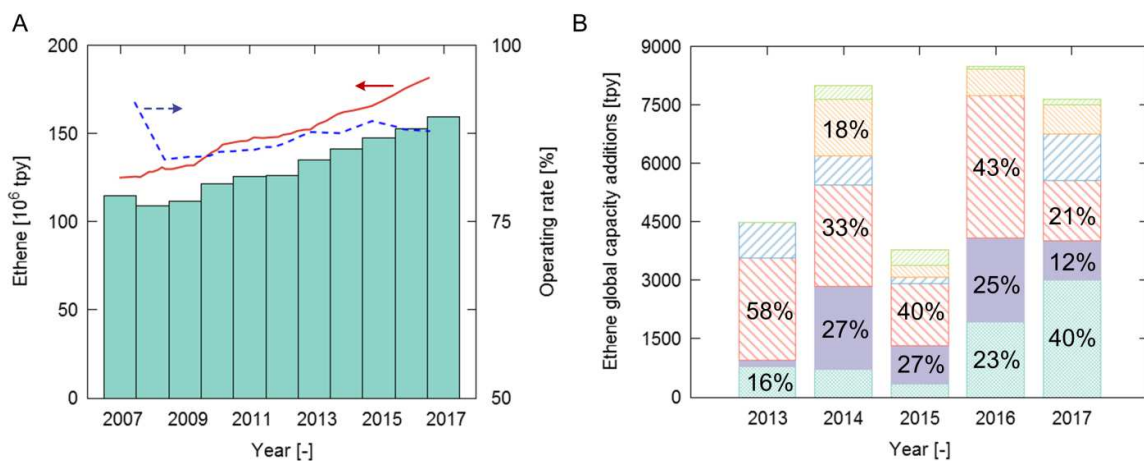
Figure 1-3: Global ethene market (A): ———— **- global production capacity [tpy];** ▦ **- actual production [tpy]; and** – – – – **- operating range [%] as a function of time [-], Global ethene capacity additions [tpy] as a function of time (B):** ▨ **- North America;** ▦ **- Middle East ;** ╲╲ **- North-East Asia;** ╱╱ **- South-East Asia;** ▨ **- Indian subcontinent and** ╱╱╱ **- Others [3].**

1.2 Steam cracking process

A wide variety of feedstocks is used in the steam cracking process, ranging from light gasses such as ethane, propane and butane, to liquids such as naphtha's, gas oils, vacuum gas oils and recently even crude oils [4]. A steam cracking unit can be roughly divided into a hot and a cold section [5]. The most important units of the hot section are the cracking furnaces with a convection section and a radiation section as depicted in Figure 1-4. The convection section contains several heat exchanger banks where the feedstock and dilution steam are vaporized and/or heated using the flue gas of the furnace. Furthermore, extra high pressure superheated steam is produced from boiler feed water (BFW) using the hot flue gas. In the radiation section the hydrocarbons are heated rapidly and cracked in tubular reactors. Several reactors are suspended in a single furnace. The flow rate is uniformly distributed over the reactors via venturi's in the choked flow regime. Typical reactor lengths and diameters vary from 10 to 100 m and 30 to 150 mm respectively. Reactor designs range from single-tube, short length, small diameter reactors with many in one furnace, such as the Millisecond reactor designs; to longer, larger diameter reactors. Longer reactors consist of multiple straight tubes connected with return bends, often with the tubes swaged to larger diameters towards the end of the reactor. Split coils are also popular where multiple, parallel tubes in the first passes of the reactor combine to larger diameter outlet tubes. The heat is supplied by burners positioned in the furnace floor and/or sidewalls. Typical coil-outlet-temperatures (COT) range from 750-890 °C depending on the feedstock, the reactor design and the desired cracking severity. Given the high temperatures, the reactors are made out of heat-resistant, high-Cr-Ni-alloy steels. Downstream the reactors, the effluent is generally quenched in two steps in order to avoid subsequent reactions of the products:

a first indirect quench with boiling water in the so-called transfer line heat exchanger(s) (TLE) generates high pressure steam and a second direct quench with quench oil separates the heavy from the light part of the effluent. The light hydrocarbons are compressed and the heavy hydrocarbons are sent to a distillation column more downstream in the process. After compression and drying, the light hydrocarbons are sent to a series of fractionators and reactors that purify the light gases into the various plant products. Typically the following products are obtained; fuel gas, i.e. hydrogen and methane, ethene, propene, a C4-cut with high 1,3-butadiene content, mixed C5's, pyrolysis gasoline (pygas) rich in aromatics, and pyrolysis fuel oil (PFO). Ethane and propane can be recycled for cracking in a dedicated recycle furnace or used as fuels. Depending on the feedstock and the integration with other petrochemical units, the C4-cut can be further refined for butadiene, n-butenes, isobutene or mixtures thereof. Otherwise the C4-cut is hydrogenated and recycled for cracking or sold directly. The pygas can be refined for aromatics and/or hydrotreated and sent to the gasoline pool.
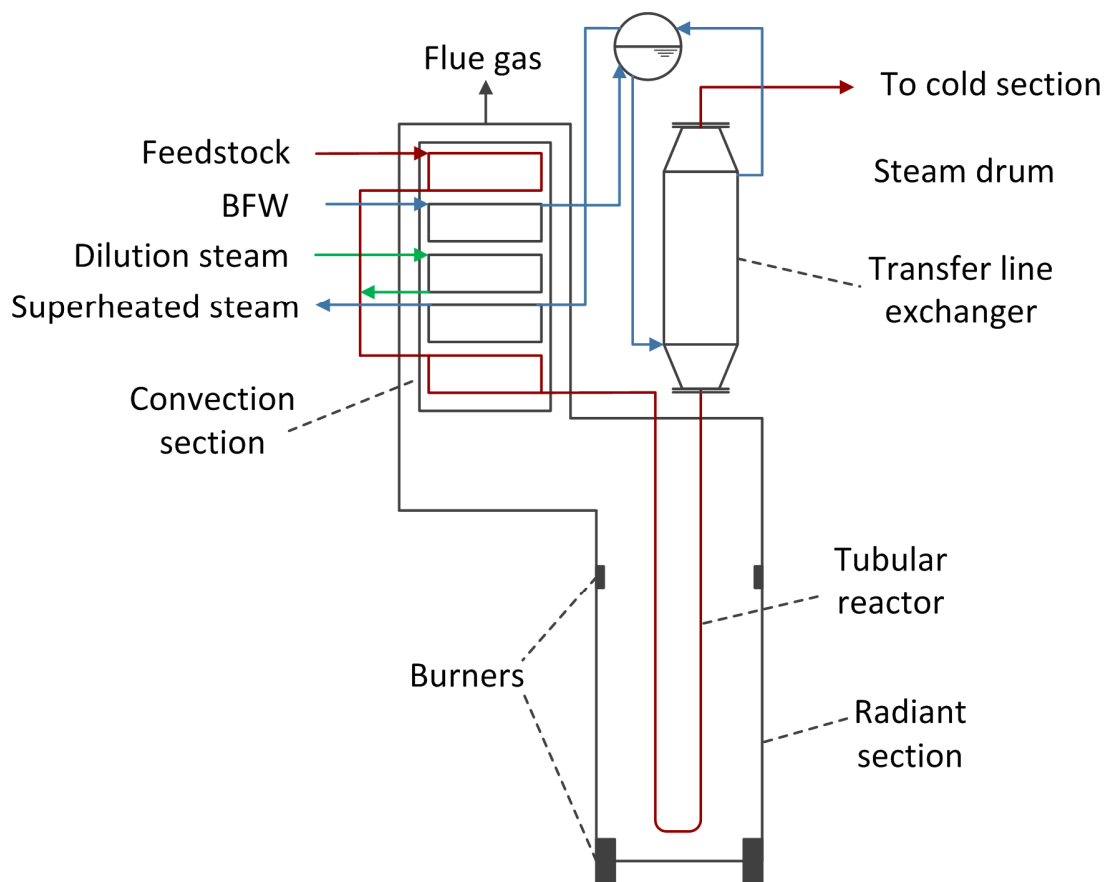
Figure 1-4: Schematic drawing of a cracking furnace.

The main factors that determine the product spectrum are the feedstock, the cracking severity, residence time, steam to oil ratio (dilution) and pressure. The heavier the feedstock and the higher its aromatics content, the lower the ethene yield. Hence, ethane has the highest ultimate ethene yield of all feeds, i.e. around 82 wt% at 65 % ethane once-through conversion. The cracking severity is quantified by the conversion for light feedstocks like ethane, propane and butane and by the propene-over-ethene ratio (P/E) for naphtha and heavier feedstocks cracking. For ethane cracking, lower conversion results in higher ethene selectivity. However, an operational limit is set by the flow rate in the ethane recycle, resulting in typical ethane conversions of 60-70 %. For

naphtha cracking, the ethene yield increases with increasing severity at relevant process conditions. An economical limit is set here by the decreasing propene yield at higher severity resulting in typical P/E-values between 0.40 and 0.65. Plehiers and Froment [6] showed that lower residence times require higher temperatures to obtain the desired cracking severity. At these high temperatures, high-activation energy reactions, such as C-C and C-H β-scissions are favored, resulting in high light olefins selectivity and low aromatics selectivity. Selectivity to light olefins is favored by low hydrocarbon partial pressure as olefins-forming reactions are often monomolecular while olefins-consuming reactions are mostly bimolecular. Therefore the reactor pressure should be minimized and steam dilution maximized. A lower limit of the coil-outlet-pressure (COP) is set by the suction pressure of the downstream process gas compressor (PGC) which is above atmospheric pressure. The operating point of the compressor and the pressure drop from the reactor outlet to the compressor results in typical COP's of 0.15-0.23 MPa abs. For the steam dilution a balance needs to be found between better ethene selectivity at high dilution and lower energy consumption at lower dilution. Furthermore, a lower limit on steam dilution is set by coke formation as further discussed in section 1.3 and by vaporization of the hydrocarbons in the convection section in the case of heavy feed cracking. Indeed part of the vaporization of the feedstock is accomplished by mixing the hot dilution steam with the partly vaporized feedstock. These considerations have resulted in typical steam dilutions of 0.25-0.4 for ethane and 0.35-0.60 for naphthas.

1.3 Coke formation and mitigation

Since the 1930's it is well known that the cracking of hydrocarbons at elevated temperature, proceeds mainly through a radical reaction mechanism [7, 8]. These gas-phase cracking reactions are accompanied by the formation of a carbonaceous layer on the reactor inner wall [9]. This so-called coke layer exhibits a number of negative effects on the steam cracking process' economics [10]. Firstly, the growing coke layer reduces the cross-sectional flow area of the reactor resulting in higher pressure drop over time. As stated previously, a higher pressure has a detrimental effect on the selectivity to ethene. Furthermore, coke is highly insulating and adds a growing extra conductive resistance to the heat transfer from the furnace to the process gas. To maintain the cracking severity, the fuel flow rate to the furnace burners is increased over time. Consequently, the external tube metal temperature (TMT) increases over time. When the TMT reaches the maximum allowable value or when the venturi pressure ratio (VPR) reaches a maximum permitted value (typically 0.9), production is halted, the furnace is taken off-line and the coke layer is burned off the reactors' inner walls using a steam-air mixture. After ca. 20 h the decoking of the reactors is finished and the TLEs can be decoked. Total decoking time of both reactors and TLEs typically requires 36 h [5]. Obviously, these periodic production interruptions have a negative effect on the process economics. Furthermore, the reactor material deteriorates with successive coking-decoking cycles by tube corrosion, carburization and erosion [11-14]. Therefore the reactor coils need to be replaced every 4 to 10 years. Given the negative impact of coking on the process economics, a fundamental understanding of coke formation and the dependency of coke formation on process conditions is important for plant design and optimization. The coke deposited in steam cracking reactors is formed via three different

mechanisms: the catalytic, the heterogeneous non-catalytic and the homogeneous non-catalytic coke formation mechanism.

When the gas-phase hydrocarbons are in direct contact with the reactor alloy, coke is formed through a catalytic mechanism with the alloy providing catalytic active sites [15-18]. Evidently, the reactor surface composition greatly influences the rate of coke formation during this catalytic coke formation [14, 19]. Typical alloy elements that catalyze coke formation are nickel and iron, while copper has a very low catalytic activity towards coke formation [20, 21]. In this mechanism, a hydrocarbon molecule chemisorbs on the active site and dehydrogenates to form -CH_3, -CH_2 and -CH groups on the surface together with gas-phase hydrogen [17]. The carbon atoms left on the metal site dissolve in and diffuse through the metal particle. When the carbon atoms exert a pressure on the metal particle higher than the tensile strength of the metal, the particle gets lifted from the surface and carbon precipitates at the rear end of the particle. As more carbon atoms dissolve, diffuse and precipitate, a carbon stem, so-called whisker or filament, is formed with the metal particle at the top. During precipitation, structural deficiencies can occur in the whiskers on which gas-phase radicals and molecules can react. This results in lateral growth of the whiskers and interweaving of whiskers. Finally, the metal particle at the tip of the whisker is encapsulated by coke stopping further catalytic growth of the filament.

Whereas catalytic coke formation decreases over time due to encapsulation of the active sites, the heterogeneous, non-catalytic mechanism proceeds throughout the entire run of the reactors. As such, the run length of industrial reactors is mainly determined by heterogeneous, non-catalytic coke formation [22]. In this mechanism, gas-phase species react with the coke layer itself through a radical mechanism. Wauters and Marin [10] suggested that the mechanism can be reduced to five families of reversible elementary reactions: hydrogen abstraction from the coke layer by a

gas-phase radical, substitution reaction of a gas-phase radical on the coke layer, radical addition of a gas-phase radical to a surface olefinic bond, addition of a gas-phase olefinic bond to a surface radical and cyclization of a surface radical. In theory all gas-phase radicals and molecules can react with the coke layer, but given their respective reactivity caused by their reactive groups and their concentration, a limited number of components, i.e. the coke precursors, dictate coke formation.

In the third mechanism, i.e. the homogeneous, non-catalytic coke formation, small droplets prevalent in the process gas impinge on the reactor inner wall. These droplets can rebound, splash or stick [23]. The droplets consist of polyaromatic hydrocarbons (PAH) either present in the feed or formed through secondary condensation reactions [24]. The PAHs form tar droplets in the gas phase through condensation and nucleation. When the droplets stick to the wall, they dehydrogenate to form coke due to the higher temperature of the inner wall. Although this mechanism is very relevant for coke formation in the TLEs and in the convection section, its importance in the reactors is believed to be limited to heavy feed cracking [24].

Because of the many adverse effects of coke formation on the profitability of steam cracking units, the large scale of the process and low profit margins, many technologies to reduce coke formation have been developed and installed commercially over the last decades. These technologies can be roughly divided into three groups: feed additives, surface technologies and three-dimensional (3D) reactor technologies. The first category of feed additives is one of the most widely applied techniques to reduce coke formation. For some additives a combination of pretreatment and continuous addition is applied, while for others only continuous addition is beneficial. Sulfur-containing compounds are the most widely studied group of additives [25-32]. The role of sulfur additives on diminishing carbon monoxide formation is well established, but

their effect on coke formation is debated [25]. Besides sulfur-containing additives, components with phosphor [33-35] and silicon [26, 36] have also been investigated.

The category of surface technologies comprises high performance alloys and coatings. Steam cracking reactors are typically made out of heat-resistant Ni-Cr alloys resisting catalytic coke formation by the formation of a chromia oxide layer at the surface [14, 37]. Often aluminum and manganese are added to enhance the coking resistance of the alloys by forming a protective alumina or a manganese chromite ($MnCr_2O_4$) spinel layer respectively [37, 38]. Alternatively, a thin layer of a coating can be deposited on the reactor base alloy surface. A distinction can be made between barrier coatings [12, 39-45] that passivate the inner wall, and catalytic coatings [46-49] that convert coke to carbon oxides and hydrogen by reaction with dilution steam. A barrier coating passivates the base alloy by covering the catalytically active sites and prevents catalytic coke formation. However, non-catalytic coke formation is still possible. In contrast, recently developed catalytic coatings eliminate catalytic coke formation by covering the active sites and convert non-catalytically formed coke to carbon oxides and hydrogen by reaction with steam. Hence, a positive catalytic activity is added besides the elimination of the negative catalytic activity of the base alloy. In Chapter 6, the performance of a new catalytic coating, called YieldUp®, was assessed experimentally and numerically.

In the last category of three-dimensional reactor technologies, the reactor tube inner geometry is altered from the conventional bare, straight tube to a more complex geometry to enhance convective heat transfer and/or increase heat transfer area. For example, finned tubes [50, 51], ribbed [52] or partially ribbed [53] tubes and swirl flow tubes [54] have been investigated to enhance heat transfer to reduce the tube metal temperature. As all these technologies lead to an increased pressure drop compared to conventional bare tubes, the selectivity towards light olefins

is probably reduced [55]. The beneficial effect on coking rates and run lengths by these technologies is well established. However, the quantification of the effect on product selectivity is still a challenge. Indeed, measurement of the selectivity loss in an industrial unit is difficult as differences of the order of 0.1 wt% are to be expected which are within the uncertainty of the measurement. Furthermore, for a fair comparison, two similar furnaces, one with and one without a 3D technology, cracking the same feedstock at the same severity, at identical time on stream, should be compared which is impossible to achieve. Quantification of the selectivity loss in pilot plant experiments is also questionable due to the difference in tube diameter and attainable Reynolds numbers between a pilot plant and an industrial unit. Hence, in the present work three-dimensional reactor models with detailed reaction mechanisms are developed and used to quantify the impact of the geometry on product selectivities and coking rate.

1.4 Fundamental modeling approach

Chemical process simulation tools are used for the design, development, analysis and optimization of chemical processes. The simulated processes range from unit operations such as distillation, extraction and filtration, to chemical reactors and combinations of both such as reactive distillation columns. Often a purpose-built flow sheet like program with several sub-models that represent the different interconnected units of the chemical plant is used. Whereas general, non-fundamental models that are tuned to a limited experimental database will only give reliable results when applied within the scope of their experimental database, truly fundamental models accounting for the elementary physical and chemical processes can be applied to a wider range of process conditions and geometries. Once developed, these models enable the design and optimization of chemical units without the need for extensive time-consuming and expensive lab-

scale and pilot experiments. The main goal of a fundamental chemical reactor model is to relate the feedstock properties with the product properties for given reactor specifications and process conditions. At a fundamental level, this requires the combination of a reaction network and a reactor model. Furthermore adequate numerical solvers are needed to solve the resulting set of algebraic and/or (partial) differential equations. As the dominant reaction families dictating the chemistry in steam cracking reactors have been well-known for many years, fundamental process simulation tools for the simulation of steam cracking reactors have been used extensively since the pioneering work of Dente et al. [56] in the late seventies. The present work further improves the fundamental modeling of steam cracking reactors by the development of a dedicated three-dimensional reactor model.

1.4.1 **Reaction network**

As mentioned above, the main part of the steam cracking chemistry proceeds through a free-radical mechanism. This results in a vast number of species and reactions, with modern reaction mechanisms having hundreds of species and thousands of reactions [57]. Fortunately, the occurring reactions can be grouped into a limited number of elementary reaction families. Methods to describe these reaction families together with systematic methods to calculate the necessary kinetic and thermodynamic parameters, have been implemented in a number of software codes such as NETGEN [58-60], RMG [61-65], GENESYS [66], REACTION [67-69] and RING [70, 71]. These programs allow the automatic generation of reaction networks for the thermochemical conversion of a multitude of species. The size of these reaction networks is limited by rate- and/or rule-based criteria. However, the size of these reaction networks - both in number of species as in number of reactions - increases exponentially with the carbon number of

the feedstock molecule [57]. The computational time associated with these large kinetic networks prohibits reactor simulations within a manageable time frame, certainly when multidimensional reactor models are used [72, 73]. Besides the large size, fundamental reaction mechanisms also show dramatic differences in time scales associated with species and reactions resulting in severe stiffness when implemented in a reactor model. These differences originate from highly reactive radical species and fast reversible reactions in partial equilibrium. The above two characteristics, i.e. large size and stiffness, often force the application of reduction methods to limit computational time without sacrificing too much of the comprehensiveness of the complex reaction network. These reduction methods include among others, horizontal and vertical lumping [74, 75], pseudo-steady-state assumption (PSSA) [76-78], partial equilibrium assumption (PE) [79, 80], intrinsic lower dimensional manifold (ILDM) [81], computational singular perturbation (CSP) [82] and directed relation graph (DRG) [83]. Reduction methods can be applied a priori, a posteriori or on the fly. A-priori application, limits the reaction network size during reaction network generation. For example the software code PRIM [84-87] applies the pseudo-steady-state approximation to all μ-radicals, i.e. radicals for which bimolecular reactions can be neglected, that appear in the primary decomposition schemes. The μ-radicals' concentrations are determined by solving the resulting algebraic equations and substituted in the continuity equations of the non-PSS species. This reduces both the number of differential equations and the stiffness of the system as the short time-scales introduced by the fast reacting μ-radicals are removed. A posteriori application of reduction techniques results in a so-called skeletal mechanism; a number of species and/or reactions are removed from the reaction mechanism in-between the reaction mechanism generation and the actual reactor simulation. Methods representative for this approach include sensitivity analysis, direct relational graph and

chemical time scale analysis-based methods such as PSSA, PE and ILDM [73]. When the chemistry of the reaction network is not well-known, these methods require the comprehensive model to be used in a test set of simple zero-dimensional and/or one-dimensional simulations to derive some of the networks' characteristics to perform the reduction. This does not only add additional computational burden but also limits the applicability range of the network when it is reduced too severely. On the fly reduction of the reaction network circumvents these problems by generating a new network and/or reducing the network dynamically during the reactor simulation [88-90]. The resulting reaction networks are tailored to a very specific problem, e.g. describing the chemistry at a certain time step and at a certain position in the reactor. As the resulting networks are much smaller than the skeletal mechanisms obtained by a-priori reduction, the number of governing equations and the time needed to solve them is lower. Nonetheless, a certain - often significant - computational overhead is associated with on the fly application of network generation and/or reduction.

1.4.2 **Reactor model**

Modeling a steam cracking reactor includes all the phenomena occurring in the reactor, i.e. reaction, transfer of heat, mass and momentum [91]. The reactor model is based on the governing equations describing these phenomena: the reaction rate equations, the continuity, energy and momentum equations. Derivation of these equations is based on expressing a conservation law in an infinitesimal part of the reactor and has been elaborated in many transport-related books, e.g. Bird et al. [92]. The continuity equation for a chemical species j in a flowing fluid is:

$$\frac{\partial C_j}{\partial t} + \nabla \cdot \left(\overline{\boldsymbol{u}} C_j \right) = -\nabla \cdot \overline{\boldsymbol{J}}_j + R_j \, , \forall j = 1, nspec \tag{1.1}$$

with C_j the concentration of species j, $\overline{\boldsymbol{u}}$ the velocity vector, $\overline{\boldsymbol{J}}_{\boldsymbol{j}}$ the laminar and turbulent diffusional flux of species j vector [mol$_j$/m^2/s^1] and R_j the net rate of production of species j. R_j is calculated as $\sum_{i=1}^{nreac} \alpha_{ij} r_i$ with α_{ij} the stoichiometric coefficient of species j in reaction i and r_i the reaction rate of reaction i determined by the used reaction network.

The global continuity equation can be derived by summation of all $nspec$ species continuity equations multiplied by the respective species molecular mass:

$$\frac{\partial \rho}{\partial t} + \nabla \cdot (\rho \overline{\boldsymbol{u}}) = 0 \tag{1.2}$$

with ρ the mixture density [kg/m^3]. By similarly expressing conservation of momentum and energy, the momentum equations, also known as Navier-Stokes equations, and the energy conservation equation are derived respectively:

$$\frac{\partial (\rho \overline{\boldsymbol{u}})}{\partial t} + \nabla \cdot (\rho \overline{\boldsymbol{u}}\,\overline{\boldsymbol{u}}) = -\nabla p + \nabla \cdot (\overline{\overline{\boldsymbol{\tau}}}) + \boldsymbol{S_M} \tag{1.3}$$

$$\frac{\partial (\rho E)}{\partial t} + \nabla \cdot \left(\overline{\boldsymbol{u}}(\rho E + p) \right) = \nabla \cdot \left(\lambda_{eff} \nabla \mathrm{T} - \sum_j^{nspec} h_j \overline{\boldsymbol{J}}_{\boldsymbol{j}} + (\overline{\overline{\boldsymbol{\tau}}} \cdot \overline{\boldsymbol{u}}) \right) + S_E \tag{1.4}$$

with $\overline{\overline{\boldsymbol{\tau}}}$ the stress tensor [Pa], E the specific total energy [J/kg$_f$], λ_{eff} the effective thermal conductivity [W/mK] including both laminar and turbulent contributions, h_j the specific enthalpy of species j [J/mol], $\boldsymbol{S_M}$ any extra momentum source terms [kg/m²s²], e.g. by gravitational force and S_E any extra energy source terms [J/m³s], e.g. by radiation. In the energy equation, the specific total energy is calculated as $E = h - \frac{p}{\rho} + \frac{|\overline{\boldsymbol{u}}|^2}{2}$ with the sensible enthalpy of the ideal gas mixture calculated as $h = \sum_{j=1}^{nspec} x_j h_j$ and $h_j = \int_{T_{ref}}^{T} C_{p,j}(T) dT$.

The fundamental equations (1.1) - (1-4) can be solved by CFD. However, they are often simplified by neglecting some terms or by integration over some spatial direction(s) as the above-mentioned form is too time-consuming for routine design and optimization. The large length-over-diameter ratio of steam cracking reactors makes that the concentration gradients in radial and azimuthal direction are typically not modeled, resulting in a one-dimensional reactor model. Furthermore, assumption of dominance of convective over diffusive transport due to the high Reynolds numbers in steam crackers, yields the plug flow model [91]. Software programs using a plug flow reactor model are commercially available [56, 93] and are routinely used for the optimization and design of steam cracking reactors. Nonetheless, the one-dimensional modeling of steam cracking reactors shows several shortcomings. Firstly, the heat flux from the furnace to the reactors induces a non-uniform radial temperature profile. This introduces non-uniform radial concentration profiles and an error in the rate of production calculation in a one-dimensional model as the cross-sectional mixing-cup averaged rate of production is not equal to the rate of production calculated with the cross-sectional mixing-cup averaged temperature and concentrations, i.e. $\overline{R_j(T,\boldsymbol{C})} \neq R_j(\overline{T},\overline{\boldsymbol{C}})$. Secondly, coke formation occurs at the coke-gas interface where temperature is higher than in the gas phase. In one-dimensional models, this interface temperature is calculated using a laminar film model based on a Nusselt number obtained via a correlation [94]. The effect on coke formation of different concentrations at the coke-gas interface compared to the bulk is not accounted for. Thirdly, a shortcoming of the one-dimensional plug flow model is the inability of including azimuthal non-uniformities in heat flux and temperature due to shadow effects in the furnace which result in azimuthally non-uniform coking rates [95, 96]. Finally, the one-dimensional flow pattern is not able to accurately model

the effect of three-dimensional reactor geometries and return bends. Considering these shortcomings, several authors have used two-dimensional [97, 98] and three-dimensional [50, 51, 99, 100] reactor models for the simulation of steam cracking reactors. Most of these studies used severely reduced, often global reaction networks, which results are often biased. In the present work, a three-dimensional reactor model tailored to the simulation of steam cracking reactors is developed based on the free and open-source software package OpenFOAM® [101, 102].

1.5 Outline

This thesis is a compilation of published journal papers and manuscripts that have been submitted or are to be submitted for publication in the near future. Every chapter has a short introduction describing the relevant context.

In Chapter 2, the potential of a new three-dimensional reactor technology, called Swirl Flow Tube®, is assessed. A comprehensive experimental dataset has been acquired on a newly built test set-up covering a wide range of Reynolds numbers (30,000 – 120,000) and different swirl flow tube designs. A computational fluid dynamics model was adopted that is able to capture the main flow properties of the Swirl Flow Tube®. The experimental and simulation results confirm the potential for the application of the SFT technology in steam cracking furnaces because of the lower average wall temperatures and the resulting reduction of coke formation in the reactor coil.

In Chapter 3, reactive CFD simulations of steam cracking reactors are performed accounting for the detailed free-radical gas-phase chemistry. The application of finned tubes as steam cracking reactors is studied. A non-reactive parametric study was used to optimize the fin parameters by finding a balance between the desired increase in heat transfer and the unwanted increase in pressure drop. An industrial reactor was simulated using four different reactors. Application of a

finned reactor resulted in a drastic decrease of coking rate at the cost of a loss in ethene selectivity.

As the implementation of large reaction mechanisms in CFD simulations requires long CPU times, the reaction mechanism used in Chapter 3 consisted only of 26 species. Therefore, in Chapter 4, a methodology was developed to use detailed single-event microkinetic models in CFD simulations by on the fly application of the pseudo-steady state assumption on the reactive intermediates. This allowed the implementation of large reaction mechanisms and hence the accurate quantification of the effect of a three-dimensional reactor technology on the product selectivities. Furthermore, comparison of the results when using a 1D reactor model or a 3D reactor model showed that a 1D reactor model does not correctly simulate the effect of a 3D reactor model on product yields.

The CFD simulations discussed in Chapter 2 to 4 were performed using the commercial CFD package FLUENT®. Commercial CFD packages have two disadvantages. First, the source code is not accessible which limits the users' possibilities to tailor the code to the problem at hand. Second, the number of CPU's used for parallelization of a simulation is limited by license requirements as typically every extra CPU requires an extra license. Therefore, in Chapter 5, a code for the three-dimensional simulation of steam cracking reactors based on the free and open-source CFD package OpenFOAM® is developed. Besides the methodology of applying PSSA discussed in Chapter 4, a dynamic zoning method was implemented to further reduce the required computational time. Also, two extra continuity equations can be solved to include the effect of turbulence-chemistry interaction on the reaction rates.

Chapter 6 discusses a catalytic coating to reduce coke formation, called YieldUp®. As the coating catalytically converts coke to carbon oxides by reaction with dilution steam, it reduces the coke

formation by all of the three mechanisms discussed in paragraph 1.3. Different coating formulations were tested in a jet-stirred reactor setup and the best performing formulation was further tested in a pilot plant setup. The coating reduced the coke formation by about 75% and remained constant over several coking/decoking cycles. Based on the experimental results, the scale-up to an industrial steam cracking unit was simulated by coupled furnace-reactor simulations.

Finally in Chapter 7, the general conclusions are presented and perspectives for future research are proposed.

References

[1] International Energy Agency, World Energy Outlook 2014, 2014.

[2] J. Foster, Can shale gas save the naphtha crackers?, Platts, 2013.

[3] Asia Pacific Region will Continue to Dominate the Ethylene Market, Chemical Engineering World, Jasubhai Media, Mumbai, India, 2013.

[4] F. Tan, S.L. Peng, Exxon starts world's 1st crude-cracking petrochemical unit, Reuters, Singapore, 2014.

[5] H. Zimmermann, R. Walzl, Ethylene, in: Ullmann's Encyclopedia of Industrial Chemistry, Wiley-VCH Verlag GmbH & Co. KGaA, 2000.

[6] P.M. Plehiers, G.F. Froment, Reversed split coil improves ethylene yields, Oil & Gas Journal, 85 (1987) 41-&.

[7] F.O. Rice, K.F. Herzfeld, The Thermal Decomposition of Organic Compounds from the Standpoint of Free Radicals. VI. The Mechanism of Some Chain Reactions, Journal of the American Chemical Society, 56 (1934) 284-289.

[8] F.O. Rice, The Thermal Decomposition of Organic Compounds from the Standpoint of Free Radicals. I. Saturated Hydrocarbons, Journal of the American Chemical Society, 53 (1931) 1959-1972.

[9] M.J. Bennett, J.B. Price, A physical and chemical examination of an ethylene steam cracker coke and of the underlying pyrolysis tube, J Mater Sci, 16 (1981) 170-188.

[10] S. Wauters, G.B. Marin, Kinetic Modeling of Coke Formation during Steam Cracking, Industrial & Engineering Chemistry Research, 41 (2002) 2379-2391.

[11] Y. Nishiyama, N. Otsuka, Degradation of Surface Oxide Scale on Fe-Ni-Cr-Si Alloys upon Cyclic Coking and Decoking Procedures in a Simulated Ethylene Pyrolysis Gas Environment, Corrosion, 61 (2005) 84-93.

[12] W. Zychlinski, K.A. Wynns, B. Ganser, Characterization of material samples for coking behavior of HP40 material both coated and uncoated using naphtha and ethane feedstock, Materials and Corrosion-Werkstoffe Und Korrosion, 53 (2002) 30-36.

[13] G. Zimmermann, W. Zychlinski, H.M. Woerde, P. van den Oosterkamp, Absolute Rates of Coke Formation: A Relative Measure for the Assessment of the Chemical Behavior of High-Temperature Steels of Different Sources, Industrial & Engineering Chemistry Research, 37 (1998) 4302-4305.

[14] A.E. Munoz Gandarillas, K.M. Van Geem, M.-F. Reyniers, G.B. Marin, Influence of the Reactor Material Composition on Coke Formation during Ethane Steam Cracking, Industrial & Engineering Chemistry Research, 53 (2014) 6358-6371.

[15] J. Rostrup-Nielsen, D.L. Trimm, Mechanisms of carbon formation on nickel-containing catalysts, Journal of Catalysis, 48 (1977) 155-165.

[16] R.T.K. Baker, D.J.C. Yates, J.A. Dumesic, Filamentous Carbon Formation over Iron Surfaces, in: Coke Formation on Metal Surfaces, American Chemical Society, 1983, pp. 1-21.

[17] J.W. Snoeck, G.F. Froment, M. Fowles, Filamentous Carbon Formation and Gasification: Thermodynamics, Driving Force, Nucleation, and Steady-State Growth, Journal of Catalysis, 169 (1997) 240-249.

[18] T.V. Reshetenko, L.B. Avdeeva, Z.R. Ismagilov, V.V. Pushkarev, S.V. Cherepanova, A.L. Chuvilin, V.A. Likholobov, Catalytic filamentous carbon: Structural and textural properties, Carbon, 41 (2003) 1605-1615.

[19] A.E. Muñoz Gandarillas, K.M. Van Geem, M.-F. Reyniers, G.B. Marin, Coking Resistance of Specialized Coil Materials during Steam Cracking of Sulfur-Free Naphtha, Industrial & Engineering Chemistry Research, 53 (2014) 13644-13655.

[20] P. Geurts, A. Vanderavoird, Hartree-Fock-Slater-LCAO studies of the acetythylene-transition metal interaction. 2. Chemisorption on Fe and Cu - Cluster-models, Surface Science, 103 (1981) 416-430.

[21] P. Geurts, A. Vanderavoird, Hartree-Fock-Slater-LCAO studies of the acetythylene-transition metal interaction. 2. Chemisorption on Ni surfaces - Cluster-models, Surface Science, 102 (1981) 185-206.

[22] G. Reyniers, Cokesvorming bij het thermisch kraken van koolwaterstoffen, Ghent university, 1991.

[23] A.V. Mahulkar, G.J. Heynderickx, G.B. Marin, Simulation of the coking phenomenon in the superheater of a steam cracker, Chemical Engineering Science, 110 (2014) 31-43.

[24] K.M. Van Geem, I. Dhuyvetter, S. Prokopiev, M.F. Reyniers, D. Viennet, G.B. Marin, Coke Formation in the Transfer Line Exchanger during Steam Cracking of Hydrocarbons, Industrial & Engineering Chemistry Research, 48 (2009) 10343-10358.

[25] J. Wang, M.-F. Reyniers, G.B. Marin, Influence of dimethyl disulfide on coke formation during steam cracking of hydrocarbons, Industrial & Engineering Chemistry Research, 46 (2007) 4134-4148.

[26] J. Wang, M.-F. Reyniers, K.M. Van Geem, G.B. Marin, Influence of silicon and silicon/sulfur-containing additives on coke formation during steam cracking of hydrocarbons, Industrial & Engineering Chemistry Research, 47 (2008) 1468-1482.

[27] M. Reyniers, G.F. Froment, Influence of metal-surface and sulfur addition on coke deposition in the thermal cracking of hydrocarbons, Industrial & Engineering Chemistry Research, 34 (1995) 773-785.

[28] I. Dhuyvetter, M.F. Reyniers, G.F. Froment, G.B. Marin, D. Viennet, The influence of dimethyl disulfide on naphtha steam cracking, Industrial & Engineering Chemistry Research, 40 (2001) 4353-4362.

[29] M. Bajus, J. Baxa, Coke formation during the pyrolysis of hydrocarbons in the presence of sulfur-compounds, Collection of Czechoslovak Chemical Communications, 50 (1985) 2903-2909.

[30] M. Bajus, J. Baxa, P.A. Leclercq, J.A. Rijks, Steam cracking of hydrocarbons: 6. Effect of dibenzyl sulfide and dibenzyl disulfide on reaction-kinetics and coking, Industrial & Engineering Chemistry Product Research and Development, 22 (1983) 335-343.

[31] M. Bajus, V. Vesely, Pyrolysis of hydrocarbons in the presence of elemental sulfur, Collection of Czechoslovak Chemical Communications, 45 (1980) 238-254.

[32] M. Bajus, V. Vesely, J. Baxa, P.A. Leclercq, J.A. Rijks, Steam cracking of hydrocarbons: 5. Effect of thiophene on reaction-kinetics and coking, Industrial & Engineering Chemistry Product Research and Development, 20 (1981) 741-745.

[33] J.D. Wang, M.F. Reyniers, G.B. Marin, The influence of phosphorus containing compounds on steam cracking of n-hexane, Journal of Analytical and Applied Pyrolysis, 77 (2006) 133-148.

[34] S. Vaish, D. Kunzru, Triphenyl phosphite as a coke inhibitor during naphtha pyrolysis, Industrial & Engineering Chemistry Research, 28 (1989) 1293-1299.

[35] K.K. Ghosh, D. Kunzru, Reduction of coke formation during naphtha pyrolysis using triethyl phosphite, Industrial & Engineering Chemistry Research, 27 (1988) 559-565.

[36] D.E. Brown, J.T.K. Clark, A.I. Foster, J.J. McCarroll, M.L. Sims, Inhibition of coke formation in ethylene steam cracking, Acs Symposium Series, 202 (1982) 23-43.

[37] G. Verdier, F. Carpentier, Consider new materials for ethylene furnace applications, Hydrocarbon Processing, 90 (2011) 61-62.

[38] J. Yan, Y. Gao, F. Yang, Y. Bai, Y. Liu, C. Yao, S. Hou, G. Liu, Cyclic carburizing behaviour of Al modified high Si-containing HP40 alloy, Corrosion Science, 67 (2013) 161-168.

[39] B. Ganser, K.A. Wynns, A. Kurlekar, Operational experience with diffusion coatings on steam cracker tubes, Materials and Corrosion, 50 (1999) 700-705.

[40] L. Benum, Achieving longer furnace runs at NOVA Chemicals, 2002 AIChE Spring Meeting, New Orleans, LA, 2002.

[41] M. Györffy, L. Benum, L. Sakamoto, Increased run length and furnace performance with Kubota and NOVA Chemicals' ANK 400 anticoking technology; data from current installations as well as technologyimprovements for higher thermal stability and decoking robustness, 2006 AIChE National Meeting, Orlando, FL, 2006.

[42] M. Bergeron, E. Maharajh, T. McCall, A low coking environment for pyrolysis furnace - CoatAlloy, 11th Annual Ethylene Producers' Conference, Houston, TX, 1999.

[43] T. Redmond, A. Bailey, Y. Chen, G. Fisher, R. Miller, Performance of Coatalloy coating systems in ethylene pyrolysis furnaces using different feedstocks, 12th Annual Ethylene Producers' Conference, Atlanta, GA, 2000.

[44] S. Petrone, R. Mandyam, A. Wysiekierski, Surface alloyed high temperature alloys, S.E.P. Corp., (1997).

[45] S. Petrone, R. Manyam, A. Wysiekierski, K. Tzatzov, Y. Chen, A "carbon-like" coating to improved coking resistance in pyrolysis furnaces, 10th Annual Ethylene Producers' Conference, New Orleans, LA, 1998.

[46] S. Petrone, Y. Chen, R. Deuis, L. Benum, R. Saunders, C. Wong, Catalyzed-assisted manufacture of olefins (CAMOL): Realizing novel operational benefits from furnace coil surfaces, 20th Ethylene Producers' Conference, New Orleans, LA, 2008.

[47] S. Petrone, R. Deuis, P. Unwin, Catalyzed-assisted manufactur of olefins (CAMOL): Year-(4) update on commercial furnace installations, 22th Ethylene Producers's Conference San Antonio, TX, 2010.

[48] S. Rech, Catalyzed-Assisted Manufacture of Olefins (CAMOL™): Updated for Use in Naphtha Service, http://www.basf-qtech.com/, 2013.

[49] SK-Corporation, Coke Inhibition Technologies - Commercial Experience: F. SK Corporation - PY-COAT, 13th Ethylene Producers' Conference, Houston, TX, 2001.

[50] J.J. De Saegher, T. Detemmerman, G.F. Froment, Three dimensional simulation of high severity internally finned cracking coils for olefins production, Revue De L'Institut Français Du Pétrole, 51 (1996) 245-260.

[51] T. Detemmerman, F. Froment, Three dimensional coupled simulation of furnaces and reactor tubes for the thermal cracking of hydrocarbons, Revue De L'Institut Français Du Pétrole, 53 (1998) 181-194.

[52] T. Torigoe, K. Hamada, M. Furuta, M. Sakashita, K. Otsubo, M. Tomita, Mixing element radiant tube (MERT) improves cracking furnace performance, 11th Ethylene Producers' Conference, Houston, TX, 1999.

[53] M. Györffy, M. Hineno, K. Hashimoto, S.-H. Park, M.-S. You, MERT performance and technology update, 21st Ethylene Producers' Conference, Tampa, FL, 2009.

[54] C.M. Schietekat, M.W.M. van Goethem, K.M. Van Geem, G.B. Marin, Swirl flow tube reactor technology: An experimental and computational fluid dynamics study, Chemical Engineering Journal, 238 (2014) 56-65.

[55] C.M. Schietekat, D.J. Van Cauwenberge, K.M. Van Geem, G.B. Marin, Computational fluid dynamics-based design of finned steam cracking reactors, AIChE Journal, 60 (2014) 794-808.

[56] M. Dente, E. Ranzi, A.G. Goossens, Detailed prediction of olefin yields from hydrocarbon pyrolysis through a fundamental simulation model (SPYRO), Computers & Chemical Engineering, 3 (1979) 61-75.

[57] T. Lu, C.K. Law, Toward accommodating realistic fuel chemistry in large-scale computations, Progress in Energy and Combustion Science, 35 (2009) 192-215.

[58] L.J. Broadbelt, S.M. Stark, M.T. Klein, Computer-generated pyrolysis modeling - On the fly generation of species, reactions and rates, Industrial & Engineering Chemistry Research, 33 (1994) 790-799.

[59] L.J. Broadbelt, S.M. Stark, M.T. Klein, Computer generated reaction modelling: Decomposition and encoding algorithms for determining species uniqueness, Computers & Chemical Engineering, 20 (1996) 113-129.

[60] L.J. Broadbelt, S.M. Stark, M.T. Klein, Computer-generated pyrolysis modeling: on- the-fly generation of species, reactions and rates, Industrial & Engineering Chemistry Research, 33 (1994) 790-799.

[61] W.H. Green, J.W. Allen, R.W. Ashcraft, G.J. Beran, C.F. Goldsmith, M.R. Harper, A. Jalan, G.R. Magoon, D.M. Matheu, S. Petway, S. Raman, S. Sharma, K.M. Van Geem, J. Song, J. Wen, R.H. West, A. Wong, H.-W. Wong, P.E. Yelvington, Y. J., RMG - Reaction Mechanism Generator v3.3, 2011.

[62] M.R. Harper, K.M. Van Geem, S.P. Pyl, G.B. Marin, W.H. Green, Comprehensive reaction mechanism for n-butanol pyrolysis and combustion, Combustion and Flame, 158 (2011) 16-41.

[63] D.M. Matheu, T.A. Lada, W.H. Green, A.M. Dean, J.M. Grenda, Rate-based screening of pressure-dependent reaction networks, Computer Physics Communications, 138 (2001) 237-249.

[64] R.G. Susnow, A.M. Dean, W.H. Green, P. Peczak, L.J. Broadbelt, Rate-based construction of kinetic models for complex systems, J. Phys. Chem. A, 101 (1997) 3731-3740.

[65] K.M. Van Geem, M.F. Reyniers, G.B. Marin, J. Song, W.H. Green, D.M. Matheu, Automatic reaction network generation using RMG for steam cracking of n-hexane, AIChE Journal, 52 (2006) 718-730.

[66] N.M. Vandewiele, K.M. Van Geem, M.F. Reyniers, G.B. Marin, Genesys: Kinetic model construction using chemo-informatics, Chemical Engineering Journal, 207 (2012) 526-538.

[67] E.S. Blurock, Reaction - System For Modeleling Chemical Reactions, Journal of Chemical Information and Computer Sciences, 35 (1995) 607-616.

[68] E.S. Blurock, Detailed mechanism generation. 1. Generalized reactive properties as reaction class substructures, Journal of Chemical Information and Computer Sciences, 44 (2004) 1336-1347.

[69] E.S. Blurock, Detailed mechanism generation. 2. Aldehydes, ketones, and olefins, Journal of Chemical Information and Computer Sciences, 44 (2004) 1348-1357.

[70] S. Rangarajan, A. Bhan, P. Daoutidis, Language-oriented rule-based reaction network generation and analysis: Description of RING, Computers & Chemical Engineering, 45 (2012) 114-123.

[71] S. Rangarajan, A. Bhan, P. Daoutidis, Language-oriented rule-based reaction network generation and analysis: Applications of RING, Computers & Chemical Engineering, 46 (2012) 141-152.

[72] L. Liang, J.G. Stevens, S. Raman, J.T. Farrell, The use of dynamic adaptive chemistry in combustion simulation of gasoline surrogate fuels, Combustion and Flame, 156 (2009) 1493-1502.

[73] L. Tosatto, B.A.V. Bennett, M.D. Smooke, A transport-flux-based directed relation graph method for the spatially inhomogeneous instantaneous reduction of chemical kinetic mechanisms, Combustion and Flame, 158 (2011) 820-835.

[74] E. Ranzi, M. Dente, A. Goldaniga, G. Bozzano, T. Faravelli, Lumping procedures in detailed kinetic modeling of gasification, pyrolysis, partial oxidation and combustion of hydrocarbon mixtures, Progress in Energy and Combustion Science, 27 (2001) 99-139.

[75] M. Dente, G. Bozzano, T. Faravelli, A. Marongiu, S. Pierucci, E. Ranzi, Kinetic Modelling of Pyrolysis Processes in Gas and Condensed Phase, in: G.B. Marin (Ed.) Advances in Chemical Engineering, Academic Press, 2007, pp. 51-166.

[76] T. Turanyi, A.S. Tomlin, M.J. Pilling, On the error of the quasi-steady-state approximation, Journal of Physical Chemistry, 97 (1993) 163-172.

[77] T. Turanyi, J. Toth, Classics revisited - comments to an article of Frank Kamenetskii on the quasi-steady-state approximation, Acta Chimica Hungarica-Models in Chemistry, 129 (1992) 903-907.

[78] M. Bodenstein, Eine Theorie der photochemischen Reaktionsgeschwindigkeiten, Zeitschrift für Physikalische Chemie, 85 (1913) 329-397.

[79] J.Y. Chen, A general procedure for constructing reduced reaction-mechanisms with given independent relations, Combustion Science and Technology, 57 (1988) 89-94.

[80] N. Peters, F.A. Williams, The asymptotic structure of stoichiometric methane air flames, Combustion and Flame, 68 (1987) 185-207.

[81] U. Maas, S.B. Pope, Simpifying chemical-kinetics - intrinsic low-dimensional manifolds in composition space, Combustion and Flame, 88 (1992) 239-264.

[82] T.F. Lu, Y.G. Ju, C.K. Law, Complex CSP for chemistry reduction and analysis, Combustion and Flame, 126 (2001) 1445-1455.

[83] T. Lu, C.K. Law, On the applicability of directed relation graphs to the reduction of reaction mechanisms, Combustion and Flame, 146 (2006) 472-483.

[84] P.J. Clymans, G.F. Froment, Computer-generation of reaction paths and rate-equations in the thermal-cracking of normal and branched paraffins, Computers & Chemical Engineering, 8 (1984) 137-142.

[85] L.P. Hillewaert, J.L. Dierickx, G.F. Froment, Computer-Generation of Reaction Schemes and Rate-Equations for Thermal Cracking, AIChE Journal, 34 (1988) 17-24.

[86] K.M. Van Geem, M.F. Reyniers, G.B. Marin, Challenges of modeling steam cracking of heavy feedstocks, Oil & Gas Science and Technology-Revue De L Institut Francais Du Petrole, 63 (2008) 79-94.

[87] T. Dijkmans, S.P. Pyl, M.-F. Reyniers, R. Abhari, K.M. Van Geem, G.B. Marin, Production of bio-ethene and propene: alternatives for bulk chemicals and polymers, Green Chemistry, 15 (2013) 3064-3076.

[88] S.L. Zhang, L.J. Broadbelt, I.P. Androulakis, M.G. Ierapetritout, Reactive Flow Simulation Based on the Integration of Automated Mechanism Generation and On the fly Reduction, Energy & Fuels, 28 (2014) 4801-4811.

[89] K.Y. He, I.P. Androulakis, M.G. Ierapetritou, Numerical Investigation of Homogeneous Charge Compression Ignition (HCCI) Combustion with Detailed Chemical Kinetics Using On the fly Reduction, Energy & Fuels, 25 (2011) 3369-3376.

[90] S.L. Zhang, I.P. Androulakis, M.G. Ierapetritou, A hybrid kinetic mechanism reduction scheme based on the on the fly reduction and quasi-steady-state approximation, Chemical Engineering Science, 93 (2013) 150-162.

[91] G.F. Froment, K.B. Bischoff, Chemical reactor analysis and design, 2nd edition ed., Wiley, 1990.

[92] R.B. Bird, W.E. Stewart, E.N. Lightfoot, Transport Phenomena, 2nd edition ed., John Wiley & Sons, New York, 2006.

[93] K.M. Van Geem, G.B. Marin, Computer aided design and optimization of olefin production plants, Computer Aided Process Engineering, 20th European symposium, Ischia, Italy, 2010.

[94] K.M. Van Geem, Single Event Microkinetic Model for Steam Cracking of Hydrocarbons, Chemische Proceskunde en Technische Chemie, Ugent, 2005-2006.

[95] G.J. Heynderickx, G.F. Froment, Simulation and comparison of the run length of an ethane cracking furnace with reactor tubes of circular and elliptical cross sections, Industrial & Engineering Chemistry Research, 37 (1998) 914-922.

[96] G.J. Heynderickx, G.G. Cornelis, G.F. Froment, Circumferential tube skin temperature profiles in thermal cracking coils, AIChE Journal, 38 (1992) 1905-1912.

[97] K.M. Sundaram, G.F. Froment, Two dimensional model for the simulation of tubular reactors for thermal cracking, Chemical Engineering Science, 35 (1980) 364-371.

[98] K.M. Van Geem, G.J. Heynderickx, G.B. Marin, Effect of radial temperature profiles on yields in steam cracking, AIChE Journal, 50 (2004) 173-183.

[99] G.H. Hu, H.G. Wang, F. Qian, Y. Zhang, J.L. Li, K.M. Van Geem, G.B. Marin, Comprehensive CFD Simulation of Product Yields and Coking Rates for a Floor- and Wall-Fired Naphtha Cracking Furnace, Industrial & Engineering Chemistry Research, 50 (2011) 13672-13685.

[100] X. Lan, J. Gao, C. Xu, H. Zhang, Numerical simulation of transfer and reaction processes in ethylene furnaces, Chemical Engineering Research & Design, 85 (2007) 1565-1579.

[101] OpenFOAM - The Open Source CFD Toolbox - User's Guide, OpenCFD Ltd, United Kingdom.

[102] OpenFOAM - The Open Source CFD Toolbox - Programmer's Guide, OpenCFD Ltd, United Kingdom.

Chapter 2:

Swirl Flow Tube reactor technology:

experimental and computational fluid

dynamics study

This chapter has been published as:

Abstract

A novel reactor technology for steam cracking reactors, called Swirl Flow Tube[®] (SFT[®]), has been evaluated experimentally and computationally. A comprehensive experimental dataset has been acquired on a newly built test set-up covering a wide range of Reynolds numbers (30,000 – 120,000) and different Swirl Flow Tube[®] designs. The Swirl Flow Tubes[®] result in an increase of heat transfer by a factor of 1.2 to 1.5 compared to a straight tube. The increased heat transfer is accompanied by an increased pressure drop by a factor 1.4 to 2.2 compared to a straight tube depending on Reynolds number and geometry. A computational fluid dynamics model was adopted that is able to capture the main flow properties of the Swirl Flow Tube[®] and this model allows to attribute the increased heat transfer and pressure drop to a higher wall shear stress. The experimental and simulation results confirm the great potential for the application of the SFT[®] technology in steam cracking furnaces because of the lower average wall temperatures and the resulting reduction of coke formation in the reactor coil.

2.1 Introduction

Steam cracking of hydrocarbons is the main industrial process for the production of almost all important base chemicals [1, 2]. In this process classically tubular reactors suspended in large gas-fired furnaces are adopted. Two side reactions detrimentally influence the process operation and profit margins, i.e. carbon oxide formation and coke deposition on the inner wall of the cracking coils and the transfer line heat exchangers [3-5]. Accumulation of coke on the reactor wall on the one hand reduces the cross-sectional flow area of the tubes, resulting in an increased pressure drop over the reactor coil. On the other hand the coke layer inhibits heat transfer from

the tube to the process gas, and hence is responsible for the rising tube wall temperatures [6]. If the reactor pressure drop is too high or the external tube skin temperature exceeds the metallurgical allowable temperature, operation is halted and the coke layer is burned off with a steam/air mixture. On the mechanical side, carburization can lead to deterioration and/or damage to the tube material. In short, coke formation affects the steam cracker's economics in 3 ways: increased energy consumption, loss of furnace availability because of decoking/mechanical failure and a decrease in ethene selectivity due to an increased pressure drop [7].

A lot of effort has been spent in the past 30 years to find appropriate methods to suppress coke formation [3, 8-18]. These technologies can be roughly divided in three categories: the use of additives [5, 13, 14], metal surface technologies [19, 20] and three-dimensional (3D) reactor technologies for enhanced heat transfer [21-25]. In the last category, three-dimensional reactor designs are used to enhance heat transfer [21], resulting in lower wall temperatures and coking rates. Designs can be divided into two classes based on the physical reason of increased heat transfer, i.e. increased internal surface area or enhanced mixing. Examples of designs belonging to this first class are finned tubes, which have been intensively studied and have been installed industrially [21, 22]. As shown in Brown et al. [25] the ratio of heat transfer improvement of a straight finned tube is linearly dependent on the surface increase. This work focusses on the second class of reactor designs, that achieves enhanced heat transfer by increasing mixing of the process gas.

Enhanced mixing leads to a more effective and homogeneous heating of the process gas. As shown from two-dimensional [26] and three-dimensional simulations [21, 27], large radial

concentration and temperature gradients exist in industrial crackers and better mixing could reduce these gradients leading to lower coking rates. Moreover, the more uniform radial temperature profile limits under- and over- cracking. One of the most applied examples is the Mixing Element Radiant Tube® (MERT®) patented by Kubota [23, 28] and claiming an increase of the heat transfer coefficient by 20-50 % compared to a straight tube [23]. This increase is explained by increased fluid mixing and break down of the thermal boundary layer on the tube internal surface by the mixing element. Progressively, the design of this element has been optimized to reduce pressure drop, first through the use of the Slit-MERT® product and nowadays with X-MERT® design. For an increase of heat transfer by a factor of 1.4 compared to a straight tube, the increase in pressure drop is reduced from 3.0 for the original MERT® to 2.4 and 2.1 for the Slit-MERT® and X-MERT® respectively.

A second approach has been developed by the Lummus Technology division in cooperation with Sinopec. Their Intensified Heat Transfer Technology (IHT) is based on the use of radiant coil inserts at certain locations in the tube [24]. The coil inserts have a twisted (100-360°) baffle integrated within their inner surface and have the same diameter and metallurgy as the radiant coil. By strategic placement, these inserts create turbulence in the process fluid, thus reducing the boundary layer and improving mixing and heat transfer while limiting the added pressure drop as much as possible. The pressure drop increases by a factor of 1.15 to 1.20 compared to a straight tube. A CFD analysis confirmed the beneficial effect on the heat transfer and uniformity of the temperature profile while only simulating a friction increase of 15 %. The helicoidal effect of the insert on the flow tends to fade away with distance, allowing careful evaluation of the optimum

locations for the inserts. A distance equal to 10-15 times the reactor inner diameter proved to be a good tradeoff between swirl flow intensity and pressure loss.

Recently a new steam cracking reactor technology aimed at enhanced mixing, the so-called Swirl Flow Tube[®] (SFT[®]) technology, was patented [29]. The cross section of the SFT[®] remains circular but the centerline follows a "small amplitude" helicoidal path providing enhanced mixing. The term "small amplitude" refers to the amplitude of the helicoidal path being equal to or smaller than the radius of the tube, leaving a line of sight through the tube. Figure 2-1 shows one helicoidal turn of a Swirl Flow Tube[®] characterized by the helix pitch P and the helix amplitude A. The relative amplitude and relative pitch are defined with respect to the tube inner diameter. At each position in the tube, the cross-sectional area is perpendicular to the helicoidal centerline. Hence the tube does not have the shape of a set of stapled coins but truly is a bended tube.
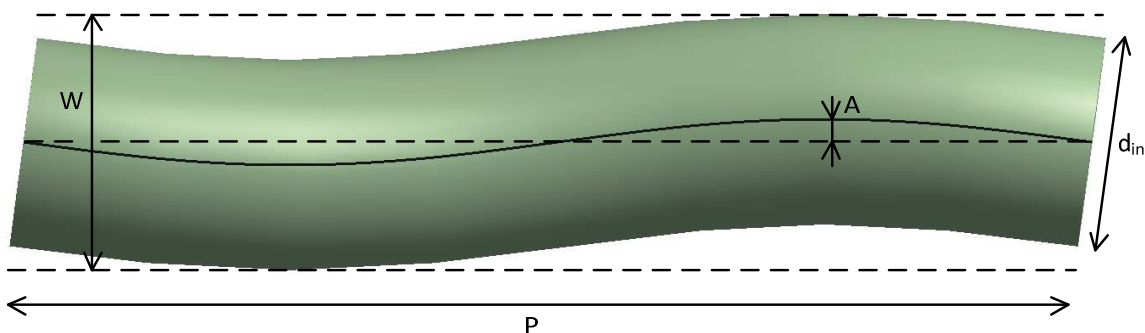
Figure 2-1: Schematic drawing of one helicoidal turn of a Swirl Flow Tube[®] (A: helix amplitude; P: helix pitch; d_{int}: tube inner diameter; W: tube width).

This technology finds its origin in biological fluid mechanics where it is seen that helicoidal stents reduce stagnation zones compared to clinical arterial bypass grafts. This led to less

instances of intimal hyperplasia which is promoted by regions with low wall shear [30]. Although the flow regime in biological fluid mechanics is laminar in contrast to the highly turbulent flow regime in steam cracking reactors, the potential advantage of these tubes for steam cracking is the high degree of swirl flow that is induced. This can be described as a rotation of the flow about the main axis of the pipe, which in this case is helicoidal itself. The net flow field can therefore be considered as a primary axial and a secondary rotating flow that rotates about this helicoidal centerline. Cookson et al. [31] numerically studied the performance of SFT$^{®}$ in laminar liquid flows. Similarly Lee et al. [32] numerically studied the effect of geometrical parameters on the steady flow hydrodynamics in helicoidally sinuous vascular prostheses.

In the present work, the performance of the SFT$^{®}$ technology at steam cracking reactor conditions is investigated. These conditions differ strongly from those of previous studies for biological fluid applications as the fluid is a gas rather than a viscous liquid. Moreover, the flow regime is highly turbulent instead of the typically studied Poisseuille blood flow in arteries. Non-reactive experiments were carried out over a wide range of relevant Reynolds numbers. A CFD model was established that allows to assess potential enhanced heat transfer. The CFD model is validated with the experimental data obtained on the test set-up.

2.2 Experimental set-up and procedure

A schematic overview of the experimental set-up is given in Figure 2-2. Air is pressurized using a compressor (1) and then reduced to operating pressure using a pressure reducer (3). The flow is measured using a thermal mass flow meter (4). Downstream of the flow meter, 2 m of straight tubing was placed to ensure that the flow is fully developed when entering the test tube. At the

inlet of the test tube, the temperature and pressure were measured using a PT100 Resistive

Temperature Device (6) and a water manometer (5). The test tube was 4 m long and had an

internal and external diameter of $28 \cdot 10^{-3}$ and $32 \cdot 10^{-3}$ m respectively.
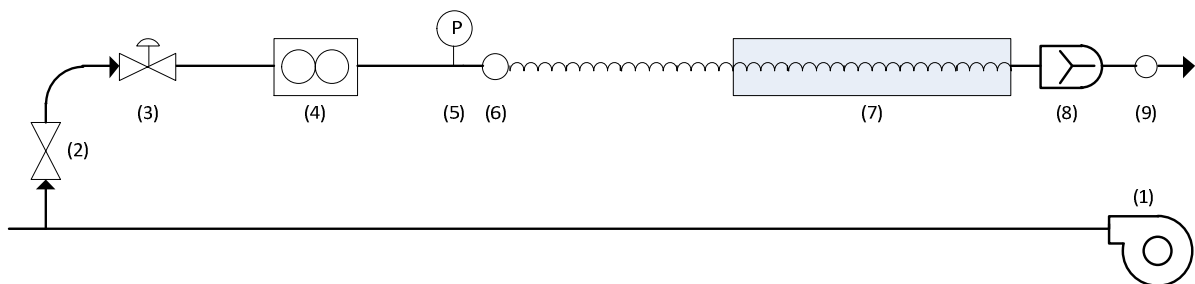
Figure 2-2: Schematic of the experimental set-up for evaluation of heat transfer enhancement (1: compressor,

2: valve, 3: pressure reducer, 4: flow meter, 5: manometer, 6: thermocouple, 7: shell and tube heat exchanger,

8: static mixer, 9: thermocouple).

Three test tubes were used: a straight tube (Straight), a mild Swirl Flow Tube® (SFT-M) and a

high Swirl Flow Tube® (SFT-H). The geometry definitions of the tubes are given in Table 1.

Table 1: Geometry definitions of adopted test tubes.

	STRAIGHT	**SFT-M**	**SFT-H**
Inside diameter [m]	0.028	0.028	0.028
Outside diameter [m]	0.032	0.032	0.032
Relative amplitude [-]	-	0.2179	0.2964
Relative pitch [-]	-	10.22	7.78
Absolute amplitude [m]	-	0.0061	0.0083
Absolute pitch [m]	-	0.2862	0.2178
Helix angle [°]	-	7.63	13.47

Two sets of experiments were performed; 14 pressure-drop experiments and 14 heat-transfer experiments. The inlet Reynolds number was varied between 30,000 and 120,000. During the pressure-drop experiments the test tube was operated adiabatically as no heating was applied and all tubing was insulated. For the heat-transfer experiments, a shell and tube heat exchanger configuration was applied by placing a steam jacket (7) around the test tube, keeping the test tube outer wall temperature at 373.15 K. Only the last 2 m of the test tube were heated to avoid asymptotic heating while the first 2 m were insulated. At the test tube outlet the temperature was again measured using a PT100 thermocouple (9). A static mixer was placed just before this thermocouple to ensure measurement of the mixing cup temperature. To compare the performance of different test tubes the classical approach based on characteristic numbers is used in line with previous works [33, 34].

For the pressure-drop experiments, the experimental data are compared in terms of Reynolds number and Fanning friction factor. The pressure drop along a straight tube can be estimated with the Darcy-Weisbach equation as denoted in the following equation:

$$\Delta p = 4 f_f \frac{L}{d_{int}} \rho |\bar{u}|^2 = 4 f_f \frac{L}{d_{int}} \frac{1}{2} \left(\frac{\phi_m}{\Omega} \right)^2 \frac{1}{\rho} \tag{2.1}$$

Hence the pressure drop along the test tube as measured experimentally can be used to determine the Fanning friction factor, according to;

$$f_f = \frac{\Delta p \, d_{int} \rho}{2L} \left(\frac{\Omega}{\phi_m} \right)^2 \tag{2.2}$$

For the heat-transfer experiments, the experimental data are compared in terms of Reynolds and

Nusselt numbers. The amount of energy transferred to the air equals:

$$Q = \phi_m c_p (T_{outlet} - T_{inlet}) \tag{2.3}$$

This amount of energy can also be estimated in heat-transfer terms as:

$$Q = \pi\, d_{int} L_h U\; LMTD \tag{2.4}$$

Where for the calculation of the LMTD, it is assumed that the wall temperature is uniformly

equal to 373.15 K as a steam jacket is placed around the test tube.

The Nusselt number is defined by the following equation:

$$Nu = \frac{U\, d_{int}}{\lambda} \tag{2.5}$$

By combination of equation (2.3), (2.4),(2.5) and (2.7), the Nusselt number can be expressed as:

$$Nu = \frac{\phi_m\, c_P\, (T_{outlet} - T_{inlet})}{\pi\, \lambda\, L_h\; LMTD} \tag{2.6}$$

All fluid properties like density, viscosity, thermal conductivity and specific heat are calculated

as the average of their values at the measured inlet and the outlet temperature.

2.3 Numerical simulation procedure

2.3.1 Mathematical model

For all simulations the steady-state condition has been considered. The 3D turbulent flow field in

the test tube is based on the solution of the RANS equations in compressible formulation. The

steady-state governing equations for continuity, momentum and energy respectively, are the

following:

$$\nabla \cdot (\rho \overline{\pmb{u}}) = 0 \tag{2.7}$$

$$\nabla \cdot (\rho \overline{\pmb{u}}\,\overline{\pmb{u}}) = -\nabla p + \nabla \cdot \overline{\overline{\tau}} \tag{2.8}$$

$$\nabla \cdot \left(\overline{\pmb{u}}(\rho E + p)\right) = \nabla \cdot \left(\lambda_{eff} \nabla T - \sum_i h_i \overline{\pmb{J}}_i\right) \tag{2.9}$$

Equation (2.8) is closed using the Reynolds Stress Model (RSM). The superior performance of this model compared to isotropic eddy-viscosity models is well known for flows with highly anisotropic Reynolds stresses as is the case of swirling flow [35, 36]. In this study also, a better agreement to experimental data was found using RSM compared to the more standard k-ε models. To avoid initial divergence of the simulations, the standard k-ε turbulence model was first used for 1000 iterations after which was switched to the RSM model.

To properly resolve the viscosity affected near-wall region, a two-layer model was adopted. This model has been shown suitable for swirling flow [34, 37]. In this model, the domain is subdivided into a viscosity-affected region and a fully turbulent region by evaluation of a wall-distance-based turbulent Reynolds number, Re_y defined as:

$$Re_y = \frac{\rho y \sqrt{k}}{\mu} \tag{2.10}$$

where y is the distance between the cell center and the nearest wall cell.

In the fully turbulent region (Re_y>200) the RSM equations are used. In the viscosity affected region (Re_y<200), the one-equation model of Wolfshtein [38] is adopted. Continuity between the two regions is provided by the blending equation of Jongen [39].

2.3.2 **Grid generation**

Figure 2-3 shows the grid of the test tube cross section. The mesh was generated using Gambit 2.4.6. The thickness of wall-adjacent cells equals 10 µm to ensure a y^+ around 1-2 for all simulations as necessary for the Wolfshtein model. This cross-sectional grid was then extruded along the test tube centerline, i.e. a line for the straight tube and a helix for the Swirl Flow Tubes®. Important to note is that the cross-sectional area is perpendicular to the centerline inside the tube as is the case for the experimentally tested Swirl Flow Tubes®. Hence, the tube does not have the shape of stapled coins but truly is a bended tube. Mesh independence tests showed that a cell size of 0.8 mm in both axial as tangential direction was necessary. For all test tubes this resulted in more than 15 million cells.
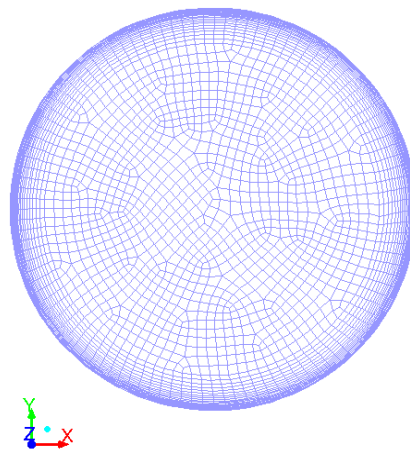
Figure 2-3: Cross-sectional grid mesh of the computational domain.

2.3.3 **Boundary conditions**

In the experimental set-up a developing tube is placed upstream of the test tube leading to fully developed flow at the inlet. Therefore a straight tube of 1 m is placed before the test tube in the simulation grid to avoid entrance effects and to assure fully developed flow. For the air inlet boundary the total mass flow rate is specified. As the outlet flow leaves to the atmosphere, a pressure outlet condition equal to 101325 Pa is specified at the outlet boundary. All walls are assumed to be smooth and a no-slip condition was adopted. An isotropic, uniform distribution for the inlet and outlet boundary condition variables was assumed. The Reynolds stresses at the inlet were assumed to be uniform and isotropic and calculated from the following empirical correlations [34] for turbulence intensity and turbulence length scale for fully developed flow:

$$I = 0.16 Re^{-\frac{1}{8}} \tag{2.11}$$

$$l = 0.07 d_{int} \tag{2.12}$$

with d_{int} the tube inner diameter.

2.3.4 **Numerical solution**

The governing equations were solved numerically using the commercial CFD code FLUENT 13.0 which is based on the finite volume method. The SIMPLE scheme was used for pressure-velocity coupling. The QUICK scheme was used for the spatial discretization of all variables. As no convergence issues were experienced default relaxation factors were adopted. Convergence was judged by monitoring residuals, inlet pressure and outlet temperature. The residual convergence criterion was set to 10^{-6} for all equations, only the energy equation criterion was set

lower to 10^{-9}. Furthermore the inlet pressure and outlet temperature were monitored and they were seen to change less than 1 Pa and 0.05 K respectively over the last 50 iterations for all simulations.

2.4 Results and discussion

2.4.1 Experimental results

Pressure-drop experiments

Figure 2-4 shows the experimental Fanning friction factors for all three test tubes and the correlation proposed by Chen et al. [40] for straight tubes with the tube surface roughness E_a set equal to 0:

$$f_f^{corr}(E_a, d_{int}, Re) = \frac{0.331369}{ln\left(\dfrac{0.269796}{d_{int}} - \dfrac{2.1911 ln\left(0.353895\left(\frac{E_a}{d_{int}}\right) + \frac{5.8506}{Re^{0.8981}}\right)}{Re}\right)^2} \quad (2.13)$$

Comparing the Swirl Flow Tubes® with the straight tube for Reynolds numbers of 35,000 to 110,000 an increase in Fanning friction factor compared to Straight by a factor of about 2.2 to 1.4 and of 2.5 to 1.8 is observed for SFT-M and SFT-H respectively.
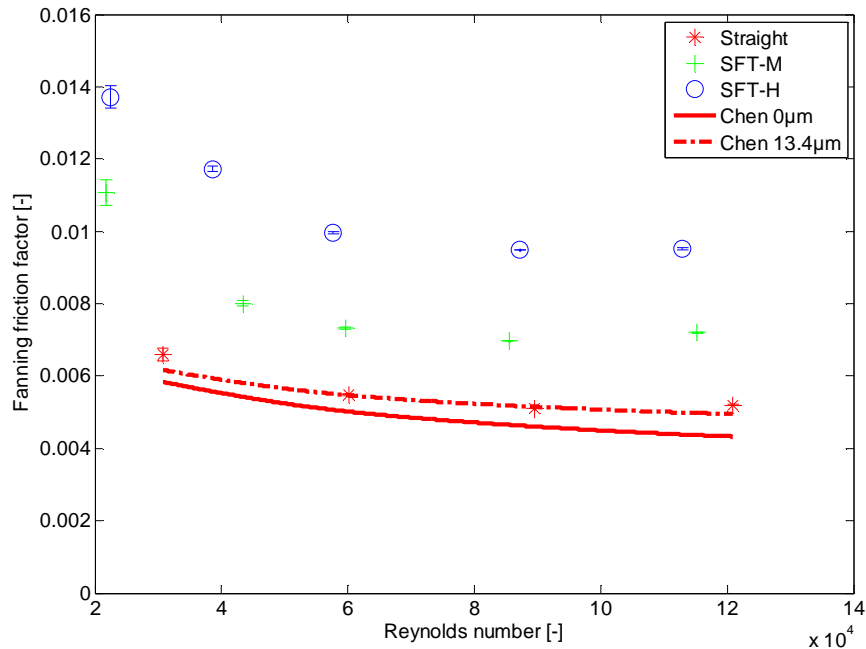
Figure 2-4: Fanning friction factor as a function of inlet Reynolds number for pressure-drop experiments: experimental values: ✳ **- Straight;** + **- SFT-M;** ○ **- SFT-H, Chen correlation by Eq. (2.13):** ▬ **- $E_a = 0$ m;** ┊ ▬ · ▬ **- $E_a = 13.4\,\mu m$).**

The experimental values for the straight tube are underpredicted by the correlation when assuming a tube surface roughness equal to 0. This is caused by the experimental tube not being ideally smooth. As all CFD simulations are performed for smooth tubes, a correction factor needs to be applied for comparison with experimental Fanning friction factors. As the tube roughness is unknown, the tube roughness in equation (2.13) is calibrated to the experimental data for the straight tubes using the following equation:

$$\min_{E_a} \sum_{i=1}^{4} \left(\frac{f_{f,i}^{exp} - f_{f,i}^{corr}(E_a, d_{int}, Re_i)}{f_{f,i}^{exp}} \right)^2 \tag{2.14}$$

By solving equation (2.14), an absolute roughness of 13.4 µm is found. This roughness is assumed to be the roughness of all test tubes and is in line with the typical roughness of fresh steel tubes [41]. Hence, all Fanning friction factors calculated from CFD simulations are multiplied with the following correction factor for comparison with experimental Fanning friction factors:

$$\alpha(d_{int}, Re) = \frac{f_f^{corr}(13.4 \cdot 10^{-6}, d_{int}, Re)}{f_f^{corr}(0, d_{int}, Re)} \tag{2.15}$$

$$ff_{sim} = ff_{CFD} \cdot \alpha(d_{int}, Re) \tag{2.16}$$

Based on the pressure-drop experiments the SFT-M tube has higher potential for steam cracking applications because of the reduced pressure drop compared to the SFT-H tube. Higher pressures affect light olefin selectivity [42], and hence, strongly influence the steam cracking economics.

Heat-transfer experiments

Figure 2-5 shows the experimental Nusselt numbers for all three test tubes and the correlation proposed by Gnielinski et al. [43] for straight tubes:

$$Nu = \frac{(\varepsilon/8)(Re - 1000)Pr}{1 + 12.7(\varepsilon/8)^{1/2}(Pr^{2/3} - 1)} \tag{2.17}$$

where $\varepsilon = (1.82 log(Re) - 1.64)^{-2}$.

Comparing the Swirl Flow Tubes$^{\circledR}$ with the straight tube for Reynolds numbers from 30,000 to 110,000 an increase in Nusselt number compared to Straight by a factor of 1.26 to 1.22 and from

1.49 to 1.45 is observed for SFT-M and SFT-H respectively. The better heat transfer for the SFT-H tube will result in lower wall temperatures in steam cracking reactors, and hence, in line with the coking model of Plehiers and Froment [44], this can result in lower coking rates if the concentrations of coke precursors are identical. Taking into account these considerations the SFT-H tube would be preferred to the SFT-M tube for steam cracking purposes if reduced coke formation is taken as sole criterion.

Furthermore it is seen that the Gnielinski correlation overpredicts the experimentally obtained values for the straight tube. However the agreement provides sufficient accuracy for the scope of this work.
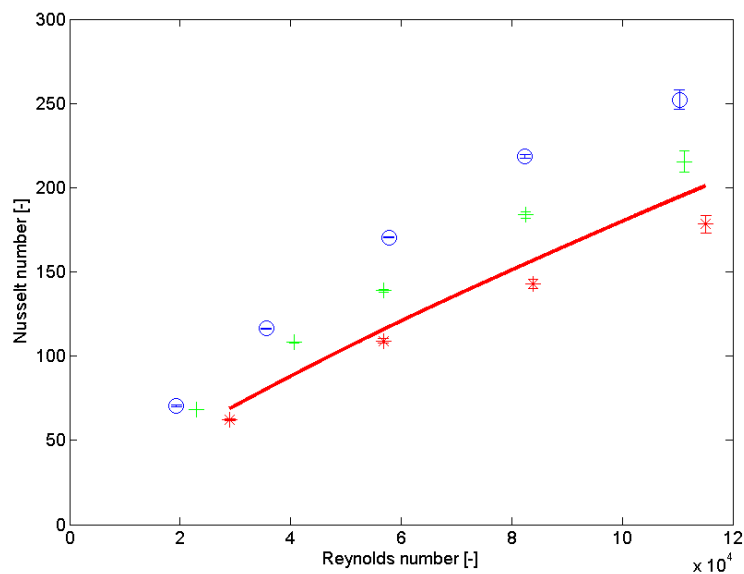
Figure 2-5: Global Nusselt number as a function of inlet Reynolds number for heat-transfer experiments: experimental values: ✳ - Straight; ✛ - -SFT-M; ◯ - SFT-H, lines: ▬ - Gnielinski correlation by Eq. (2.17).

2.4.2 **Simulation results**

Pressure drop

Figure 2-6 shows a comparison between experimental and simulated Fanning friction factors for all 14 pressure-drop experiments. In general the agreement is good with average relative deviations equal to 2.5, 4.4 and 2.4 % for the straight, SFT-M and SFT-H test tube respectively. For the straight tube the largest deviations are obtained at the lowest and highest Reynolds numbers which is in agreement with the deviations of the Chen correlation to the experimental results as shown in Figure 2-4.

Figure 2-7A and B show the velocity magnitude in a cross section at different axial positions along test tube SFT-M at an inlet Reynolds number of 21,740 and 115,270 respectively. As the centrifugal force acts on the fluid, the position of maximum velocity magnitude shifts closer to the tube wall as can be seen in Figure 2-7A. After 6 pitches the velocity field breaks up into two vortices creating a C-shaped region of high velocity while a local minimum is created close to the tube wall where the two vortices touch and leave the tube inner wall as described by Cookson et al. for laminar flow [31]. Comparing the velocity fields in the cross section after 6 and 12 pitches, it is observed that the shape of the velocity field in a cross-section no longer changes as fully-developed turbulent flow is established. Comparing Figure 2-7A and B the shape of the velocity magnitude continues to change so no fully developed flow is yet established at the highest adopted Reynolds number.
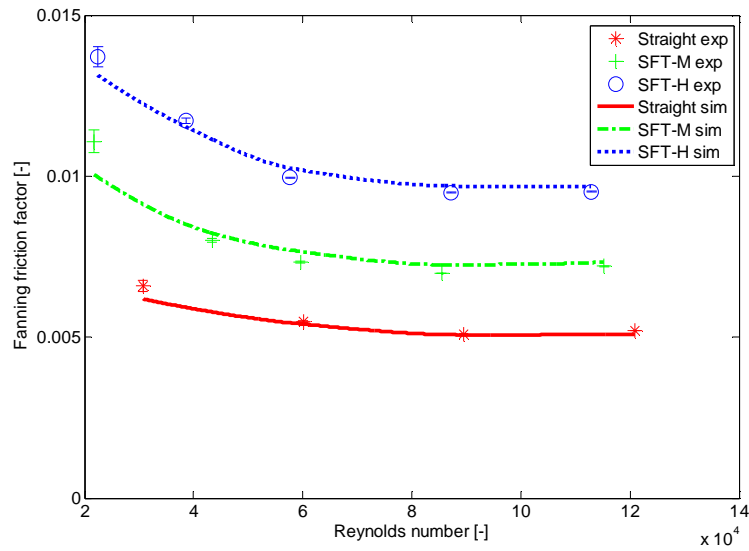
Figure 2-6: Fanning friction factor as a function of Reynolds number for pressure-drop experiments; experimental values: ✳ - Straight; ✛ - SFT-M; ◯ - SFT-H and simulated values: ▬ - Straight; ▬·▬· - SFT-M; ▪▪▪▪ - SFT-H.

Figure 2-7: Velocity (m/s) field at an inlet Reynolds number of (A) $21·10^3$ (B) $115·10^3$ at different axial positions along test tube SFT-M (from left to right: after 0, 3, 6, 9 and 12 pitches).

Figure 2-8 shows the wall shear stress in a cross section at four axial positions along the azimuthal coordinate of the cross section. The changing velocity field has a profound effect on the wall shear stress. After 3 pitches, the wall shear stress profile has a rather broad maximum corresponding to the broad velocity maximum close to the wall seen in the second cross section of Figure 2-7A. However, after 6 pitches a narrow minimum in the wall shear stress profile is simulated. This minimum corresponds to the local velocity minimum seen in the cross sections of Figure 2-7A.

Figure 2-8: Wall shear stress as a function of azimuthal coordinate at an inlet Reynolds number of $21 \cdot 10^3$ at different axial positions along test tube SFT-M; after 3 (A), 6 (B), 9 (C) and 12 (D) pitches.

Heat transfer

Figure 2-9 shows a comparison between experimental and simulated Nusselt numbers for all 14 heat-transfer experiments. A general overprediction is simulated with average relative deviations equal to 13.4, 9.4 and 8.1 % for the Straight, SFT-M and SFT-H test tube respectively. As the simulated results for the straight tube are in good agreement with the Gnielinski correlation and the relative errors for the SFT-M and SFT-H are lower than for the straight tube, the simulated results are considered to provide sufficient accuracy.
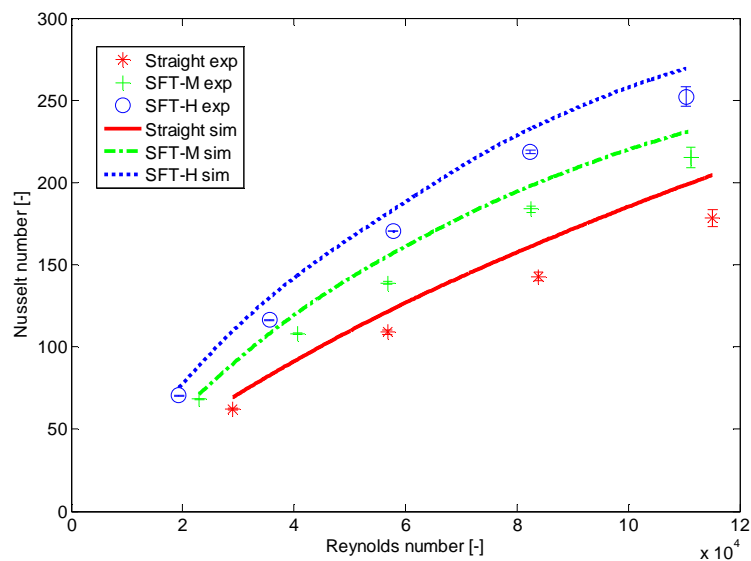
Figure 2-9: Nusselt number as a function of Reynolds number for heat-transfer experiments; experimental values; ✳ - Straight; + - SFT-M; ◯ - SFT-H and simulated values: ▬▬ - Straight; ▬·▬ - SFT-M; ▪▪▪▪▪ - SFT-H.

Figure 2-10A and B show the temperature of the air at several axial positions for an inlet Reynolds number of $23 \cdot 10^3$ and $113 \cdot 10^3$ respectively. Comparing with Figure 2-7, a high

similarity between the temperature and velocity field can be noted. First the minimum in temperature is shifted towards the tube wall as is the velocity magnitude maximum in Figure 2-7. After several helices as the velocity profile breaks up into two vortices, the temperature profile shows a C-shaped region of low temperature corresponding to the C-shaped region of high velocity in Figure 2-7. A region of higher temperature is created close to the tube wall corresponding to the low velocity regions seen in Figure 2-7. Comparing the low and high inlet Reynolds number simulations in Figure 2-10, a faster development of the C-shaped region is noted.
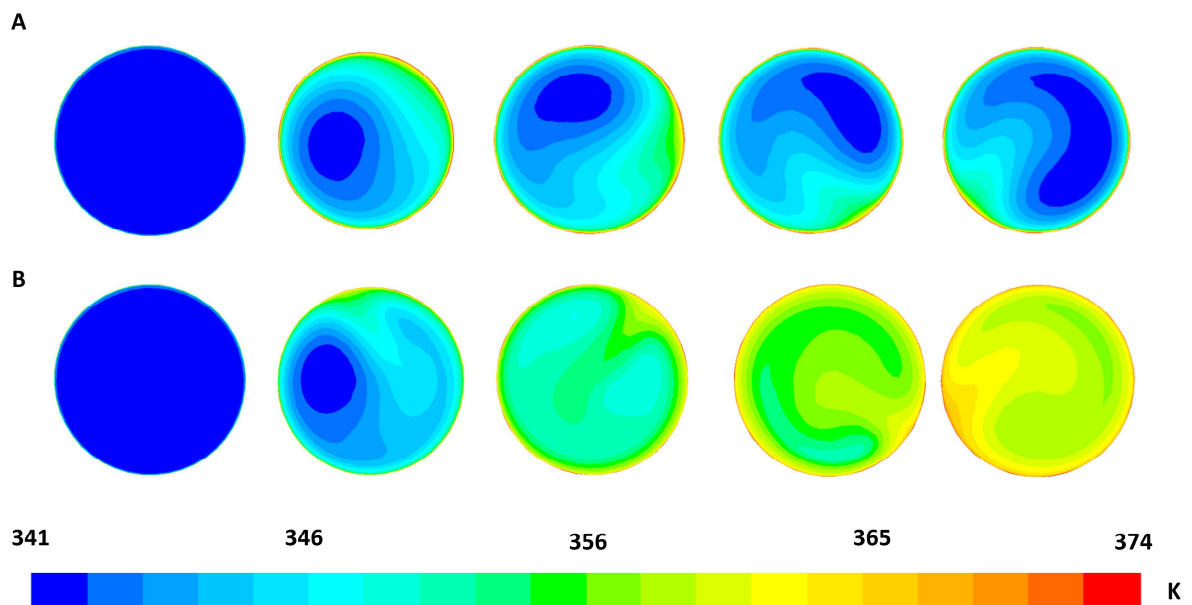
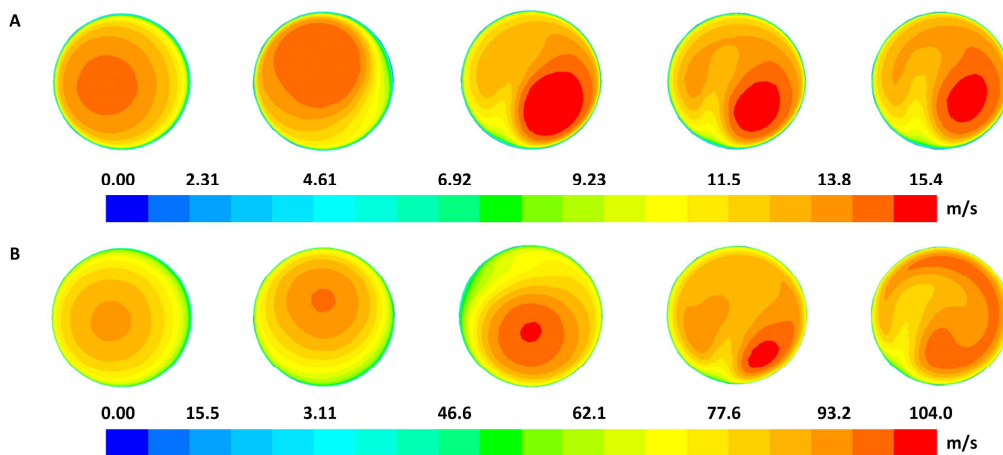**Figure 2-10: Temperature (K) at an inlet Reynolds number of (A) $23 \cdot 10^3$ (B) $111 \cdot 10^3$ at different axial positions along test tube SFT-M (from left to right: 0, 0.5, 1, 1.5 and 2 m).**

Figure 2-11 and Figure 2-12 show respectively the heat flux profile and the wall shear stress at the tube inner wall at several axial positions for the straight and SFT-M test tube. Comparing the wall shear stress and the heat flux profile shapes, large similarity is again seen. At positions with high wall shear stress, high heat fluxes are located due to the gas scouring the tube inner wall, reducing the boundary layer thickness. At the positions where the narrow minimum in wall shear stress occurs a similar minimum in heat flux is located. Comparing the profiles for both the wall shear stress and the heat flux for the Straight and the SFT-M test tube, it is seen that the minima for the SFT-M test tube are lower than the uniform value simulated for the straight tube, however the main part of the SFT-M profiles is higher than their counterpart in the Straight test tube. This results in higher average values for the SFT-M as also shown on Figure 2-11. The higher heat transfer and higher pressure drop for the SFT$^{®}$ can thus be attributed to the higher average wall shear stress due to the higher velocities close to the tube wall. Further downstream the tube, the heat flux values of the Straight tube get closer to the SFT-M values as the air temperature in the SFT-M is higher downstream due to better heat transfer resulting in a lower driving force for heat transfer as the wall temperature is uniform along the tube.
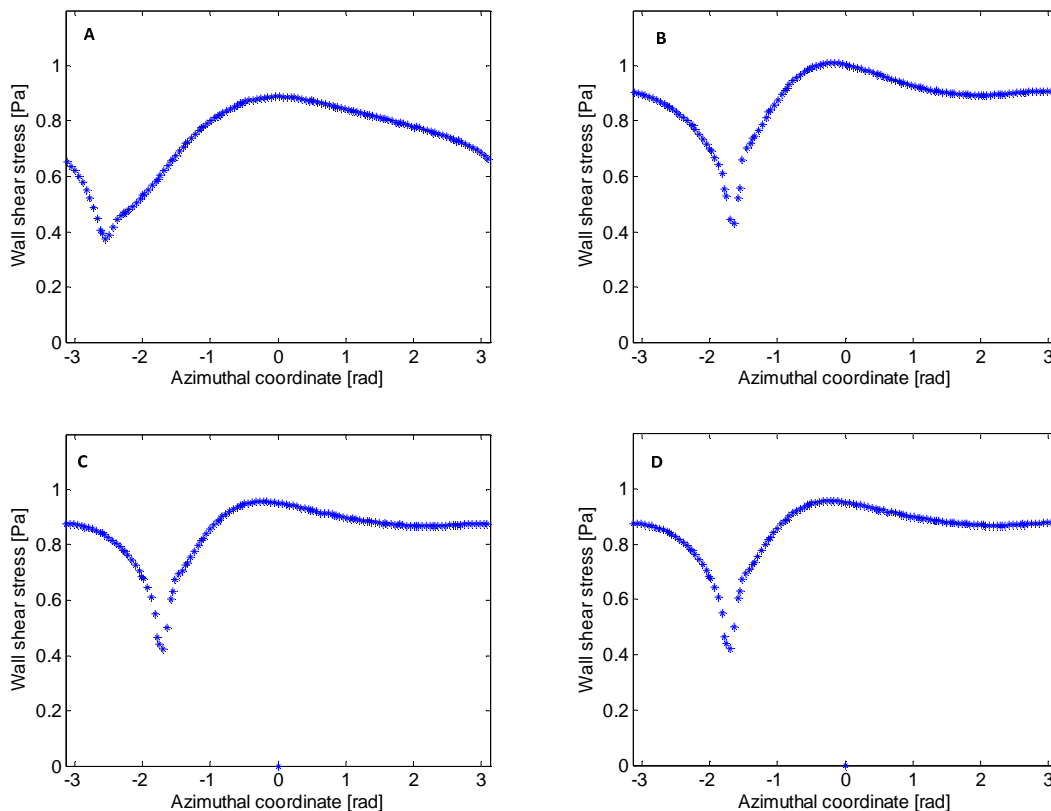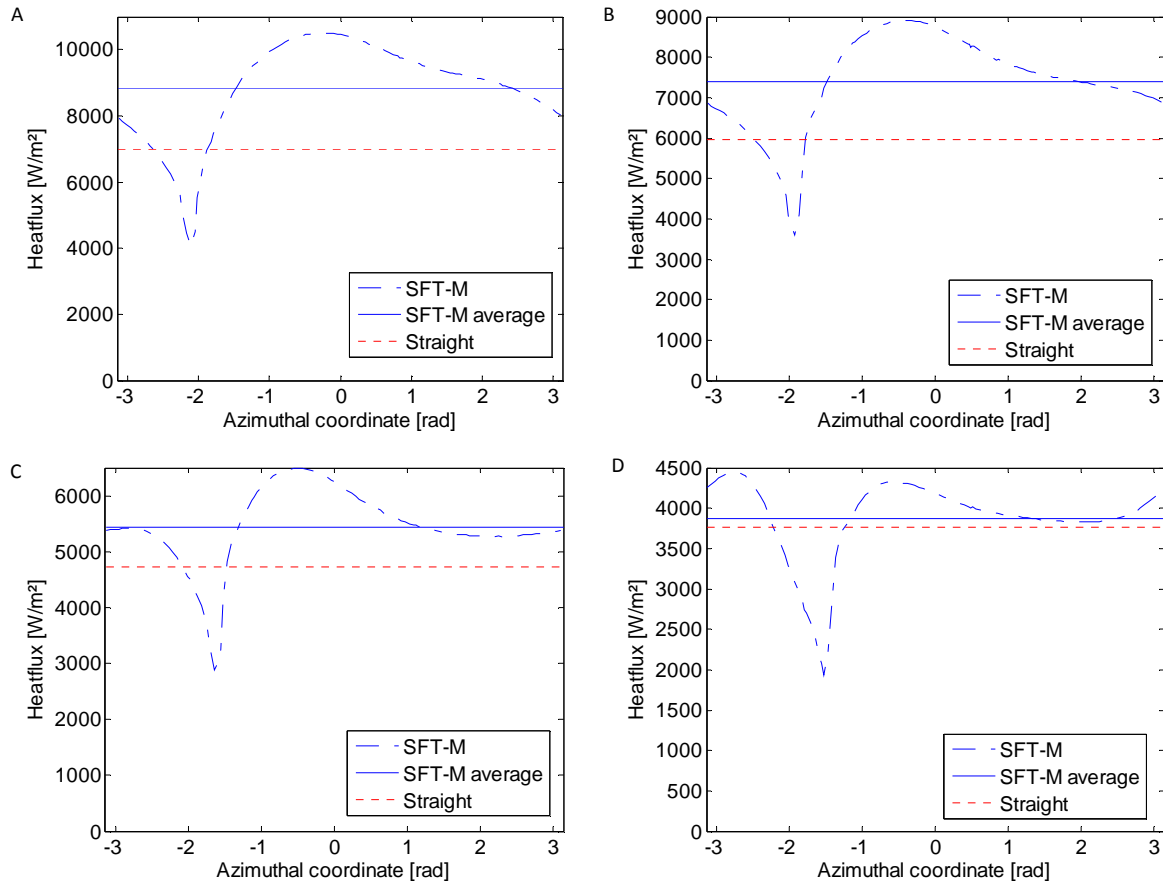
Figure 2-11: Heat flux as a function of azimuthal coordinate at an inlet Reynolds number of 60·10³ at different axial positions along the test tube;   ⸺ · SFT-M;   ⸺ - SFT-M average;   --- - Straight; A: after 1 (A), 2 (B), 4 (C) and 6 (D) pitches after heating is applied (i.e. after 2 m).
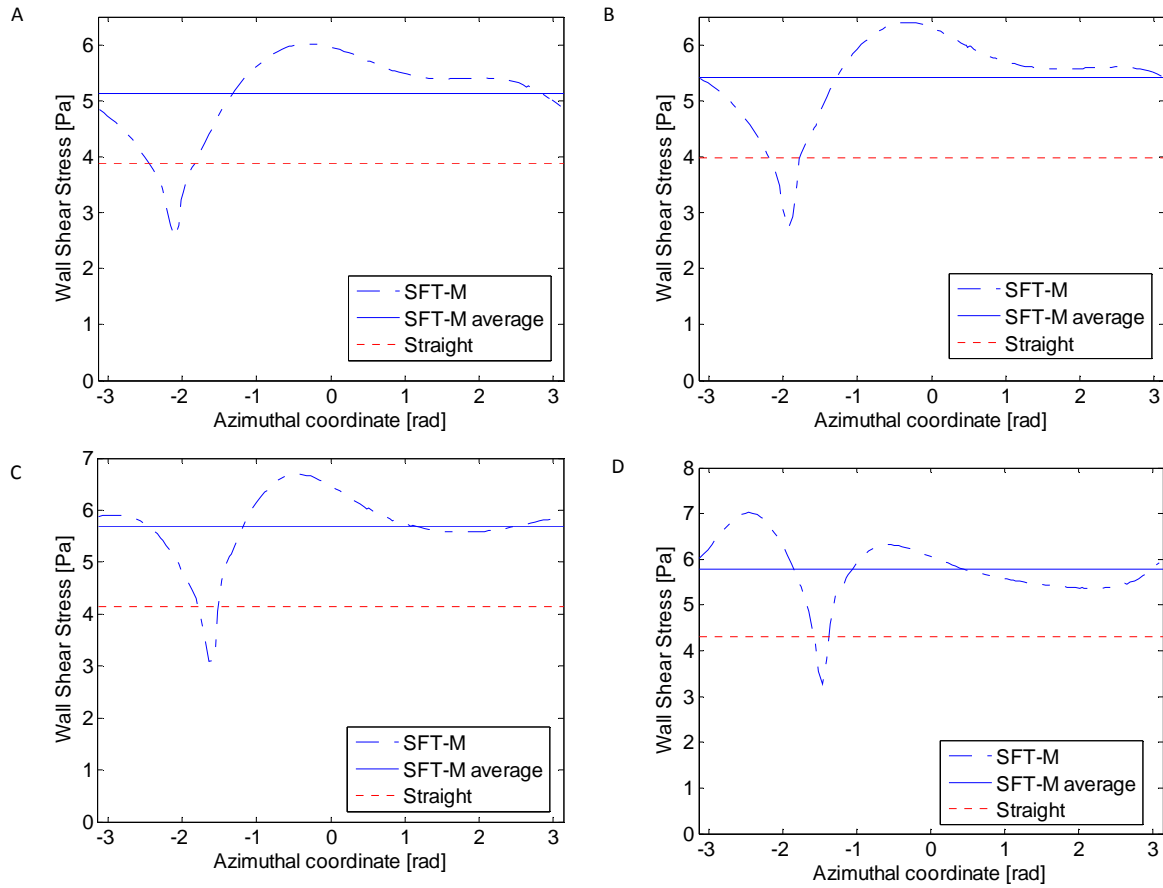
Figure 2-12: Wall shear stress in a cross section at an inlet Reynolds number of $60 \cdot 10^3$ at different axial positions along the test tube; ; — · - SFT-M; —— - SFT-M average; - - - - Straight; after 1 (A), 2 (B), 4 (C) and 6 (D) pitches after heating is applied (i.e. after 2 m).

To assess the uniformity in a cross section, a weighed temperature variance is calculated from the discrete temperatures from the computational surfaces at the tube cross section:

$$\frac{\sqrt{\dfrac{\sum_{i=1}^{N} \phi_{m,i}\left(T_i - T_{avg}\right)^2}{\phi_{m,tot}}}}{T_{avg}} \tag{2.18}$$

with $\phi_{m,i}$ the mass flow rate leaving the local surface i, $\phi_{m,tot}$ the total mass flow rate, T_i the local gas temperature and T_{avg} the mixing cup temperature of the cross section. This coefficient is shown in Figure 2-13 as a function of the axial length for the Straight, SFT-M and SFT-H test tube at an inlet Reynolds number of $60 \cdot 10^3$. As seen from this figure, the temperature variance is lower for the SFT® test tubes so a more uniform temperature profile is obtained by adopting a SFT®. The SFT-H tube shows the best results at the expense of a higher pressure drop as mentioned before. The more uniform temperature can be attributed to the stronger in-plane mixing by the swirl flow induced by the SFT® and the higher heat transfer rate.
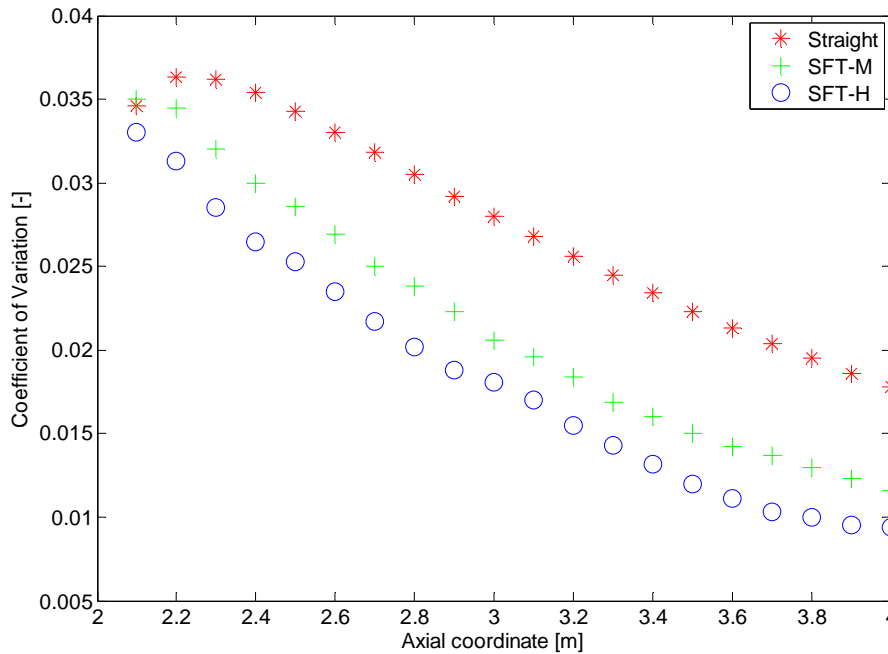
Figure 2-13: Mixing cup weighted temperature variance as a function of the axial coordinate for the heat-transfer experiments: ✳ - Straight; + - SFT-M; ○ - SFT-H.

These considerations are interesting for non-reactive flow, but are even more relevant in the case of reactive flow in steam crackers. As a greater temperature uniformity goes coupled with greater species concentration uniformity, a more uniform profile will provide lower coking rates and more controlled cracking, i.e. less under- and overcracking [21]. However, the area of high temperature close to the wall can induce a local high coke formation. Hence, the coke thickness will not grow uniform in a cross-section. Obviously, incorporation of detailed chemistry drastically increases computational cost [45-48]. Implementing chemical gas-phase reactions and a coking model in the 3D flow model is discussed in Chapter 3, 4 and 5 of this thesis.

2.5 Conclusions

A novel reactor design for steam cracking reactors, called Swirl Flow Tube® has been evaluated experimentally in a newly constructed test set-up. Three test tubes were used: a straight tube, a mild Swirl Flow Tube® (SFT-M) and a high Swirl Flow Tube® (SFT-H). For Re numbers in the range of 30,000 – 120,000, the SFT-M tube has a lower pressure drop compared to the SFT-H tube. However, the latter results in an increase of heat transfer by 20 % compared to the SFT-M tube and up to 50 % compared to the straight tube. The results prove that indeed for swirl flow reactors higher heat transfer rates can be obtained compared to conventional straight tubes at the cost of a higher pressure drop. This is a factor 1.4 to 2.2 higher depending on Reynolds number and geometry.

A CFD model was adopted that is able to capture the main flow properties of the SFT®. Mesh independence tests showed that a cell size of 0.8 mm in both axial as tangential direction was necessary, resulting in meshes of more than 15 million cells. The increased heat transfer and pressure drop result from a higher wall shear stress. A narrow area of low velocity and high temperature close to the tube wall is simulated. The effect of the latter on coke formation on the reactor wall in processes like steam cracking can be accounted for by implementing a gas-phase reaction model and a coking model. This is discussed further in Chapter 3, 4 and 5 of this thesis.

References

[1] T. Ren, B. Daniëls, M.K. Patel, K. Blok, Petrochemicals from oil, natural gas, coal and biomass: Production costs in 2030–2050, Resources, Conservation and Recycling, 53 (2009) 653-663.

[2] T. Ren, M.K. Patel, K. Blok, Steam cracking and methane to olefins: Energy use, CO2 emissions and production costs, Energy, 33 (2008) 817-833.

[3] S. Wauters, G.B. Marin, Kinetic Modeling of Coke Formation during Steam Cracking, Industrial & Engineering Chemistry Research, 41 (2002) 2379-2391.

[4] K.M. Van Geem, R. Zajdlik, M.F. Reyniers, G.B. Marin, Dimensional analysis for scaling up and down steam cracking coils, Chemical Engineering Journal, 134 (2007) 3-10.

[5] J. Wang, M.-F. Reyniers, K.M. Van Geem, G.B. Marin, Influence of silicon and silicon/sulfur-containing additives on coke formation during steam cracking of hydrocarbons, Industrial & Engineering Chemistry Research, 47 (2008) 1468-1482.

[6] H. Zimmermann, R. Walzl, Ethylene, in: Ullmann's Encyclopedia of Industrial Chemistry, Wiley-VCH Verlag GmbH & Co. KGaA, 2000.

[7] E. Ranzi, M. Dente, S. Pierucci, S. Barendregt, P. Cronin, Coking simulation aids on-stream time, Oil & Gas Journal, 83 (1985) 49-52.

[8] R.E. Lobnig, H.J. Grabke, Mechanisms of simultaneous sulfidation and oxidation of Fe-Cr and Fe-Cr-Ni-alloys and of the failure of protective chromia scales, Corrosion Science, 30 (1990) 1045-1071.

[9] M. Bajus, J. Baxa, Coke formation during the pyrolysis of hydrocarbons in the presence of sulfur-compounds, Collection of Czechoslovak Chemical Communications, 50 (1985) 2903-2909.

[10] W. Anon, New additive retards coke formation in ethylene furnace tubes, Oil & Gas Journal, 92 (1994) 73-75.

[11] K.K. Ghosh, D. Kunzru, Sodium-silicate as a coke inhibitor during naphtha pyrolysis, Canadian Journal of Chemical Engineering, 70 (1992) 394-397.

[12] A.G. Goossens, M. Dente, E. Ranzi, Improve steam cracker operation, Hydrocarbon Processing, 57 (1978) 227-236.

[13] P. Das, S. Prasad, D. Kunzru, Organophosphorus compounds as coke inhibitors during naphtha pyrolysis - effect of benzyl diethyl phosphite and triphenylphosphine sulfide, Industrial & Engineering Chemistry Research, 31 (1992) 2251-2255.

[14] S. Vaish, D. Kunzru, Triphenyl phosphite as a coke inhibitor during naphtha pyrolysis, Industrial & Engineering Chemistry Research, 28 (1989) 1293-1299.

[15] H.M. Woerde, S. Barendregt, F. Humblot, C. Brun, Mitigate coke formation, Hydrocarbon Processing, 81 (2002) 45-50.

[16] I. Dhuyvetter, M.-F. Reyniers, G.F. Froment, G.B. Marin, D. Viennet, The influence of dimethyl disulfide on naphtha steam cracking, Industrial & Engineering Chemistry Research, 40 (2001) 4353-4362.

[17] M.-F. Reyniers, G.F. Froment, Influence of metal-surface and sulfur addition on coke deposition in the thermal-cracking of hydrocarbons, Industrial & Engineering Chemistry Research, 34 (1995) 773-785.

[18] D.E. Brown, J.T.K. Clark, A.I. Foster, J.J. McCarroll, M.L. Sims, Inhibition of coke formation in ethylene steam cracking, Acs Symposium Series, 202 (1982) 23-43.

[19] P. Broutin, F. Ropital, M.-F. Reyniers, G.F. Froment, Anticoking coatings for high temperature petrochemical reactors, Oil & Gas Science and Technology - Revue D'Institut Français du Pétrole Energies Nouvelles, 54 (1999) 375-385.

[20] S.B. Parks, C.M. Schillmoller, Use alloys to improve ethylene production, Hydrocarbon Processing, 75 (1996) 53-&.

[21] J.J. De Saegher, T. Detemmerman, G.F. Froment, Three dimensional simulation of high severity internally finned cracking coils for olefins production, Revue De L'Institut Français Du Pétrole, 51 (1996) 245-260.

[22] T. Detemmerman, G.F. Froment, Three dimensional coupled simulation of furnaces and reactor tubes for the thermal cracking of hydrocarbons, Revue De L'Institut Français Du Pétrole, 53 (1998) 181-194.

[23] M. Györffy, M. Hineno, H. Kunihude, P. Seong-Hoan, Y. Min-Soo, MERT performance and technology update, AIChE Spring Meeting: Ethylene producers meeting, Tampa Bay, US, 2009, pp. 7.

[24] A. Carrillo, Intensified Heat Transfer technology - CFD analysis to explain how and why IHT increases runlength in commercial furnaces, AIChE Spring Meeting 2010: Ethylene producers meeting, San Antonio, TX, 2010.

[25] D.J. Brown, Internally finned radiant coils: a valuable tool for improving ethylene plant economics, 6th EMEA Petrochemicals Technology Conference, London, U.K., 2004.

[26] K.M. Van Geem, G.J. Heynderickx, G.B. Marin, Effect of radial temperature profiles on yields in steam cracking, AIChE Journal, 50 (2004) 173-183.

[27] G.H. Hu, H.G. Wang, F. Qian, Y. Zhang, J.L. Li, K.M. Van Geem, G.B. Marin, Comprehensive CFD Simulation of Product Yields and Coking Rates for a Floor- and Wall-Fired Naphtha Cracking Furnace, Industrial & Engineering Chemistry Research, 50 (2011) 13672-13685.

[28] T. Torigoe, K. Hamada, M. Furuta, M. Sakashita, K. Otsubo, M. Tomita, Mixing element radiant tube (MERT) improves cracking furnace performance, 11th Ethylene Producers' Conference, Houston, TX, 1999.

[29] C.G. Caro, P.L. Birch, W. Tallis, Olefin production furnace with a helical tube, T. S.A.S., European Patent Source, (2010).

[30] C.G. Caro, N.J. Cheshire, N. Watkins, Preliminary comparative study of small amplitude helical and conventional ePTFE arteriovenous shunts in pigs, J. R. Soc. Interface, 2 (2005) 261-266.

[31] A.N. Cookson, D.J. Doorly, S.J. Sherwin, Mixing Through Stirring of Steady Flow in Small Amplitude Helical Tubes, Annals of Biomedical Engineering, 37 (2009) 710-721.

[32] K.E. Lee, J.S. Lee, J.Y. Yoo, A numerical study on steady flow in helically sinuous vascular prostheses, Medical Engineering & Physics, 33 (2011) 38-46.

[33] J.V. Albano, K.M. Sundaram, M.J. Maddock, Applications of Extended Surfaces in Pyrolysis Coils, Energy Progress, 8 (1988) 160-168.

[34] M. Ahmadvand, A.F. Najafi, S. Shahidinejad, An experimental study and CFD analysis towards heat transfer and fluid flow characteristics of decaying swirl pipe flow generated by axial vanes, Meccanica, 45 (2010) 111-129.

[35] A.M. Jawarneh, G.H. Vatistas, Reynolds stress model in the prediction of confined turbulent swirling flows, Journal of Fluids Engineering-Transactions of the Asme, 128 (2006) 1377-1382.

[36] S.L. Yang, Y.K. Siow, B.D. Peschke, R.R. Tacina, Numerical study of nonreacting gas turbine combustor swirl flow using Reynolds stress model, J. Eng. Gas. Turbines Power-Trans. ASME, 125 (2003) 804-811.

[37] A.F. Najafi, M.H. Saidi, M.S. Sadeghipour, M. Souhar, Numerical analysis of turbulent swirling decay pipe flow, International Communications in Heat and Mass Transfer, 32 (2005) 627-638.

[38] M. Wolfshtein, The velocity and temperature distribution in one-dimensional flow with turbulence augmentation and pressure gradient, International Journal of Heat and Mass Transfer, 12 (1969) 301-318.

[39] T. Jongen, Simulation and modeling of turbulent incompressible fluid flows, EPFL, 1998.

[40] N.H. Chen, An explicit equation for friction factor in pipe, Ind. Eng. Chem. Fundam., 18 (1979) 296-297297.

[41] D.W. Green, R.H. Perry, Perry's chemical engineers' handbook 8th edition, 2007.

[42] K.M. Van Geem, M.F. Reyniers, G.B. Marin, Two severity indices for scale-up of steam cracking coils, Industrial & Engineering Chemistry Research, 44 (2005) 3402-3411.

[43] V. Gnielinski, New equations for heat and mass-transfer in turbulent pipe and channel flow, International Chemical Engineering, 16 (1976) 359-368.

[44] P.M. Plehiers, G.F. Froment, Firebox simulation of olefin units, Chemical Engineering Communications, 80 (1989) 81-99.

[45] W.J. Pitz, C.J. Mueller, Recent progress in the development of diesel surrogate fuels, Progress in Energy and Combustion Science, 37 (2011) 330-350.

[46] T. Lu, C.K. Law, Toward accommodating realistic fuel chemistry in large-scale computations, Progress in Energy and Combustion Science, 35 (2009) 192-215.

[47] K.Y. He, M.G. Ierapetritou, I.P. Androulakis, Integration of On-The-Fly Kinetic Reduction with Multidimensional CFD, AIChE Journal, 56 (2010) 1305-1314.

[48] L. Liang, J.G. Stevens, J.T. Farrell, A dynamic adaptive chemistry scheme for reactive flow computations, Proceedings of the Combustion Institute, 32 (2009) 527-534.

Chapter 3:

Computational Fluid Dynamics-based design of finned steam cracking reactors

This chapter has been published as:

Abstract

The use of one-dimensional reactor models to simulate industrial steam cracking reactors has been one of the main limiting factors for the development of new reactor designs and the evaluation of existing three-dimensional (3D) reactor configurations. Therefore a three-dimensional computational fluid dynamics approach is proposed in which the detailed free-radical chemistry is accounted for. As a demonstration case the application of longitudinally and helicoidally finned tubes as steam cracking reactors was investigated under industrially relevant conditions. After experimental validation of the modeling approach, a comprehensive parametric study allowed to identify optimal values of the fin parameters, i.e. fin height, number of fins and helix angle to maximize heat transfer. Reactive simulations of an industrial Millisecond propane cracker were performed for four distinct finned reactors using a reaction network of 26 species and 203 elementary reactions. The start-of-run external tube metal temperatures could be reduced by up to 50 K compared to conventionally applied bare tubular reactors when applying optimal fin parameters. Implementation of a validated coking model for light feedstocks showed that coking rates are reduced up to 50 %. However, the increased friction and inner surface area lead to pressure drops higher by a factor from 1.22 to 1.66 causing minor but significant shifts in light olefin selectivity. For the optimized helicoidally finned reactor the ethene selectivity dropped, while propene and 1,3-butadiene selectivity increased with a similar amount.

Keywords: steam cracking, CFD, olefins, coke formation, finned reactor, enhanced heat transfer

3.1 Introduction

Steam cracking of hydrocarbons is the predominant commercial process for producing many platform chemicals such as light olefins (i.e. ethene, propene and butadiene) and aromatics (i.e. benzene, toluene and xylenes). These platform chemicals are the building blocks for most polymers and the starting molecules for the production of many additives, solvents and other high-value chemicals. The process is one of the most energy-intensive processes in the chemical industry using about 8 % of the industry's primary energy consumption [1]. This is mainly associated with the energy consumed in the separation section, in which temperatures lower than 160 K can be encountered [2]. However, also in the furnace considerable energy efficiency improvements are possible. Per ton high value chemicals approximately 1 ton of CO_2 is produced and depending on the cracker's design and feedstock 10 – 15 GJ energy is consumed [1, 3]. A major factor for the process energy efficiency is the formation of coke on the inner wall of the tubular cracking reactors. This carbonaceous coke layer reduces the cross-sectional area and leads to an increasing reactor pressure drop over time. The latter promotes bimolecular reactions over monomolecular reactions, typically associated with a loss in olefin selectivity [4]. Moreover, this coke layer is highly insulating, increasing the conductive resistance for heat transfer from the furnace to the process gas. To maintain the same cracking severity, this increased heat transfer resistance is compensated by increasing the fuel input to the furnace burners. This leads to higher external tube metal temperatures (TMT). Eventually, either metallurgical constraints of the reactor alloy or an excessive pressure drop over the reactor will force the operators to cease production and decoke the reactors. Typically this will require production to be halted for 36-48 hours, having a considerable adverse effect on the economics of the process.

In light of this energetic and economic drawback, many efforts have been made towards the development of technologies to reduce coke formation. These technologies can be divided into three groups: additives, surface technologies and three-dimensional reactor configurations for heat transfer enhancement. As additives mainly sulfur-containing components [5, 6] are used. While a general consensus exists on the beneficial effect for the suppression of CO production, the reported effect on coke formation is contradictory [5, 7]. For metal surface technologies, low-coking alloys [8, 9] and (catalytic) coatings [10-15] are typically studied.

In this chapter, the focus is on the third group, i.e. the application of three-dimensional reactor configurations. By means of improved heat transfer, lower temperatures at the coke-gas interface and thus lower coking rates are obtained compared to conventional tubular reactors. Alternatively, the reactor throughput and the furnace fuel flow rate could be increased while maintaining the tube skin temperature. One such three-dimensional reactor configuration is the use of longitudinal or helicoidal fins on the reactor tube inner surface, allowing improved heat transfer mainly because of an increased internal surface area.

Although the literature on this topic for heat exchanger applications is extensive [16-18], the characteristics of the flow inside finned tubes are still not well understood due to the limited availability of accurate experimental data [18]. Water flow visualization studies indicate the existence of different regimes, depending on the angle between the fins and the tube axis [17, 19]. For helix angles smaller than 30° and for relatively tall and few fins, a rotational pattern dominates as the flow follows the space in between the fins and swirling flow, i.e. a large azimuthal velocity component, is established. However, when using larger helix angles the flow is seen to be prone to coring, i.e. the main portion of the flow is constrained to the core of the

tube. A number of correlations for the Nusselt numbers and friction factors of these tubes have already been proposed, but none of these are valid over the entire range of fin dimensions and Reynolds numbers [18].

While in heat exchangers a wide variety of fin shapes is used, the fins typically applied in pyrolysis reactors are rounded fins with a smooth concave-convex structure in order to avoid flow separation and possible local hot spots for coke formation. Figure 3-1 shows the cross section of the adopted tubes. The geometric parameters are the tube outer diameter, the maximum inner diameter, the fin height e, the minimum metal thickness t and the fin width w. The curvature of the fins is determined by two touching circles as shown in dashed lines in Figure 3-1. Only four parameters can be chosen independently. Typically the tube outer and maximum inner diameter, the fin height and the number of fins are chosen. In longitudinally finned tubes, the cross section is extruded along the tube centerline, i.e. the fins are parallel to the tube centerline. In helicoidally finned tubes, the fins are extruded along a helix. Hence, for helicoidally finned tubes an additional geometric parameter can be chosen, i.e. the helix angle. This helix angle corresponds to the angle between the helicoidal fins and the tube centerline.
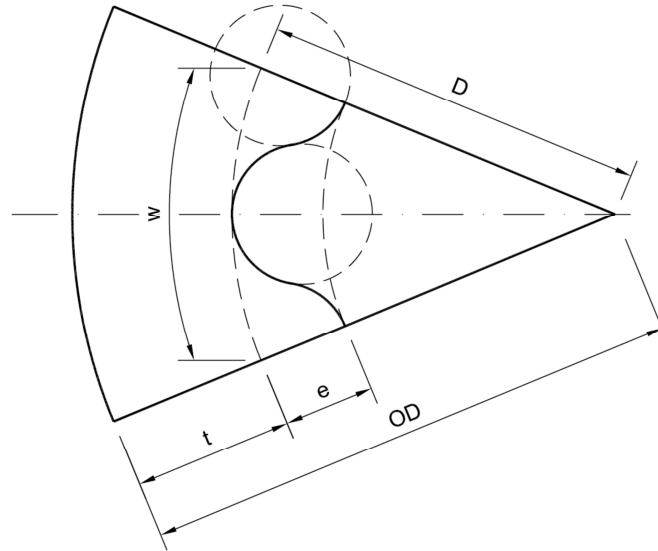
Figure 3-1: Part of the cross section of a finned tube (OD: outer diameter, D: inner diameter, w: fin width, e:

fin height, t: minimum metal thickness).

A study by Brown on these geometries indicated that the heat transfer improvement for longitudinally finned tubes follows a linear relationship with the surface area increase [20]. Albano et al. compared a longitudinally and helicoidally finned tube by performing air flow experiments through a heated tube [21]. The Colburn j-factors for the longitudinally and helicoidally finned tubes were found to be respectively 20 % and 40 % lower than for bare tubes. However, this loss was offset by a 44 % increase in internal surface area compared to an equivalent bare tube, i.e. a bare tube with the same cross-sectional surface area. The better performance of the longitudinally finned compared to the helicoidally finned tubes was attributed to a greater tendency of the air to bypass the fins in the latter. Pressure drops were measured to be higher for the helicoidally finned tubes compared to longitudinally finned tubes. The latter was confirmed by the simulation results obtained by De Saegher et al. [22] for an industrial propane

cracking reactor. In contrast to Albano et al. [21], these authors simulated a higher heat transfer coefficient for the helicoidally finned tube compared to the corresponding longitudinally finned tube. This was attributed to more intense mixing and reduced radial temperature gradients in the helicoidally finned tubes. The accuracy of the results of De Saegher et al. [22] can be debated because of the adopted coarse computational grid and the first-order discretization schemes that were used due to much lower computational capabilities. A recent patent by Higuchi et al. [23] covers a slightly different geometry where the fins cover only part of the tube perimeter with bare spaces in-between. Based on CFD simulations of air flow, favorable ranges for the fin dimensions were determined. The optimal helix angle was found to be around 25-30°, while the optimal fin height-to-diameter ratio was determined to be between 0.1 and 0.2. Increasing the fin height-to-width ratio was found to be favorable as more intense heating was achieved. An upper limit of 0.7 was determined based on the limitations of the fin welding process and practical implications for e.g. plugging of the reactor during decoking operation by spalled coke. Wolpert et al. [24] also recently proposed helicoidally finned tubes with a lower fin height than the aforementioned references. The authors state that this allows the generation of swirling flow in the immediate vicinity of the fins and that this swirling flow spreads to the tube core.

The above clearly shows that in order to properly assess the full potential of finned reactors, the influence of each of the geometric parameters needs to be investigated systematically. To the authors' knowledge, this has not been done before. More importantly the availability of a reliable simulation model for 3D reactor geometries in which the free-radical gas-phase chemistry is accounted for next to coke formation and fluid dynamics would open the door for a more rapid evaluation of new and existing 3D reactor designs. Although many efforts have been made

towards the accurate CFD simulation of the fire-side of steam cracking units [25-34], the literature on CFD simulations of the reactor-side is limited [22, 30, 32, 34]. Besides the work of De Saegher et al. [22], all aforementioned references use highly simplified global reaction networks. Only detailed free-radical reaction networks capture the essential chemistry to allow a trustworthy prediction of the effect of reactor configuration on product yields. As mentioned before the simulations of De Saegher et al. [22] were performed on a coarse computational grid and adopted first-order discretization schemes. To the authors' knowledge, no grid-independent simulations of steam cracking reactors with higher-order discretization schemes and a free-radical reaction network have been published. Therefore in this work the Reynolds-Averaged Navier-Stokes (RANS) approach is combined with such a detailed single-event microkinetic model. The first step is the validation of the CFD model using available experimental data. Secondly, the potential of the application of internally finned tubes in steam crackers is assessed by performing a comprehensive non-reactive parametric CFD study providing guidelines for optimal design. Finally, optimal designs are evaluated in an industrial propane cracking Millisecond furnace. The effect of the selected 3D reactor geometries on product selectivities and coking tendency is evaluated. The results are validated with industrial data from a Millisecond furnace operated under similar conditions.

3.2 CFD model setup

3.2.1 Governing equations

For a steady-state three-dimensional simulation of compressible reactive gas flow, the governing equations are the following:

- Global continuity equation

$$\nabla \cdot (\rho \overline{\boldsymbol{u}}) = 0 \tag{3.1}$$

- Navier-Stokes equations

$$\nabla \cdot (\rho \overline{\boldsymbol{u}} \overline{\boldsymbol{u}}) = -\nabla p + \nabla \cdot \overline{\overline{\boldsymbol{\tau}}} \tag{3.2}$$

- Energy equation

$$\nabla \cdot (\overline{\boldsymbol{u}}(\rho E + p)) = \nabla \cdot \left(\lambda_{eff} \nabla T - \sum_i h_i \bar{\boldsymbol{J}}_i \right) + S_h \tag{3.3}$$

- Species transport equations

$$\nabla \cdot (\overline{\boldsymbol{u}} C_j) = -\nabla \cdot \bar{\boldsymbol{J}}_j + R_j \ , \forall j = 1, nspec \tag{3.4}$$

In these equations $\bar{\boldsymbol{J}}_j$ is the diffusion flux of species j, including contributions from both the laminar and turbulent diffusivity as well as the thermal (Soret) diffusivity. S_h is the heat of reaction, C_j the concentration of species j, R_j the net rate of production of species j and $nspec$ the number of species. The performed simulations showed that in future work the laminar and thermal diffusivity do not need to be explicitly accounted for because the turbulent diffusion is always at least two orders of magnitude greater than the sum of both.

3.2.2 **Turbulence modeling**

The flow properties are Reynolds-decomposed to a steady mean value and a fluctuating turbulent contribution. This generates an additional stress tensor, characterizing the transfer of momentum by turbulence, the so-called Reynolds stresses: $\tau_{ij}^t = -\rho \overline{u_i' u_j'}$. Closure for these additional unknowns was provided by use of the Boussinesq approximation, expressing the Reynolds stresses in terms of the mean velocities. If the transport of momentum is assumed to be a diffusive process, an eddy viscosity can be introduced, analog to the molecular viscosity. One of the most widely applied models for determining this eddy viscosity is the standard k-ε model, where two additional transport equations are solved for the turbulent kinetic energy k and the energy dissipation rate ε respectively. For swirling flow, results can be further improved by use of the k-ε RNG model as an extra source term is introduced to the dissipation equation in regions with large strain rate. Although at the basis of some very successful models, the Boussinesq approximation assumes isotropic eddy viscosity. Abandoning this concept, the Reynolds stress model (RSM) solves 6 additional transport equations for each of the components of the symmetric Reynolds stress tensor, along with an equation for the energy dissipation rate. Given the strong coupling between these 7 additional partial differential equations, this makes computation much more expensive. As the RSM can model flow characteristics resulting from anisotropy of the Reynolds stresses, more accurate results are to be expected in highly swirling flows.

In the present work, the k-ε RNG model was used for the bare tubes and for the tubes with longitudinal fins. For the more complex, swirling flow inside the helicoidally finned tubes the k-ε

RNG model was used for initial convergence. In a second step RSM was used because it gave a better agreement with the experimental validation data discussed in section 3.4.

3.2.3 **Boundary conditions**

At the tube inlet, the temperature, mass flow rate, turbulence parameters k and ε and the composition of the process gas were imposed. The turbulence parameters were calculated for a turbulence intensity of 8 % and a characteristic length scale of 10 % of the tube hydraulic diameter. At the outlet of the tube, a constant pressure boundary condition was set. All other variables were extrapolated from the integration field. The no-slip boundary condition was set at the tube inner walls. In order to apply this condition for highly turbulent flow, FLUENT's enhanced wall treatment was used to "bridge" the solution variables in the near-wall cells. This model combines a two-layer model with enhanced wall functions by blending linear and logarithmic laws-of-the-wall. Validity of the use of a two-layer model was ensured by placing computational cells within the viscous sub-layer, with the near-wall cells satisfying the $y^+ < 1$ condition. The energy equation was solved by imposing either a temperature or a heat flux profile to the tube outer walls.

3.2.4 **Chemistry model**

Steam cracking of hydrocarbons mainly proceeds through a free-radical mechanism, which is characterized by a vast number of species and reactions [35-38]. The incorporation of such detailed chemical networks is computationally expensive [39]. Hence, to limit computational cost, a network specifically geared at propane cracking was used by reducing the full single-event microkinetic CRACKSIM model [40-42] to its relevant core for propane cracking. The final

network consisted of 203 reactions between 26 species, of which 13 radical species. Validation of the reduced network by comparison to the full network is provided in Appendix A.

The RMG Transport estimator was used for predicting the Lennard-Jones characteristic length and energy parameters [43]. These were then applied in FLUENT's kinetic theory method for calculation of thermal conductivity and viscosity for each individual species [44, 45]. Diffusion coefficients were quantified on this basis as well by using a modification of the Chapman-Enskog formula [46]. Finally, thermal diffusion was taken into account by using an empirical composition-dependent form of the Soret diffusion coefficient [47]. Properties of the multi-component mixture were calculated by ideal gas mixing laws.

3.2.5 **Numerical model**

The commercial CFD code ANSYS FLUENT 13.0 was adopted to solve the governing equations. This general-purpose CFD package uses the finite-volume method. Discretization of all equations was achieved using the Quadratic Upstream Interpolation for Convective Kinetics (QUICK) scheme, combining the strengths of both upwind and central differencing schemes by using a three-point upstream quadratic interpolation. Although an unbounded scheme, it was selected based on the reported improved accuracy for rotating and swirling flows compared to the second-order up-wind scheme [48]. It can be proven that the scheme is third order accurate [48, 49]. The residual convergence criterion was set to 10^{-6} for all equations, only the energy and species equations were set lower to 10^{-9}. Furthermore the inlet pressure, outlet temperature and species concentrations were monitored. The inlet pressure and outlet temperature were seen to change less than 1 Pa and 0.05 K respectively over the last 50 iterations for all simulations. The relative

change over the last 50 iterations of all species concentrations were seen to change less than 0.1%.

3.2.6 **Computational grid**

The computational grid was constructed from a 2D triangular mesh which was extruded along the axial coordinate. For the helicoidally finned tubes a twist vector was applied to obtain the correct helix angle. By symmetry considerations, the computational domain can be limited to one fin of the tube to reduce computational time. Periodic boundary conditions are applied to allow flow through the azimuthal boundaries in case of swirling flow. A fine boundary layer near the tube inner wall is added to ensure computational cells in the viscous sub-layer having a $y^+ < 1$ as required by the enhanced wall treatment model. Grid independence for the tubes adopted by Albano et al. [50] was achieved at a mesh density of approximately 5.10^5 and 3.10^5 cells/meter for the fluid and metal volume respectively as shown in Appendix B. Grid sizes in wall units [51] for grid independence were seen to be $\left\{\frac{d_{int}}{2}\Delta\theta^+, \ \Delta y^+, \ \Delta z^+\right\} = \{50, 0.8 - 50, 333\}$. These values were used as upper limits for all grids. These grids used in the reactive simulations were further refined based on the temperature gradient of the converged solution. The results of this grid refinement are also shown in Appendix B. No significant change in the results is seen by the grid refinement. The grid independent mesh for the tubes adopted by Albano et al. [50] is shown in Figure 3-2.
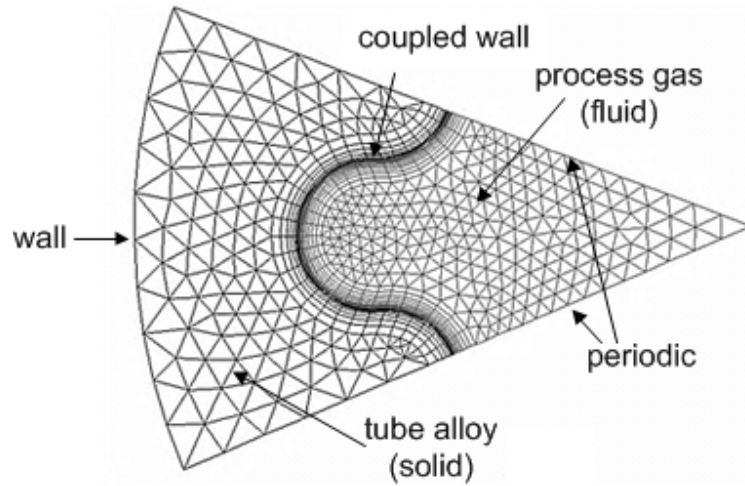
Figure 3-2: Grid independent mesh of a cross section of the tubes adopted by Albano et al. [50].

3.3 CFD model validation

The CFD model was validated by comparison with the experimental results obtained by Albano et al. [50]. By means of an experimental setup capable of measuring pressure drop and temperature along the axial coordinate, Albano et al. evaluated the heating performance of a longitudinally and a helicoidally finned tube. In their experimental setup, air flows through a steam-heated finned tube containing four thermocouples to measure the air temperature in the center of the tube at different axial positions. As the air is being released to the atmosphere, the pressure at which the inlet diaphragm pump is operating indicates the pressure drop over the tube. For the exact dimensions of the tubes, reference is made to the original paper of Albano et al. [50].

The experiments with a longitudinally and a helicoidally finned tube were performed at air mass flow rates of 0.107 and 0.103 kg/s respectively, which correspond to an inlet Reynolds number of approximately $230 \cdot 10^3$. It is important to stress that the experiments did not involve a sufficiently long inlet section to avoid entrance effects. In the performed CFD simulations a small inlet section of 0.2 m length was included as the exact dimensions of the experimental inlet section are unknown. Furthermore, the temperatures measured on the outside of the tube were flawed due to steam condensation, leaving only the inner wall temperatures as reliable data. Hence, in the CFD simulations the inner wall temperature profile was imposed without taking conduction through the metal into account. The latter implies that the temperatures in the peaks and valleys were assumed to be equal, whereas in reality they differed by 1-2 K. Air was treated as an ideal gas with viscosity, specific heat capacity and thermal conductivity following a piecewise-linear temperature dependence. The simulation results for pressure and temperature are compared to experimental data in Figure 3-3 for the longitudinally and helicoidally finned tube.

Pressure drops were simulated accurately with relative errors of 3.2 % and 4.9 % for the longitudinally and helicoidally finned tube respectively. Temperatures were underpredicted for both tubes but it can be seen that the major difference lies in the entrance region. As the experimental setup did not include a sufficiently long adiabatic inlet section, the deviations near the inlet can be explained by the development of turbulent phenomena. Nevertheless, relative errors for the heat transfer were limited to 4.6 % and 7.6 %, which can be considered satisfactory given the experimental errors and the use of an azimuthally uniform internal wall temperature profile in the simulations.
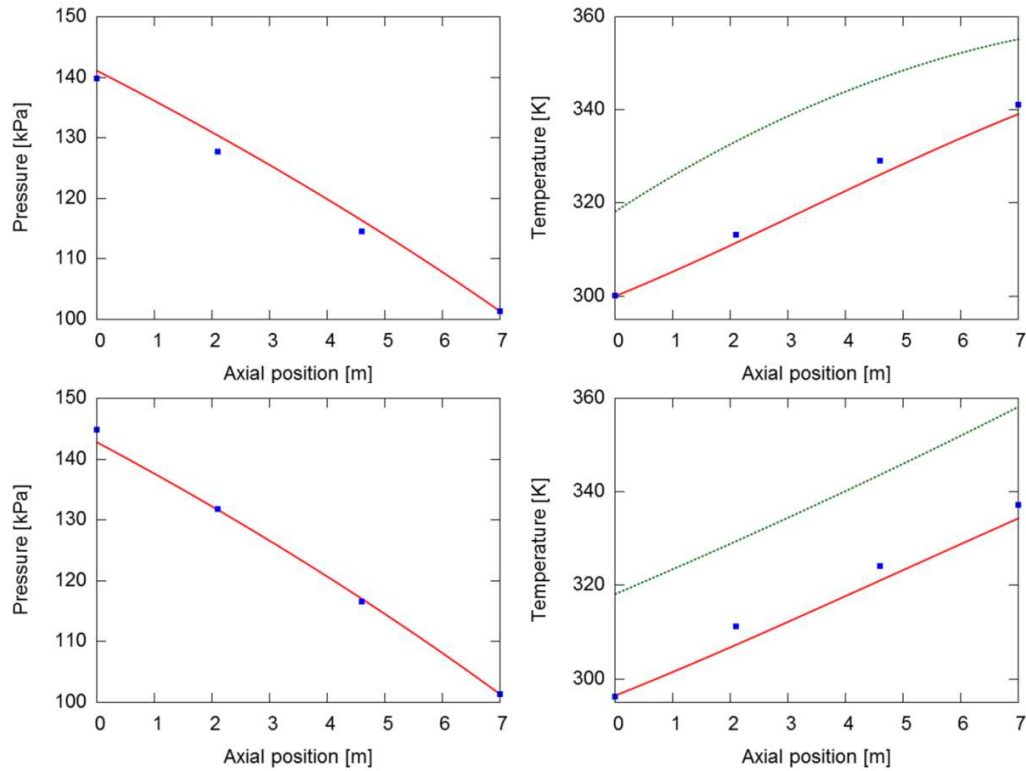
Figure 3-3: Pressure [kPa] (left) and temperature [K] (right) as a function of axial position [m] in the longitudinally finned tube (top) at Re = 233 10³ and the helicoidally finned tube (bottom) at Re = 224 10³: ■ - experimental process gas values of Albano et al. [50]; ———— - simulated process gas values; ⋯⋯⋯ - set wall temperature.

3.4 Parametric study

The validated CFD model was used to study the effect of the fin parameters on heat transfer and pressure drop through non-reactive air flow simulations. The dimensions studied are close to the typical ranges of patent and scientific literature [50, 52]. However, the ranges studied in this work are broader than those discussed in previous studies [50, 52]. The fins are distributed over the entire tube inner perimeter, i.e. there are no locations without fins. The computational domain consisted of a 2 m long inlet section and a 4 m long test tube. The inlet section was an adiabatic tube and was

used to provide fully developed flow at the test tube inlet. Both pressure-drop and temperature simulations were performed. In the former the entire tube was simulated adiabatically, while in the latter the outer wall temperature was set to 373.15 K for the last 2 m of the test tube. The air inlet temperature was set to 300 K. This study was carried out at two flow rates ($59.7 \cdot 10^{-3}$ kg/s and $86.3 \cdot 10^{-3}$ kg/s), which corresponds to an inlet Reynolds number of $90 \cdot 10^{3}$ and $130 \cdot 10^{3}$ respectively based on the equivalent diameter of the finned tubes, i.e. the diameter of a bare tube with the same cross-sectional surface area, adopted by Albano et al. [50]. The outlet pressure was set to 101325 Pa as in the experiments performed by Albano et al. [50]. In the following, results are given for the lowest inlet Reynolds number unless stated differently.

Heat transfer was quantified by calculating a heat transfer coefficient based on the internal surface area of a bare tube with the same equivalent inner diameter. This heat transfer coefficient was calculated based on the inlet and outlet temperatures, from which the amount of energy absorbed by the air can be calculated as follows:

$$Q = \phi_m c_P (T_{out} - T_{in}) \tag{3.5}$$

This same amount of absorbed energy can also be estimated in heat transfer terms as:

$$Q = \pi \, d_{eq} L_h U \, LMTD \tag{3.6}$$

By combination of equation (3.5) and (3.6), the global heat transfer coefficient based on the internal surface area of an equivalent bare tube can be expressed as:

$$U = \frac{\phi_m \, c_P \, (T_{out} - T_{in})}{\pi \, d_{eq} L_h \, LMTD} \tag{3.7}$$

All fluid properties like density, viscosity, thermal conductivity and specific heat are evaluated at the average of their values at the simulated mixing cup inlet and outlet temperature.

3.4.1 **Fin height**

The influence of the fin height on the pressure drop and the heat transfer coefficient was quantified by altering the fin height-to-diameter ratio of the tube, e/D, between 0, i.e. a bare tube, and 0.196. Eight fins were adopted in all simulations. For the helicoidally finned tubes, a helix angle of 15.88° was used. The mass flow rate and the cross-sectional flow area were kept constant, i.e. preserving space-time if the gas density at the inlet is constant. It was chosen to keep the minimum metal thickness t fixed to a value of $7.0 \cdot 10^{-3}$ m. This is industrial practice to assure structural stability of the reactors. This method allows a bare tube with the same equivalent inner diameter to be used as a base case for all finned tubes. The concept is visualized in Figure 3-4 where the prevalent velocity (A) and temperature (B) at the tube outlet are plotted for helicoidally finned tubes with different fin height. The dimensions of the depicted tubes are summarized in Table 3-1.

Table 3-1: Dimensions of helicoidally finned tubes used in fin height study.

Tube ID	F1	F2	F3	F4	F5	F6	F7	F8	Bare
Inner diameter D [10^{-3} m]	39.0	36.8	36.0	35.3	34.6	33.9	33.2	32.6	31.6
Fin height e [10^{-3} m]	7.6	5.4	4.6	3.9	3.2	2.5	1.8	1.2	-
e/D [-]	0.195	0.147	0.128	0.110	0.092	0.074	0.054	0.037	-
Number of fins [-]	8	8	8	8	8	8	8	8	0
Wetted perimeter ratio [-]	1.81	1.44	1.33	1.24	1.16	1.10	1.06	1.02	1.00
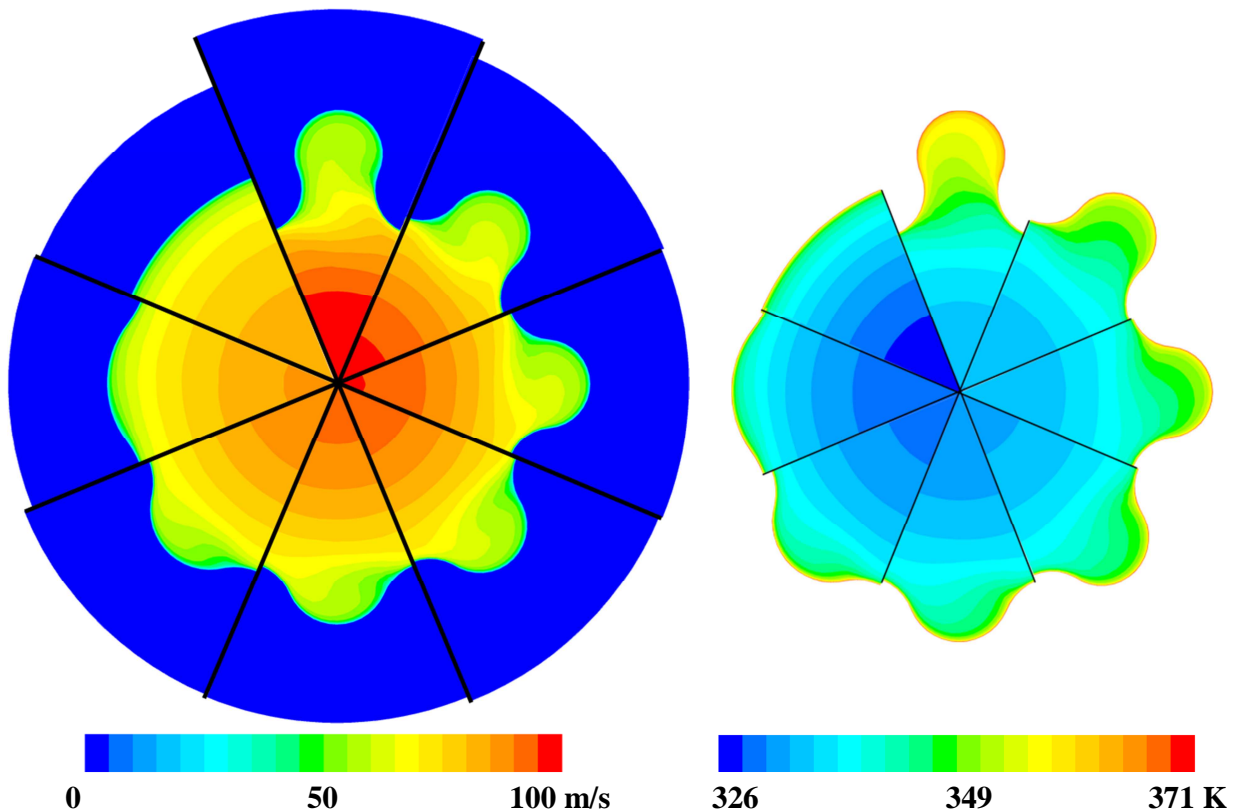
Figure 3-4: Velocity [m/s] (A) and temperature [K] (B) at the outlet of helicoidally finned tubes with different fin height; clockwise starting at top: F1, F2, F3, F4, F5, F6, F8 and bare, viz. Table 3-1.

Figure 3-5 shows the heat transfer coefficient and the pressure drop normalized to the corresponding value of a bare tube as a function of the wetted perimeter. Both types of finned tubes offer substantial improvements in heat transfer. For the longitudinal fins the heat transfer improvements can be assigned solely to the increase in internal surface area as a linear relationship is observed between the heat transfer ratio and the wetted perimeter. However, this is not the case for the helicoidally finned tubes.
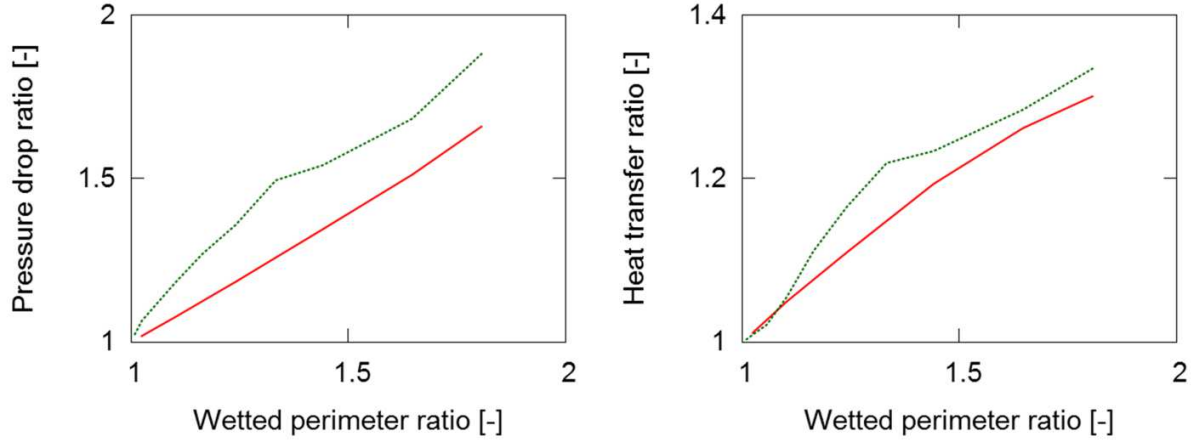
Figure 3-5: Pressure drop ratio [-] (left) and heat transfer ratio [-] (right) at Re = 9 · 10⁴ as a function of wetted perimeter ratio [-]: ——— - longitudinally finned; ……… - helicoidally finned.

An enhanced cross-sectional mixing can explain the local bump in the heat transfer coefficient seen in Figure 3-5. In order to quantify this cross-sectional mixing, a dimensionless mixing cup temperature variance in a cross section, Θ_T is introduced:

$$\Theta_T = \frac{\sqrt{\dfrac{\sum \left(\phi_{m,i} \left(T_i - T_{avg} \right)^2 \right)}{\phi_{m,tot}}}}{T_{avg}} \tag{1}$$

In this equation $\phi_{m,i}$ represents the mass flow rate through the face i, T_i the temperature of face i and T_{avg} the mixing cup temperature over all faces of the cross section. Lower values of Θ_T correspond to a more uniform temperature distribution in the cross section. Figure 3-6 shows this dimensionless mixing cup averaged temperature variance. For all longitudinally finned tubes a lower uniformity is obtained than for the bare tube. For helicoidally finned tubes, a more uniform cross-sectional temperature profile is obtained at low e/D ratios. Hence, better cross-mixing is established leading to a higher heat transfer coefficient at low e/D ratios. However, the lowest

e/D ratios also offer the smallest increase in internal surface area. The combination of these two opposing effects explains the non-linear behavior of the heat transfer coefficient as a function of the wetted perimeter ratio for helicoidally finned tubes and that an optimal ratio of fin height-to-diameter exists. The performed simulations for the helicoidal fins indicate this value to be around 0.12. Tubes with an e/D higher than 0.12 will offer additional heating improvements but at the cost of a higher pressure drop.
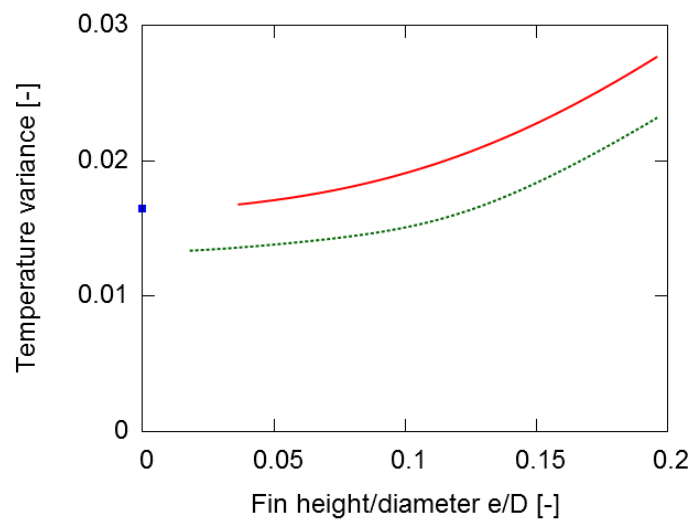
Figure 3-6: Dimensionless mixing cup averaged temperature variance [-], viz. equation (1) as a function of wetted perimeter ratio [-]: ——— - longitudinally finned; ········ - helicoidally finned; bare - ■ .

3.4.2 **Helix angle**

Helix angles ranging from 0°, i.e. longitudinal fins to 48° were studied. Two different fin height-to-diameter ratios of 0.037 and 0.147 were studied. Eight fins were adopted in all simulations.

The pressure drop ratio and heat transfer ratio compared to a bare tube as a function of the helix angle are shown in Figure 3-7. These results indicate that larger helix angles improve heat transfer. Indeed, at higher helix angles swirling flow is induced providing better cross-sectional mixing. As a result of the increased wall shear stresses, also higher pressure drops are simulated. The upper limit of optimal helix angle for the tall fins is in the range between 25-30°, because increasing the helix angle further makes the pressure drop increase strongly while gain in heat transfer remains constant. These results correspond with the values proposed by Higuchi et al. [23] for a similar geometry. Alternatively, fins with a reduced height can be used at higher helix angles as they only result in a moderate pressure drop increase.
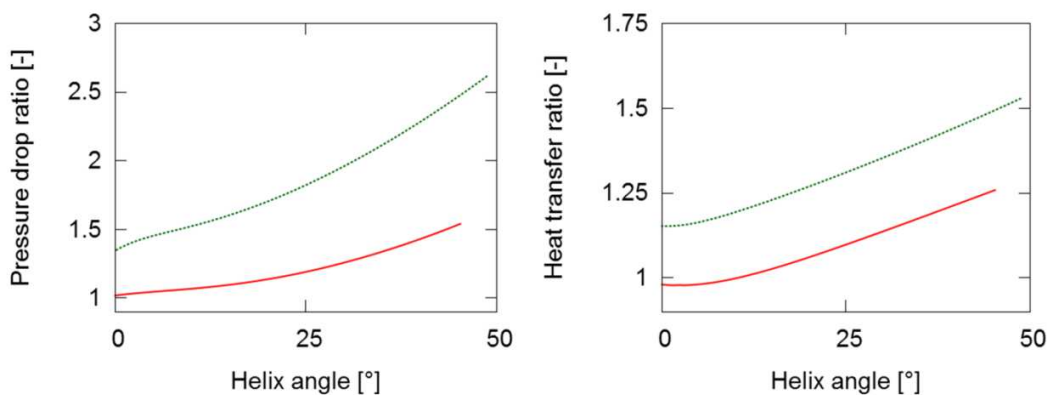
Figure 3-7: Pressure drop ratio [-] (left) and heat transfer ratio [-] (right) at Re = 90 · 10³ as a function of helix angle [°]: ——— - fin height-to-diameter ratio of 0.037; ········· - fin height-to-diameter ratio of 0.147.

3.4.3 **Number of fins**

Typically between 6 and 12 fins are used in finned steam cracking reactors [53]. The simulation results obtained for an e/D ratio of 0.147 with finned tubes containing between 4 and 12 fins are

shown in Figure 3-8. The tubes with 4, 6, 8, 10 and 12 fins have a wetted perimeter ratio of 1.11, 1.26, 1.44, 1.78 and 1.90 respectively. For the helicoidally finned tubes, the helix angle was again 15.88°. A linear relation between the number of fins and pressure drop is observed for both the longitudinally finned and helicoidally finned tubes. However, the heat transfer ratio increases only up to 8 to 10 fins. For tubes with more than 10 fins, it was seen that the flow inside the fin valley gets isolated from the tube center leading to lower velocities. As soon as flow isolation inside the fin occurs, an additional heat transfer resistance emerges due to the narrow passing from the fin valley to the tube center. The simulations illustrate that the optimal number of fins depends strongly on the chosen fin height, which in this case results in an optimal value of 8 to 10 fins. For fins with a small fin height-to-diameter ratio a higher number of fins can be adopted.
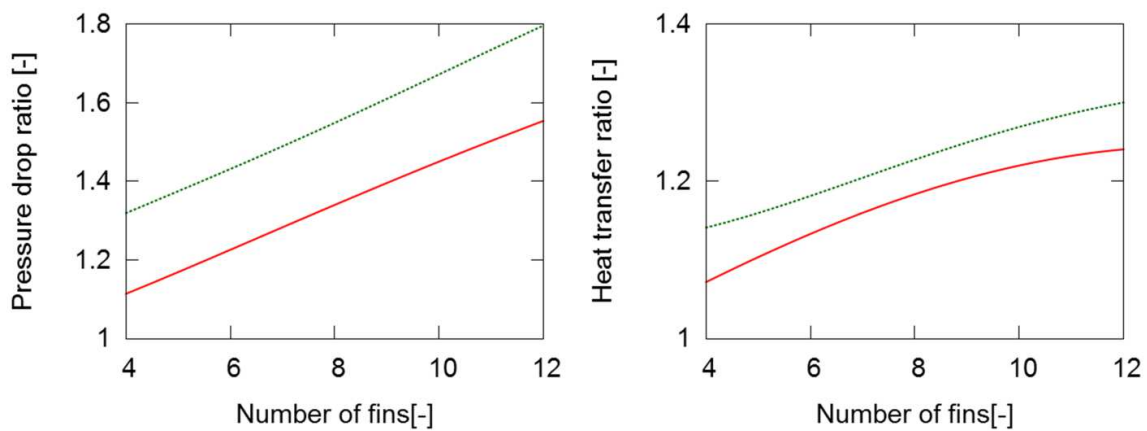
Figure 3-8: Pressure drop ratio [-] (left) and heat transfer ratio [-] (right) at Re = 90 10^3 as a function of

number of fins [-]: ——— - longitudinally finned; ········ - helicoidally finned.

3.4.4 **Geometry optimization**

The parametric study assessed the performance of finned tubes for non-reactive air flow in terms of pressure drop and heat transfer. It allows formulating several guidelines towards optimal steam cracking reactor design. Ideally low pressure drops are combined with a high radial temperature uniformity, giving rise to high light olefin selectivity and a reduced coking tendency [54]. Hence, based on the results of the preceding parametric study, a design with a small fin height seems potentially attractive because this allows to take maximal advantage of the lower pressure drops these fins induce. In combination with a large value for the helix angle, this could lead to a large increase in heat transfer by swirling flow for a low pressure drop increase. In any case, a clear trade-off between heat transfer enhancement and additional pressure drop needs to be made. This becomes clear from Figure 3-9, in which all simulation data points acquired throughout the parametric study are plotted. The relationship between the relative heat transfer and relative pressure drop is highly linear, but it is not obvious to assess the effect on product selectivities and run length based on these data. Translating these guidelines to optimal fin height and number of fins has allowed defining two optimal geometries that should significantly outperform the previously studied tubes. The dimensions of these optimized designs are summarized in Table 3-2.

Table 3-2: Dimensions of optimal tube geometries.

Tube ID	O1	O2
Inner diameter [10^{-3} m]	35.34	31.32
Fin height [10^{-3} m]	3.89	1.15
Number of fins [-]	10	24
Helix angle [°]	28.7	44.1
Wetted perimeter ratio [-]	1.367	1.212
U ratio [-] for inlet Reynolds number of $90 \cdot 10^3$/ $130 \cdot 10^3$	1.31 / 1.33	1.53 / 1.43
Pressure drop ratio [-] for inlet Reynolds number of $90 \cdot 10^3$ / $130 \cdot 10^3$	1.48 / 1.56	1.99 / 1.83

Geometry "O1" has fins with an e/D ratio of 0.11. The helix angle and number of fins were chosen at the optimal values found in the parametric study for the taller fins, i.e. 8 to 10 fins and a helix angle between 25° and 30°. For geometry "O2", 24 small fins are combined with a high helix angle. Both optimized geometries were found to offer increased heating characteristics as seen in Figure 3-9. Mainly at the highest Reynolds number a better performance is simulated, i.e. for a given pressure drop the heat transfer is higher.
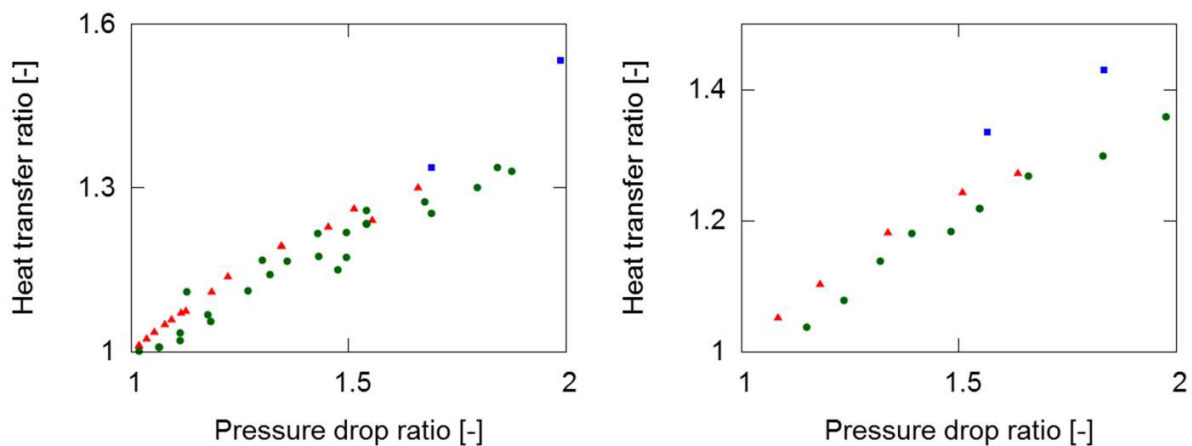
Figure 3-9: Heat transfer ratio [-] as a function of pressure drop ratio [-] at Re = $90 \cdot 10^3$ (left) and $130 \cdot 10^3$ (right) for longitudinally finned; ▲, helicoidally finned; ● and optimized geometries; ■ .

For application in steam cracking reactors, it can be concluded that the optimal geometry will be largely dependent on the process conditions, i.e. mainly the Reynolds number. Furthermore a trade-off between improved heat transfer and increased pressure drop must be made, which depends on the applied feedstock as changes in product selectivity due to the higher pressure drop will differ for different feedstocks [54]. Hence, non-reactive experiments and simulations can offer guidelines for design, but reactive CFD simulations are necessary to assess the actual effect on product yields and coking.

3.5 Reactive simulations of an industrial propane cracker

Reactive simulations of one of the reactors in an industrial Millisecond furnace were performed to assess the effect of finned reactors on product yields and coking tendency. Millisecond furnaces operate at very high severity and a residence time of approximately 0.1 seconds. Millisecond furnaces are designed to achieve maximum ethene yield resulting in high operating temperatures and very short run lengths, sometimes as short as one week.

3.5.1 Process conditions and reactor configurations

A 100 % pure propane feedstock was adopted. The hydrocarbon and steam flow rate were set to 0.03292 kg/s and 0.01075 kg/s respectively, resulting in a steam dilution 0.33. The reactor inlet temperature was equal to 903.7 K while the reactor outlet pressure, i.e. just upstream the transfer line exchanger, was set to be 170 kPa, i.e. the industrially applied value.

A coupled three-dimensional furnace-reactor simulation requires several iterations between the reactor and furnace simulations and is at present difficult due to too high computational cost and is considered outside of the scope of this work. Therefore a heat flux profile was set as boundary condition on the outer wall of the reactor. This heat flux profile was taken from a furnace simulation where the boundary condition applied to the outer wall of the reactor tubes was the industrially measured outer wall temperature profile. The adopted models in the furnace simulation were similar to those of Hu et al. [55].

Four different reactor configurations were simulated. Their dimensions are summarized in Table 3-3. First, a bare tube (Bare) was simulated as a reference case. Second, an industrially applied helicoidally finned reactor (Helix) was considered. The fin dimensions of this reactor are close to those of the optimized geometry "O1", viz. Table 3-2, of the parametric study. Third, the same fin parameters were applied in simulating a reactor with longitudinal fins (Straight). Finally, a tube with significantly smaller fins was simulated (SmallFins) corresponding to the optimized geometry "O2".

Table 3-3: Reactor dimensions.

Reactor ID	Bare	Helix	Straight	SmallFins
Reactor length [m]	10.556	10.556	10.556	10.556
Adiabatic inlet section [m]	0.444	0.444	0.444	0.444
Maximum inner diameter [10^{-3} m]	30.2	34.8	34.8	31.3
Number of fins [-]	-	8	8	24
Helix angle [°]	-	15.7	-	33.1
Outer diameter [10^{-3} m]	43.7	48.3	48.3	44.8
Metal thickness [10^{-3} m]	6.75	6.75	6.75	6.75
Fin height [10^{-3} m]	-	4.8	4.8	1.15
Cross-sectional surface area [10^{-6} m²]	715.7	715.7	715.7	715.7
Cross-sectional perimeter [m]	0.0948	0.1315	0.1315	0.1150

3.5.2 **Results and discussion**

The computational grid was constructed by extruding a 2D mesh of $1/8^{th}$ of the cross section applying the required twist vector for the helicoidally finned reactors. The grid size in wall units was maintained at the values used throughout the parametric study which were confirmed to provide grid-independent results, see Appendix B. This led to computational grids consisting of 6 to 11 million cells.

Computation was performed on 32-core Dell C6145 computing nodes with AMD Magny-Cours Opteron 6136 processors and an Infiniband Double QDR communications link. Total CPU time amounted to around 25000 hours per simulation, i.e. about one month of clock time. In the following, many averaged variables are reported. The equations used to calculate the different averages are given in Appendix C.

Figure 3-10 A and B show the mixing cup temperature and pressure as a function of the axial position for the four reactor configurations. Little differences between the process gas temperature profiles are simulated as the same heat input, reactor volume and mass flow rate are adopted. However, the pressure drop varies drastically with SmallFins showing the highest pressure drop. This higher pressure drop results in a higher inlet density yielding small differences in residence time, calculated here as reactor volume divided by volumetric inlet flow rate, as shown in Table 3-4.
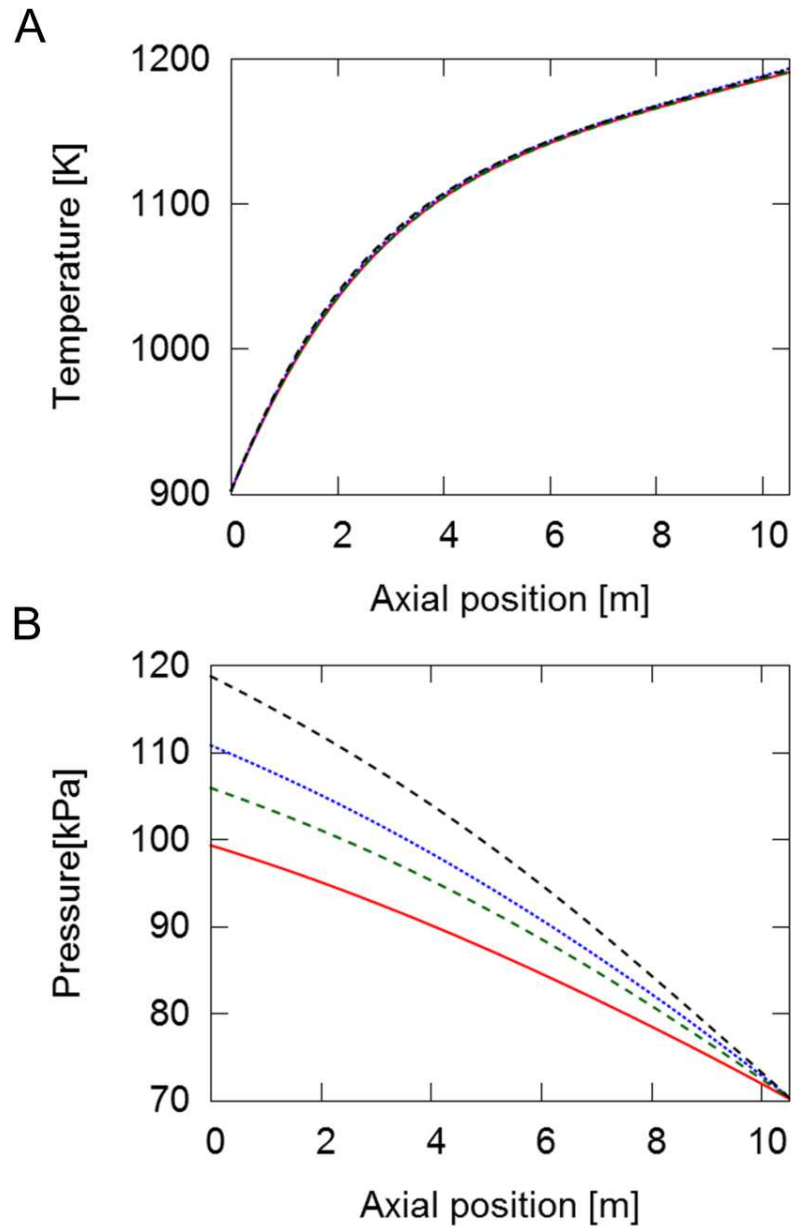
Figure 3-10: Process gas temperature [K] (A) and pressure [kPa] (B) mixing cup averaged over a cross section as a function of axial position [m]: ———— - Bare; ·············- Helix; ------ - Straight ; ------ - SmallFins.

Figure 3-11 shows the azimuthally area-averaged external tube metal temperature as a function of the axial position. The maximum external tube metal temperature occurs at around 3.5 m corresponding to the maximum of the heat flux to the reactor. For the Bare reactor, the maximum temperature is 1334 K, which is close to the maximum allowable TMT of 1363 K. This is caused by the high cracking severity, i.e. the coil-outlet-temperature (COT) is above 1190 K. The maximum TMT is 29, 26 and 51 K lower than the Bare reactor for Helix, Straight and SmallFins respectively. For Millisecond furnaces the maximum tube metal temperature is typically the limiting factor for the run length. Hence, decreasing this temperature by adopting finned tubes will significantly increase the reactor run length.
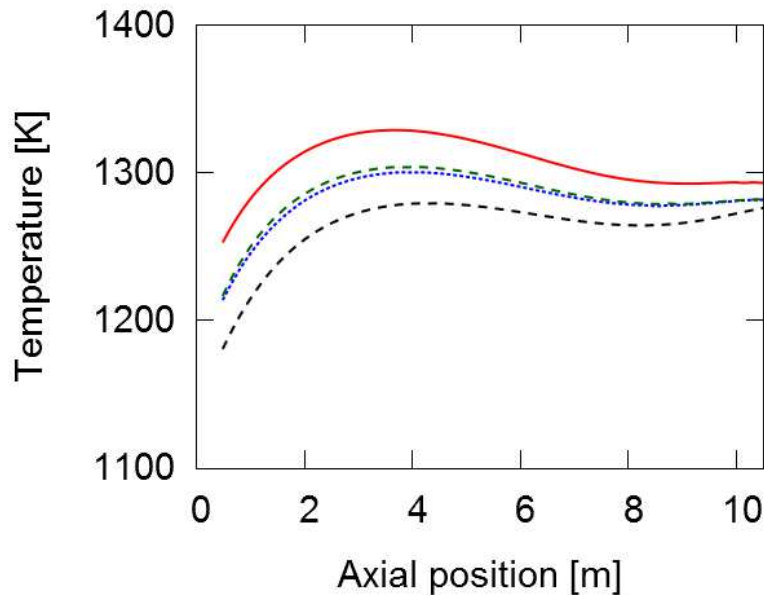
Figure 3-11: Azimuthally area-averaged external tube metal temperature [K] as a function of axial position

[m]: ———— **- Bare;** ·············**- Helix;** - - - - - - **- Straight;** - - - - - - **- SmallFins.**

Table 3-4 summarizes the most important process conditions, product yields and selectivities. For validation, data of an industrial bare tube Millisecond reactor running with a crude propane feedstock, i.e. 95 % pure propane or higher, under similar, but not identical conditions have been added. Considering the accuracy of the industrial yield measurements, the purity of the feed and accounting for the fact that the industrial data are for a slightly lower cracking severity, the agreement between the simulated Bare reactor and the industrial data is reasonable. Comparing the four simulation cases some small differences in COT are observed. These can be attributed to different reaction rates due to different pressure and temperature fields in the reactors. The coil-inlet-pressure (CIP) increases drastically with a factor 1.22 and 1.39 for the Straight and Helix reactor respectively. As expected from the parametric study, the SmallFins reactor shows the highest pressure drop. The propane conversion is slightly higher for Helix and SmallFins, which can be attributed to a higher space time due to the higher pressure drop. To limit the effect of differences in propane conversion, comparison should be made on the basis of selectivities expressed as product yield divided by propane conversion. As bimolecular reactions are favored over monomolecular reactions at higher pressure, the selectivity to light olefins produced by monomolecular beta scissions is reduced at higher reactor pressure. This effect can be clearly seen in Table 3-4, where the ethene selectivity decreases monotonically with increasing pressure drop ratio. The effect is limited as ethene selectivity only decreases by 0.56 wt%. However, given the large scale of the steam cracking process, this difference is economically significant. The selectivity to methane and 1,3-butadiene is increased as these are formed by a series of bimolecular reaction steps.

Surprisingly the SmallFins reactor has the highest propene selectivity although the conversion in this reactor is higher than in all other reactors. Typically the propene yield decreases with increasing conversion [56]. A rate of production analysis of the reaction mechanism reveals that propene is primarily formed by C-H beta scissions of the 2-propyl radical while the addition reaction of the hydrogen radical to propene results in the 1-propyl radical that further decomposes to ethene and methyl:

(R1)

(R2)
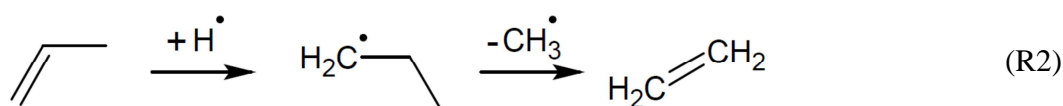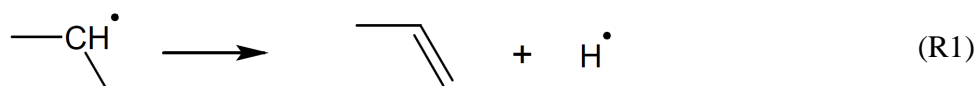
As reported by Van Geem et al. [54] radial temperature gradients strongly affect the radical concentrations and seem to be very likely responsible for the higher propene selectivity. To further assess the effect of conversion on selectivities, a second simulation for the Bare reactor configuration was performed at the same propane conversion of the SmallFins reactor. To this end, the total heat input to the reactor was increased with 0.8 %. The results of this simulation are summarized under Bare HighFlux in Table 3-4. Comparing these results with the SmallFins simulation, it is clear that the reduced ethene selectivity for the SmallFins reactor is completely balanced by the increased selectivity to propene and 1,3-butadiene as the total selectivity to valuable light olefins is almost identical. Hence, application of optimal fin parameters does not necessarily result in a loss of the total olefin selectivity and can be economically more attractive for example during periods where propene and 1,3-butadiene are more valuable than ethene.

Table 3-4: Reactor conditions, product yields and selectivities for the four reactor configurations.

	Bare	Straight	Helix	SmallFins	Bare HighFlux	Bare Industrial[&]
Coil-outlet-temperature [K]	1190.9	1191.2	1193.5	1192.7	1192.8	-
Pressure drop [kPa]	29.13	35.68	40.49	48.42	28.92	-
Pressure drop ratio [-]	1.00	1.22	1.39	1.66	0.99	-
Propane conversion [-]	84.55	84.74	85.42	85.16	85.20	-
P/E ratio [wt%/wt%]	0.476	0.471	0.471	0.485	0.467	0.50
Residence time [s]	0.149	0.154	0.157	0.163	0.149	-
Product Yields [wt%]						
H_2	1.52	1.51	1.51	1.49	1.53	-
CH_4	18.75	19.03	19.22	19.25	18.88	19
C_2H_2	1.03	1.05	1.06	0.98	1.08	-
C_2H_4	38.31	38.39	38.58	38.11	38.67	36
C_2H_6	3.65	3.59	3.58	3.46	3.69	3.5
C_3H_4	1.20	1.24	1.26	1.22	1.25	-
C_3H_6	18.24	18.08	18.17	18.47	18.05	18
C_3H_8	15.45	15.26	14.58	14.84	14.80	17
$1,3\text{-}C_4H_6$	1.23	1.23	1.43	1.53	1.44	1.5
$1\text{-}C_4H_8$	0.54	0.53	0.54	0.56	0.54	-
$2\text{-}C_4H_8$	0.02	0.02	0.03	0.03	0.03	-
$n\text{-}C_4H_{10}$	0.02	0.02	0.02	0.02	0.02	-
Valuable light olefins*	57.78	57.70	58.18	58.11	58.15	55
Product Selectivity [-]						
H_2	1.80	1.78	1.77	1.75	1.80	-
CH_4	22.18	22.46	22.50	22.61	22.15	-
C_2H_2	1.21	1.24	1.24	1.15	1.27	-
C_2H_4	45.31	45.31	45.16	44.75	45.38	-
C_2H_6	4.31	4.24	4.19	4.07	4.33	-
C_3H_4	1.42	1.47	1.48	1.43	1.47	-
C_3H_6	21.57	21.34	21.27	21.69	21.18	-
$1,3\text{-}C_4H_6$	1.46	1.45	1.67	1.79	1.69	-
$1\text{-}C_4H_8$	0.64	0.62	0.63	0.65	0.63	-
$2\text{-}C_4H_8$	0.03	0.03	0.03	0.03	0.03	-
$n\text{-}C_4H_{10}$	0.02	0.02	0.02	0.02	0.02	-
Valuable light olefins*	68.34	68.10	68.10	68.24	68.25	-

*Valuable light olefins is the sum of ethene, propene and 1,3-butadiene.
[&] Detailed feed composition not available.

Figure 3-12 A shows the azimuthally mixing cup averaged process gas temperature as a function of the radial position at an axial position of 10.5 m, i.e. near the reactor outlet. As the reactor inner radii vary, the radial position is normalized. The Bare reactor has a temperature difference between centerline and innerwall equal to 95.6 K. This value is in the same range as reported previously by Van Geem et al. [54] using a 2D model and De Saegher et al. [53] using a 3D model, although for different reactors and/or feedstocks. The temperature difference in comparison with Bare is 13.3, 6.9 and 21.4 K lower for the Helix, Straight and SmallFins respectively. Because of the lower inner wall temperatures, the finned reactors will yield lower coking rates. The small maximum seen at 0.013 m for Helix and at 0.014 m for SmallFins is a result of a zone with higher temperature in the wake of the fins as was also seen in Figure 3-4. Figure 3-12 B shows the mixing cup propane yield as a function of the radial position at an axial position of 10.5 m. The profiles are normalized to their respective value at the reactor centerline to limit the effect of small differences in conversion. A relative difference of up to 10 % is simulated between the center of the reactor and the reactor inner wall for the Bare reactor. Surprisingly a larger difference of 18 % is observed for the Straight reactor. This is attributed to the larger reactor maximum inner diameter compared to the Bare reactor and the absence of enhanced mixing from swirling flow. The better mixing in the Helix reactor reduces the non-uniformity although still not making up completely for the larger reactor inner diameter compared to the Bare reactor. The SmallFins reactor benefits both from better mixing and a lower tube diameter compared to Helix and Straight, yielding the most uniform profile. Figure 3-12 C shows the mixing cup hydrogen radical yield as a function of radial position at an axial position of 10.5 m. Again the values are normalized to their respective value at the reactor centerline to

limit the effect of small differences in conversion. Comparing these profiles with Figure 3-12 B, it is clear that the hydrogen radical yield shows a much steeper profile close to the reactor wall than the propane yield. This comparison holds for all radicals and molecules. The formation of radicals through C-C and C-H scissions has a high activation energy, whereas the activation energy of radical-consuming recombinations is close to zero. Hence, the formation of radicals is favored at high temperatures. The ranking of radical uniformity between the reactors is therefore equal to the ranking of temperature uniformity with Bare being the worst and Smallfins performing best. Taking into account reactions R1 and R2 as determining the propene selectivity, a higher hydrogen concentration near the wall will result in lower propene selectivity as reaction R2 is favored over R1. Higher radial temperature uniformity results in a reduction of propene consuming reactions, leading to a higher propene selectivity.
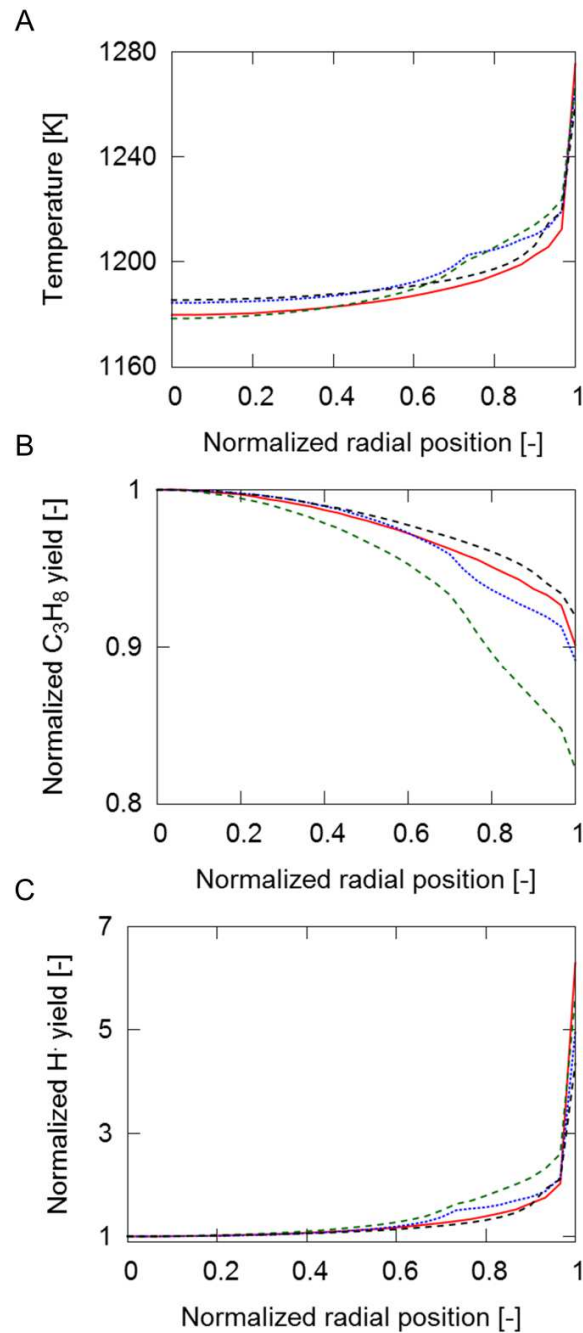
Figure 3-12: Azimuthally mixing cup averaged process gas temperature [K] (A), normalized propane yield [wt%/wt%] (B) and normalized hydrogen radical yield [wt%/wt%] (C) as a function of radial position at an axial position of 10.5 m: ———— - Bare; ··········· - Helix; - - - - - - Straight; - - - - - - SmallFins.

As discussed in Chapter 1, coke formation during steam cracking of hydrocarbons is a complex process. Three distinct mechanisms have been proposed [57]. First, there is a catalytic phase in which the properties of the reactor alloy are important. Afterwards, a heterogeneous, non-catalytic mechanism dominates. Coke can also be formed through a homogeneous non-catalytic mechanism in which high-molecular polyaromatics condense, collide with the coke surface and get incorporated in the coke layer. In steam cracking reactors, most coke is formed through the heterogeneous, non-catalytic mechanism. The modeling of the coke formation is therefore focused on this mechanism [58]. In this mechanism, radical active sites are formed on the coke layer by abstraction reactions by gas-phase radicals followed by additions of gas phase olefins, terminations by radicals, cyclizations and dehydrogenation [59]. Hence, the coking rate is determined by the temperature and both molecular and radical gas-phase concentrations near the gas-coke interface. As the time-scale for coke formation is much smaller than for gas-phase reactions, a discrete approximation can be adopted. This means that coke formation can be assumed constant in a certain time interval, typically 24 to 48 hours is sufficient [60, 61]. From the performed simulations, the coking rate at start-of-run conditions, can thus be calculated in a post-processing step from the species concentrations and inner wall temperature.

The semi-empirical coking model of Plehiers was used [60]. The parameters in this model were fitted to experimental data using a one-dimensional plug flow reactor model and it has shown to give reasonable agreement with both pilot and industrial coking rates [60]. The coking model of Plehiers considers only ethene and propene as coke precursors. Given the typical species concentrations in a propane cracker, these are indeed the main molecules adding to the active

radical sites on the coke layer. As the model kinetic parameters were fitted to experimental data using a 1D model, the mixing cup ethene and propene concentrations are used. However, the kinetic parameter estimation was performed for the coke-gas interface temperature. Hence, the inner wall temperature is used here, rather than the mixing cup gas temperature.

Figure 3-13 shows the azimuthally area-averaged coking rate as a function of axial position for the four reactor configurations. All profiles show two high values; the first around 6 m and the second at the reactor outlet. This shape can be explained by considering the three contributions to the coking rate, i.e. the inner wall temperature, the ethene concentration and the propene concentration. The inner wall temperature shows a similar profile as the outer wall temperature profile shown in Figure 3-11 having a maximum around an axial position of 4 m.
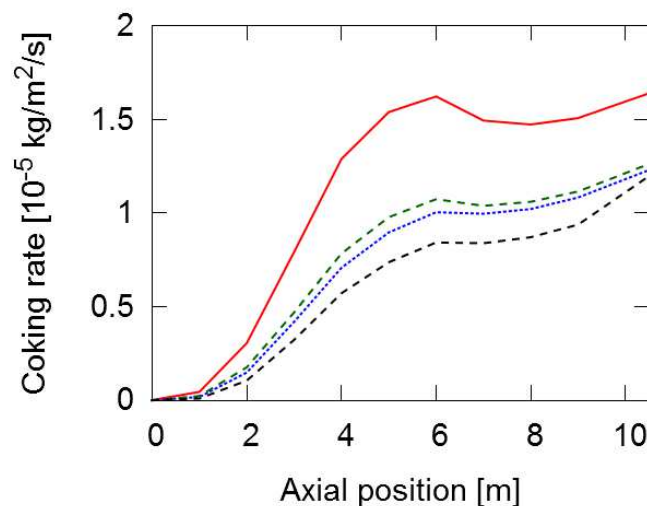
Figure 3-13: Azimuthally area-averaged coking rate [10^{-5} kg/m²/s] as a function of axial position [m]: ———— **- Bare;** ·············- **Helix;** - - - - - - **- Straight;** - - - - - - **- SmallFins.**

The ethene and propene concentrations are depicted in Figure 3-14 A and B respectively. The reactors with the highest pressure drop obviously show the highest concentrations due to a higher gas density. The ethene concentration increases monotonically along the reactor. The propene concentration has a maximum at 6 m. Hence, the maximum in coking rate at 6 m is a result of the temperature and propene concentration maximum. The high value at the outlet results from the high ethene concentration. Comparing SmallFins to Bare, coking rates are lowered by 48 % and 27 % at 6 m and 10 m respectively. Hence, run length can be extended greatly by application of finned tubes as a given reduction in the coking rate results in a more than proportional increase of the run length as shown by Wang et al. [62].
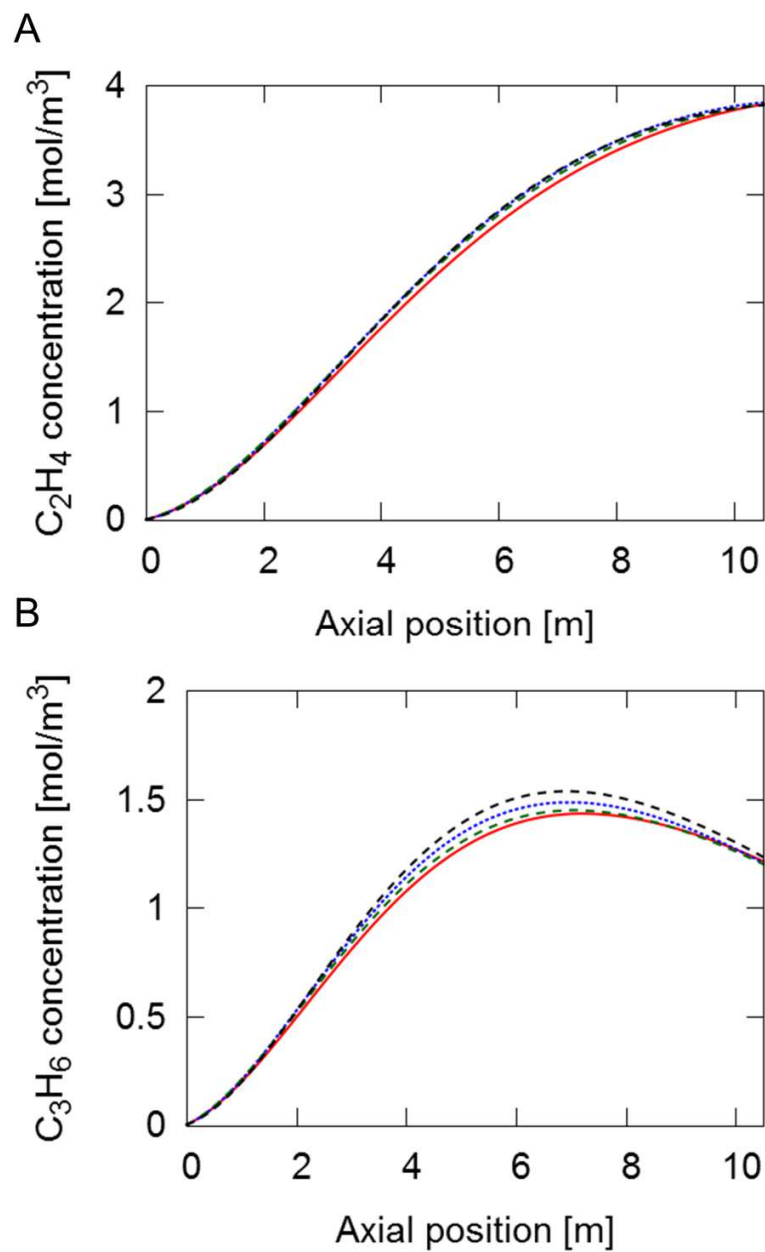
Figure 3-14: Ethene (A) and propene (B) concentration [mol/m³] mixing cup averaged over a cross section as a function of axial position [m]: ——— - Bare; ....- Helix; ------ - Straight; - - - - - - SmallFins.

Figure 3-15 A shows the coking rate as a function of the relative fin arc length. This relative fin arc length is defined as the running arc length from one fin top to the next divided by the total arc length of one fin. This normalization is necessary as the total fin arc length differs between SmallFins on one side and Helix and Straight on the other. The shape is a direct result of the non-uniform temperature at the reactor inner wall shown in Figure 3-15 B. The average inner wall temperature is 17.2, 16.8 and 18.5 K lower than the temperature of the Bare reactor for the Helix, Straight and SmallFins reactor respectively. The difference between minimum and maximum temperature is about 15 K for Helix and Straight, whereas it is only 6 K for SmallFins. At a relative fin arc length of 0.11, Helix shows a small bump. This is again caused by the higher temperature in the wake of the fin also seen in Figure 3-4. The higher inner wall temperature in the fin valley and resulting higher coke formation will lead to a reduction of the fin height by coke filling up the fin valleys. This will be most pronounced for the Helix and Straight reactor as coke in the fin valley grows about 30 % faster compared to the coke at the fin top. The more uniform temperature profile for SmallFins results in a more uniform growth of the coke layer. Here the difference in coking rate between fin top and valley is only 10%. Hence it is expected that the increased heat transfer due to the finned structure will persist longer for SmallFins. The large non-uniformity of the coking rate shows that azimuthally averaging the coking rate for run length predictions of finned reactors as typically done for bare reactors in 1D and 2D reactor models can severely bias the results. For future work it is therefore advised to take the non-uniform buildup of coke over time into account in order to make realistic run length predictions.

A

B
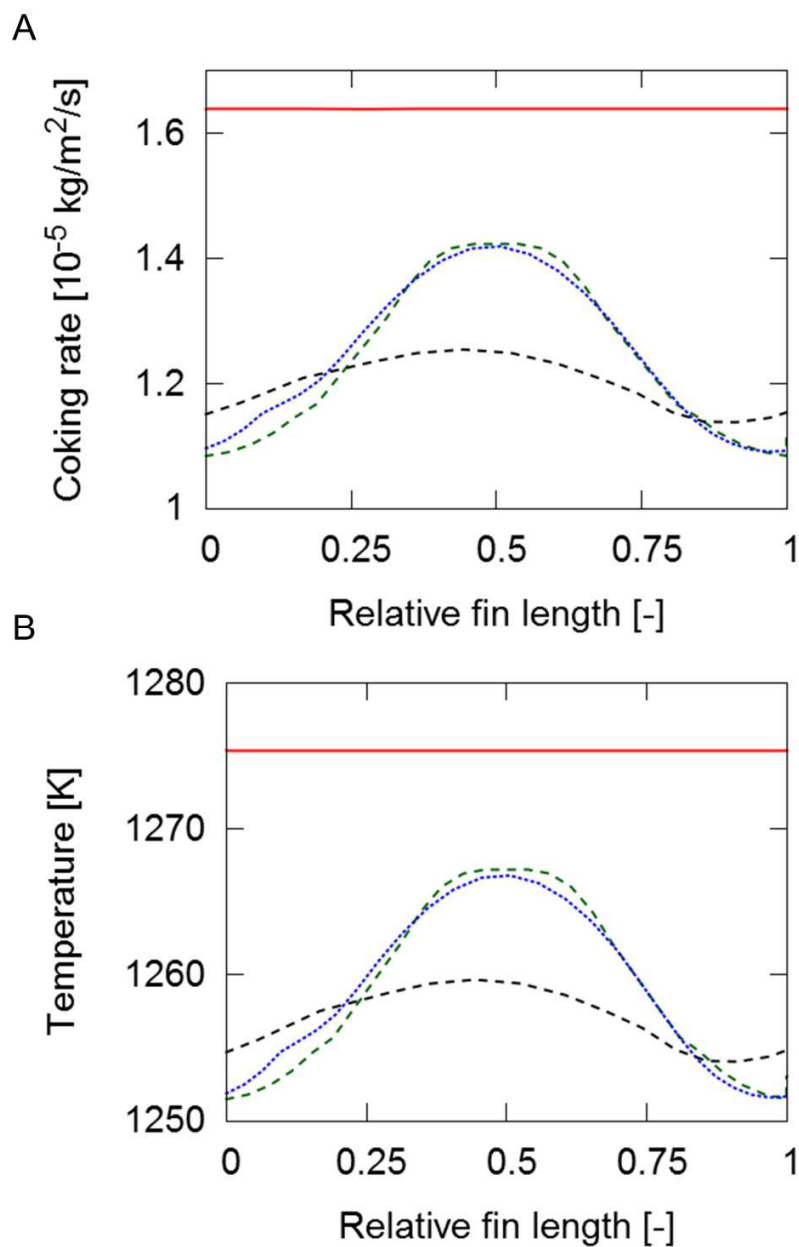
Figure 3-15: Coking rate [10^{-5} kg/m²/s] (A) and inner wall temperature [K] (B) as a function of the relative fin arc length (0: top; 0.5: valley; 1.0: top) at an axial position of 10.5 m: ────── **- Bare;** ·········· **- Helix;** ------ **- Straight;** ------ **- SmallFins.**

3.6 Conclusions

A three-dimensional reactor model was used for the simulation of internally finned steam cracking reactor tubes. The model agreed well with the experimental validation data of Albano et al. [50] obtained with air. A parametric study optimizing the fin parameters, i.e. fin height, helix angle and number of fins, to maximize heat transfer revealed that the application of small fins with a large helix angle leads to an overall increase in heat transfer for a similar pressure drop. Two optimized designs outperformed all other tube geometries of the parametric study regarding heat transfer. These optimized designs were compared with conventionally used bare reactor tubes for an industrial Millisecond furnace. The reactive simulations with a detailed free-radical reaction mechanism of 203 reactions and 26 species showed that helicoidally finned tubes performed better in comparison to longitudinally finned tubes. Mainly the configuration with 24 small fins and a high helix angle outperformed all other configurations in terms of heat transfer. The corresponding coking rates were found to be 30-50 % lower than for the bare tube depending on the fin parameters, which will lead to improved run lengths. However, the large non-uniformity of the coking rates in the azimuthal coordinate could lead to local buildup of coke over time and could affect the performance. The calculated pressure drop for the finned geometries is significantly higher, especially for the helicoidally finned reactors. It was seen that this can reduce the relative ethene selectivity by more than 1 %, while it increases selectivity to propene and 1,3-butadiene. An economic trade-off for a specific unit, evaluating the effect of longer run length and shift in light olefin selectivity, should determine the final decision of application of finned reactors. The presented CFD simulations can provide data for such evaluations.

References

[1] T. Ren, M. Patel, K. Blok, Olefins from conventional and heavy feedstocks: Energy use in steam cracking and alternative processes, Energy, 31 (2006) 425-451.

[2] K.M. Van Geem, G.B. Marin, N. Hedebouin, J. Grootjans, Energy efficiency of the cold train of an ethylene cracker, Oil Gas-Eur. Mag., 34 (2008) 95-99.

[3] T. Ren, M.K. Patel, K. Blok, Steam cracking and methane to olefins: Energy use, CO2 emissions and production costs, Energy, 33 (2008) 817-833.

[4] K.M. Van Geem, M.F. Reyniers, G.B. Marin, Two severity indices for scale-up of steam cracking coils, Industrial & Engineering Chemistry Research, 44 (2005) 3402-3411.

[5] J. Wang, M.-F. Reyniers, G.B. Marin, Influence of dimethyl disulfide on coke formation during steam cracking of hydrocarbons, Industrial & Engineering Chemistry Research, 46 (2007) 4134-4148.

[6] J. Wang, M.-F. Reyniers, K.M. Van Geem, G.B. Marin, Influence of silicon and silicon/sulfur-containing additives on coke formation during steam cracking of hydrocarbons, Industrial & Engineering Chemistry Research, 47 (2008) 1468-1482.

[7] M.-F. Reyniers, G.F. Froment, Influence of metal-surface and sulfur addition on coke deposition in the thermal-cracking of hydrocarbons, Industrial & Engineering Chemistry Research, 34 (1995) 773-785.

[8] S.B. Parks, C.M. Schillmoller, Use alloys to improve ethylene production, Hydrocarbon Processing, 75 (1996) 53-&.

[9] P. Broutin, F. Ropital, M.-F. Reyniers, G.F. Froment, Anticoking coatings for high temperature petrochemical reactors, Oil & Gas Science and Technology - Revue D'Institut Français du Pétrole Energies Nouvelles, 54 (1999) 375-385.

[10] T. Redmond, M.P. Bergeron, Tests demonstrate anticoking capability of new coating, Oil & Gas Journal, 97 (1999) 39-42.

[11] S. Petrone, Y. Chen, R. Deuis, L. Benum, D. Gent, R. Saunders, C. Wong, Catalyzed-assisted Manufacture of Olefins (CAMOL): Realizing Novel Operational Benefits from Furnace Coil Surfaces, AIChE 2008 Spring National Meeting, New Orleans, Louisiana, 2008.

[12] S. Petrone, R. Deuis, F. Kong, Y. Chen, Catalytic surfaces and coatings for the manufacture of petrochemicals, B. Corporation, (2013).

[13] S. Petrone, R. Mandyam, A. Wysiekierski, Surface alloyed high temperature alloys, S.E.P. Corp., (1997).

[14] S. Petrone, R. Manyam, A. Wysiekierski, K. Tzatzov, Y. Chen, A "carbon-like" coating to improved coking resistance in pyrolysis furnaces, 10th Annual Ethylene Producers' Conference, New Orleans, LA, 1998.

[15] A. Ganser, K.A. Wynns, A. Kurlekar, Operational experience with diffusion coatings on steam cracker tubes, Materials and Corrosion-Werkstoffe Und Korrosion, 50 (1999) 700-705.

[16] T.S. Ravigururajan, A.E. Bergles, Development and verification of general correlations for pressure drop and heat transfer in single-phase turbulent flow in enhanced tubes, Experimental Thermal and Fluid Science, 13 (1996) 55-70.

[17] M.K. Jensen, A. Vlakancic, Experimental investigation of turbulent heat transfer and fluid flow in internally finned tubes, International Journal of Heat and Mass Transfer, 42 (1999) 1343-1351.

[18] G.J. Zdaniuk, L.M. Chamra, P.J. Mago, Experimental determination of heat transfer and friction in helically-finned tubes, Experimental Thermal and Fluid Science, 32 (2008) 15.

[19] T.S. Ravigururajan, A.E. Bergles, Visualization of Flow Phenomena Near Enhanced Surfaces, Journal of Heat Transfer, 116 (1994) 54-57.

[20] D.J. Brown, Internally finned radiant coils: a valuable tool for improving ethylene plant economics, 6th EMEA Petrochemicals Technology Conference, London, U.K., 2004.

[21] J.V. Albano, K.M. Sundaram, M.J. Maddock, Applications of Extended Surfaces in Pyrolysis Coils, Energy Progress, 8 (1988) 160-168.

[22] J.J. De Saegher, T. Detemmerman, G.F. Froment, Three dimensional simulation of high severity internally finned cracking coils for olefins production, Revue De L'Institut Français Du Pétrole, 51 (1996) 245-260.

[23] J. Higuchi, K. Hamaogi, Metal Tube for Pyrolysis Reaction, (2009).

[24] P. Wolpert, B. Ganser, D. Jakobi, R. Kirchheiner, Process and finned tube for the thermal cracking of hydrocarbons, US 2005/0131263 (2005) 18.

[25] G.D. Stefanidis, B. Merci, G.J. Heynderickx, G.B. Marin, CFD simulations of steam cracking furnaces using detailed combustion mechanisms, Computers & Chemical Engineering, 30 (2006) 635-649.

[26] G.D. Stefanidis, B. Merci, G.J. Heynderickx, G.B. Marin, Gray/nongray gas radiation modeling in steam cracker CFD calculations, Aiche Journal, 53 (2007) 1658-1669.

[27] G.D. Stefanidis, K.M. Van Geem, G.J. Heynderickx, G.B. Marin, Evaluation of high-emissivity coatings in steam cracking furnaces using a non-grey gas radiation model, Chemical Engineering Journal 137 (2008) 411-421.

[28] A. Habibi, B. Merci, G.J. Heynderickx, Impact of radiation models in CFD simulations of steam cracking furnaces, Computers & Chemical Engineering, 31 (2007) 1389-1406.

[29] A. Habibi, B. Merci, G.J. Heynderickx, Multiscale modeling of turbulent combustion and NOx emission in steam crackers, Aiche Journal, 53 (2007) 2384-2398.

[30] G. Hu, H. Wang, F. Qian, Numerical simulation on flow, combustion and heat transfer of ethylene cracking furnaces, Chemical Engineering Science, 66 (2011) 1600-1611.

[31] G. Hu, H. Wang, F. Qian, K.M. Van Geem, C.M. Schietekat, G.B. Marin, Coupled simulation of an industrial naphtha cracking furnace equipped with long-flame and radiation burners, Computers & Chemical Engineering, 38 (2012) 24-34.

[32] G.H. Hu, H.G. Wang, F. Qian, Y. Zhang, J.L. Li, K.M. Van Geem, G.B. Marin, Comprehensive CFD Simulation of Product Yields and Coking Rates for a Floor- and Wall-Fired Naphtha Cracking Furnace, Industrial & Engineering Chemistry Research, 50 (2011) 13672-13685.

[33] Q. Tang, M. Denison, B. Adams, D. Brown, Towards comprehensive computational fluid dynamics modeling of pyrolysis furnaces with next generation low-NO(x) burners using finite-rate chemistry, Proceedings of the Combustion Institute, 32 (2009) 2649-2657.

[34] X. Lan, J. Gao, C. Xu, H. Zhang, Numerical simulation of transfer and reaction processes in ethylene furnaces, Chemical Engineering Research & Design, 85 (2007) 1565-1579.

[35] M.K. Sabbe, K.M. Van Geem, M.-F. Reyniers, G.B. Marin, First Principle-Based Simulation of Ethane Steam Cracking, Aiche Journal, 57 (2011) 482-496.

[36] W. Sun, M. Saeys, Construction of an Ab Initio Kinetic Model for Industrial Ethane Pyrolysis, Aiche Journal, 57 (2011) 2458-2471.

[37] K.M. Van Geem, M.F. Reyniers, G.B. Marin, J. Song, W.H. Green, D.M. Matheu, Automatic reaction network generation using RMG for steam cracking of n-hexane, AIChE Journal, 52 (2006) 718-730.

[38] E. Ranzi, A. Frassoldati, S. Granata, T. Faravelli, Wide-range kinetic modeling study of the pyrolysis, partial oxidation, and combustion of heavy n-alkanes, Industrial & Engineering Chemistry Research, 44 (2005) 5170-5183.

[39] W.J. Pitz, C.J. Mueller, Recent progress in the development of diesel surrogate fuels, Progress in Energy and Combustion Science, 37 (2011) 330-350.

[40] P.J. Clymans, G.F. Froment, Computer-generation of reaction paths and rate-equations in the thermal cracking of normal and branched paraffins, Computers & Chemical Engineering, 8 (1984) 137-142.

[41] K.M. Van Geem, D. Hudebine, M.-F. Reyniers, F. Wahl, J.J. Verstraete, G.B. Marin, Molecular reconstruction of naphtha steam cracking feedstocks based on commercial indices, Computers & Chemical Engineering, 31 (2007) 1020-1034.

[42] K.M. Van Geem, R. Zajdlik, M.-F. Reyniers, G.B. Marin, Dimensional analysis for scaling up and down steam cracking coils, Chemical Engineering Journal, 134 (2007) 3-10.

[43] J.E. Jones, On the Determination of Molecular Fields. I. From the Variation of the Viscosity of a Gas with Temperature, Proceedings of the Royal Society of London. Series A, 106 (1924) 441-462.

[44] R.B. Bird, W.E. Stewart, E.N. Lightfoot, Transport Phenomena, Wiley, 2006.

[45] E.W. Lemmon, R.T. Jacobsen, Viscosity and Thermal Conductivity Equations for Nitrogen, Oxygen, Argon, and Air, International Journal of Thermophysics, 25 (2004) 21-69.

[46] H.A. McGee, Molecular Engineering, McGraw-Hill, New York, 1991.

[47] K.K.Y. Kuo, Principles of Combustion, Wiley-Interscience, New York, 2005.

[48] B.P. Leonard, Order of accuracy of QUICK and related convection-diffusion schemes, Applied Mathematical Modelling, 19 (1995) 640-653.

[49] B. Andersson, R. Andersson, L. Hakansson, M. Mortensen, R. Sudiyo, B. van Wachem, Computational Fluid Dynamics for Engineers, 7th ed., Cambridge University Press, 2012.

[50] J.V. Albano, K.M. Sundaram, M.J. Maddock, Applications of extended surfaces in pyrolysis coils, Energy Progress, 8 (1988) 9.

[51] T. Von Kármán, Mechanical similitude and turbulence, National Advisory Committee for Aeronautics, Washington D.C., 1931.

[52] P. Wolpert, B. Ganser, D. Jakobi, R. Kirchheiner, Process and finned tube for the thermal cracking of hydrocarbons, (2005).

[53] J.J. De Saegher, T. Detemmerman, G.F. Froment, Three dimensional simulation of high severity internally finned cracking coils for olefins production, Oil & Gas Science and Technology - Revue de l'Institut Francais du Petrole, 51 (1996) 245-260.

[54] K.M. Van Geem, G.J. Heynderickx, G.B. Marin, Effect of radial temperature profiles on yields in steam cracking, AIChE Journal, 50 (2004) 173-183.

[55] G. Hu, H. Wang, Q. Feng, K.M. Van Geem, C.M. Schietekat, G.B. Marin, Coupled simulation of an industrial naphtha cracking furnace equipped with long-flame and radiation burners, Computers & Chemical Engineering, 38 (2012) 24-34.

[56] G.F. Froment, Kinetics and reactor design in the thermal-cracking for olefins production, Chemical Engineering Science, 47 (1992) 2163-2177.

[57] S. Wauters, G.B. Marin, Kinetic Modeling of Coke Formation during Steam Cracking, Industrial & Engineering Chemistry Research, 41 (2002) 2379-2391.

[58] S. Wauters, G.B. Marin, Computer generation of a network of elementary steps for coke formation during the thermal cracking of hydrocarbons, Chemical Engineering Journal, 82 (2001) 267-279.

[59] G.C. Reyniers, G.F. Froment, F.D. Kopinke, G. Zimmermann, Coke Formation in the Thermal Cracking of Hydrocarbons. 4. Modeling of Coke Formation in Naphtha Cracking, Industrial & Engineering Chemistry Research, 33 (1994) 2584-2590.

[60] P.M. Plehiers, G.C. Reyniers, G.F. Froment, Simulation of the run length of an ethane cracking furnace, Industrial & Engineering Chemistry Research, 29 (1990) 636-641.

[61] G.J. Heynderickx, G.F. Froment, Simulation and comparison of the run length of an ethane cracking furnace with reactor tubes of circular and elliptical cross sections, Industrial & Engineering Chemistry Research, 37 (1998) 914-922.

[62] J.D. Wang, M.F. Reyniers, K.M. Van Geem, G.B. Marin, Influence of silicon and silicon/sulfur-containing additives on coke formation during steam cracking of hydrocarbons, Industrial & Engineering Chemistry Research, 47 (2008).

Chapter 4:

Computational Fluid Dynamics simulations with detailed chemistry: Application of Pseudo-Steady State Approximation

Abstract

Using detailed kinetic models in computational fluid dynamics (CFD) simulations is extremely challenging because of the large number of species that are nowadays considered in these models and the stiffness of the associated set of differential equations. A simplified 1D model does not capture the required detail that reactor engineers need and leads to substantial differences compared to the reference 3D simulations as is illustrated for propane steam cracking. A methodology was developed to use detailed single-event microkinetic models in CFD simulations of steam cracking reactors by on the fly application of the pseudo-steady state assumption on the radicals. Depending on the reaction network size, a speedup factor from 7 to 54 was obtained compared to the standard FLUENT routines. The yields of molecules matched those from the standard routines well. For the concentration of the radicals near the reactor inner wall, there is an average relative error of around 10 %. The methodology was then applied to the simulation of an industrial propane cracking reactor. A conventional bare reactor and a helicoidally finned reactor were compared. The adopted reaction network contained 85 species, of which 41 were radicals and 44 were molecules. By application of the finned reactor, the maximum external tube temperature is reduced by 44 K. The ethene selectivity is reduced by 0.17 % while propene and 1,3-butadiene selectivity increased by 0.08 and 0.03 % respectively. The benzene selectivity is 0.05 wt% higher in the helicoidally finned reactor because of the higher pressure drop.

Keywords: Computational fluid dynamics, detailed chemistry, pseudo-steady state approximation, steam cracking, ethene, enhanced heat transfer

4.1 Introduction

Accurate simulation of reactive fluid flow requires first principles models for both the chemistry and the fluid flow. For the former only comprehensive kinetic models consisting of elementary reaction steps will yield accurate results over a wide range of conditions. In the field of combustion, oxidation and pyrolysis, the fundamental modeling of gas-phase chemistry has thrived over the last two decades driven by an improved knowledge of the reaction families, the availability of rate coefficients [1] and the automation of kinetic model generation through computer codes [2-10]. This increase in modeling accuracy is accompanied by a steep increase in the size of kinetic models, with state of the art combustion and pyrolysis kinetic models easily containing several hundred species and thousands of reactions [11-14] to account for all reaction pathways and the intermediate species. Figure 4-1 displays the size of selected kinetic models for thermal decomposition, oxidation and combustion processes over the last two decades. It is clear that the number of species and reactions of the reaction networks has increased drastically.

Chapter 4:

110   **Computational Fluid Dynamics simulations with detailed chemistry: Application**
of Pseudo-Steady State Approximation
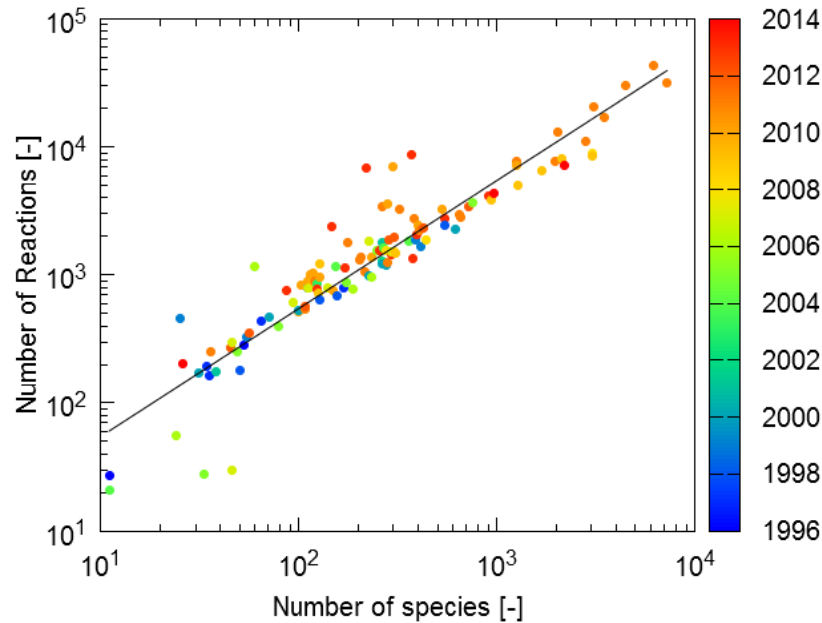
Figure 4-1: Number of reactions [-] as a function of number of species [-] of selected reaction networks for

oxidation, pyrolysis and combustion (after Lu and Law [15]) over the last two decades.

Notwithstanding the developments in accurate chemistry modeling, the implementation of these

detailed kinetic models in computational fluid dynamics (CFD) simulations remains a daunting

task because of two specific characteristics of these kinetic models. First, the simulation time

increases drastically with increasing size of the kinetic model as each species adds an extra

continuity equation to the system to be integrated. Second, these kinetic models show a large

spread in time scales associated with species and reactions [16]. This spread originates from the

distinct difference in reactivity of radical and molecular species and from reactions in partial

equilibrium. These two characteristics of the kinetic models, large size and stiffness, render

multidimensional CFD simulations very CPU time-intensive and often beyond the capabilities of

computers available in most research centers [17]. This has resulted in two main categories of reactive flow simulations [17]. On the one hand, one-dimensional models using detailed kinetic models are often used for the assessment of the accuracy of (automatically generated) kinetic models and for the simulation of lab-scale setups or even for industrial reactors if simplification of the fluid flow to one dimension is possible. On the other hand, advanced engineering tools relying on CFD methods used for the design of industrially relevant geometries usually model the chemistry rather approximately by a few reactions [18, 19]. Merging these two categories, i.e. unification of detailed kinetic models and CFD simulations, would allow the more accurate design and optimization of reactive flows. This challenge has been widely recognized in the combustion engineering community [20] and several methods for reducing the computational cost associated with detailed kinetic models have been proposed. These can be roughly divided into three categories: kinetic model reduction methods, storage/retrieval-based methods and adaptive chemistry methods. Model reduction decreases the number of reactions and/or species or reduces the number of independent variables by application of e.g. the pseudo-steady state assumption (PSSA) [21-25], partial equilibrium (PE) [26, 27], vertical and horizontal lumping [28, 29], intrinsic low dimensional manifold (ILDM) [30], directed relation graph (DRG) [31] and computational singular perturbation (CSP) [32]. Storage/retrieval methods are based on tabulation strategies for the species rate of formation. In-situ adaptive tabulation (ISAT) [33] and Piecewise reusable implementation of solution mapping (PRISM) [34] are two examples with the former using Taylor series and the latter using polynomial regression to obtain rates of formation based on tabulated points. Finally, adaptive chemistry methods use several reduced kinetic models, each valid for a subset of space of the simulation [35-39]. As the kinetic models are

Chapter 4:

112   **Computational Fluid Dynamics simulations with detailed chemistry: Application of Pseudo-Steady State Approximation**

tailored to a more narrow range of thermochemical conditions, they are smaller and a significant speedup can be obtained.

For the steam cracking of hydrocarbons, there is an interest in shifting from conventional one-dimensional plug flow modeling towards more fundamental, multidimensional reactive flow modeling. First, the heat flux from the furnace to the reactors causes a radial gradient in the process gas temperature and this radial temperature profile produces radial concentration profiles. In the plug flow reactor model the rate of formation of a species is calculated using the cross-sectional mixing cup temperature and concentrations. This value is not equal to the mixing cup average rate of formation, i.e. $R_j(\boldsymbol{C_{avg}}, T_{avg}) \neq R_{j,avg}(\boldsymbol{C}, T)$. Hence, depending on the magnitude of the radial gradient, an error in the predicted product yields is made. In addition coke is formed on the inside of the reactor. The rate of coke formation depends -among other variables- largely on the inner wall temperature and on the gas-phase concentrations near the inner wall. In a one-dimensional reactor model, the inner wall temperature is obtained via correlations for the Nusselt number for fully developed, turbulent pipe flow such as the Gnielinski correlation [40]. These correlations target at non-reactive flows and application to endothermic reactive flows results in an overprediction of the difference between the inner wall and the mixing cup process gas temperature as shown by Sundaram and Froment [41]. Also the mixing cup species concentrations are typically used in the calculation of the coking rate even though it has been shown that the near-wall concentrations differ significantly from the mixing cup concentrations, most certainly for radicals [42, 43]. Secondly, the plug flow reactor model fails to account for azimuthal non-uniformities in the heat flux profile to the reactors, e.g. because

of shadow effects in the furnace. Heynderickx and Froment [44] showed that these azimuthal heat flux non-uniformities can cause an azimuthal variation of 50 K in temperature and a 100 % azimuthal variation in coking rate, but did not quantify the effect on the product yields. Finally, the plug flow reactor model fails to account for the complex flow pattern caused by emerging three-dimensional reactor technologies [43, 45, 46] and return bends [19]. Reckoning these shortcomings, several authors have simulated steam cracking reactors with two-dimensional [42, 47-49] and three-dimensional reactor models [19, 43, 50-52]. In most of these studies, a severely reduced kinetic model was used because of extremely large simulation times and difficulties in achieving a converged solution with a detailed kinetic model.

In the present work, steam cracking reactors are simulated using detailed kinetic models. To limit computational time, the pseudo-steady state assumption is applied to the radicals both a-priori and on the fly. First, the three-dimensional simulation results are compared to one-dimensional plug flow results. To this end, the one-dimensional simulation program COILSIM1D was extended to account for radial non-uniformities in temperature and radical concentrations. After an overview of the 3D model, the methodology is validated and the speedup in CPU time is quantified. Next, the application of an optimized finned reactor technology in an industrial steam cracking unit is simulated and the effect of the reactor geometry on product yields in analyzed.

4.2 Numerical models

4.2.1   Governing equations

4.2.1.1   One-dimensional reactor model

Instead of performing CPU-intensive simulations with a three-dimensional reactor model, plug flow reactor models are more routinely used to simulate steam cracking reactors. The common method to account for the effect of three-dimensional reactor technologies on product yields and maximum external tube metal temperatures is by multiplication of the friction factor and Nusselt number by a factor derived from non-reactive experiments or simulations as e.g. reported by Albano et al. [53] and Schietekat et al. [45]. COILSIM1D is such a 1D reactor model for steam cracking reactors incorporating a single-event microkinetic model of more than 700 species [13]. The governing equations of COILSIM1D are:

$$\frac{dF_j}{dz} = \frac{\pi d^2}{4} R_{avg,j} \tag{4.1}$$

$$-\frac{dp}{dz} = \left(\frac{2f_f}{d_{int}} + \frac{\zeta}{\pi r_b}\right)\rho u^2 + \rho u \frac{du}{dz} \tag{4.2}$$

$$\sum_{j=1}^{N_s} F_j c_{p_j} \frac{dT_{avg}}{dz} = \pi d_{int} q_{int} + \frac{\pi d_{int}^2}{4} \sum_{i=1}^{nreac} r_i \left(-\Delta H_i\right) \tag{4.3}$$

with $f_f = \alpha_f f_{corr}$, f_{corr} calculated from the Colebrook equation [54] and α_f a user-supplied correction factor to account for the increased pressure drop by application of a three-dimensional reactor technology. For the simulations in paragraph 4.3.3, α_f was set to unity for the Bare tube

while for the SmallFins tube α_f was set to 1.99. These values were obtained from the non-reactive flow simulations of Chapter 3 [43].

COILSIM1D was extended to account for the influence of the radial temperature and β-radical concentration profiles on product yields and heat transfer by calculating the mixing cup rate of formation $R_{avg,j}$ in equation (4.1) over the cross-sectional area at each axial grid point z_i during numerical integration of the ordinary differential equations (4.1), (4.2) and (4.3). The well-known power law velocity profile for fully developed pipe flow proposed by Prandtl [55] is assumed:

$$u(r) = u_{max} \left(1 - \frac{2r}{d_{int}}\right)^{1/n} \tag{4.4}$$

where n is typically taken to be 7 resulting in the one-seventh law. From heat-momentum similarity, the following radial temperature distribution is assumed:

$$T(r) = T_{int} + (T_{center} - T_{int}) \left(1 - \frac{2r}{d_{int}}\right)^{1/n} \tag{4.5}$$

Figure 4-2 shows a flow sheet of the adopted calculation procedure. At the first point of the axial grid, i.e. i=0 in Figure 4-2, the average temperature T_{avg} is the reactor inlet temperature supplied by the user and the inner wall temperature is calculated using the heat flux at this axial position:

$$q_{int} = h(T_{int} - T_{avg}) \tag{4.6}$$

with q_{int} the heat flux per inner wall surface area, $h = \alpha_h h_{corr}$, α_h a user-supplied correction factor and h_{corr} calculated from the Gnielinski correlation [40]. For the simulations in paragraph 4.3.3, α_h was set to unity for the Bare tube while for the SmallFins tube α_h was set to 1.53. These values were obtained from the non-reactive flow simulations of Chapter 3

Chapter 4:

116   **Computational Fluid Dynamics simulations with detailed chemistry: Application of Pseudo-Steady State Approximation**

$$Nu = \frac{\frac{f_f}{8}(Re - 1000)Pr}{1 + 12.7\left(\frac{f_f}{8}\right)^{1/2}\left(Pr^{2/3} - 1\right)} \qquad (4.7)$$

Next, T_{center} is calculated by calculating the mixing cup temperature from equation (4.5) and setting it equal to the value of the reactor inlet temperature:

$$T_{avg} = \frac{\int_0^\Omega \phi_m(r)T(r)dA}{\int_0^\Omega \phi_m(r)dA} \qquad (4.8)$$

Hence, the radial temperature profile of equation (4.5) is defined. From this profile, the mixing cup rates of formation $R_{avg,j}$ are calculated:

$$R_{avg,j} = \frac{\int_0^{\frac{d_{int}}{2}} \rho(r)u(r)R_j\big(\boldsymbol{C}(r), T(r)\big)dr}{\int_0^{\frac{d_{int}}{2}} \rho(r)u(r)dr} \qquad (4.9)$$

By substitution of the ideal gas law and neglecting the radial variation of pressure and molecular mass, equation (4.9) becomes:

$$R_{avg,j} = \frac{\int_0^{\frac{d_{int}}{2}} \frac{u(r)R_j\big(\boldsymbol{C}(r), T(r)\big)}{T(r)}dr}{\int_0^{\frac{d_{int}}{2}} \frac{u(r)}{T(r)}dr} \qquad (4.10)$$

With this $R_{avg,j}$, the plug flow equations (4.1), (4.2) and (4.3) are integrated over Δz_i, the axial length of the axial grid point z_i. Hence, updated values for $\boldsymbol{C}$ and T_{avg} are available. From equation (4.6), T_{int} is updated. If the difference between the old and the updated value of T_{avg} is smaller than the threshold value ε_T, set to 0.01%, convergence is reached in this axial grid point and the simulation is proceeded to the next axial grid point. The converged T_{avg} and T_{int} are used

as initial guess for the next grid point. This procedure is repeated until the end of the reactor is

reached, i.e. $z_i = L$.
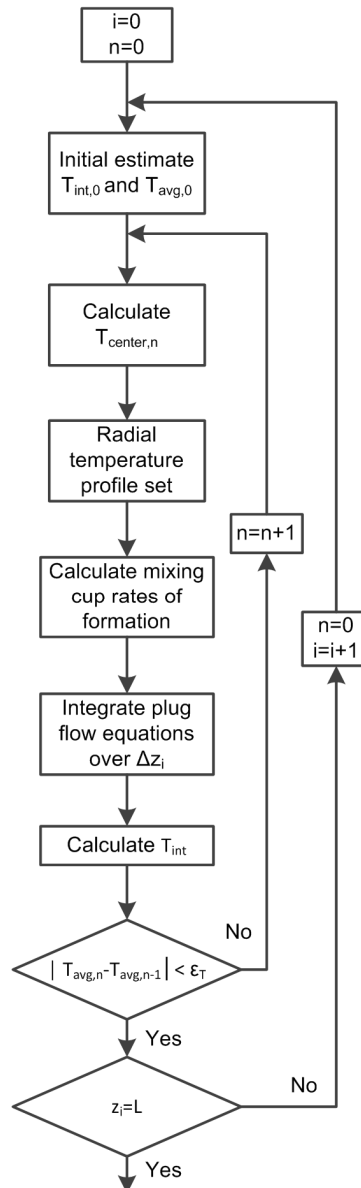
Figure 4-2: Flow sheet of calculation procedure in COILSIM1D to account for radial profiles.

Three types of simulations were performed. First without taking into account any radial variation, referred to as '1D'. Second, taking into account the radial temperature profile, referred to as '1D T', without accounting for radial variation in the species concentrations:

$$R_{avg,j} = \frac{\int_0^{\frac{d_{int}}{2}} \frac{u(r)R_j\big(\mathbf{C},T(r)\big)}{T(r)} dr}{\int_0^{\frac{d_{int}}{2}} \frac{u(r)}{T(r)} dr}$$
(4.11)

Finally, by taking into account both the radial temperature profile and the radial β-radials concentration profile. The radial variation of the concentration of the molecules is neglected in all simulations as it has been shown in Chapter 3 to be much smaller than the radial variation of the β-radicals concentration [42, 43]. The β-radicals concentrations as a function of radial coordinate are obtained by solving the algebraic equations resulting from application of the PSSA to the β-radicals as a function of the radial coordinate:

$$-R_{\beta_j}^c\big(\mathbf{C_M},\mathbf{C_\beta}(r),T(r)\big) = R_{\beta_j}^f\big(\mathbf{C_M},\mathbf{C_\beta}(r),T(r)\big)$$
(4.12)

Hence, equation (4.9) becomes:

$$R_{avg,j} = \frac{\int_0^{\frac{d_{int}}{2}} \frac{u(r)R_j\big(\mathbf{C_M},\mathbf{C_\beta}(r),T(r)\big)}{T(r)} dr}{\int_0^{\frac{d_{int}}{2}} \frac{u(r)}{T(r)} dr}$$
(4.13)

4.2.1.2 Three-dimensional reactor model

The steady-state governing equations of a compressible, reactive, single-phase, fluid flow are summarized in Table 4-1.

Table 4-1: Continuity equations.

Total mass balance	$\nabla \cdot (\rho \overline{\boldsymbol{u}}) = 0$	(4.14)
Navier-Stokes equations	$\nabla \cdot (\rho \overline{\boldsymbol{u}} \overline{\boldsymbol{u}}) = -\nabla p + \nabla \cdot \overline{\overline{\boldsymbol{\tau}}}$	(4.15)
Process gas region energy equation	$\nabla \cdot \left(\overline{\boldsymbol{u}}(\rho E + p) \right) = \nabla \cdot \left(\lambda_{f,eff} \nabla T - \sum_j h_j \bar{\boldsymbol{J}}_j \right) + S_h$	(4.16)
Reactor metal region energy equation	$\nabla \cdot (\lambda_s \nabla T) = 0$	(4.17)
Species continuity equation	$\nabla \cdot \left(\overline{\boldsymbol{u}} c_j \right) = -\nabla \cdot \bar{\boldsymbol{J}}_j + R_j \, , \forall j = 1, nspec - 1$	(4.18)

In the gas-phase energy equation, $E = h - \frac{p}{\rho} + \frac{|\overline{\boldsymbol{u}}|^2}{2}$ with the sensible enthalpy of the ideal gas mixture calculated as $h = \sum_{j=1}^{nspec} x_j h_j$ and $h_j = \int_{T_{ref}}^{T} C_P(T) dT$ with $C_{p,j}$ defined as a temperature polynomial with coefficients for the different species estimated with RMG's ThermoDataEstimator [5]. The effective conductivity of the process gas $\lambda_{f,eff}$ is the sum of the laminar and turbulent thermal conductivity $\lambda_{f,eff} = \lambda_{f,l} + \lambda_{f,t}$ with $\lambda_{f,l}$ calculated from kinetic theory and $\lambda_{f,t} = \frac{c_p \mu_t}{Pr_t}$ with $Pr_t = 0.85$. $\bar{\boldsymbol{J}}_j$ is the diffusion flux of species j, including contributions from both the laminar and turbulent diffusivity, i.e. $\bar{\boldsymbol{J}}_j = -\frac{1}{MM_j} \left(\rho D_{j,m} + \frac{\mu_t}{Sc_t} \right) \nabla C_j$ with $Sc_t = 0.7$. Turbulent diffusion overwhelms laminar and thermal or Soret diffusion in steam cracking reactors [43]. Hence, laminar diffusion is modeled rather approximate using kinetic theory and Soret diffusion is neglected. The final term S_h in the gas-phase energy equation is the heat of reaction. For the metal tube, an energy equation is solved to account for conductive heat transfer. The metal thermal conductivity λ_s is modeled as a temperature polynomial. R_j is the rate

Chapter 4:

120   Computational Fluid Dynamics simulations with detailed chemistry: Application of Pseudo-Steady State Approximation

of formation of species j and $nspec$ is the number of species. The k-ε RNG model was used for the bare tubes while the Reynolds Stress Model was used for the helicoidally finned tube as it showed better agreement to experimental data in Chapter 3 [43].

An adiabatic entrance zone with a length of 1.5 m was added upstream all reactors to ensure fully developed velocity and turbulence parameters profiles at the reactor inlet. At the inlet boundary, the process gas temperature, mass flow rate, turbulence parameters k and ε and the composition of the process gas were imposed. The turbulence parameters were calculated for a turbulence intensity of 8 % and a characteristic length scale of 10 % of the tube hydraulic diameter. At the reactor outlet, a constant pressure boundary condition was set. The no-slip boundary condition was set at the tube inner walls. The enhanced wall treatment was used to "bridge" the solution variables in the near-wall cells. This model combines a two-layer model with enhanced wall functions by blending linear and logarithmic laws-of-the-wall. Similar grids as in our previous work were used, ensuring that the near-wall cells are within the viscous sub-layer, satisfying the $y^+<1$ condition [43]. A heat flux profile was applied to the reactor outer walls. The commercial CFD code ANSYS FLUENT 13.0 was adopted to solve the governing equations.

4.2.2   Calculation rate of production term

The calculation routine for the rate of production terms R_j in the species continuity equations (4.18) was tailored to steam cracking kinetics and implemented in a user-defined function (UDF).

4.2.2.1   Single-event microkinetic model

The adopted single-event microkinetic model was generated using the same methodology as applied by Dijkmans et al. [56]. As the details of the methodology have been explained previously [13, 56-58], only a brief summary of the key aspects is given here. The reaction network consists of two parts: the β-network and the μ-network. The β-network contains the reactions between molecules with less than 6 carbon atoms and radicals that can undergo only bimolecular reactions or both mono- and bimolecular reactions, i.e. so-called β and βμ-radicals respectively. The adopted β-network was obtained by reducing the β-network of Dijkmans et al. [56] to the species relevant for propane cracking, the feedstock studied in this chapter. This resulted in a β-network of 758 elementary reversible reactions between 42 molecules and 41 radicals. The β-network is appended with the μ-network, which is a collection of independent sub-networks. In total, 31 sub-networks were included to account for the formation of aromatics. In 15 sub-networks, a β(μ)-radical adds to an olefin to produce a C_6+ radical. These radicals are assumed to only undergo monomolecular reactions, i.e. the so-called μ-radical hypothesis. Unsaturated μ-radicals can undergo ring closure reactions to form cyclic (di-)olefins. These cyclic species can subsequently dehydrogenate to form aromatics via hydrogen abstractions, β-scissions and C-H scissions which is described by the remaining 16 sub-networks. During

Chapter 4:

122   Computational Fluid Dynamics simulations with detailed chemistry: Application of Pseudo-Steady State Approximation

generation of a μ-network, the pseudo-steady state assumption is applied on the μ-radicals. In combination with the μ-radical hypothesis, this results in a set of algebraic equations that can be solved analytically to the μ-radicals' concentrations. Hence, the concentration of each μ-radical can be expressed as a function of the concentration of the starting species of the μ-network. Substitution of these concentrations in the rate of formation terms makes the latter only dependent on the concentrations of molecules and β(μ)-radicals. This not only reduces the number of species continuity equations to be solved, but also greatly reduces the stiffness of the set of differential equations. Consequently, the complete network contains 85 species, of which 41 radicals and 44 molecules. Validation of the reduced kinetic model for propane cracking was performed by comparison to the full network of Dijkmans et al. [56] and is available in Appendix A.

The thermodynamic data of the C_4^- molecules and β(μ)-radicals were derived from first principles CBS-QB3 calculations of Sabbe et al. [59, 60]. Thermodynamic data of the μ-molecules was estimated using RMG's ThermoDataEstimator.

The Arrhenius parameters necessary to calculate the reaction rate coefficients are calculated using a group additivity framework that is an extension of Benson's group additivity [61-63]. The reference parameters and group additive values used by Dijkmans et al. [56] were also adopted here. Most are based on first principles calculations and none were fitted to experimental data. To avoid time-consuming calculation of the reverse reaction rate coefficient by expressing thermodynamic consistency during the fluid dynamics simulation, the reversible β-reactions were split into two irreversible reactions by a-priori performing an linear regression of the reverse

Arrhenius parameters to the values expressed by thermodynamic consistency in the relevant temperature range, i.e. between 700 and 1300 K.

4.2.2.2 Pseudo-steady state assumption for β(μ)-radicals

Elimination of the μ-radicals by expressing the PSSA during network generation, greatly reduces the number of species continuity equations and the system stiffness. However, the difference in time scales between molecules and β-radicals is so large that significant stiffness still remains in the system. This requires very strong under relaxation of the continuity equations of the β-radicals to avoid divergence, making the simulation of industrial reactors computationally impossible. Therefore the PSSA is applied to the β-radicals also. As the rate of formation of these β-radicals contains terms that are second order in the PSS species, a-priori analytic calculation of the β-radicals concentration as done for the μ-radicals is impossible. Lu and Law [64] developed a method to obtain analytic solutions even when second order terms in the PSS species concentrations are present. The nonlinear algebraic equations are first linearized and then analytically solved with a directed graph. A good agreement was seen for the ignition delay time. This methodology was not applied here as the nonlinear terms in the PSS equations are strongly influenced by the higher pressure drop induced by three-dimensional reactor technologies and contribute more than 10 % to the rate of consumption for some PSS species, such as methyl and allyl radicals. Hence, to accurately model the effect of the reactor geometry on product yields, accounting for these terms is necessary. Hence, the concentration of the β-radical β_j is calculated numerically on the fly, i.e. during the flow simulations by expressing the rate for consumption $R_{\beta_j}^c$ to be equal to the rate of production $R_{\beta_j}^p$:

Chapter 4:

124   **Computational Fluid Dynamics simulations with detailed chemistry: Application of Pseudo-Steady State Approximation**

$$-R_{\beta_j}^c\left(\boldsymbol{C_M}, \boldsymbol{C_\beta}\right) = R_{\beta_j}^p\left(\boldsymbol{C_M}, \boldsymbol{C_\beta}\right) \tag{4.19}$$

Solving equation (4.19) numerically to $\boldsymbol{C_\beta}$ can be unstable [64] while a robust solution method is required as divergence of this algebraic solver would terminate the time-consuming flow simulation. A tailored algebraic solver was used here that updates the concentration of the β-radical j in iteration step n+1 via:

$$C_{\beta_j}^{n+1} = C_{\beta_j}^n \sqrt{\left|\frac{R_{\beta_j}^p}{R_{\beta_j}^c}\right|}, n = 1 .. nmax \tag{4.20}$$

The concentration will increase if $\left|R_{\beta_j}^p\right| > \left|R_{\beta_j}^c\right|$ and decrease if the opposite holds. Convergence is reached when $\left|R_{\beta_j}^p\right| = \left|R_{\beta_j}^c\right|$, i.e. equation (4.19) expressing the PSSA for β-radical j holds. The recursive relation is used until the relative change in concentration drops below a certain user-specified threshold value ε for all PSS species or the maximum number of solver iteration steps $nmax$ is surpassed:

$$\max_{\forall j}\left(\left|\frac{C_{\beta_j}^{n+1} - C_{\beta_j}^n}{C_{\beta_j}^n}\right|\right) < \varepsilon \ or \ n = nmax$$

A value of 1 % for the threshold value ε and 100 for the maximum number of iterations $nmax$ was found to be sufficient. In the first iteration steps of the flow solver, $nmax$ is the limiting factor. However, after several flow iterations, the PSS species concentration profiles change only slightly and as the PSS concentrations of the previous iteration are taken as an initial guess for C_{β_j}, convergence is reached rapidly. Applying the PSSA to the β-radicals further reduces the number of continuity equations to be integrated. As shown by Ren and Pope, the reactive system

is regarded solely to consist of the non-PSS species to guarantee element conservation and to satisfy the first and second law of thermodynamics [65].

To quantify the error made by application of the PSSA on the β-radicals, the pyrolysis of propane was simulated with the one-dimensional plug flow model CHEMKIN [66]. CHEMKIN uses a proprietary stiff solver based on DASPK [67, 68] and PSSA is not applied to any species. Subsequently, KINALC [23, 69] was used to calculate the instantaneous error on the concentration of species j when applying PSSA for this species, denoted as $\Delta C_j^{PSSA}(z)$, and the chemical lifetime of each species j, defined as $C_j(z) \Big/ \sum_i v_{ij} r_i(z)$ at the axial coordinate z. Details regarding the procedure utilized in KINALC to calculate these properties can be found elsewhere [23, 69]. Two isothermal reactor simulations were performed at 873.15 K and at 1073.15 K respectively. In both simulations, the propane mass flow rate, steam dilution and pressure were set to $43.66 \cdot 10^{-3}$ kg/s, 0.325 kg/kg and 200 kPa abs respectively. The reactor inner diameter was 30.2 mm.

Table 4-2 shows the results for a selection of important radicals during propane pyrolysis for both simulations. The relative error on the concentration of a radical when applying the PSSA is found to be negligible, below 0.5 %. The lifetime of the majority of radicals is below 10^{-4} s. The lifetime of the allyl radical (C_3H_5-3•) is about two to three orders of magnitude larger than the lifetime of most other β-radicals at 873 K. This is caused by the resonance stabilization of this radical and results in a larger error when applying PSSA to the allyl radical. However, at 1073 K the effect of the resonance stabilization is lower and the relative error is of the same order of magnitude as for the other β-radicals. These results only quantify the error made on a specific radical when

applying PSSA to that radical. In paragraph 4.3.2, the error on both molecules and radicals is assessed by application of PSSA on all radicals by direct comparison to simulations without application of PSSA.

Table 4-2: The chemical lifetime of and the relative error on species j when applying the PSSA to species j for a selection of radicals at z=5 m.

	873 K		1073 K	
	Lifetime (s)	$\left\lvert\Delta C_i^{PSSA}/C_i\right\rvert$	**Lifetime (s)**	$\left\lvert\Delta C_i^{PSSA}/C_i\right\rvert$
H•	$8.72 \cdot 10^{-8}$	$2.01 \cdot 10^{-5}$	$9.93 \cdot 10^{-9}$	$3.21 \cdot 10^{-3}$
CH$_3$•	$2.69 \cdot 10^{-5}$	$1.57 \cdot 10^{-4}$	$2.46 \cdot 10^{-7}$	$3.35 \cdot 10^{-3}$
C$_2$H3•	$1.44 \cdot 10^{-6}$	$-2.96 \cdot 10^{-5}$	$3.09 \cdot 10^{-7}$	$-5.05 \cdot 10^{-4}$
C$_2$H5•	$4.39 \cdot 10^{-5}$	$-3.38 \cdot 10^{-4}$	$6.93 \cdot 10^{-7}$	$-2.93 \cdot 10^{-3}$
C$_3$H$_5$-1•	$7.15 \cdot 10^{-7}$	$-3.88 \cdot 10^{-5}$	$2.61 \cdot 10^{-8}$	$-3.14 \cdot 10^{-3}$
C$_3$H$_5$-2•	$3.28 \cdot 10^{-6}$	$-4.90 \cdot 10^{-5}$	$3.45 \cdot 10^{-7}$	$-2.15 \cdot 10^{-3}$
C$_3$H$_5$-3•	$3.94 \cdot 10^{-3}$	$-3.94 \cdot 10^{-2}$	$4.39 \cdot 10^{-5}$	$2.51 \cdot 10^{-3}$
C$_3$H$_7$-1•	$6.01 \cdot 10^{-7}$	$-1.54 \cdot 10^{-5}$	$2.04 \cdot 10^{-8}$	$-3.37 \cdot 10^{-3}$
C$_3$H$_7$-2•	$2.37 \cdot 10^{-5}$	$1.38 \cdot 10^{-4}$	$3.68 \cdot 10^{-7}$	$-3.33 \cdot 10^{-3}$
C$_4$H$_9$-1•	$6.72 \cdot 10^{-7}$	$9.30 \cdot 10^{-4}$	$3.14 \cdot 10^{-8}$	$-3.38 \cdot 10^{-3}$
C$_4$H$_9$-2•	$3.96 \cdot 10^{-7}$	$-2.30 \cdot 10^{-5}$	$1.29 \cdot 10^{-8}$	$-3.38 \cdot 10^{-3}$

4.2.2.3   Computation cost minimization

As the reaction rates and rates of formation are calculated multiple times during each flow iteration in the solver, the total simulation time depends strongly on the efficiency of these calculations. Therefore, the generation of the UDF file was automated with a Python® script. Typically, reaction coefficients are stored in so-called stoichiometric matrices and calculation of the rates of formation requires several do-loops over the number of species and number of reactions. These large do-loops were eliminated by hard-coding the values of all variables needed for the calculation of the reaction rates and the rates of formation. To further reduce the CPU

time the calculations are processed using Maple$^{®}$'s CodeGeneration package to generate an optimal calculation procedure for the rates. This package detects common subexpressions, calculates them once and stores them for subsequent use. An obvious example is to only calculate the denominator $1/(RT)$ once and to store its value instead of calculating it again for every reaction rate coefficient.

4.3 Results and discussion

4.3.1   One-dimensional vs. three-dimensional reactor model

In this section, the 3D simulation results of Chapter 3 [43] are compared to one-dimensional plug flow simulation results to study the necessity of using a three-dimensional reactor model for steam cracking reactors. As the PSSA was not applied in these 3D simulations, the plug flow reactor model CHEMKIN was used [66]. The two reactor configurations referred to as Bare and SmallFins reactor are discussed here. For both reactors, two one-dimensional simulations were performed. In the first type of 1D simulations, referred to with 'T', the mixing cup temperature profile from the corresponding 3D simulation is imposed. These simulations correspond to the theoretical case where one would have perfect correlations for the friction and Nusselt numbers resulting in perfect temperature and pressure profiles. In the second type of 1D simulation, referred to with 'Q', the heat flux profile was applied to the reactor inner wall and scaled to obtain the same conversion as in the corresponding 3D simulation. Both type of simulations use the mixing cup pressure profile from the 3D simulations. Table 4-3 compares the 3D and the 1D results and shows that in the 1D simulations with the imposed temperature profile, the conversion is lower than in the corresponding 3D simulations. The difference is 2.57 wt% and 1.65 wt% for

the Bare and SmallFins reactor respectively. The higher conversion in the 3D simulations is explained by accounting for the high temperature film near the reactor inner wall. As this high temperature zone is less distinct in the SmallFins reactor, the agreement between the 1D and 3D simulations is better. By matching the conversion, the total heat input is overpredicted by 1.07 and 2.59 % in the 1D simulations. This shows that when a coupled furnace-reactor simulation [70, 71] is performed where the fuel flow rate to the furnace burners is adjusted to match a desired cracking severity, e.g. conversion, the simulated fuel flow rate will be overestimated by adopting a one-dimensional reactor model. Furthermore, the effect of the SmallFins reactor on product selectivities compared to the Bare reactor is not well captured by the 1D simulations. For ethene, the 1D simulations show a decrease in selectivity of 0.1 wt% while the 3D simulations show a much larger decrease of 0.6 wt%. In contrast to the increase of 0.1 wt% in propene selectivity simulated with the 3D model, a decrease of 0.2 wt% is seen from the 1D simulations. Finally, the increase of 1,3-butadiene selectivity is underestimated; 0.1 wt% with the 1D compared to 0.3 wt% with the 3D model. Although these differences are small, they are significant to the economics of an industrial cracker. Hence, an accurate prediction of the effect of a 3D reactor technology on product yields based on a 3D reactor model is necessary upon evaluation of the installation of such a technology. Nonetheless, only detailed single-event microkinetic models guarantee the desired accuracy. As stated above, the implementation of these models in CFD simulations calls for CPU-time reducing methods such as the PSSA applied here.

Table 4-3: Comparison simulation results of three-dimensional simulations of Chapter 3 [43] and one-dimensional plug flow simulations with the 3D mixing cup temperature and pressure profile (T,p) and with the 3D mixing cup pressure profile and heat flux profile scaled to the same conversion.

	Bare_3D	Bare_1D T, p	Bare_1D Q, p	SmallFins	SmallFins_1D T, p	SmallFins_1D Q, p
Coil-outlet-temperature [K]	1190.9	1190.9	1192.6	1192.7	1192.7	1192.6
Pressure drop [kPa]	29.13	29.13	29.13	48.42	48.42	48.42
Propane conversion [-]	84.55	81.99	84.55	85.16	83.50	85.16
Product Yields [wt%]						
H_2	1.52	1.43	1.47	1.49	1.44	1.47
CH_4	18.75	18.13	18.90	19.25	18.69	19.21
C_2H_2	1.03	0.78	0.92	0.98	0.84	0.93
C_2H_4	38.31	35.89	37.45	38.11	36.66	37.66
C_2H_6	3.65	3.21	3.34	3.46	3.28	3.35
C_3H_4 (PD)	1.20	1.01	1.16	1.22	1.08	1.19
C_3H_6	18.24	19.01	18.56	18.47	18.85	18.52
C_3H_8	15.45	18.01	15.45	14.84	16.50	14.84
$1,3-C_4H_6$	1.23	1.79	2.06	1.53	1.95	2.14
$1-C_4H_8$	0.54	0.62	0.59	0.56	0.61	0.59
$2-C_4H_8$	0.02	0.04	0.04	0.03	0.04	0.04
$n-C_4H_{10}$	0.02	0.02	0.02	0.02	0.02	0.02
Product Selectivity [wt%]						
H_2	1.80	1.75	1.74	1.75	1.73	1.72
CH_4	22.18	22.11	22.35	22.61	22.38	22.56
C_2H_2	1.21	0.96	1.09	1.15	1.00	1.09
C_2H_4	45.31	43.78	44.29	44.75	43.90	44.23
C_2H_6	4.31	3.92	3.95	4.07	3.92	3.94
C_3H_4 (PD)	1.42	1.23	1.37	1.43	1.30	1.39

130

Chapter 4:
Computational Fluid Dynamics simulations with detailed chemistry: Application
of Pseudo-Steady State Approximation

C_3H_6	21.57	23.19	21.95	21.69	22.57	21.75
C_3H_8	1.46	2.19	2.43	1.79	2.33	2.51
$1,3\text{-}C_4H_6$	0.64	0.76	0.70	0.65	0.73	0.69
$1\text{-}C_4H_8$	0.03	0.04	0.04	0.03	0.05	0.05
$2\text{-}C_4H_8$	0.02	0.02	0.02	0.02	0.02	0.02
Valuable olefins[a]	68.34	69.15	68.67	68.24	68.81	68.49

[a] Valuable light olefins is defined as the sum of ethene, propene and 1,3-butadiene.

4.3.2   **Validation and speedup**

To validate the application of the PSSA on the β-radicals and to quantify the obtained speedup, three cases with different β-networks were studied. For all cases, a simulation was performed with the developed UDF and with the standard FLUENT routines for calculating the rates of formation. Simulations were performed for a bare tube on a 2D grid of 280,000 cells. An external tube wall temperature profile was imposed on the reactor outer wall. The simulated reactor had a length of 10 m, an internal diameter of 0.032 m and a wall thickness of 6 mm. The mass flow rate was set to 0.01 kg/s and the inlet temperature to 873.15 K. The details of the used reaction networks and the obtained speedup factor by application of the developed UDF compared to the standard FLUENT routines are shown in Table 4-4.

Table 4-4: Specifications of the reaction networks and the obtained speedup factor in the 3D validation simulations.

Feedstock	Nr molecules	Nr radicals	Nr reactions	Speedup factor
Ethane	6	3	9	7.4
Butane	8	6	57	51.8
Propane	13	11	100	54.2

The speedup factor is seen to increase with the network size up to a speedup factor around 50. The reason for the large speedup factor is threefold. Firstly, less continuity equations are to be solved by application of PSSA on the radicals. Secondly, the calculation of the reaction rates and rates of formation is optimized. Finally, the stiffness of the system is reduced. To avoid divergence without application of PSSA, under-relaxation factors of 0.001 on the continuity

Chapter 4:

132   **Computational Fluid Dynamics simulations with detailed chemistry: Application of Pseudo-Steady State Approximation**

equations of the radicals were necessary. By application of PSSA, the under-relaxation factors of all species continuity equations can be set to 0.9.

Figure 4-3 shows the mixing cup yields of the most abundant molecules as a function of the axial coordinate in the Butane case. A good agreement between the PSSA and non-PSSA cases is seen for all molecules. Figure 4-4 shows the mixing cup yields of several radicals as a function of the axial coordinate in the Butane case. Some differences are seen here. Most notably, the radicals that can be formed directly from the feedstock molecule butane have a non-zero value at the reactor inlet which is most clearly seen for the methyl and ethyl radical. In general a small underestimation is seen towards the end of the reactor as most clearly seen for the methyl radical. Nonetheless the agreement is satisfactory.
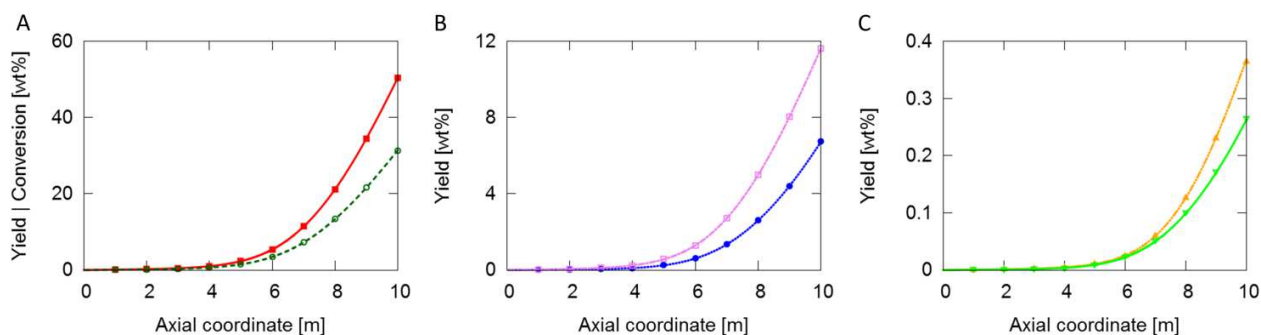

Figure 4-3: Yields of molecules and butane conversion as a function of axial coordinate [m] in 3D validation simulation 'Butane': symbols without PSSA; ■ - butane conversion; O - propene; ● - methane; □ - ethene; ▲ - hydrogen; ▽ - ethane; full lines with PSSA.
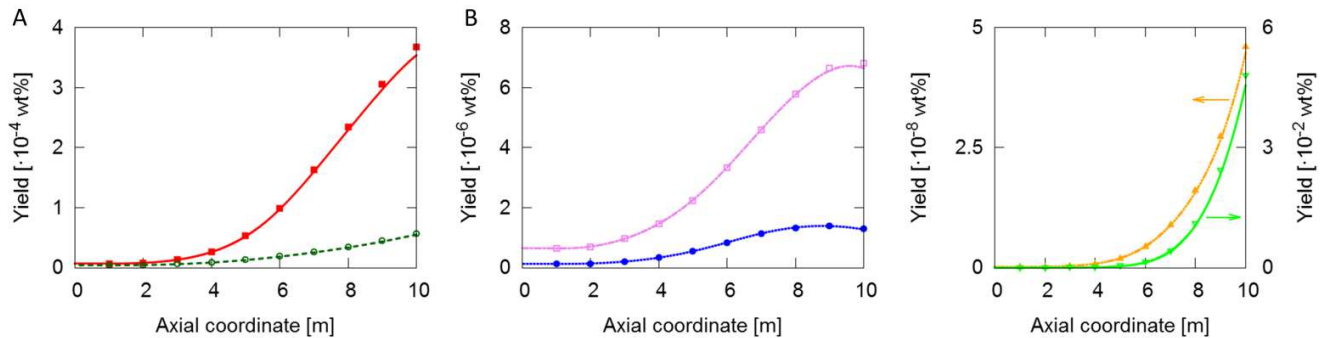
Figure 4-4: Yields of radicals as a function of axial coordinate [m] in 3D validation simulation 'Butane'; ■ - methyl; ○ - ethyl; ● - 1-butyl; □ - 2-butyl; ▲ - hydrogen radical; ▽ - allyl; full lines with PSSA.

As the species concentrations vary significantly from the reactor centerline to the reactor inner wall [43] and as the concentrations near the wall are important for an accurate calculation of the coke formation rate when using a fundamental coke formation model [42, 72, 73], the concentrations in the Butane case as a function of radial coordinate at an axial position of 9.5 m are compared in Figure 4-5 and Figure 4-6 for molecules and radicals respectively. When applying PSSA on the β-radicals, the conversion near the reactor inner wall at an axial coordinate of 9.5 m is 0.27 wt% higher than in the non-PSSA case. Consequently, the yield of the different products is also slightly higher. A good agreement between the PSSA and non-PSSA case is seen for the radical concentrations at the center of the reactor. Near the reactor inner wall, the radical concentrations are overpredicted by applying the PSSA. The average relative error is about 10 %. For the most important radical coke precursors, i.e. hydrogen, methyl and ethyl, the relative error is 9, 15 and 9 % respectively. In the fundamental coking model of Wauters and Marin [72, 73], an increase of the concentration of these radicals by 90 %, resulted in an increase of the coking

Chapter 4:

134   **Computational Fluid Dynamics simulations with detailed chemistry: Application**
of Pseudo-Steady State Approximation

rate by about 640, 165 and 10 % respectively. Hence, it is clear that the error made on the radical

concentrations near the wall by application of PSSA is small but can have a significant influence
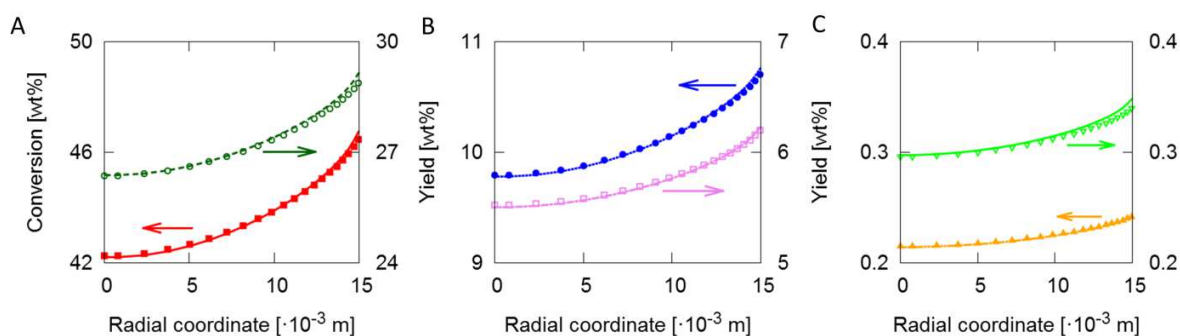
on the simulated coking rates.

Figure 4-5: Yields of molecules and butane conversion as a function of radial coordinate [·10^{-3} m] at an axial position of 9.5 m in 3D validation simulation 'Butane': symbols without PSSA; ■ - butane conversion; ○ - propene; ● - methane; □ - ethene; ▲ - hydrogen; ▽ - ethane; full lines with PSSA.

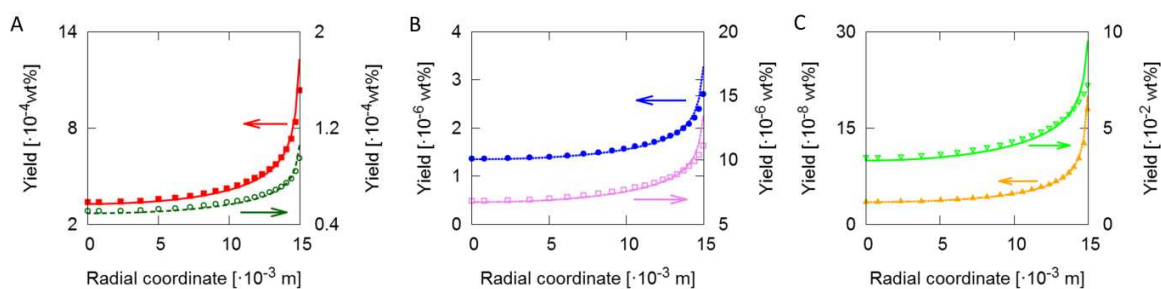**Figure 4-6: Yields of radicals as a function of radial coordinate [·10^{-3} m] at an axial position of 9.5 m in 3D validation simulation 'Butane': symbols without PSSA; ■ - methyl; ○ - ethyl; ● - 1-butyl; □ - 2-butyl; ▲ - hydrogen radical; ▽ - allyl; full lines with PSSA.**

4.3.3   Simulation of an industrial propane-cracking reactor

An industrial propane cracking reactor was simulated. The reactor is of the Millisecond type, i.e. a straight tube with rather small length and diameter compared to other reactor designs. The reactor length is 10.55 m and the tube cross-sectional flow area is 715.72 mm². A pure propane feedstock is assumed. The dilution is 0.325 and the inlet temperature is 903.7 K. The outlet pressure is 205.7 kPa abs. A heat flux profile as a function of axial coordinate is applied to the reactor outer wall. The total heat input is 102.7 kW per reactor. A conventional bare reactor (Bare) is compared to the optimized finned reactor 'SmallFins' of Chapter 3. The reactor details are given in Chapter 3. As in Chapter 3, the cross-sectional flow area, reactor length, flow rate and heat input are the same for the two simulations [43].

4.3.3.1   Discussion of three-dimensional simulation results

Figure 4-7 shows the external and internal tube metal temperature as a function of axial coordinate. Maximum values occur where the heat flux to the reactor is maximal. The maximum external tube temperature is 44 K lower in the SmallFins case compared to the Bare case. Obviously, this will result in a significant increase of the run length. Table 4-5 shows the 3D simulation results in the columns denoted with 'Bare 3D' and 'SmallFins 3D'.

Chapter 4:

136 Computational Fluid Dynamics simulations with detailed chemistry: Application of Pseudo-Steady State Approximation
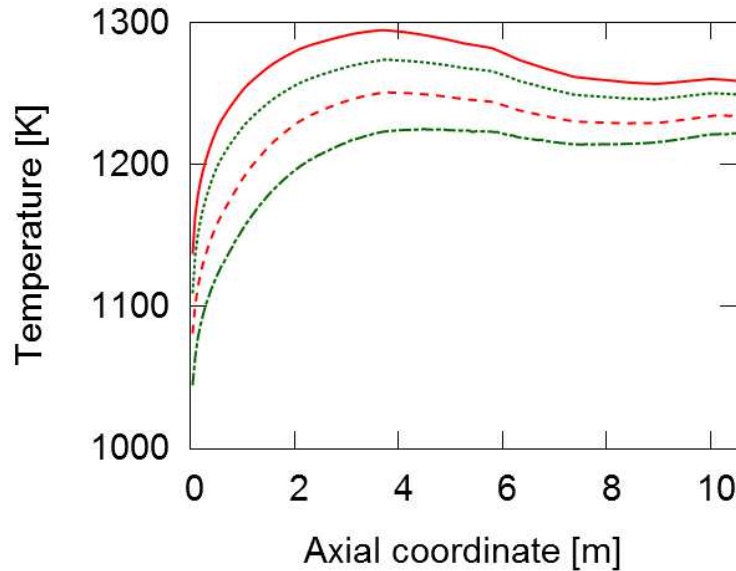
Figure 4-7: External and internal wall temperature [K] as a function of axial coordinate [m] in the 3D simulations of the industrial propane-cracking reactor: ——— - Bare external wall temperature; – – – – - Bare internal wall temperature: ·········· - SmallFins external wall temperature; ·—·—· - SmallFins internal wall temperature.

Figure 4-8 shows the azimuthally averaged mixing cup process gas temperature as a function of the radial coordinate at an axial coordinate of 10.5 m for the two reactors. The temperature difference between center and inner wall is 91 K for the Bare reactor. This is reduced to 65 K by application of the SmallFins reactor. A small bump is seen at a radial coordinate of 15 mm for the SmallFins reactor which can be attributed to the higher temperature in the wake of the fins [43].
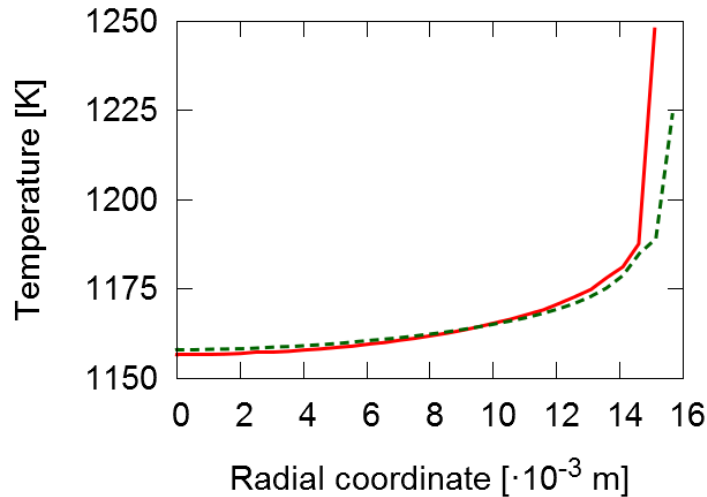
Figure 4-8: Azimuthally averaged mixing cup process gas temperature [K] as a function of the radial

coordinate at an axial coordinate of 10.5 m in the 3D simulations of the industrial propane-cracking reactor:

——— - Bare; ------ - SmallFins.

Two phenomena influence the product selectivities in the SmallFins reactor compared to the Bare

reactor: the larger reactor pressure drop and the more uniform cross-sectional temperature profile.

Depending on the reaction path through which a certain product is formed, the former or the latter

might have a decisive influence. The less uniform cross-sectional temperature profile in the Bare

reactor will enhance the rate of reactions with a high activation energy. On the other hand, the

higher reactor pressure drop in the SmallFins will favor bimolecular over monomolecular

reactions.

For the same heat input, the conversion is 0.44 wt% higher in the SmallFins reactor than in the

Bare reactor. The mixing cup averaged propane conversion as a function of axial coordinate is

Chapter 4:

138   **Computational Fluid Dynamics simulations with detailed chemistry: Application**
of Pseudo-Steady State Approximation

shown in Figure 4-9. The conversion initially increases faster in the Bare reactor as the induction period for heating of the process gas is shorter. Indeed, the high temperature zone near the reactor inner wall already induces C-C scissions more upstream resulting in the formation of radicals to start reactions as shown in the insert of Figure 4-9. Further downstream the reactor, the mixing cup averaged temperature profile of the two reactors is very similar and the higher pressure in the SmallFins reactor results in higher reaction rates explaining the higher conversion in the SmallFins reactor.
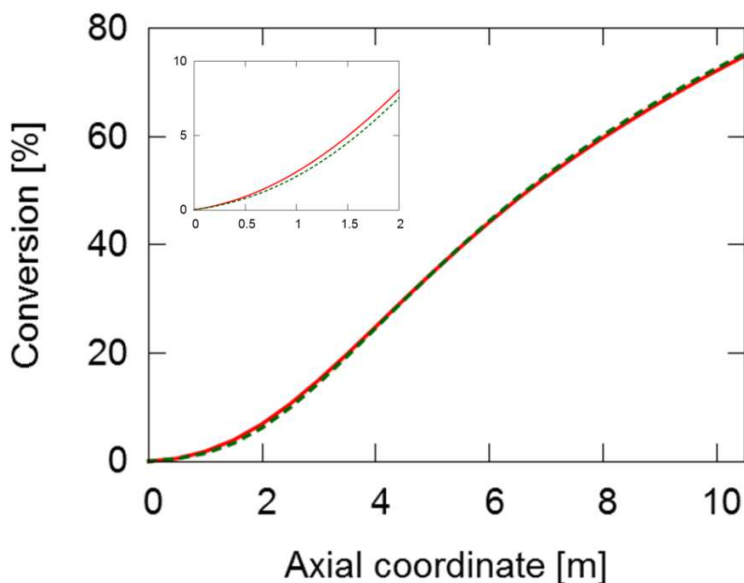

Figure 4-9: Mixing cup averaged propane conversion [%] as a function of axial coordinate [m] in the 3D simulations of the industrial propane-cracking reactor: ——— - Bare; - - - - - - - SmallFins.

As seen from Table 4-5, the selectivity towards methane is higher in the SmallFins reactor. Methane is mainly formed by hydrogen abstractions on propane by the methyl radical. Van Geem

et al. [42] simulated a higher methane yield using a two-dimensional simulation model compared to a one-dimensional simulation model during cracking of ethane. This was attributed to the higher concentration of the methyl radical because of the high temperature zone near the reactor inner wall in the 2D model. Following this reasoning, a higher methane selectivity would be expected in the Bare reactor. During cracking of ethane, the methyl radical is formed by C-C scission of ethane, which has a high activation energy, i.e. about 377 kJ/mol [74]. However, during cracking of propane, methyl is mainly formed by β-scission of the 1-propyl radical. This reaction has a much lower activation energy (137 kJ/mol) and hence, a negligible difference in mixing cup average concentration of the methyl radical is simulated. As formation of methane from methyl mainly proceeds via bimolecular abstraction, the higher pressure drop in the SmallFins reactor causes the higher methane selectivity.
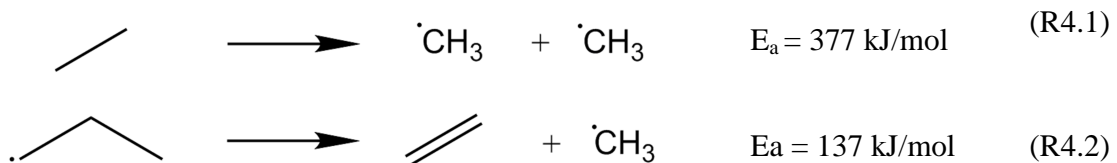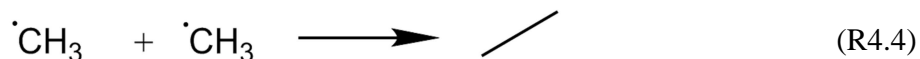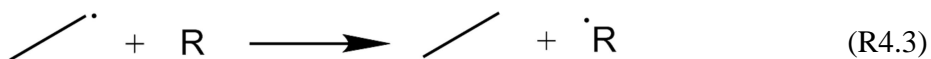

$$ \longrightarrow \quad {}^{\bullet}CH_3 \;+\; {}^{\bullet}CH_3 \qquad E_a = 377 \text{ kJ/mol} \qquad (R4.1)$$

$$ \longrightarrow \quad +\; {}^{\bullet}CH_3 \qquad Ea = 137 \text{ kJ/mol} \qquad (R4.2)$$

Table 4-5: Comparison simulation results for Bare and SmallFins reactor using a 3D model and the one-dimensional models 1D, 1D T and 1D T, β.

	Bare 3D	Bare 1D	Bare 1D T	Bare 1D T, β	SmallFins 3D	SmallFins 1D	SmallFins 1D T	SmallFins 1D T, β
Coil-outlet-temperature [K]	1168	1170	1169	1166	1167	1171	1170	1169
Heat input [kW]	102.7	104.3	103.2	103.1	102.7	104.0	103.4	103.2
Pressure drop [kPa]	23.0	25.5	25.5	25.6	45.6	45.1	45.0	45.6
P/E ratio [wt%/wt%]	0.70	0.73	0.73	0.73	0.71	0.72	0.72	0.72
Propane conversion [-]	75.1	75.1	75.1	75.1	75.6	75.6	75.6	75.6
Product Yields [wt%]								
C4-	93.52	93.72	93.72	93.68	93.50	93.59	93.62	93.58
[C5+-Benzene[	2.68	2.62	2.62	2.63	2.69	2.64	2.64	2.64
[Benzene-Naphthalene]	3.80	3.66	3.66	3.69	3.80	3.77	3.74	3.78
H_2	2.05	2.04	2.04	2.04	2.05	2.04	2.03	2.05
CH_4	15.00	15.10	15.10	15.10	15.22	15.32	15.32	15.32
C_2H_2	0.71	0.65	0.65	0.66	0.69	0.66	0.65	0.67
C_2H_4	27.26	26.86	26.86	26.89	27.29	27.10	27.10	27.12
C_2H_6	1.19	1.12	1.12	1.13	1.17	1.16	1.17	1.14
C_3H_4	0.82	0.79	0.79	0.80	0.80	0.79	0.78	0.80
C_3H_6	19.13	19.72	19.72	19.68	19.30	19.61	19.61	19.58
C_3H_8	24.85	24.91	24.91	24.87	24.41	24.38	24.41	24.39
$1,3-C_4H_6$	1.42	1.39	1.39	1.38	1.45	1.40	1.41	1.39
$1-C_4H_8$	0.89	0.94	0.94	0.93	0.93	0.93	0.94	0.93
$2-C_4H_8$	0.12	0.13	0.13	0.13	0.13	0.13	0.13	0.13
$i-C_4H_8$	0.06	0.07	0.07	0.07	0.07	0.07	0.07	0.07
$n-C_4H_{10}$	0.01	0.01	0.01	0.01	0.01	0.01	0.01	0.01
1,3-Cyclopentadiene	1.64	1.58	1.58	1.59	1.61	1.59	1.58	1.60
Me-1,3-Cyclopentadiene	0.36	0.35	0.35	0.35	0.36	0.35	0.34	0.34

Benzene	2.43	2.46	2.46	2.48	2.48	2.53	2.51	2.54
Toluene	0.41	0.35	0.35	0.35	0.39	0.36	0.36	0.36
Styrene	0.10	0.08	0.08	0.08	0.10	0.08	0.08	0.09
Naphthalene	0.85	0.77	0.77	0.77	0.84	0.80	0.79	0.80
Product Selectivity [wt%]								
C4-	91.37	91.64	91.64	91.59	91.52	91.56	91.51	91.37
[C5+-Benzene[	3.57	3.49	3.50	3.50	3.50	3.49	3.49	3.57
[Benzene-Naphthalene]	5.06	4.91	4.98	4.95	4.98	4.95	5.00	5.06
H_2	2.73	2.71	2.71	2.72	2.71	2.70	2.69	2.70
CH_4	19.96	20.11	20.11	20.10	20.14	20.26	20.26	20.26
C_2H_2	0.94	0.87	0.87	0.88	0.91	0.87	0.86	0.89
C_2H_4	36.27	35.76	35.76	35.79	36.10	35.83	35.86	35.86
C_2H_6	1.58	1.49	1.49	1.50	1.55	1.53	1.54	1.51
C_3H_4	1.09	1.05	1.05	1.06	1.06	1.04	1.04	1.06
C_3H_6	25.45	26.26	26.26	26.20	25.53	25.93	25.94	25.90
$1,3\text{-}C_4H_6$	1.88	1.85	1.85	1.83	1.91	1.85	1.86	1.83
$1\text{-}C_4H_8$	1.19	1.25	1.25	1.24	1.23	1.23	1.24	1.23
$2\text{-}C_4H_8$	0.16	0.17	0.17	0.17	0.17	0.17	0.17	0.17
$i\text{-}C_4H_8$	0.09	0.09	0.09	0.09	0.09	0.09	0.09	0.09
$n\text{-}C_4H_{10}$	0.01	0.01	0.01	0.01	0.01	0.01	0.01	0.01
1,3-Cyclopentadiene	2.18	2.10	2.10	2.11	2.13	2.11	2.09	2.12
Me-1,3-Cyclopentadiene	0.48	0.46	0.46	0.46	0.48	0.46	0.46	0.45
Benzene	3.24	3.27	3.27	3.30	3.28	3.34	3.32	3.36
Toluene	0.55	0.46	0.46	0.47	0.52	0.47	0.47	0.48
Styrene	0.14	0.11	0.11	0.11	0.13	0.11	0.11	0.11
Naphthalene	1.13	1.02	1.02	1.03	1.11	1.05	1.05	1.05

The selectivity towards ethane is lower in the SmallFins reactor than in the Bare reactor. Ethane is mainly formed by hydrogen abstraction by the ethyl radical and by recombination of two methyl radicals. Figure 4-10 shows the rate of formation of ethane by these two contributions. The methyl recombination is bimolecular and hence is favored at higher pressure. The concentration of the ethyl radical in the Bare reactor is higher than in the SmallFins reactors because of the high temperature zone near the reactor inner wall. Ethyl radicals are mainly formed via C-C scission of propane having a high activation energy, i.e. about 370 kJ/mol [74]. As the lion's share of the ethane formation goes through ethyl radicals as shown in Figure 4-10, the higher ethane formation via the ethyl radical in the Bare reactor compensates the high pressure effect on the bimolecular recombination reaction in the SmallFins reactor.
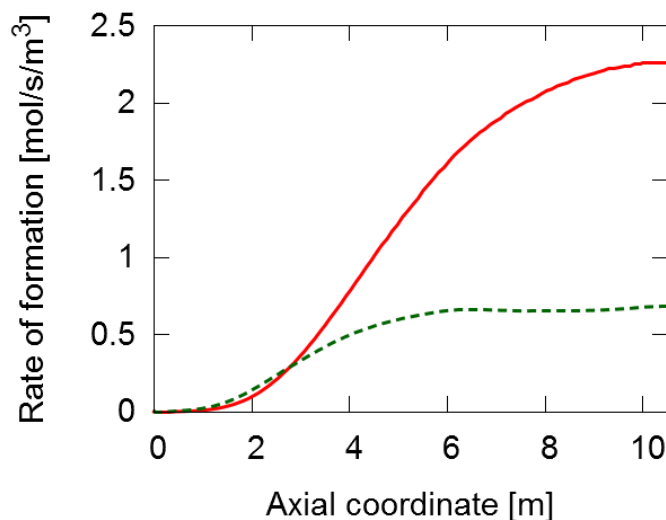
$$\text{\Large$\diagup^{\bullet}$} + R \longrightarrow \text{\Large$\diagup$} + {}^{\bullet}R \qquad\qquad (R4.3)$$

$$^{\bullet}CH_3 + {}^{\bullet}CH_3 \longrightarrow \text{\Large$\diagup$} \qquad\qquad (R4.4)$$

Figure 4-10: Rate of formation [mol/m³/s] of ethane as a function of axial coordinate [m]: ———— **- by ethyl hydrogen abstraction;** ------ **- by methyl-methyl recombination.**

A lower ethene selectivity is simulated by application of the SmallFins reactor compared to the Bare reactor. Ethene is mainly formed by the β-scission of the 1-propyl radical. This 1-propyl radical is formed by hydrogen addition to propene. As shown in Figure 4-11, the hydrogen radical yield is higher in the Bare than in the SmallFins reactor. This higher hydrogen radical yield results in a higher rate of formation of 1-propyl and subsequently a higher ethene production. As this pathway consumes propene, it also explains the higher propene selectivity in the SmallFins reactor.
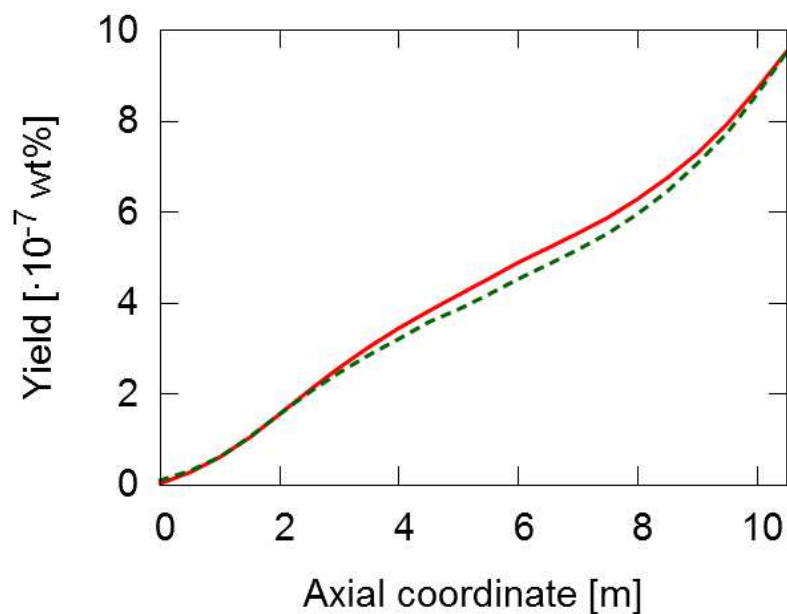
Chapter 4:

144   Computational Fluid Dynamics simulations with detailed chemistry: Application of Pseudo-Steady State Approximation

Figure 4-11: Hydrogen radical yield [10^{-7} wt%] as a function of axial coordinate [m] in the 3D simulations of the industrial propane-cracking reactor: ―――― - Bare; ------ - SmallFins.

A slightly higher selectivity towards 1,3-butadiene, 1-butene and 2-butene is simulated. Figure 4-12 shows a scheme of the most important reactions leading to the formation of these components.
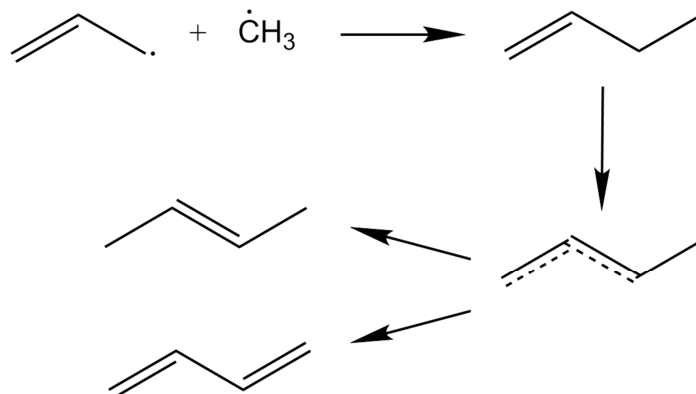
Figure 4-12: Reaction pathway to C$_4$-olefins.

1-Butene is formed via the recombination of a methyl and an allyl radical. Subsequent hydrogen abstraction yields the 1-buten-3-yl radical, which can form 2-butene or 1,3-butadiene. As the formation of 1-butene is bimolecular, this reaction is favored at high pressure, explaining the higher yields of the C$_4$-olefins. It is noted that during steam cracking of heavier paraffins, e.g. present in naphtha feedstocks, 1-butene is mainly formed via β-scissions, e.g. via β-scission of the 3-hexyl radical forming 1-butene and ethyl during thermal cracking of hexane [75]. Hence, a higher C$_4$-olefins selectivity is probably not to be expected by application of a 3D reactor technology when cracking heavier feedstocks.

The increase in 1,3-butadiene selectivity by application of the SmallFins reactor is smaller than in Chapter 3 [43]. This is caused by part of 1,3-butadiene reacting with vinyl radicals to yield benzene as shown by Sabbe et al. [76] and Dijkmans et al. [56] not accounted for in the kinetic model used in Chapter 3. Another main route to benzene is the addition of allyl to propadiene and propyne. These pathways are accounted for in the β-network by reactions involving benzyl and

cyclopentadienyl radicals taken from the high temperature combustion kinetic model developed by the CRECK modeling group [77]. As both these routes involve a bimolecular first reaction, they are favored at higher pressure, i.e. in the SmallFins reactor. Based on these considerations solely, a much higher increase in benzene selectivity would be expected in the SmallFins reactor. However, both routes to benzene involve typical high-temperature species, i.e. vinyl and propyne or propadiene respectively. Vinyl is formed by hydrogen abstraction from ethene, mainly by methyl and hydrogen radicals which are hydrogen abstractions with high activation energies (84.4 and 72.1 kJ/mol respectively). Propyne and propadiene are formed by a hydrogen abstraction from propene to form propen-2-yl and a subsequent β-scission. Like the formation of vinyl, the formation of propen-2-yl has a high activation energy. These considerations make that the vinyl, propyne and propadiene yields are higher in the Bare reactor as shown in Figure 4-13.
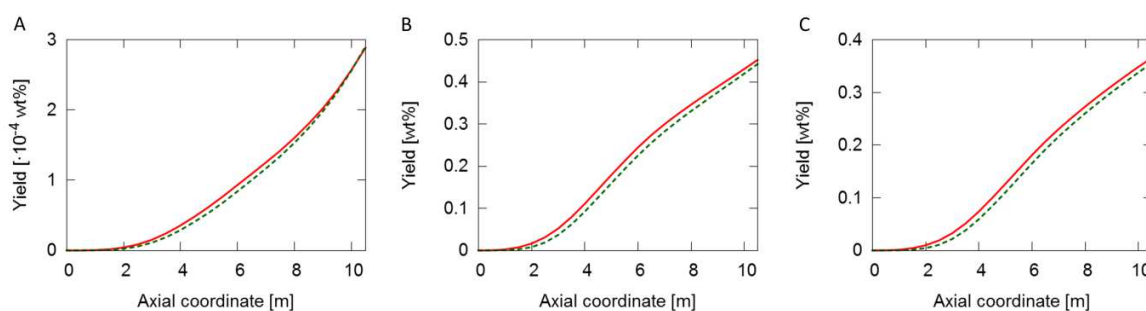

Figure 4-13: Mixing cup average yield of vinyl radical [10^{-4} wt%] (A), propyne [10^{-4} wt%] (B) and propadiene [10^{-4} wt%] (A) as a function of axial coordinate [m] in the 3D simulations of the industrial propane-cracking reactor: ———— **- Bare;** ‐ ‐ ‐ ‐ ‐ ‐ **- SmallFins.**

Hence, the rate of formation of benzene in the SmallFins reactor in comparison to the Bare reactor, is a balance between an increase caused by a higher pressure and a decrease caused by a greater cross-sectional temperature uniformity. This statement is corroborated by Figure 4-14, showing the benzene rate of formation as a function of radial coordinate at an axial coordinate of 7 m. In the reactor center, a higher rate of formation is seen in the SmallFins reactor caused by the higher pressure. However, near the reactor inner wall, the rate of formation is lower caused by the lower temperature. For the here adopted reactor designs, feedstock and process conditions, the balance tips slightly in favor of the increase caused by the higher pressure. However, for other designs, conditions and/or feedstocks, the opposite might hold, showing the need for these highly detailed three-dimensional simulations upon evaluation of the application of a 3D reactor design in a specific cracker.

Chapter 4:

148   **Computational Fluid Dynamics simulations with detailed chemistry: Application of Pseudo-Steady State Approximation**
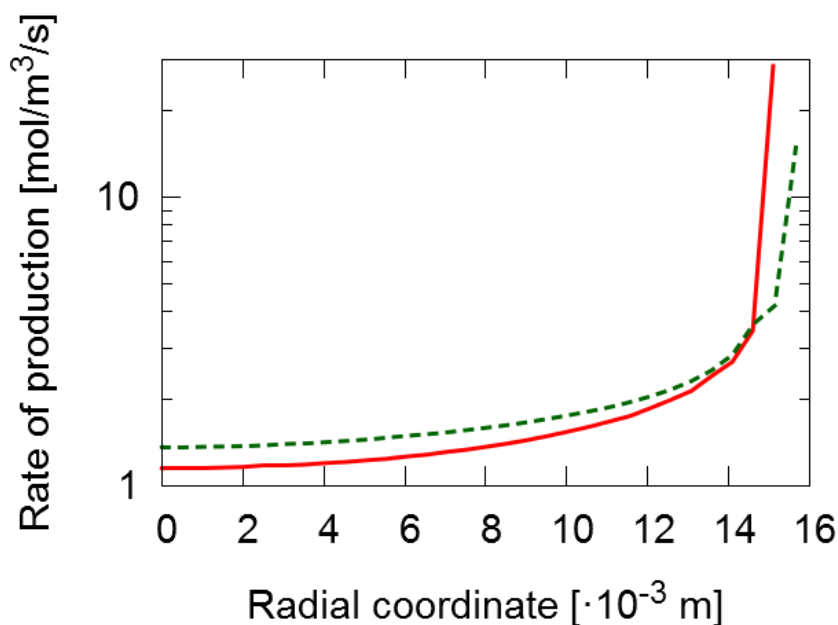

Figure 4-14: Rate of formation of benzene [mol/m³/s] as a function of radial coordinate [m] at an axial coordinate of 7 m in the 3D simulations of the industrial propane-cracking reactor: ————— - Bare 3D; ------- - SmallFins 3D.

4.3.3.2   Comparison to one-dimensional plug flow simulations

To assess the error when using a one-dimensional plug flow model, simulations were performed using COILSIM1D. Although COILSIM1D normally comes with an extensive single-event microkinetic model containing about 700 species and thousands of reactions, the microkinetic model adopted in the 3D simulations was used in these COILSIM1D simulations. Furthermore, the algorithm of application of PSSA on the β-radicals, the thermodynamic data of the species and the reactor alloy properties of the 3D simulations were implemented to isolate the effect of

the adopted reactor model on the simulation results. For the simulations of the Bare tube, α_f and α_h were set to unity, while for the SmallFins tube, α_f and α_h were set to 1.98 and 1.52 respectively, values obtained from the non-reactive flow simulations of Chapter 3.

Table 4-5 compares the 1D simulation results with the 3D simulation results of the two reactors discussed above. For the two reactor designs, three 1D simulations were performed; without radial profiles (1D), with a radial temperature profile (1D T) and with a radial temperature and β-radicals profile (1D T, β). In all 1D simulations, the heat flux profile to the reactors was scaled to obtain the same propane conversion as in the corresponding 3D simulation. In the 1D model without radial profiles, the heat input necessary for the desired conversion is 1.5 % and 1.2 % higher for the Bare and SmallFins reactor respectively. These errors are small but are significant when considering that a similar error on the fuel flow rate to the furnace will be simulated when performing coupled furnace-reactor simulations. When accounting for the radial temperature profile, these differences decrease to 0.45 % and 0.66 % for the Bare and SmallFins reactor respectively. Accounting for the radial non-uniformity of the β-radicals further reduces the differences to 0.37 % and 0.49 %. The COT in the 1D simulations is higher than in the 3D simulations. Taking into account radial profiles results in a closer agreement between the 1D and 3D simulated COT's. The pressure drop in the Bare reactor is slightly overpredicted in the 1D model compared to the 3D results. For the SmallFins reactor, a good agreement is obtained. This shows that using a correction factor obtained from non-reactive CFD simulations can give accurate pressure drop predictions for reactive 1D simulations. However, it should be noted that

Chapter 4:

150   **Computational Fluid Dynamics simulations with detailed chemistry: Application of Pseudo-Steady State Approximation**

the Reynolds number of the non-reactive simulation and this reactor simulation is the same which is obviously important to obtain a correct scaling factor.

Figure 4-15A and B compare the external tube wall temperature (TMT) in the 3D and the 1D simulations for the Bare and the SmallFins reactor respectively. For the Bare reactor, the maximum tube metal temperature is overpredicted by 26 K using the 1D model without radial profiles. As shown by Sundaram and Froment [41], the temperature difference between the inner wall temperature and the mixing cup process gas temperature is indeed larger when using a correlation for the Nusselt number derived for non-reactive flow than when accounting for the endothermic reactions. Consequently, a good agreement is seen between 1D and 3D TMT's towards the end of the reactor where the endothermic heat of reaction is lower. Furthermore, axial conduction in the tube metal is not accounted for in the 1D model, which flattens out the TMT profile in the 3D simulations, reducing the TMT maximum. Taking into account the effect of only the radial temperature and also β-radicals concentration profile reduces the overprediction of the maximum TMT to 20 and 13 K respectively. Similar considerations as made for the Bare reactor can be made for the SmallFins reactor, with a maximum TMT difference compared to the 3D simulation equal to 20, 18 and 14 K for 1D, 1D T and 1D T, β respectively.
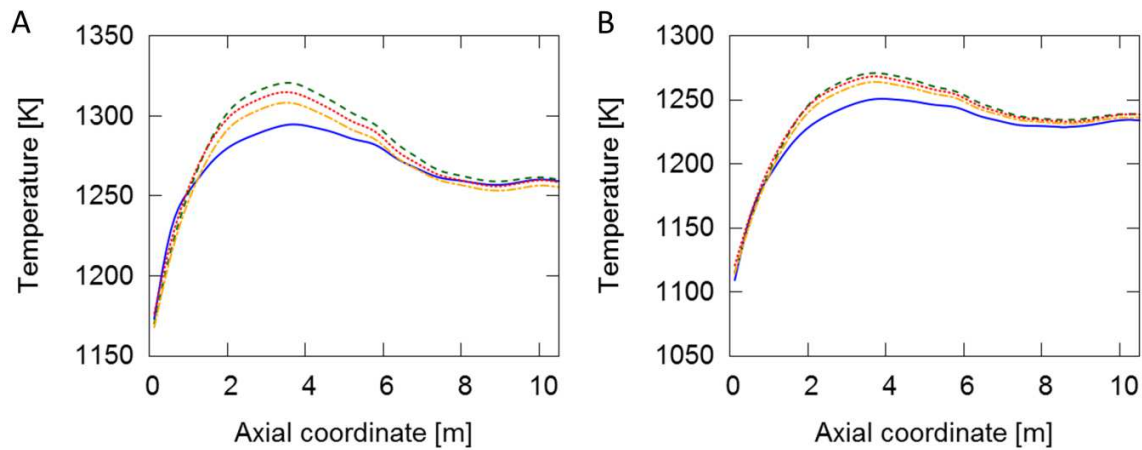
Figure 4-15: External tube metal temperature [K] for the Bare (A) and SmallFins (B) reactor: ▬▬ - Bare

3D; ‑ ‑ ‑ - Bare 1D; ······· - Bare 1D T; ‑··‑ - Bare 1D T, β.

Figure 4-16 shows the propane conversion for the three-dimensional and the one-dimensional simulations of the Bare reactor. Without accounting for radial profiles, the induction length for reaction to start is longer compared to the 3D simulation. When accounting for radial temperature and β-radical concentrations in the 1D simulations, the agreement with the 3D conversion profile at the start of the reactor is better as seen from the insert in Figure 4-16.
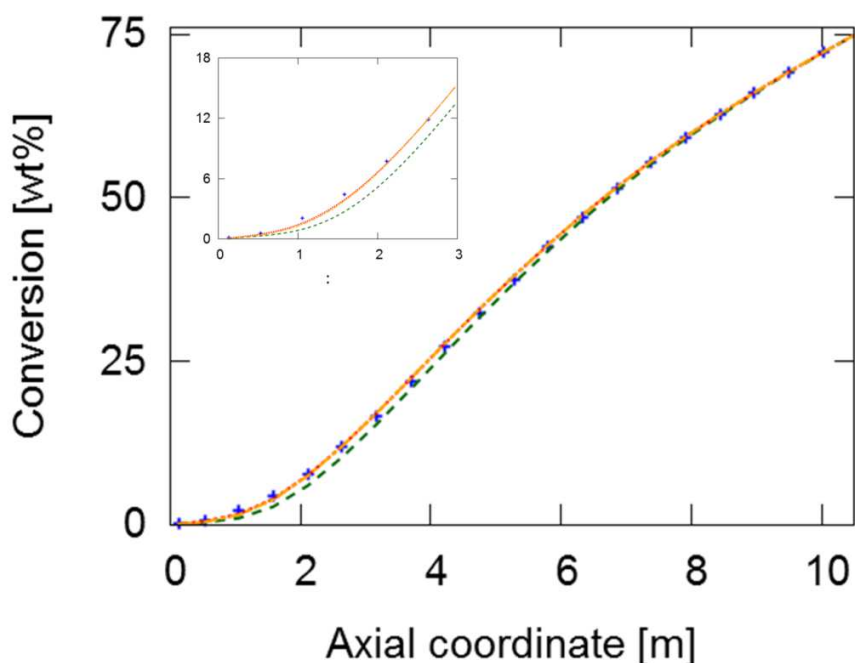
Chapter 4:

152   Computational Fluid Dynamics simulations with detailed chemistry: Application of Pseudo-Steady State Approximation

Figure 4-16: Propane conversion [wt%] as a function of axial coordinate [m]: ✚ - Bare 3D; – – – - Bare 1D; ······· - Bare 1D T; –·–·– - Bare 1D T, β.

Besides for ethene and propene, the agreement between the 1D model without accounting for radial profiles and the 3D model for the product yields is satisfactory for the Bare reactor. The propene yield is overpredicted by 0.6 wt% in the 1D model and consequently the ethene yield is underpredicted by 0.4 wt%. Accounting for radial profiles of temperature and β-radicals concentrations slightly improves the agreement but a significant deviation remains. The difference between the 1D model without accounting for radial profiles and the 3D model for the ethene and propene yield is smaller for the SmallFins reactor, i.e. 0.2 wt% and 0.3 wt% respectively. Indeed, the radial temperature and concentration profiles are less pronounced in the SmallFins reactor making the plug flow assumption more accurate for this reactor. When

analyzing the effect of the reactor geometry on the product selectivities, it is seen that only for some products the right trends are predicted by the 1D model, even when radial profiles of temperature and β-radicals are accounted for. The increase in methane, propene and benzene selectivity by application of the SmallFins reactor is well captured. On the contrary, the decrease in ethene selectivity and the small increase in C_4-(di)olefins selectivity is not captured by the 1D T,β model.

4.4 Conclusions

A methodology was developed to adopt detailed kinetic models in computational fluid dynamics simulations of steam cracking reactors. Eventually 3D simulations should become the industrial standard for design because comparison to 1D plug flow reactor simulations shows that a small but significant error is made by neglecting the increased reaction rates in the film near the reactor inner wall. Significant speedup in the 3D simulations was achieved by a combination of three techniques. Firstly, the application of the μ-radical hypothesis and PSSA on μ-radicals during network generation reduces the number of and the stiffness of the species continuity equations. Secondly, on the fly application of the PSSA on the $\beta(\mu)$-radicals further reduces the number of continuity equations and the stiffness of the system. Finally, Maple$^{®}$'s CodeGeneration package was used to generate an optimal calculation procedure for the reaction rates and the rates of formation. Depending on the kinetic model's size, a speedup factor from 7.4 to 54.2 was obtained compared to the standard FLUENT routines. A good agreement was seen for the species yields compared to the conventional 3D simulations. The deviations are the largest for the radicals weight fraction near the reactor inner wall with an average relative error of 10 %, which could be

significant for example when fundamental coking models are considered. Application to a propane-cracking conventional bare reactor and a helicoidally finned reactor shows that considering a kinetic model of 85 species, the finned reactor outperforms the bare reactor if only coke formation is considered as the maximum tube temperature was reduced by 44 K. However, the ethene selectivity is reduced by 0.17 % while propene and 1,3-butadiene selectivity increased by 0.08 and 0.03 % respectively. Reaction path analysis on the detailed kinetic model reveals that the change in ethene and propene selectivity are correlated as less propene is converted to ethene in the SmallFins reactor because of the lower hydrogen radical concentration. The increase in 1,3-butadiene is caused by the higher pressure drop as the first step in 1,3-butadiene formation is the bimolecular recombination of methyl and allyl. Also the benzene selectivity is 0.05 wt% higher in the SmallFins reactor because of the higher pressure drop. Accounting for radial temperature and radicals concentration profiles in a 1D model, improves the agreement between the 1D and 3D simulated heat input, tube metal temperature and coil-outlet temperature. However, the effect of a 3D reactor technology on product selectivities is not well captured by a 1D model. Accounting for radial temperature and radicals concentration profiles only results in a marginal improvement. This illustrates the need for 3D reactor simulations upon economic evaluation of a 3D reactor technology, where the trade-off between the run length improvement and the change in products selectivity is key.

References

[1] R. Vinu, L.J. Broadbelt, Unraveling Reaction Pathways and Specifying Reaction Kinetics for Complex Systems, in: J.M. Prausnitz (Ed.) Annual Review of Chemical and Biomolecular Engineering, Vol 3, 2012, pp. 29-54.

[2] E. Ranzi, T. Faravelli, P. Gaffuri, A. Sogaro, Low-temperature combustion: Automatic generation of primary oxidation reactions and lumping procedures, Combustion and Flame, 102 (1995) 179-192.

[3] G.M. Côme, V. Warth, P.A. Glaude, R. Fournet, F. Battin-Leclerc, G. Scacchi, Computer-aided design of gas-phase oxidation mechanisms—Application to the modeling of n-heptane and iso-octane oxidation, Symposium (International) on Combustion, 26 (1996) 755-762.

[4] L.J. Broadbelt, S.M. Stark, M.T. Klein, Computer-generated pyrolysis modeling - On the fly generation of species, reactions and rates, Industrial & Engineering Chemistry Research, 33 (1994) 790-799.

[5] W.H. Green, J.W. Allen, R.W. Ashcraft, G.J. Beran, C.F. Goldsmith, M.R. Harper, A. Jalan, G.R. Magoon, D.M. Matheu, S. Petway, S. Raman, S. Sharma, K.M. Van Geem, J. Song, J. Wen, R.H. West, A. Wong, H.-W. Wong, P.E. Yelvington, Y. J., RMG - Reaction Mechanism Generator v3.3, 2011.

[6] N.M. Vandewiele, K.M. Van Geem, M.F. Reyniers, G.B. Marin, Genesys: Kinetic model construction using chemo-informatics, Chemical Engineering Journal, 207 (2012) 526-538.

[7] E.S. Blurock, Detailed mechanism generation. 1. Generalized reactive properties as reaction class substructures, Journal of Chemical Information and Computer Sciences, 44 (2004) 1336-1347.

[8] E.S. Blurock, Detailed mechanism generation. 2. Aldehydes, ketones, and olefins, Journal of Chemical Information and Computer Sciences, 44 (2004) 1348-1357.

[9] S. Rangarajan, A. Bhan, P. Daoutidis, Language-oriented rule-based reaction network generation and analysis: Description of RING, Computers & Chemical Engineering, 45 (2012) 114-123.

[10] S. Rangarajan, A. Bhan, P. Daoutidis, Language-oriented rule-based reaction network generation and analysis: Applications of RING, Computers & Chemical Engineering, 46 (2012) 141-152.

[11] O. Herbinet, W.J. Pitz, C.K. Westbrook, Detailed chemical kinetic oxidation mechanism for a biodiesel surrogate, Combustion and Flame, 154 (2008) 507-528.

[12] P.A. Glaude, O. Herbinet, S. Bax, J. Biet, V. Warth, F. Battin-Leclerc, Modeling of the oxidation of methyl esters-Validation for methyl hexanoate, methyl heptanoate, and methyl decanoate in a jet-stirred reactor, Combustion and Flame, 157 (2010) 2035-2050.

[13] K.M. Van Geem, M.F. Reyniers, G.B. Marin, Challenges of modeling steam cracking of heavy feedstocks, Oil & Gas Science and Technology-Revue De L Institut Francais Du Petrole, 63 (2008) 79-94.

[14] M.W.M. van Goethem, F.I. Kleinendorst, C. van Leeuwen, N. van Velzen, Equation-based SPYRO® model and solver for the simulation of the steam cracking process, Computers & Chemical Engineering, 25 (2001) 905-911.

[15] T. Lu, C.K. Law, Toward accommodating realistic fuel chemistry in large-scale computations, Progress in Energy and Combustion Science, 35 (2009) 192-215.

[16] T. Dijkmans, C.M. Schietekat, K.M. Van Geem, G.B. Marin, GPU based simulation of reactive mixtures with detailed chemistry in combination with tabulation and an analytical Jacobian, Computers & Chemical Engineering, 71 (2014) 521-531.

[17] L. Tosatto, B.A.V. Bennett, M.D. Smooke, A transport-flux-based directed relation graph method for the spatially inhomogeneous instantaneous reduction of chemical kinetic mechanisms, Combustion and Flame, 158 (2011) 820-835.

[18] M. Boileau, G. Staffelbach, B. Cuenot, T. Poinsot, C. Berat, LES of an ignition sequence in a gas turbine engine, Combustion and Flame, 154 (2008) 2-22.

[19] G. Hu, H. Wang, F. Qian, Y. Zhang, J. Li, K.M. Van Geem, G.B. Marin, Comprehensive CFD Simulation of Product Yields and Coking Rates for a Floor- and Wall-Fired Naphtha Cracking Furnace, Industrial & Engineering Chemistry Research, 50 (2011) 13672-13685.

[20] L. Liang, J.G. Stevens, J.T. Farrell, A Dynamic Multi-Zone Partitioning Scheme for Solving Detailed Chemical Kinetics in Reactive Flow Computations, Combustion Science and Technology, 181 (2009) 1345-1371.

[21] M. Bodenstein, Eine Theorie der photochemischen Reaktionsgeschwindigkeiten, Zeitschrift für Physikalische Chemie, 85 (1913) 329-397.

[22] D.A. Frank-Kamenetskii, Conditions for the applicability of the Bodenstein method in chemical kinetics, Zhurnal Fizicheskoy Himii, 14 (1940).

[23] T. Turanyi, A.S. Tomlin, M.J. Pilling, On the error of the quasi-steady-state approximation, Journal of Physical Chemistry, 97 (1993) 163-172.

[24] T. Kovács, I.G. Zsély, Á. Kramarics, T. Turányi, Kinetic analysis of mechanisms of complex pyrolytic reactions, Journal of Analytical and Applied Pyrolysis, 79 (2007) 252-258.

[25] D.L. Chapman, L.K. Underhill, The interaction of chlorine and hydrogen. The influence of mass., Journal of the Chemical Society, Transactions, 103 (1913) 496-508.

[26] J.Y. Chen, A general procedure for constructing reduced reaction-mechanisms with given independent relations, Combustion Science and Technology, 57 (1988) 89-94.

[27] N. Peters, F.A. Williams, The asymptotic structure of stoichiometric methane air flames, Combustion and Flame, 68 (1987) 185-207.

[28] E. Ranzi, M. Dente, A. Goldaniga, G. Bozzano, T. Faravelli, Lumping procedures in detailed kinetic modeling of gasification, pyrolysis, partial oxidation and combustion of hydrocarbon mixtures, Progress in Energy and Combustion Science, 27 (2001) 99-139.

[29] M. Dente, G. Bozzano, T. Faravelli, A. Marongiu, S. Pierucci, E. Ranzi, Kinetic Modelling of Pyrolysis Processes in Gas and Condensed Phase, in: G.B. Marin (Ed.) Advances in Chemical Engineering, Academic Press, 2007, pp. 51-166.

[30] U. Maas, S.B. Pope, Simplifying chemical-kinetics: Intrinsic low-dimensional manifolds in composition space, Combustion and Flame, 88 (1992) 239-264.

[31] T. Lu, C.K. Law, On the applicability of directed relation graphs to the reduction of reaction mechanisms, Combustion and Flame, 146 (2006) 472-483.

[32] T.F. Lu, Y.G. Ju, C.K. Law, Complex CSP for chemistry reduction and analysis, Combustion and Flame, 126 (2001) 1445-1455.

[33] S.B. Pope, Computationally efficient implementation of combustion chemistry using in situ adaptive tabulation, Combustion Theory and Modelling, 1 (1997) 41-63.

[34] S.R. Tonse, N.W. Moriarty, N.J. Brown, M. Frenklach, PRISM: Piecewise reusable implementation of solution mapping. an economical strategy for chemical kinetics, Isr. J. Chem., 39 (1999) 97-106.

[35] D.A. Schwer, P.S. Lu, W.H. Green, An adaptive chemistry approach to modeling complex kinetics in reacting flows, Combustion and Flame, 133 (2003) 451-465.

[36] I. Banerjee, M.G. Ierapetritou, An adaptive reduction scheme to model reactive flow, Combustion and Flame, 144 (2006) 619-633.

[37] M. Valorani, F. Creta, D.A. Goussis, J.C. Lee, H.N. Najm, An automatic procedure for the simplification of chemical kinetic mechanisms based on CSP, Combustion and Flame, 146 (2006) 29-51.

[38] L. Liang, J.G. Stevens, S. Raman, J.T. Farrell, The use of dynamic adaptive chemistry in combustion simulation of gasoline surrogate fuels, Combustion and Flame, 156 (2009) 1493-1502.

[39] K.Y. He, M.G. Ierapetritou, I.P. Androulakis, Integration of On-The-Fly Kinetic Reduction with Multidimensional CFD, AIChE Journal, 56 (2010) 1305-1314.

[40] V. Gnielinski, New equations for heat and mass-transfer in turbulent pipe and channel flow, International Chemical Engineering, 16 (1976) 359-368.

[41] K.M. Sundaram, G.F. Froment, A comparison of simulation models for empty tubular reactors, Chemical Engineering Science, 34 (1979) 117-124.

[42] K.M. Van Geem, G.J. Heynderickx, G.B. Marin, Effect of radial temperature profiles on yields in steam cracking, AIChE Journal, 50 (2004) 173-183.

[43] C.M. Schietekat, D.J. Van Cauwenberge, K.M. Van Geem, G.B. Marin, Computational fluid dynamics-based design of finned steam cracking reactors, AIChE Journal, 60 (2014) 794-808.

[44] G.J. Heynderickx, G.G. Cornelis, G.F. Froment, Circumferential tube skin temperature profiles in thermal cracking coils, AIChE Journal, 38 (1992) 1905-1912.

[45] C.M. Schietekat, M.W.M. van Goethem, K.M. Van Geem, G.B. Marin, Swirl flow tube reactor technology: An experimental and computational fluid dynamics study, Chemical Engineering Journal, 238 (2014) 56-65.

[46] M.W.M. van Goethem, E. Jelsma, Numerical and experimental study of enhanced heat transfer and pressure drop for high temperature applications, Chemical Engineering Research & Design, 92 (2014) 663-671.

[47] K.M. Sundaram, G.F. Froment, Two dimensional model for the simulation of tubular reactors for thermal cracking, Chemical Engineering Science, 35 (1980) 364-371.

[48] J.C. Fagley, Simulation of transport in laminar, tubular reactors and application to ethane pyrolysis, Industrial & Engineering Chemistry Research, 31 (1992) 58-69.

[49] L.J. Velenyi, Y. Song, J.C. Fagley, Carbon deposition in ethane pyrolysis reactors, Industrial & Engineering Chemistry Research, 30 (1991) 1708-1712.

[50] J.J. De Saegher, T. Detemmerman, G.F. Froment, Three dimensional simulation of high severity internally finned cracking coils for olefins production, Revue De L'Institut Français Du Pétrole, 51 (1996) 245-260.

[51] T. Detemmerman, G.F. Froment, Three dimensional coupled simulation of furnaces and reactor tubes for the thermal cracking of hydrocarbons, Revue De L'Institut Français Du Pétrole, 53 (1998) 181-194.

[52] X. Lan, J. Gao, C. Xu, H. Zhang, Numerical simulation of transfer and reaction processes in ethylene furnaces, Chemical Engineering Research & Design, 85 (2007) 1565-1579.

[53] J.V. Albano, K.M. Sundaram, M.J. Maddock, Applications of Extended Surfaces in Pyrolysis Coils, Energy Progress, 8 (1988) 160-168.

[54] C.F. Colebrook, Turbulent flow in pipes, with particular reference to the transition region between smooth and rough pipe laws, Journal of the Institution of Civil Engineers, 11 (1939).

[55] L. Prandtl, The mechanics of viscous fluids, Aerodynamics Theory, 3 (1935).

[56] T. Dijkmans, S.P. Pyl, M.-F. Reyniers, R. Abhari, K.M. Van Geem, G.B. Marin, Production of bio-ethene and propene: alternatives for bulk chemicals and polymers, Green Chemistry, 15 (2013) 3064-3076.

[57] P.J. Clymans, G.F. Froment, Computer-generation of reaction paths and rate-equations in the thermal-cracking of normal and branched paraffins, Computers & Chemical Engineering, 8 (1984) 137-142.

[58] L.P. Hillewaert, J.L. Dierickx, G.F. Froment, Computer-Generation of Reaction Schemes and Rate-Equations for Thermal Cracking, AIChE Journal, 34 (1988) 17-24.

[59] M.K. Sabbe, F. De Vleeschouwer, M.F. Reyniers, M. Waroquier, G.B. Marin, First Principles Based Group Additive Values for the Gas Phase Standard Entropy and Heat Capacity of Hydrocarbons and Hydrocarbon Radicals, J. Phys. Chem. A, 112 (2008) 12235-12251.

[60] M.K. Sabbe, M. Saeys, M.F. Reyniers, G.B. Marin, V. Van Speybroeck, M. Waroquier, Group additive values for the gas phase standard enthalpy of formation of hydrocarbons and hydrocarbon radicals, J. Phys. Chem. A, 109 (2005) 7466-7480.

[61] M.K. Sabbe, M.F. Reyniers, V. Van Speybroeck, M. Waroquier, G.B. Marin, Carbon-centered radical addition and beta-scission reactions: Modeling of activation energies and pre-exponential factors, ChemPhysChem, 9 (2008) 124-140.

[62] M.K. Sabbe, M.F. Reyniers, M. Waroquier, G.B. Marin, Hydrogen Radical Additions to Unsaturated Hydrocarbons and the Reverse beta-Scission Reactions: Modeling of Activation Energies and Pre-Exponential Factors, ChemPhysChem, 11 (2010) 195-210.

[63] M.K. Sabbe, A.G. Vandeputte, M.F. Reyniers, M. Waroquier, G.B. Marin, Modeling the influence of resonance stabilization on the kinetics of hydrogen abstractions, PCCP, 12 (2010) 1278-1298.

[64] Lu, C.K. Law, Systematic Approach To Obtain Analytic Solutions of Quasi Steady State Species in Reduced Mechanisms, The Journal of Physical Chemistry A, 110 (2006) 13202-13208.

[65] Z.Y. Ren, S.B. Pope, Entropy production and element conservation in the quasi-steady-state approximation, Combustion and Flame, 137 (2004) 251-254.

[66] R.J. Kee, F.M. Rupley, J.A. Miller, M.E. Coltrin, J.F. Grcar, E. Meeks, H.K. Moffat, G. Lutz, A.E. Dixon-Lewis, M.D. Smooke, J. Warnatz, G.H. Evans, R.S. Larson, R.E. Mitchell, L.R. Petzhold, W.C. Reynolds, M. Caracotsios, W.E. Stewart, P. Glarborg, C. Wang, O. Adigun, W.G. Houf, C.P. Chou, S.F. Miller, P. Ho, D.J. Young, CHEMKIN Release 4.1.1, Reaction Design, Inc., San Diego, CA, USA, 2007.

[67] S. Li, L. Petzold, Design of New DASPK for Sensitivity Analysis, UCSB Technical report., (1999).

[68] L. Shengtai, P. Linda, Design of new Daspk for Sensitivity Analysis, University of California at Santa Barbara, 1999.

[69] T. Kovacs, I.G. Zsely, A. Kramarics, T. Turanyi, Kinetic analysis of mechanisms of complex pyrolytic reactions, Journal of Analytical and Applied Pyrolysis, 79 (2007) 252-258.

[70] P.M. Plehiers, G.C. Reyniers, G.F. Froment, Simulation of the run length of an ethane cracking furnace, Industrial & Engineering Chemistry Research, 29 (1990) 636-641.

[71] G.J. Heynderickx, G.F. Froment, Simulation and comparison of the run length of an ethane cracking furnace with reactor tubes of circular and elliptical cross sections, Industrial & Engineering Chemistry Research, 37 (1998) 914-922.

[72] S. Wauters, G.B. Marin, Kinetic Modeling of Coke Formation during Steam Cracking, Industrial & Engineering Chemistry Research, 41 (2002) 2379-2391.

[73] S. Wauters, G.B. Marin, Computer generation of a network of elementary steps for coke formation during the thermal cracking of hydrocarbons, Chemical Engineering Journal, 82 (2001) 267-279.

[74] Y.-R. Luo, Handbook of bond dissociation energies in organic compounds, CRC Press, Boca Raton, Florida, 2003.

[75] K.M. Van Geem, M.F. Reyniers, G.B. Marin, J. Song, W.H. Green, D.M. Matheu, Automatic reaction network generation using RMG for steam cracking of n-hexane, AIChE Journal, 52 (2006) 718-730.

[76] M.K. Sabbe, K.M. Van Geem, M.-F. Reyniers, G.B. Marin, First principle-based simulation of ethane steam cracking, AIChE Journal, 57 (2011) 482-496.

[77] C. Cavallotti, D. Polino, A. Frassoldati, E. Ranzi, Analysis of Some Reaction Pathways Active during Cyclopentadiene Pyrolysis, The Journal of Physical Chemistry A, 116 (2012) 3313-3324.

Chapter 5:

The importance of turbulence-chemistry interaction for CFD simulations

5.1 Introduction

Modeling finite-rate chemistry in turbulent reactive flows presents a challenge because of the large span in length and time scales. In Large Eddy Simulations (LES) or Direct Numerical Simulations (DNS), the largest or all turbulent time scales are explicitly resolved, implying that local fluctuations and their effect on reaction rates are explicitly accounted for. Although requiring stringent computational resources, LES turbulence models have been successfully applied to reactive flows and this mainly in combustion research [1-6]. The present work focuses on steam cracking of hydrocarbons, i.e. pyrolysis, and although pyrolysis reactions are inherently a part of kinetic models for combustion, the simulation requirements for combustion and steam cracking are quite different. Indeed, as often the main objectives of a CFD simulation of a combustion process are the prediction of heat release, flame temperature and flame stability, reduced kinetic models and/or mixture fraction approaches are typically sufficient. The main exception is the simulation of NO_x formation during combustion which requires a detailed kinetic model. However, NO_x formation is mostly calculated in a post-processing step, decoupling the flow dynamics from the NO_x chemistry calculation [7]. On the contrary, one of the paramount objectives of any simulation of a steam cracking reactor, whether with a plug flow reactor model or using a CFD model, is the accurate simulation of product yields. Whereas typically combustion proceeds to full conversion to steam and carbon dioxide, steam cracking reactors are operated at a partial conversion to maximize the production of valuable light olefins. These two observations mean that the minimum size of the kinetic models necessary for steam cracking reactor simulations is larger than that required for typical combustion simulations. Secondly, the Reynolds number in industrial steam cracking reactors ranges from 80,000 to more than 200,000

[8]. The grid requirements for wall-resolved LES scale to the power of 1.8 with the Reynolds number [9, 10], currently limiting LES to Reynolds numbers of approximately 100,000. The combination of the large kinetic model and the large grid size renders a spatial LES of an industrial steam cracking reactor computationally very demanding. Therefore Reynolds Averaged turbulence models are used in this work. However, neglect of the turbulent fluctuations by using the mean temperature and concentrations for the calculation of reaction rates can induce an error:

$$\bar{r}_i \neq r_i(\overline{T}, \overline{C}) \tag{5.1}$$

and this mainly due to the highly nonlinear dependence of the reaction rate coefficient on temperature in the Arrhenius equation:

$$\bar{k}_i \neq k_i(\overline{T}) = A_i e^{-\frac{E_{a,i}}{R\overline{T}}} \tag{5.2}$$

The effect of turbulent fluctuations on the reaction rates can be accounted for in RANS simulations by scalar-variance transport equations for temperature and species concentrations. As the temperature dependence (exponential) is stronger than the concentration dependence (first or second order in pyrolysis kinetic models), only the effect of temperature fluctuations is accounted for here. Scalar-variance transport equations have been used for several applications. One of the most important being the simulation of turbulent premixed flames [11-13]. In order to reduce the computational load in this application, a chemistry model based on elementary reactions is eliminated. Instead, a so-called reaction progress variable is introduced which is defined in such a way that it spans the interval between unburned and fully burned fuel by increasing monotonically from zero to one. Transport equations for the progress variable mean and variance are solved and the species concentrations are reconstructed in a post-processing step based on a predefined probability density function (PDF) of the reaction progress variable. Scalar-variance

transport equations have also been used to predict NO_x formation in turbulent combustion [7]. In a post-processing step, the formation rate of NO_x is calculated based on the temperature mean and variance and mean species concentrations.

In this work, a code for the three-dimensional simulation of steam cracking reactors based on the free and open source CFD package OpenFOAM® was developed [14, 15]. The effect of turbulent temperature fluctuations on the reaction rates can be accounted for by solving a temperature variance transport equation. It should be noted that in contrast to non-premixed combustion, the reactants in steam cracking reactors are (pre)mixed. Hence, the effect of finite-rate mixing by e.g. the Eddy Dissipation Concept [16] or the Eddy Breakup Model [17] is not accounted for here. Pseudo-steady state is applied to the radicals as discussed in Chapter 4 to limit the computational cost while maintaining the chemical detail. To further reduce the computational cost, the code also incorporates a dynamic zoning method. In the rest of the chapter, the model equations are summarized and the solution procedures are discussed. Next, the importance of turbulence-chemistry interaction in steam cracking reactors is assessed and an industrial reactor is simulated.

5.2 Model equations

5.2.1   Conservation equations

Steam cracking reactors are gas-phase flow tubular reactors made out of high Cr-Ni-alloy steels. To account for the conductive heat transfer in the reactor metal, next to the process gas region, also the solid metal region is modeled. The process is non-isothermal and non-isobaric and hence the solution of both the momentum and the energy equation is required for the process gas. The process gas can be considered as an ideal gas mixture. In the reactor metal region, only the

conductive heat transfer equation is solved. The governing steady-state conservation equations are summarized in Table 5-1. Turbulence can be taken into account using any of the available standard RANS turbulence models of OpenFOAM® or new user-implemented turbulence models.

Table 5-1: Conservation equations.

Process gas region		
Global mass	$\nabla \cdot (\rho \overline{\boldsymbol{u}}) = 0$	(5.3)
Momentum	$\nabla \cdot (\rho \overline{\boldsymbol{u}}\,\overline{\boldsymbol{u}}) = -\nabla p + \nabla \cdot \overline{\overline{\boldsymbol{\tau}}}$	(5.4)
Energy	$\nabla \cdot \left(\rho \overline{\boldsymbol{u}} \left(h + \frac{1}{2}|\overline{\boldsymbol{u}}|^2\right)\right) = \nabla \cdot \left(\frac{\lambda_{f,eff}}{\rho c_p}\,\nabla h\right) + S_h$	(5.5)
Species	$\nabla \cdot (\overline{\boldsymbol{u}} C_j) = -\nabla \cdot \left(D_{eff,j}\nabla C_j\right) + R_j, \forall j = 1, nspec - 1$	(5.6)
Reactor metal region		
Energy	$\nabla \cdot (\lambda_s \nabla T) = 0$	(5.7)

In the Navier-Stokes equations, the laminar viscosity of the ideal gas mixture is calculated from the species laminar viscosity using an ideal mixing law. The species laminar viscosities $\mu_{l,j}$ are calculated from kinetic theory using the species Lennard-Jones well depth ε_{LJ} and σ_{LJ}, i.e. the distance at which the intermolecular potential between the two particles is zero; $\mu_{l,j} = \sqrt{\frac{MM_j T}{\sigma_{LJ,j}^2 \Omega(T_j^*)}}$

with $\Omega(T^*) = 1.16145 T^{*-0.14874} + 0.52487 e^{-0.7732 T^*} + 2.16178 e^{-2.43787 T^*}$ and $T^* = \frac{k_B T}{\varepsilon_{LJ,j}}$.

Most values for ε_{LJ} and σ_{LJ} are taken from literature [18], with the remaining estimated using RMG's TransportDataEstimator [19]. In the energy equation (5.5), $\frac{\lambda_{f,eff}}{\rho c_p}$ is the thermal diffusivity

containing contributions of laminar and turbulent diffusion, i.e. $\lambda_{f,eff} = \lambda_{f,l} + \lambda_{f,t}$. The laminar conductivity coefficient $\lambda_{f,l}$ is calculated from kinetic theory, i.e. $\lambda_{f,l,j} = \mu_{l,j}\left(c_{p,j} + \frac{5}{4}R\right)$. The turbulent conductivity coefficient $\lambda_{f,t}$ is calculated from the turbulent viscosity, i.e. $\lambda_{f,t} = \frac{\mu_t}{Pr_t}$ with $Pr_t = 0.85$. The heat of reaction S_h is calculated from the species heat of formation: $S_h = \sum_{j=1}^{nspec} R_j \Delta_{f,j}h$. The species continuity equations (5.6) are solved for $nspec - 1$ species with the concentration of the last species calculated from the global mass balance (5.3). Steam is chosen as the last component because it is present in the entire reactor in a considerable concentration because in the process it is added as a diluent. Furthermore, steam is considered to be inert in the here adopted reaction mechanisms and hence the uniformity of the steam mass fraction over the reactor acts as a double check for convergence and mass conservation of the simulation. The effective diffusion coefficient $D_{eff,j}$ in the species continuity equations has a laminar and a turbulent contribution; $D_{eff,j} = D_{l,j} + D_{t,j}$. The laminar coefficient is neglected as its contribution is minor in comparison to the turbulent contribution which is calculated from the turbulent viscosity, i.e. $D_{t,j} = \frac{\mu_t}{Sc_t}$ with $Sc_t = 0.7$ [20].

To account for the effect of local turbulent fluctuations on the reaction rates a temperature probability density function is used as explained in 5.3.2. The temperature variance is obtained by solving the scalar variance equation (5.8). The derivation of this equation is shown in Fox [21] and relies on the eddy diffusivity concept of Kolmogorov's theory for the unclosed terms. The laminar transport contribution in the first term in the right-hand side of equation (5.8) is neglected because of the high Reynolds numbers.

$$\nabla \cdot (\rho \bar{\boldsymbol{u}} \sigma_T^2) = \nabla \cdot \left(\rho \frac{\mu_t}{0.85} \nabla \sigma_T^2 \right) + 2 \frac{\mu_t}{Sc_t} (\nabla \bar{T})^2 - \varepsilon_T \tag{5.8}$$

There are two distinct ways of obtaining the temperature variance dissipation ε_T. In fully developed flow at high Reynolds numbers, the algebraic 'equilibrium' model, i.e. equation (5.8), can be used [21]. The parameter C_1 is typically set to 2.0 based on the experimental work of Beguier et al [22].

$$\varepsilon_T = C_1 \frac{\varepsilon}{k} \sigma_T^2 \tag{5.9}$$

For non-fully developed flow, the effect of turbulence anisotropy and mean shear stress can be accounted for by modeling an extra transport equation for the temperature variance dissipation (5.10).

$$\nabla(\rho \bar{\boldsymbol{u}} \varepsilon_T) = \nabla \cdot \left(\rho \frac{\mu_t}{Sc_t} \nabla \varepsilon_T \right) - C_2 \rho \frac{\varepsilon_T}{\sigma_T^2} - C_3 \rho^2 \frac{C_\mu k}{\mu_t} \varepsilon_T + C_4 \frac{\rho C_\mu k}{Sc_t} (\nabla \bar{T})^2 + C_5 \mu_t \frac{\bar{T}}{k} |\bar{\bar{\boldsymbol{S}}}| \tag{5.10}$$

The terms with the model parameters C_2 and C_3 are the respective dissipation terms due to scalar and mechanical destruction of fluctuations. The terms with the model parameters C_4 and C_5 are the respective production terms due to scalar gradients and velocity gradients. Many sets of values have been proposed for the model parameters C_2, C_3, C_4 and C_5. An extensive overview is given by Sanders and Gokalp [23]. The model parameter C_μ is part of the turbulence model and equal to 0.09 in most k-ε turbulence models. The source term $|\bar{\bar{\boldsymbol{S}}}|$ is the strain rate tensor defined as:

$$S_{ij} = \frac{1}{2} \left(\frac{\partial \bar{u}_i}{\partial x_j} + \frac{\partial \bar{u}_j}{\partial x_i} \right) \tag{5.11}$$

Based on user-input, turbulence-chemistry interaction can or cannot be taken into account. If turbulence-chemistry is accounted for, the 'equilibrium' closure model, i.e. equation (5.9), or one

of the fifteen sets of implemented parameter values for equation (5.10) can be used. To assure convergence, iterations are performed until the final residuals of all equations are below 10^{-15} and below 10^{-18} for the gas region energy equation. Furthermore, the outlet mixing cup temperature and species concentrations are monitored to be constant during the final 100 iterations.

5.2.2   **Species rate of formation**

As discussed in Chapter 1 thermal cracking of hydrocarbons proceeds mainly through a radical mechanism [24-26]. The adopted kinetic models in this work are single-event microkinetic models that only take into account elementary reactions. The kinetic models were derived from the model of Van de Vijver et al. [27] by removing species known to be unimportant during cracking of the considered feedstock molecule. The validity of the reduced network is shown in Appendix A by comparing one-dimensional plug flow simulation results obtained with the reduced and the full model to pilot plant data. Thermodynamic data of most molecules and radicals was derived from first principles CBS-QB3 calculations of Sabbe et al. [28, 29]. Missing data was estimated using RMG's ThermoDataEstimator [19]. To avoid time-consuming calculation of reverse reaction rates, reversible reactions are decoupled into two irreversible reactions with the Arrhenius parameters of the reverse reaction calculated prior to the simulation via regression to the values expressed by thermodynamic consistency over the relevant temperature range from 700 to 1300 K.

A probability density function (PDF) is used to calculate the average reaction rate coefficients to account for turbulence-chemistry interaction:

$$\bar{k}_i = \int_0^\infty k_i(T)P(T)dT \tag{5.12}$$

with $\bar{k}_i$ the mean reaction rate coefficient used for the calculation of the reaction rate $\bar{r}_i = \bar{k}_i \prod_{j=1}^{nspec} v_{i,j} C_j^{\alpha_{i,j}}$. A predefined Gaussian probability function distribution for temperature is assumed:

$$P(T) = \frac{1}{(2 \pi \sigma_T^2)^{\frac{1}{2}}} e^{-\frac{(T-\bar{T})^2}{2 \sigma_T^2}} \tag{5.13}$$

With $\bar{T}$ the mean temperature obtained by solving the energy equation (5.5) and σ_T^2 the temperature variance. The temperature variance transport equation (5.8) is solved to obtain a value for σ_T^2 in each grid cell.

5.3 Solution procedure

5.3.1 Conservation equations

OpenFOAM® applies the finite-volume method on collocated grids and adopts Gaussian integration. A segregated solver was used to solve the conservation equations given in Table 5-1. The Semi-Implicit Method for Pressure-Linked Equations (SIMPLE) algorithm was used to solve the Navier-Stokes equations. The mesh orthogonality was high enough in all simulations, not to require any non-orthogonal correctors. A 2nd order central differencing spatial discretization scheme was used, with a limiter for the species mass fractions to be non-negative and below or equal to unity. As turbulence model, the shear-stress transport (SST) k-ω model was used to calculate the eddy viscosity [30]. Using detailed kinetic models renders the species conservation equations highly stiff because of the large difference in time scales associated with species and reactions as discussed in Chapter 1. To tackle this issue, the pseudo-steady state assumption

(PSSA) is applied on the radicals on-the fly using a numerical algebraic solver. Besides reducing the stiffness of the species conservation equations, also the number of species conservation equations is reduced as the concentrations of the PSS species is calculated in the algebraic solver based on the concentrations of the non-PSS species. A more elaborate discussion on the adopted algorithm using FLUENT® was given in Chapter 4.

5.3.2   **Turbulence-chemistry interaction**

When turbulence-chemistry interaction is accounted for, the integral in equation (5.12) has to be integrated in each cell at every iteration. Combination of equation (5.12) and (5.13) gives the following expression for the mean reaction rate coefficient:

$$\bar{k}_i = E(k_i) = (2 \pi \sigma_T^2)^{-1/2} \int_{-\infty}^{\infty} A_i \exp\left(-\frac{E_{a,i}}{R\,T}\right) \exp\left(-\frac{(T - \bar{T})^2}{2\,\sigma_T^2}\right) dT \qquad (5.14)$$

A linear transformation of T to the normalized variable x is performed. The resulting expression for the mean reaction rate coefficient is given below.

$$x = \frac{T - \bar{T}}{(2\,\sigma_T^2)^{1/2}} \qquad (5.15)$$

$$\bar{k}_i = \pi^{-1/2} \int_{-\infty}^{\infty} A_i \exp\left(-\frac{E_{a,i}}{R\,((2\,\sigma_T^2)^{1/2}\,x + \bar{T})}\right) \exp(-x^2)\,dx \qquad (5.16)$$

The right-hand side of this expression can be rewritten as:

$$\pi^{-1/2} \int_{-\infty}^{\infty} \exp(-x^2) \left[A_i \exp\left(-\frac{E_{a,i}}{R\left((2\,\sigma_T^2)^{1/2}\,x + \bar{T}\right)} \right) \right] dx$$

$$= \pi^{-1/2} \int_{-\infty}^{\infty} W(x)\, f(x)\, dx$$

(5.17)

with $W(x) = \exp(-x^2)$ and $f(x) = A_i \exp\left(-\frac{E_{a,i}}{R\left((2\,\sigma_T^2)^{1/2}\,x + \bar{T}\right)} \right)$

In order to easily carry out the integral in (5.17) numerically, Gaussian quadrature is adopted. A Gaussian quadrature rule is an approximation of the integral of a function as a weighted sum of function values at specified points within the domain of integration. These specific points x_j at which the function is evaluated are called the abscissae, the weighting factors w_j are called the weights. The number of function evaluations N is called the quadrature order. Hence, the main equation of Gaussian quadrature is:

$$\int_a^b W(x)\, f(x)\, dx \approx \sum_{j=1}^{N} w_j\, f(x_j)$$

(5.18)

The concept is to project the function $f(x)$ on an orthonormal set of functions. Based on the weight function in equation (5.17) being $\exp(-x^2)$, the Gauss-Hermite polynomials are suited as a basis for the Gaussian quadrature. The recurrence relation for the Gauss-Hermite orthogonal polynomials is:

$$H_0 = 1$$

(5.19)

$$H_1 = 2x$$

(5.20)

$$H_{j+1} = 2\,x\,H_j - 2\,j\,H_{j-1}$$

(5.21)

In order to use the orthogonal set of Gauss-Hermite polynomials in Gaussian quadrature, normalization of the set of orthogonal equations is necessary. However, for higher orders, overflow of the variables can occur. Therefore, the following alternative set of recurrence relation and weights can be used which allow a direct generation of an orthonormal set of polynomials.

$$\widetilde{H}_{-1} = 0 \tag{5.22}$$

$$\widetilde{H}_0 = \frac{1}{\pi^{1/4}} \tag{5.23}$$

$$\widetilde{H}_{j+1} = x \left(\frac{2}{j+1}\right)^{1/2} \widetilde{H}_j - \left(\frac{j}{j+1}\right)^{1/2} \widetilde{H}_{j-1} \tag{5.24}$$

$$w_j = \frac{2}{\left[\widetilde{H}_N'(x_j)\right]^2} \tag{5.25}$$

$$\widetilde{H}_j' = (2\,j)^{1/2}\, \widetilde{H}_{j-1} \tag{5.26}$$

The roots of the Gauss-Hermite polynomials $\widetilde{H}_j$ can be found using Newton's method in case adequate initial estimates are available. However, a more efficient method than finding the roots of the polynomial function of order N with Newton methods is often preferred. Based on the results of Wilf [31], roots of a set of orthonormal polynomials can be found based on the matrix representation of the recurrence relation via the Golub-Welsch algorithm [32]. The recurrence relation (5.24) is rewritten and transformed to matrix form.

$$x\,\widetilde{H}_j = \left(\frac{j+1}{2}\right)^{1/2} \widetilde{H}_{j+1} + \left(\frac{j}{2}\right)^{1/2} \widetilde{H}_{j-1} \tag{5.27}$$

$$x \begin{bmatrix} \widetilde{H}_0 \\ \widetilde{H}_1 \\ \vdots \\ \widetilde{H}_{N-2} \\ \widetilde{H}_{N-1} \end{bmatrix} = \tag{5.28}$$

$$\begin{bmatrix} 0 & (1/2)^{1/2} & & & & \\ (1/2)^{1/2} & 0 & (2/2)^{1/2} & & & \\ & \vdots & \vdots & \ddots & \vdots & \vdots \\ & (2/2)^{1/2} & & 0 & ((N-1)/2)^{1/2} \\ & & & ((N-1)/2)^{1/2} & 0 \end{bmatrix} \begin{bmatrix} \widetilde{H}_0 \\ \widetilde{H}_1 \\ \vdots \\ \widetilde{H}_{N-2} \\ \widetilde{H}_{N-1} \end{bmatrix} + (N/2)^{1/2} \begin{bmatrix} 0 \\ 0 \\ 0 \\ 0 \\ \widetilde{H}_N \end{bmatrix}$$

The $N \times N$-matrix for the set of Gauss-Hermite polynomials is thus defined by the following expression for $0 \leq i < N$. All the other elements of the matrix are equal to 0.

$$J_{i,i+1} = J_{i+1,i} = \left(\frac{i+1}{2}\right)^{1/2} \tag{5.29}$$

The eigenvalues of the matrix are the abscissae x_j. The weight w_j associated with x_j is the square root of the first element of the eigenvector corresponding to x_j multiplied with the integral of the weight function over the full integration domain:

$$\int_a^b W(x)\, dx = \int_{-\infty}^{\infty} \exp(-x^2)\, dx = \pi^{1/2} \tag{5.30}$$

The eigensolver distributed by Passalacqua [33] based on the EISPACK package [34] is used to calculate the eigenvalues and eigenvectors of the $N \times N$-matrix of equation (5.28). The set of abscissae and weights for the integration of equation (5.17) are now available to calculate the mean reaction rate:

$$\bar{k}_i \cong \pi^{-\frac{1}{2}} \sum_{j=1}^{N} w_j\, A_i \exp\left(-\frac{E_{a,i}}{R\left((2\, \sigma_T^2)^{1/2}\, x_j + \overline{T}\right)}\right) \tag{5.31}$$

As calculation of the abscissae and weights is independent from the adopted reaction network, it is performed prior to the simulation. A quadrature order of 7 was seen to give satisfactory results. The on-the-fly integration of equation (5.12) thus breaks down to the inner product of the 7 pre-calculated weights and the reaction rate evaluated at the 7 abscissae, i.e. temperatures.

5.3.3   **Dynamic zoning method**

The second term on the right-hand side of the temperature variance conservation equation (5.8) is the production term caused by the temperature gradient. In steam cracking reactors, this gradient is largest near the inner wall. Furthermore, three-dimensional reactor technologies aiming at enhanced heat transfer, induce flow fluctuations and turbulence via the wall. Hence, an accurate description of the near-wall region using a low-Reynolds formulation of the turbulence model is desirable. This requires a first-cell dimensionless wall distance y^+ below unity, yielding a first-cell thickness in the µm range. Given the large length of steam cracking reactors, i.e. from 10 to 100 m, this results in grids containing tens of millions of cells. Calculation of the reaction rates and rates of formation accounts for the largest share in CPU time. Hence, significant speed-up would be realized if the chemistry calculations would not require such a fine grid. To evaluate this, a dynamic zoning partitioning scheme based on the work of Liang et al. [35] was tested. The latter comprises three steps: grouping of "thermodynamically similar" cells into zones, calculation of the reaction rates and rates of formation based on the zonal averages and mapping of the zonal averaged solution back to the individual cells. For combustion applications, several advanced algorithms [35, 36] have been proposed for grouping of cells because of the strongly varying conditions during combustion, e.g. from highly stratified to near-homogeneous. This implies that for certain outliers, e.g. cells where ignition starts, the algorithm must assure that the accuracy is maintained which results in a significant CPU overhead. In the case of pyrolysis and steam cracking, the thermodynamic state is much more uniform over the grid than in combustion applications because of the endothermic nature of the pyrolysis reactions. Therefore, a simple, fast, uniform zoning method can be applied. When neglecting turbulence-chemistry interaction,

the thermodynamic state that determines the rates of formation in cell k is $[\bar{T}_k, \bar{C}_k]$. Hence, strictly speaking grouping of cells should be performed by comparison of all species concentrations and temperature. This is inapplicable for two reasons: the CPU time associated with comparison of all these variables would be too high and it is difficult to define appropriate criteria for similarity for each species individually as one should know the expected concentration span of each species in the reactor [37]. However as an approximation, the thermodynamic state can be simply thought of as being determined by a limited number of so-called features d [35], e.g. the temperature $\bar{T}_k$ and the conversion of a feedstock component. Figure 5-1 shows the rate of formation for ethene as a function of temperature and butane conversion for all cells in the simulation of a butane cracking reactor. Indeed, the rate of formation for ethene is a smooth function of mean temperature and butane conversion and grouping of cells can be performed based on these two features. In each iteration step, the minimum and maximum values of the selected features d are determined. Next, based on user-supplied thresholds on each feature ε_d, the cells are uniformly grouped into zones as shown in Figure 5-1. Based on the zonal averages, the rates of formation and the heat of reaction are calculated for each zone [35]. Finally, the rates of formation and heat of reaction in each cell necessary for solving equations (5.5) and (5.6) are set equal to the values of their associated zone.
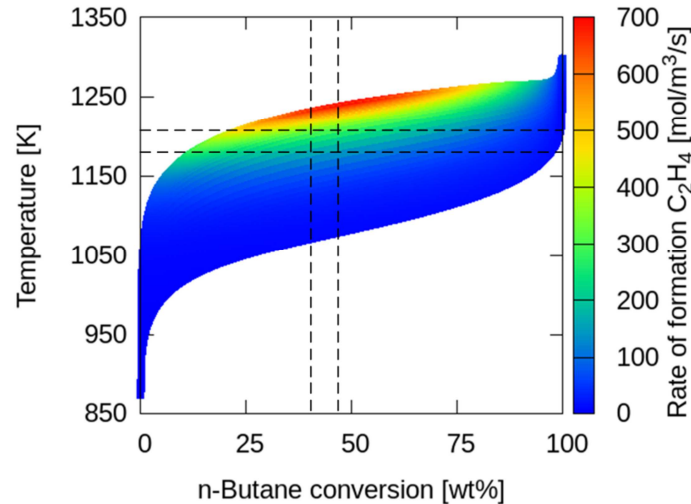
Figure 5-1: Rate of formation of ethene as a function of n-butane conversion and temperature in a butane cracking reactor.

5.4 Results and discussion

5.4.1 Dynamic zoning method

The dynamic zoning method was evaluated for the simulation of a butane cracking reactor. The goal of these simulations is to select appropriate features d for the zoning algorithm and to find user-specified thresholds ε_d for the features that balance accuracy against performance in terms of CPU time. The reactor has a length of 10.55 m, an inner diameter of 30.2 mm and a wall thickness of 6.75 mm. The reactor is modeled on a two-dimensional grid of 174,000 cells. The inlet temperature is 893 K and the steam dilution is 0.30 kg/kg. A pure n-butane feedstock was assumed. The coil outlet pressure was set to 233.15 kPa abs. The adopted single-event microkinetic network has 11 molecules and 9 radicals. A heat flux profile was applied to the reactor external wall. No turbulence-chemistry interaction was taken into account in these test

cases. All simulations were performed on one Dual Intel Xeon CPU E5-2670 octo-core processor (16 logical cores via Intel® Hyper-Threading Technology).

As stated above the rate of formation of a species in a cell k is determined by the thermochemical state $[\bar{T}_k, \overline{\boldsymbol{C}}_k]$ in that cell. Hence, an obvious choice for a first feature is the mean temperature $\bar{T}$. As a second feature, the butane conversion X is first evaluated to represent the concentrations vector $\overline{\boldsymbol{C}}_k$. The effect of the user-specified thresholds $\varepsilon_{\bar{T}}$ and ε_X on the simulation results was assessed in a parametric study. The effect of $\varepsilon_{\bar{T}}$ was evaluated by testing three values: 1, 5 and 10 K, while the effect of ε_X was tested at four values: 1, 5, 10 and 100 wt%. Setting ε_X to 100 wt% results in no zoning based on the conversion and hence using only one feature, i.e. $\varepsilon_{\bar{T}}$. A simulation without zoning, calculating the rates of formation in each cell individually, was also performed and is referred to as 'fully resolved'. This parametric study thus comprises $3 \cdot 4 + 1 = 13$ simulations.

Figure 5-2A and B show the mixing cup process gas temperature as a function of axial coordinate for the simulations with $\varepsilon_{\bar{T}} = 5\,K$ and $\varepsilon_X = 5\,wt\%$ respectively. Figure 5A shows that excellent agreement is obtained for the simulations with $\varepsilon_{\bar{T}} = 5\,K$ and ε_X at 1, 5 or 10 wt%. Zoning based solely on temperature, i.e. $\varepsilon_X = 100\,wt\%$ results in a large deviation from the fully resolved simulation. This holds for all simulations performed at $\varepsilon_X = 100\,wt\%$, regardless of the value of $\varepsilon_{\bar{T}}$. As all temperature profiles in Figure 5-2B match the fully resolved data almost exactly, $\varepsilon_{\bar{T}}$ can be set to high values without losing too much accuracy. Figure 5-3A and B show the simulated outlet conversion and ethene yield respectively as a function of ε_X for different $\varepsilon_{\bar{T}}$. The error on conversion and consequently on the ethene yield compared to the fully resolved simulation is seen to increase with increasing ε_X. However, the effect of $\varepsilon_{\bar{T}}$ is rather small.
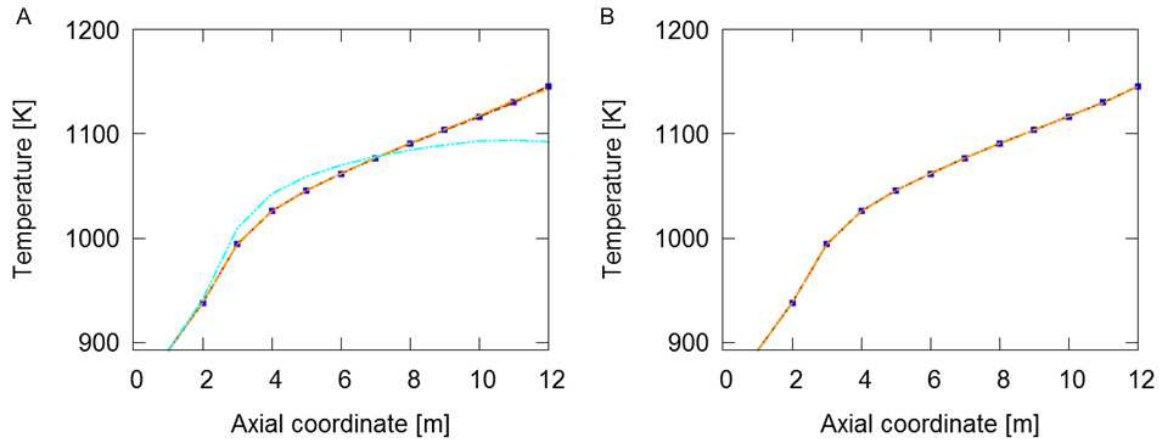
Figure 5-2: Mixing cup temperature as a function of axial coordinate [m] for $\varepsilon_{\bar{T}} = 5\ K$ (A): ■ - fully resolved, - - - - - $\varepsilon_X = 1\ wt\%$, ·········· - $\varepsilon_X = 5\ wt\%$, —·—· - $\varepsilon_X = 10\ wt\%$, —···— - $\varepsilon_X = 100\ wt\%$ and for $\varepsilon_X = 5\ wt\%$ (B): ■ - fully resolved, - - - - - $\varepsilon_{\bar{T}} = 1\ K$, ·········· - $\varepsilon_{\bar{T}} = 5\ K$, —·—· - $\varepsilon_{\bar{T}} = 10\ K$.
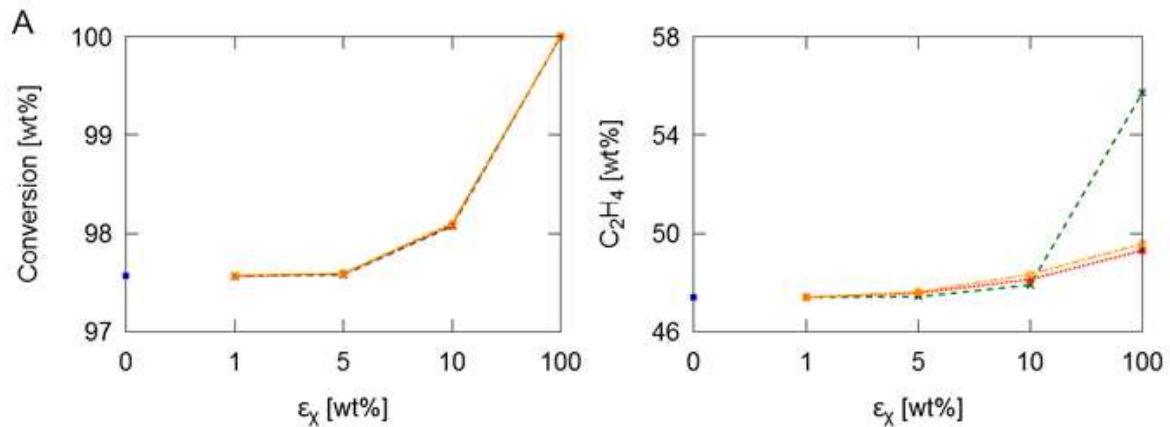
Figure 5-3: Outlet conversion (A) and ethene yield (B) as a function of ε_X: ■ - fully resolved, - - - - - $\varepsilon_{\bar{T}} = 1\ K$, ·········· - $\varepsilon_{\bar{T}} = 5\ K$, —·—· - $\varepsilon_{\bar{T}} = 10\ K$.

The CPU time consumed by calculation of the reaction rates and rates of formation (chemistry time) and the overhead of the zoning algorithm (zoning time) are shown in Figure 5-4. The

zoning overhead includes the transfer of the cell data from all logical cores to one logical core, calculation of the number of zones, distribution of the cells over the different zones and calculation of the zonal averages. The 'chemistry time' includes the calculation of the reaction rates and rates of formation based on these zonal averages. The CPU time used for zoning and chemistry calculations in the simulation with $\varepsilon_X = 1\ wt\%$ and $\varepsilon_{\bar{T}} = 1\ K$ is 2.39 times higher than in the fully resolved case. For all other simulations, a speedup factor ranging from 1.1 to 120 is obtained. The simulation with $\varepsilon_X = 5\ wt\%$ and $\varepsilon_{\bar{T}} = 10\ K$ which shows excellent agreement to the fully resolved simulation as shown in Figure 5-2 and Figure 5-3 has a speedup factor of 8.5. A significant zoning overhead is seen for all simulations, which is largely associated with collection of the data from the different logical cores on one logical core for division of the cells in zones and calculation of the zonal averages. Figure 5-5 shows the total CPU time of the different simulations. Comparison to Figure 5-4 shows that an almost constant time of about 0.4 s/iteration is associated with solving the continuity equations. The number of iterations to reach convergence was around 200,000 and was negligibly influenced by zoning. The total CPU time of the simulation with $\varepsilon_X = 5\ wt\%$ and $\varepsilon_{\bar{T}} = 10\ K$ is about 2.7 times shorter than for the fully resolved simulation.
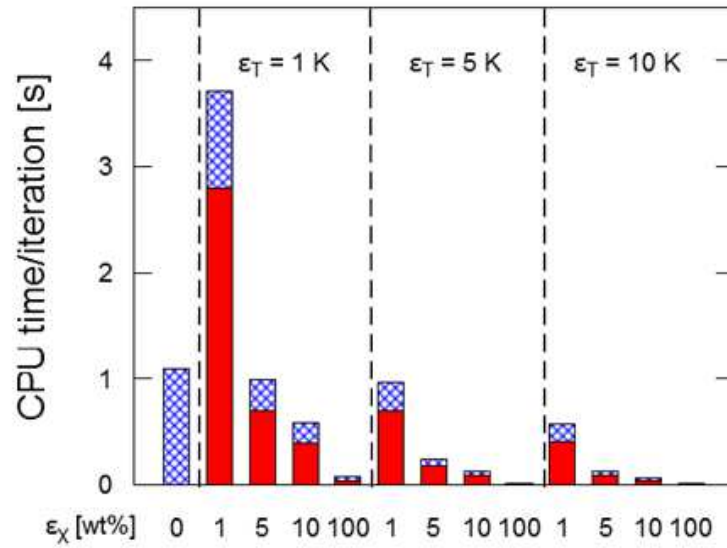
Figure 5-4: CPU time/iteration [s] for all simulations in the parametric study using $\overline{T}$ and X: ▨ **- chemistry time and** ▆ **- zoning time.**
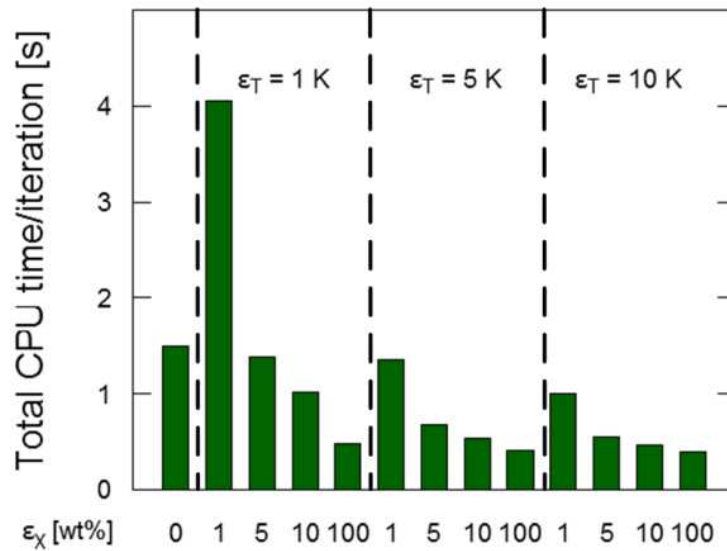

Figure 5-5: Total CPU time/iteration [s] for all simulations in the parametric study using $\overline{T}$ and X.

From the previous, conversion seems a good feature to be used during the zoning algorithm. However, when conversion reaches 100 % in the reactor, all zones with a conversion of 100 % will be grouped into a single zone, although the cracking severity in these cells can strongly vary. Indeed, secondary reactions, e.g. converting light olefins to aromatics, proceed when the feedstock molecules are fully converted. Hence, the cell concentration vectors and the correct species rates of formation will differ significantly within this zone. To resolve this problem, the methane weight fraction was evaluated as second zoning feature instead of conversion. To remove the effect of dilution on the zoning feature threshold, the dry methane weight fraction is used, i.e. normalized using the total hydrocarbon weight fraction. The dry methane weight fraction increases monotonically with cracking severity and has been proposed previously as a cracking severity index [38].

Figure 5-6A and B show the simulated outlet conversion and ethene yield respectively as a function of $\varepsilon_{Y_{CH_4}}$. Similar to the trends from the parametric study using conversion, the error on conversion and consequently on the ethene yield compared to the fully resolved simulation is seen to be largely determined by $\varepsilon_{Y_{CH_4}}$. For a given set of values for the thresholds on T and X or Y_{CH_4}, the error when using Y_{CH_4} is larger as less zones are present. Indeed, the methane weight fraction ranges from 0 to about 20 wt%, whereas the conversion ranges from 0 to almost 100 wt%. Hence, about 5 times more zones are made when using conversion instead of Y_{CH_4}. Appropriate values for $\varepsilon_{\bar{T}}$ and $\varepsilon_{Y_{CH_4}}$ are 10 K and 5 wt% respectively. Figure 5-7 shows the CPU time consumed by calculation of the reaction rates and rates of formation (chemistry time) and the overhead of the zoning algorithm (zoning time). Indeed as less zones are made, the CPU

times are lower compared to those of the parametric study using conversion. The speed-up factor

for the simulation using $\varepsilon_{Y_{CH_4}} = 5\ wt\%$ and $\varepsilon_{\bar{T}} = 10\ K$ is 36.

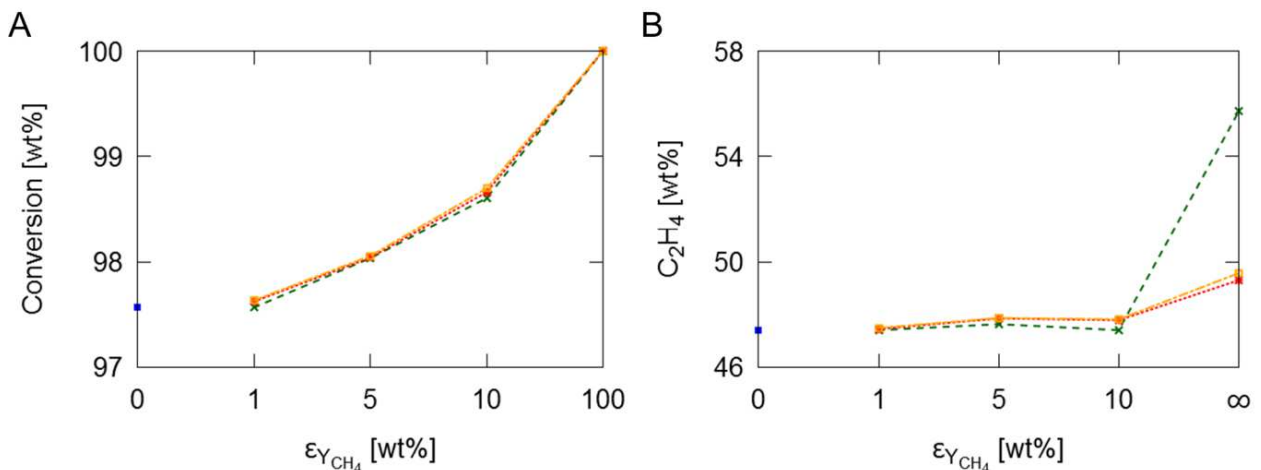**Figure 5-6: Outlet conversion (A) and ethene yield (B) as a function of $\varepsilon_{Y_{CH_4}}$: $-\ -\ -\ \cdot\ \varepsilon_{\bar{T}} = 1\ K$, $\cdots\cdots\cdots$ -**

$\varepsilon_{\bar{T}} = 5\ K$, $-\ -\ -\ \cdot\ \varepsilon_{\bar{T}} = 10\ K$.

As stated previously, gathering all cell data distributed over the different logical cores in the

parallel simulations contributes largely to the zoning overhead time. As cells with a similar

thermochemical state $[\bar{T}_k, \overline{C}_k]$ are also geometrically close to one another, zoning can

alternatively be performed logical core-wise, i.e. on each logical core the cells are grouped into

zones based on the user-specified feature thresholds without inter-logical core communication.

Figure 5-8 illustrates the difference between global zoning, i.e. over all cells of the grid and per

logical core zoning.
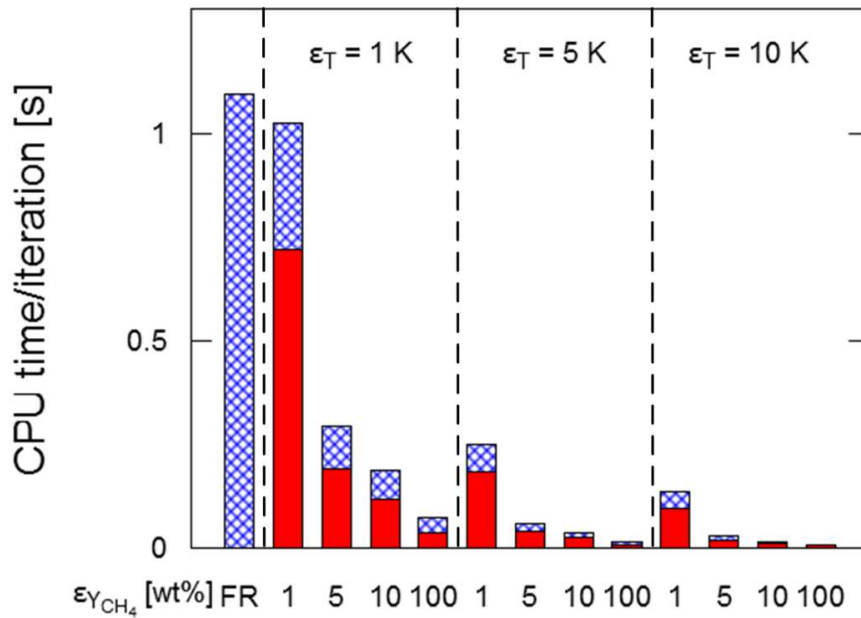
Figure 5-7: CPU time/iteration [s] for all simulations in the parametric study using $\bar{\bar{T}}$ and Y_{CH_4}: ▨ - chemistry time and ▬ - zoning time.
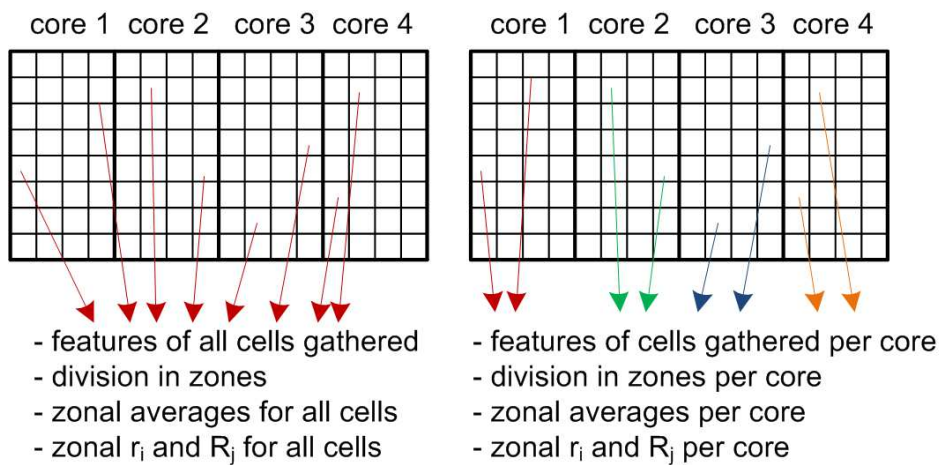
Figure 5-8: Schematic illustration of global zoning (left) and zoning per logical core (right).

Zoning per logical core was tested for the parametric study using the methane weight fraction. Figure 5-9A and B show the simulated outlet conversion and ethene yield respectively as a function of $\varepsilon_{Y_{CH_4}}$. As zoning is performed per logical core, the number of zones is higher compared to the previous parametric studies. Hence, the agreement to the fully resolved simulation data is much better than in the previous parametric studies. For all simulations, the difference to the outlet conversion in the fully resolved simulation is below 0.04 wt%. As before, the error on conversion and consequently on the ethene yield compared to the fully resolved simulation is seen to increase with increasing $\varepsilon_{Y_{CH_4}}$ while the effect of $\varepsilon_{\bar{T}}$ is rather small.
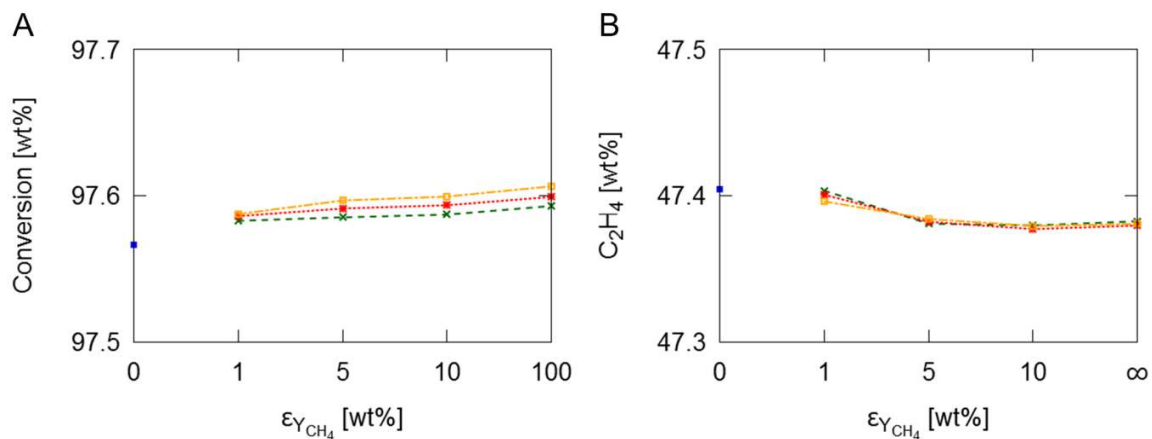
Figure 5-9: Outlet conversion (A) and ethene yield (B) as a function of $\varepsilon_{Y_{CH_4}}$ with zoning per logical core: - - - -

- $\varepsilon_{\bar{T}} = 1\ K$, ┈┈┈ - $\varepsilon_{\bar{T}} = 5\ K$, ─·─ - $\varepsilon_{\bar{T}} = 10\ K$.

Figure 5-10 shows the CPU time consumed by chemistry calculation and by zoning for the 12 cases. Note that the fully resolved simulation is not included in this figure and that the scale is different than in Figure 5-4 and Figure 5-7. Compared to the fully resolved simulation, a speedup factor from 50 to 190 is obtained for the chemistry calculations. A much higher speedup factor is obtained compared to zoning over the entire grid. The reason is two-fold. First, the time-

consuming gathering of the data spread over the different logical cores is avoided. Second, calculation of the zonal averages is faster as each zone has less cells. Little CPU time reduction is seen by increasing $\varepsilon_{Y_{CH_4}}$ above 5 wt% for a set $\varepsilon_{\bar{T}}$. This is a result of the zoning being performed per logical core. As 16 logical cores are used and the maximum methane weight fraction is around 20 wt%, the average methane weight fraction range per logical core is around 1.25 wt%. Hence, zoning with a threshold $\varepsilon_{Y_{CH_4}}$ above 5 wt% results in almost no increase in the number of zones. Figure 5-11 shows the total CPU time per iteration. It is seen that when zoning per logical core the CPU time is reduced to about 0.4 s/iteration, i.e. the CPU time associated with solving the continuity equations. By zoning per logical core, the contribution of the chemistry calculation and the zoning overhead is negligible. Summarizing, zoning per logical core has a higher accuracy and a better performance compared to zoning over the entire grid and is therefore recommended. Finally, it should be noted that as steady-state simulations are performed here, the feature threshold values can be changed along the run time of the simulation. At the start of a simulation, high feature threshold values can be applied, i.e. $\varepsilon_{\bar{T}} = 10\ K$ and $\varepsilon_{Y_{CH_4}} = 100$ wt%. This results in fast iterations that still guarantee a solution close to the fully resolved solution. Afterwards, the feature threshold values can be refined to $\varepsilon_{\bar{T}} = 1\ K$ and $\varepsilon_{Y_{CH_4}} = 1$ wt% to move closer to the fully resolved solution. Ultimately, zoning can be disabled to obtain the fully resolved solution. This way not too much CPU time associated with the fully resolved method is spent when the simulations is still far from the converged solution.
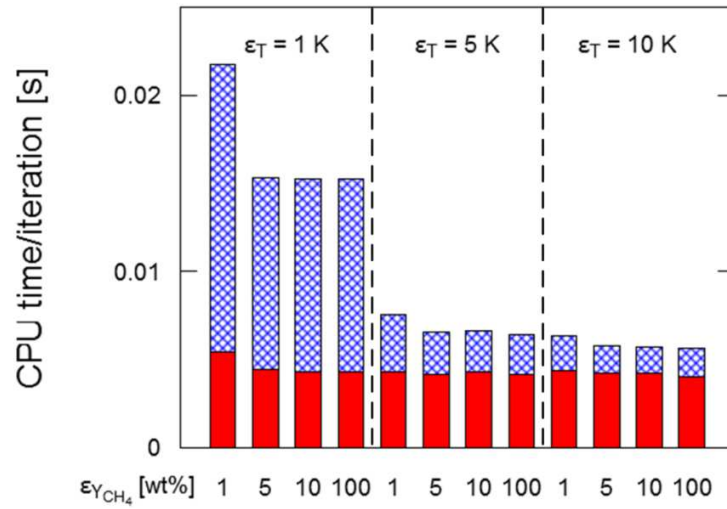
Figure 5-10: CPU time/iteration [s] for all simulations in the parametric study using T and Y_{CH_4} with zoning per logical core: ▦ - chemistry time and ▬ - zoning time.
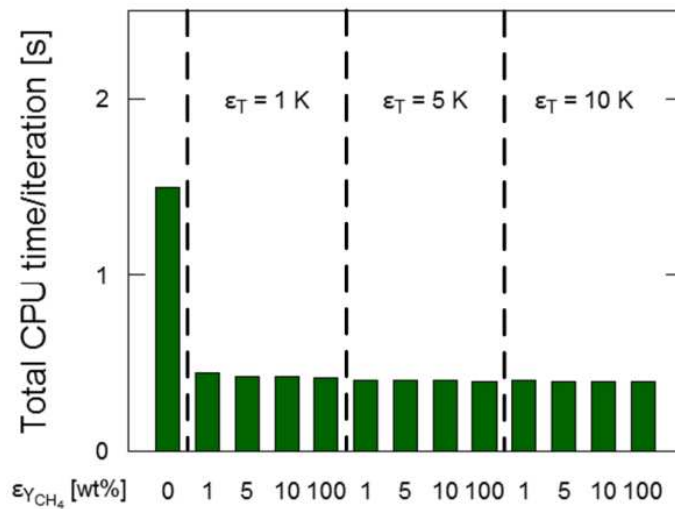

Figure 5-11: Total CPU time/iteration [s] for all simulations in the parametric study using $\bar{T}$ and Y_{CH_4}.

5.4.2 Impact of turbulence-chemistry interaction

5.4.2.1 Validation to DNS data

To validate the use of a temperature variance conservation equation, comparison is made to the DNS data of Redjem-Saad et al. [39] of turbulent pipe flow. Similar to the work of Redjem-Saad, the flow is modeled incompressible in this simulation and temperature is treated as a passive scalar. Following the methodology of Patankar et al. [40], streamwise periodic boundary conditions are applied. By application of a uniform heat flux to the tube wall, the fluctuating components of pressure and temperature can be isolated from the mean streamwise gradient. For more details on the applied methodology, reference is made to Van Cauwenberge et al. [41].

Figure 5-12 compares the results of the mean velocity (A) and temperature (B) and the root-mean-square temperature (C) as a function of the dimensionless wall distance. Good agreement is seen for the mean variables, although both mean velocity and temperature are slightly overpredicted near the tube center. The root-mean-square temperature is underpredicted near the wall. At $y^+ \approx 5$, the root-mean-square temperature increases drastically and overpredicts the DNS data for $y^+ > 10$. This behavior can be explained by the mean temperature gradient being underpredicted by the RANS simulation below a y^+ of 5 and an overprediction more towards the center of the tube. Subsequently the source term $2\frac{\mu_t}{Sc_t}(\nabla \bar{T})^2$ in equation (5.8) results in the underprediction/overprediction at low/high y^+. The location of the T_{rms}^+ maximum at $y^+ = 17$ is well predicted. However, the maximum value is overpredicted. Hence, the effect of turbulence-chemistry interaction on product yields with the RANS model will be overestimated. In other words, if a negligible influence on product yields is simulated here, the real effect of

turbulence-chemistry will certainly be negligible. The difference between using the algebraic equilibrium model (5.9) or solving an extra continuity equation of the temperature variance dissipation (5.10) is small. Using different sets of parameters for the temperature variance dissipation continuity equation showed a negligible difference as exemplified in Figure 5-12 when using the parameters of Newman et al. [42] and Elghobashi and Launder [43].
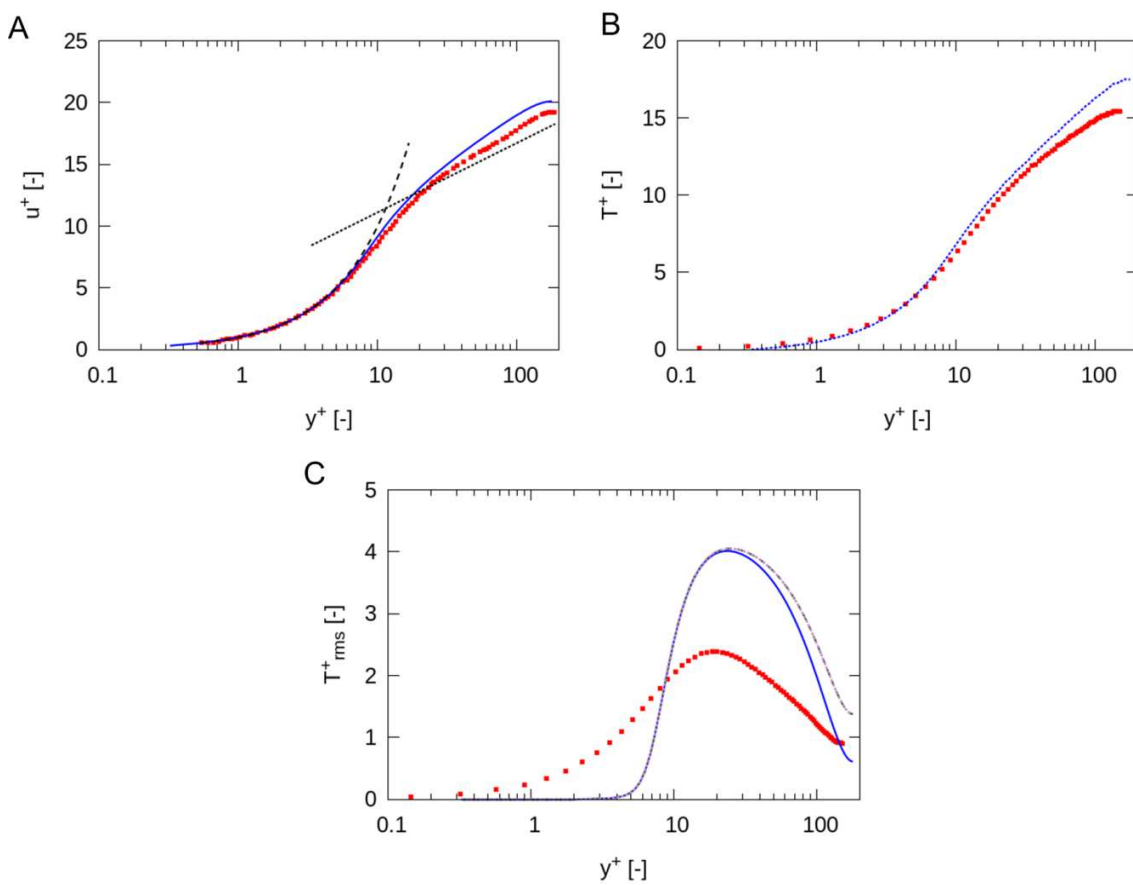

Figure 5-12: Dimensionless mean velocity u^+ (A); dimensionless mean velocity T^+ and dimensionless root-mean-square temperature as a function of dimensionless wall distance y^+: ■ **- DNS Redjem-Saad et al. [39];** **- - - - - $u^+ = y^+$;** ········· **- law of the wall;** ——— **- RANS ε_T from equation (5.9);** ········· **- RANS ε_T from equation (5.10), parameters from [42];** ——·— **- RANS ε_T from equation (5.10), parameters from [43].**

5.4.2.2 Turbulence-chemistry interaction

Two cases are studied to assess the importance of turbulence-chemistry interaction referred to as 'fixedT' and 'fixedQ'. Both are for a butane cracking reactor of 10.55 m long and with an internal diameter of 30.2 mm and a wall thickness of 6.75 mm. An entrance zone of 1.5 m was placed upstream the reactor inlet to ensure fully developed flow at the reactor inlet. The feedstock is pure butane and steam is added at a dilution of 0.30 kg/kg. The coil outlet pressure was set to 233.15 kPa abs. The two cases differ in the energy boundary conditions. In fixedT, the temperature profile shown in Figure 5-13A was applied to the reactor inner wall, while in fixedQ the heat flux profile shown in Figure 5-13B was used. In the former, only the process gas is modeled while in the latter, both the fluid and the reactor metal tube are modeled. The inlet temperature is 800 K and 923 K in the fixedT and fixedQ case respectively. The first case was set up to test the importance of turbulence-chemistry interaction under extreme conditions and does not correspond to a realistic operation of a tubular pyrolysis reactor. As seen from Figure 5-13A, the reactor inner wall makes a step change at the start of the reactor which induces a large source term in the temperature variance equation as a large radial temperature gradient exists at the reactor inlet. The second case corresponds to a set of more realistic operating conditions of an industrial cracker. A small single-event-microkinetic network containing 8 molecules and 7 radicals was used.
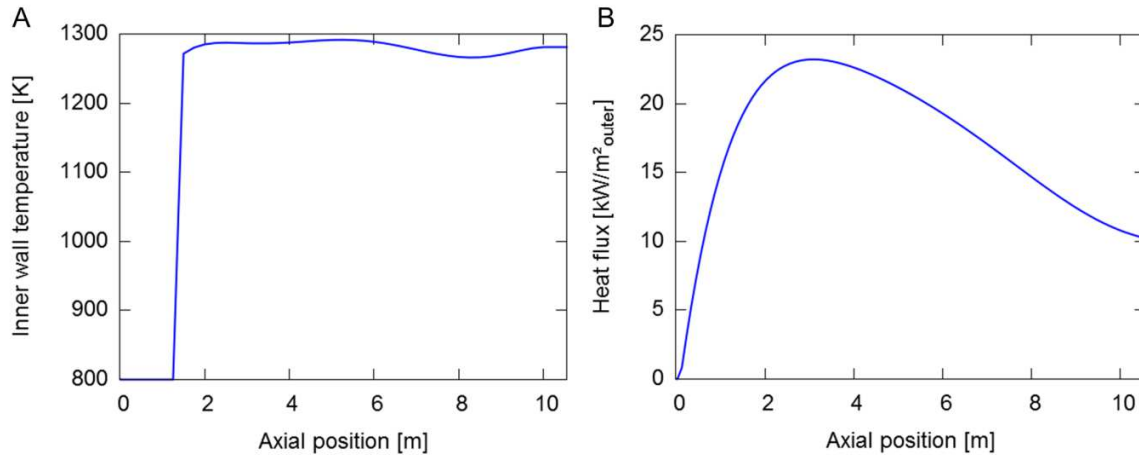
Figure 5-13: Energy boundary condition on wall: (A) Inner wall temperature [K] for case fixedT, (B) heat flux [kW/m²] for case fixedQ as function of axial coordinate [m].

Figure 5-14A and B show the temperature standard deviation σ_T as a function of the axial coordinate for the fixedT and fixedQ case respectively. The temperature standard deviation makes a sharp jump at an axial coordinate of 1.5 m i.e. where the imposed inner wall temperature suddenly increases from 800 K to 1290 K. This creates a large source term $2\frac{\mu_t}{Sc_t}(\nabla \bar{T})^2$ in equation (5.8). More downstream, the temperature standard deviation decreases as the temperature difference between center and inner wall decreases as shown in Figure 5-15A and as the temperature variance dissipation ε_T increases. Similar trends are seen for the fixedQ case, but less pronounced. The maximum temperature standard deviation is only around 15 K for this case compared to 35 K for the fixedT case. Moreover the increase and decrease are slower as the temperature gradient is smaller and changes more slowly as shown in Figure 5-15A and B. Hence, the importance of turbulence-chemistry interaction depends largely on the existing radial temperature gradient in the reactor which in turn is determined by the reactor diameter,

convective heat transfer coefficient and heat flux. The effect of turbulence-chemistry interaction on the radial temperature profile is negligible as seen from Figure 5-15A and B. The species rates of formation are slightly affected, having a small effect on the product yields as discussed further. However, the change in the species rates of formation is too small to influence the heat of reaction to the extent of having a significant influence on the mean temperature.
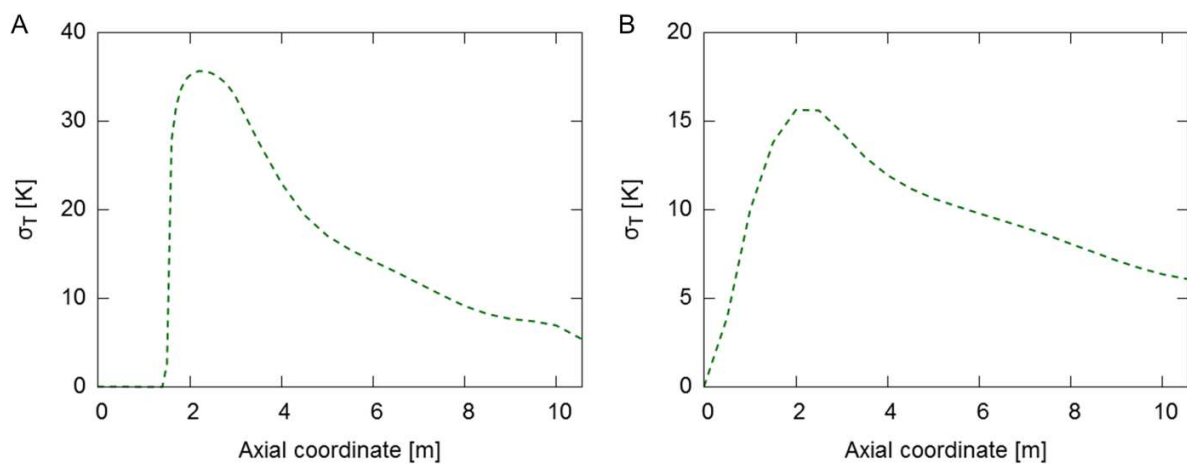

Figure 5-14: Temperature standard deviation [K] as a function of axial coordinate [m] for fixedT (A) and fixedQ (B).
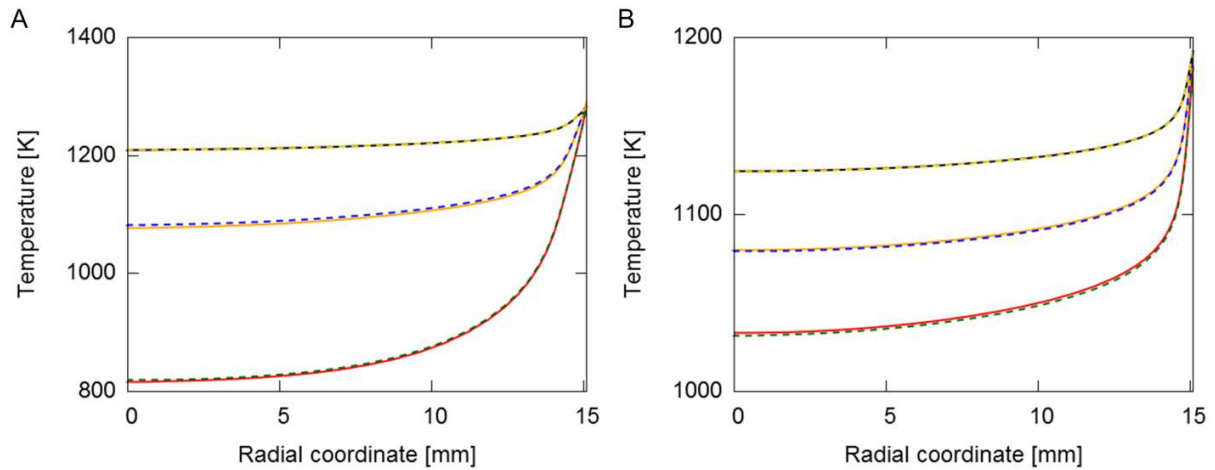
Figure 5-15: Mean temperature [K] as a function of radial coordinate [m] for fixedT (A) and fixedQ (B): ——— - without turbulence-chemistry interaction at 2 m; – – – · - with turbulence-chemistry interaction at 2 m; ——— - without turbulence-chemistry interaction at 5 m; – – – · - with turbulence-chemistry interaction at 5 m; ——— - without turbulence-chemistry interaction at 10 m; – – – · - with turbulence-chemistry interaction at 10 m.

Table 5-2 summarizes the results of the two cases, with and without accounting for turbulence-chemistry interaction. Note that only the results obtained with the algebraic equilibrium model (5.9) are shown. Negligible differences were obtained when the extra transport equation for the temperature variance dissipation (5.10) was solved. The conversion in the fixedT case is nearly 100 % showing the extreme cracking severity of this case. Accounting for turbulence-chemistry interaction results in a slightly higher cracking severity, i.e. the conversion increases and the P/E ratio decreases. The effect on most product yields is negligible in the fixedT case, except for ethene and propene. The ethene and propene yield are 0.13 wt% higher and 0.11 wt% lower respectively when accounting for turbulence-chemistry interaction. The conversion in the fixedQ case is 88.7 % without turbulence-chemistry interaction and is 0.2 %

higher when turbulence-chemistry interaction is considered. Taking turbulence-chemistry interaction into account results in a small but significant change for the ethene and propene yield, i.e. the ethene yield increases by 0.18 wt% while the propene yield decreases by 0.07 wt%. Summarizing, the effect of turbulence-chemistry interaction on conversion and product yields is small in all cases but results in a change in ethene and propene yields that is of the same order of magnitude as the effect of a three-dimensional reactor technology on these yields as shown in Chapter 3 and 4.

Table 5-2: Coil outlet temperature, P/E ratio, conversion and product yields for fixedT and fixedQ case.

Case	fixedT		fixedQ	
Turbulence-chemistry	Without	With	Without	With
COT [K]	1235.1	1235.1	1141.9	1141.9
P/E ratio [wt%/wt%]	0.193	0.191	0.904	0.897
Butane conversion [-]	99.82	99.84	88.74	88.93
Product Yields [wt%]				
H_2	1.40	1.39	0.66	0.66
CH_4	12.07	12.14	14.60	14.61
C_2H_6	7.58	7.54	7.20	7.24
C_3H_8	0.87	0.85	2.14	2.17
C_2H_4	65.32	65.45	33.69	33.87
C_3H_6	12.58	12.47	30.45	30.38
Product Selectivities [wt%]				
H_2	1.40	1.40	0.75	0.75
CH_4	12.09	12.16	16.45	16.43
C_2H_6	7.60	7.55	8.12	8.14
C_3H_8	0.87	0.85	2.41	2.44
C_2H_4	65.44	65.56	37.96	38.08
C_3H_6	12.61	12.49	34.31	34.16

5.4.3   Simulation of an industrial steam cracking reactor

An industrial-size butane-cracking U-coil reactor was simulated. A U-coil reactor has two passes referred to as the inlet and outlet leg respectively. These are connected by a return bend and a joint where the diameter gradually expands from the inlet diameter to the outlet diameter. Figure 5-16 A, B and C show a front, side and top view of the lower part of the reactor, i.e. focusing on the return bend. The first part of the return bend is a S-bend moving the reactor outside the plane defined by the inlet and outlet leg. Downstream, a U-bend connects the S-bend to the outlet leg. The most upstream part of the outlet leg is a joint where the diameter gradually expands. Upstream of the depicted part of the inlet leg, an 8 m straight tube is located, yielding a total length of the inlet leg of 9.15 m. To ensure fully developed flow at the reactor inlet, 1.5 m extra straight tube is placed upstream the inlet leg. The total outlet leg length is 10.2 m. The butane feed was modeled as pure n-butane. The coil inlet temperature and coil outlet pressure were set to 853 K and 243.18 kPa abs respectively. The butane mass flow rate and dilution are 0.4215 kg/s and 0.30 kg/kg respectively. The adopted single-event microkinetic model contains 149 reactions between 11 molecules and 9 radicals and was obtained by reducing the butane pyrolysis network of Van de Vijver et al. [27] to its main species. The validity of the reduced network was confirmed by comparison to pilot plant data as shown in Appendix A. The adopted mesh is a structured butterfly grid created using Pointwise[®]. The number of cells in the process gas fluid and reactor metal solid region is $20.03 \cdot 10^6$ and $2.55 \cdot 10^6$ respectively. An axial heat flux profile was applied to the reactor outer wall. The reactor geometry details, process conditions and product yields are summarized in Table 5-3.

Table 5-3: Geometry details and process conditions of butane-cracking U-coil reactor.

| **Reactor geometry**	
Reactor type	U-coil
Inlet leg	
Length [m]	9.15
Inner diameter [m]	0.09
Wall thickness [m]	0.0116
S-bend	
Length [m]	1.0177
Inner diameter [m]	0.09
Wall thickness [m]	0.0116
U-bend	
Length [m]	2.32
Inner diameter [m]	0.09
Wall thickness [m]	0.1016
Length [m]	0.0116
Outlet leg	
Number	1
Length	10.2
Inner diameter [m]	0.102
Wall thickness [m]	0.0156
Process conditions	
Butane mass flow rate [kg/s/reactor]	0.4215
Dilution [kg/kg]	0.30
Coil inlet temperature [K]	853
Coil outlet pressure [kPa abs]	243.18
Results	
Coil outlet temperature [K]	1129
Product yields [wt%]	
H_2	0.50
CH_4	16.55
C_2H_6	8.18
C_3H_8	1.01
$n\text{-}C_4H_{10}$	11.00
C_2H_4	38.78
C_3H_6	20.61
$1,3\text{-}C_4H_6$	2.47
$1\text{-}C_4H_8$	0.61
$2\text{-}C_4H_8$	0.29
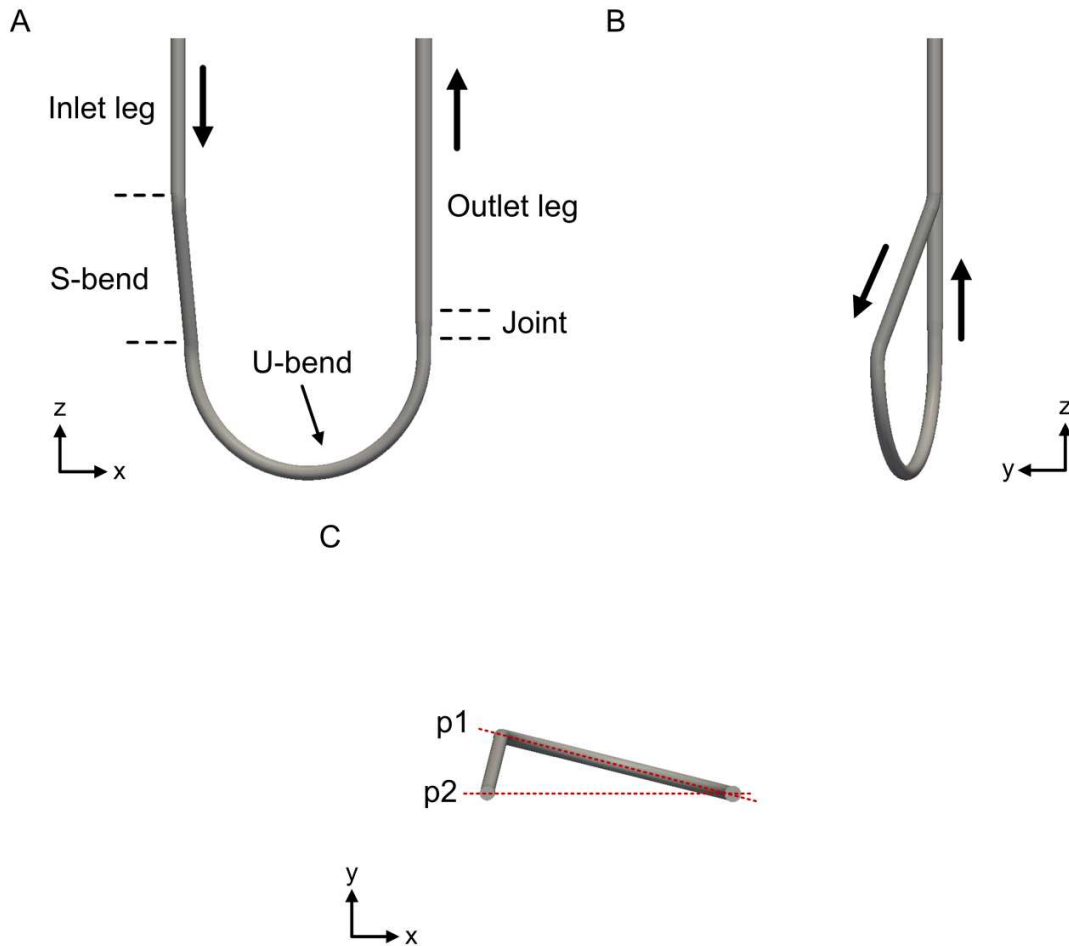
Figure 5-16: Front view (A), side view (B) and top view (C) of the simulated U-coil.

Figure 5-17 shows the velocity magnitude and the in-plane velocity vectors for six cross sections in the return bend. The cross sections are labeled from a to f. Note that the in-plane velocity vectors are not scaled to their magnitude and hence only give the direction of the occurring secondary flow. Cross section a is located in the straight inlet leg and a fully developed turbulent

flow field is simulated consequently. As the flow enters the S-bend, a low velocity zone is created near the inner curve of the bend and two counter-rotating vortices prevail. By introduction to the U-bend, the low-velocity region shifts to the inner curve of the U-coil bend from c to d. Downstream the U-bend, the two counter-rotating vortices and the dead zone remain for some length as shown in e and f. The velocity in e and f is also lower compared to the other cross sections as the inner diameter has enlarged and hence the cross-sectional area is larger. The effect of these flow patterns have a straightforward effect on temperature and conversion: low near-wall velocity results in low heat transfer and subsequently in high temperature and high conversion.
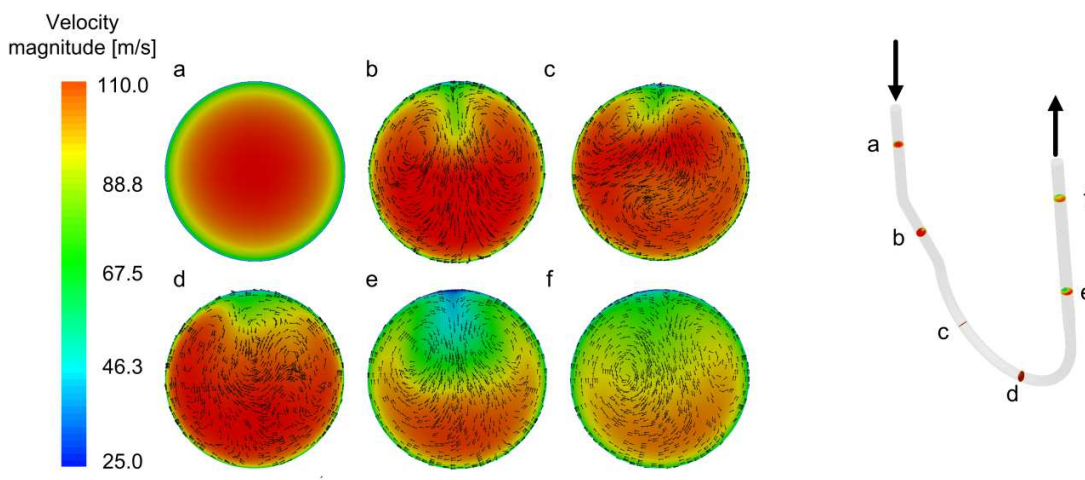

Figure 5-17: Velocity magnitude [m/s] in the six cross sections in the return bend and the location of the cross sections.

The near-wall low velocity in a U-bend prevails at the inner curve [44-46]. As the U-bend is not in the plane defined by the inner and outer leg, denoted 'p1' in Figure 5-16 C, but rather in the

plane 'p2', the near-wall low velocity zone in the outlet leg is not directed towards the inlet leg but is directed towards the start of the U-bend. Hence, it is in a location receiving a high radiative heat flux from the furnace walls and burners. Having this zone directed towards the inlet leg would be beneficial as this is the so-called 'shadow zone' receiving less heat flux [47, 48]. Figure 5-18 A, B and C show the velocity, temperature and n-butane yield in plane 'p1' shown in Figure 5-16 C in the outlet leg. As shown previously the velocity in the U-bend is higher near the outer curve of the bend. This results in a low velocity zone near the inner curve of the outlet tube that remains up to about 3 m in the outer leg. This results in a high temperature near the inner curve of the outlet leg as shown in Figure 5-18 B. Consequently the n-butane weight fraction in a cross section of the outlet leg is highly non-uniform.
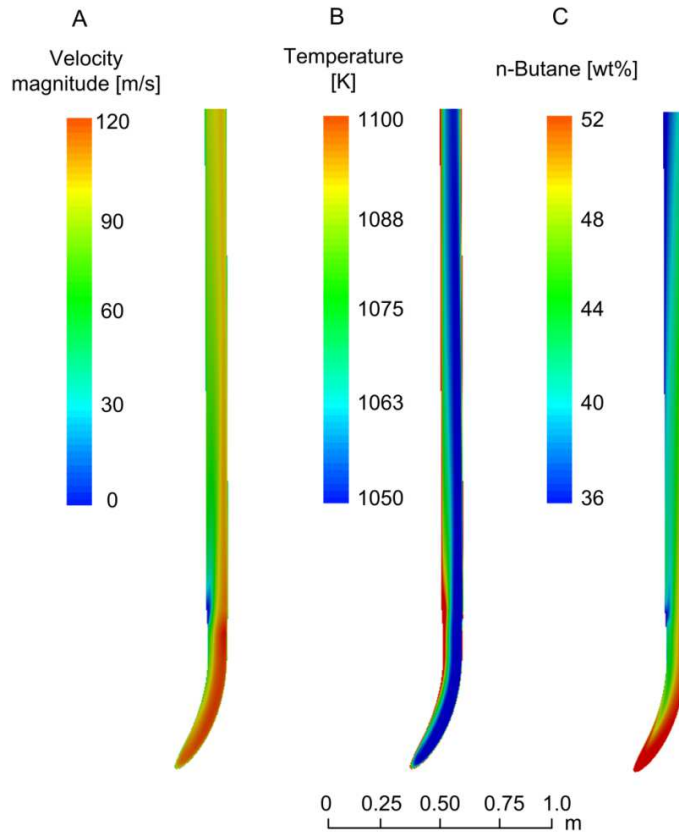
Figure 5-18: Velocity [m/s] (A), mean temperature [K] (B) and n-butane [wt%] (C) in plane 'p2' in the outlet leg, viz. Figure 5-16 C.

5.5 Conclusions

The importance of turbulence-chemistry interaction during steam cracking was assessed. To this end a code for the three-dimensional simulation of steam cracking reactors based on the free and open source CFD package OpenFOAM® was developed. The code incorporates the algorithm to apply the pseudo-steady state assumption to radicals discussed in Chapter 4 and a dynamic zoning method to speed up the chemistry calculations. The dynamic zoning method can best be applied per logical core and results in a speed up of the chemistry calculations by a factor of 190 while maintaining a similar accuracy as calculating the chemistry in every cell individually. This

reduction makes the contribution of the chemistry calculations negligible compared to the time consumed by solving the continuity equations. The effect of turbulent temperature fluctuations is accounted for by solving an extra continuity equation for temperature variance. Temperature variance dissipation can be modeled with an algebraic equilibrium model or by solving an extra continuity equation. Comparison of this approach to DNS data for non-reactive, turbulent pipe flow showed that the root-mean-square temperature is underpredicted near the wall and overpredicted in the tube center. Simulation of reactive flow indicated that neglecting the turbulence-chemistry interaction results in an error on the ethene and propene yields around 0.1-0.2 wt%. Finally the code was used to simulate butane cracking in an industrial-size U-coil reactor. Secondary flow patterns in the U-bend were visualized and showed a high temperature, high conversion zone in the outlet leg near the inner curve of the U-bend which is impossible to detect with one-dimensional simulations. These detailed simulation results show that this code can be used for the design and optimization of reactor geometries.

References

[1] M. Boileau, G. Staffelbach, B. Cuenot, T. Poinsot, C. Berat, LES of an ignition sequence in a gas turbine engine, Combustion and Flame, 154 (2008) 2-22.

[2] L. Esclapez, E. Riber, B. Cuenot, Ignition probability of a partially premixed burner using LES, Proceedings of the Combustion Institute, 35 (2015) 3133-3141.

[3] L. Hakim, A. Ruiz, T. Schmitt, M. Boileau, G. Staffelbach, S. Ducruix, B. Cuenot, S. Candel, Large eddy simulations of multiple transcritical coaxial flames submitted to a high-frequency transverse acoustic modulation, Proceedings of the Combustion Institute, 35 (2015) 1461-1468.

[4] G. Hannebique, P. Sierra, E. Riber, B. Cuenot, Large Eddy Simulation of Reactive Two-Phase Flow in an Aeronautical Multipoint Burner, Flow Turbulence and Combustion, 90 (2013) 449-469.

[5] A. Irannejad, A. Banaeizadeh, F. Jaberi, Large eddy simulation of turbulent spray combustion, Combustion and Flame, 162 (2015) 431-450.

[6] W.P. Jones, A.J. Marquis, F. Wang, Large eddy simulation of a premixed propane turbulent bluff body flame using the Eulerian stochastic field method, Fuel, 140 (2015) 514-525.

[7] A. Cuoci, A. Frassoldati, A. Stagni, T. Faravelli, E. Ranzi, G. Buzzi-Ferraris, Numerical Modeling of NOx Formation in Turbulent Flames Using a Kinetic Post-processing Technique, Energy & Fuels, 27 (2013) 1104-1122.

[8] H. Zimmermann, R. Walzl, Ethylene, in: Ullmann's Encyclopedia of Industrial Chemistry, Wiley-VCH Verlag GmbH & Co. KGaA, 2000.

[9] D.R. Chapman, Computational aerodynamics development and outlook, American Institute of Aeronautics and Astronautics Journal, 17 (1979) 1293-1313.

[10] H. Choi, P. Moin, Grid-point requirements for large eddy simulation: Chapman's estimates revisited, Physics of Fluids, 24 (2012).

[11] J.W. Rogerson, N. Swaminathan, M. Tanahashi, N. Shiwaku, Analysis of progress variable variance equations using DNS data, Third European Combustion Meeting, Chania, Crete, 2007.

[12] N. Chakraborty, N. Swaminathan, Effects of Lewis Number on Scalar Variance Transport in Premixed Flames, Flow Turbulence Combust, 87 (2011) 261-292.

[13] Y. Pei, E. Hawkes, S. Kook, A Comprehensive Study of Effects of Mixing and Chemical Kinetic Models on Predictions of n-heptane Jet Ignitions with the PDF Method, Flow Turbulence Combust, 91 (2013) 249-280.

[14] OpenFOAM - The Open Source CFD Toolbox - User's Guide, OpenCFD Ltd, United Kingdom.

[15] OpenFOAM - The Open Source CFD Toolbox - Programmer's Guide, OpenCFD Ltd, United Kingdom.

[16] I.R. Gran, B.F. Magnussen, A Numerical Study of a Bluff-Body Stabilized Diffusion Flame. Part 2. Influence of Combustion Modeling And Finite-Rate Chemistry, Combustion Science and Technology, 119 (1996) 191-217.

[17] B.F. Magnussen, B.H. Hjertager, On mathematical modeling of turbulent combustion with special emphasis on soot formation and combustion, International Symposium on Combustion, 16 (1977) 719-729.

[18] P.J.M. Reid R.C., Poling B.R., Properties of gases and liquids, McGraw-Hill, 1979.

[19] W.H. Green, J.W. Allen, R.W. Ashcraft, G.J. Beran, C.F. Goldsmith, M.R. Harper, A. Jalan, G.R. Magoon, D.M. Matheu, S. Petway, S. Raman, S. Sharma, K.M. Van Geem, J. Song, J. Wen, R.H. West, A. Wong, H.-W. Wong, P.E. Yelvington, Y. J., RMG - Reaction Mechanism Generator v3.3, 2011.

[20] C.M. Schietekat, D.J. Van Cauwenberge, K.M. Van Geem, G.B. Marin, Computational fluid dynamics-based design of finned steam cracking reactors, AIChE Journal, 60 (2014) 794-808.

[21] R.O. Fox, Computational Models for Turbulent Reacting Flows, Cambridge University Press, Camebridge, UK, 2003.

[22] C. Béguier, I. Dekeyser, B.E. Launder, Ratio of scalar and velocity dissipation time scales in shear flow turbulence, Physics of Fluids, 21 (1978) 307-310.

[23] J.P.H. Sanders, I. Gokalp, Scalar dissipation rate modelling in variable density turbulent axisymmetric jets and diffusion flames, Physics of Fluids, 10 (1998) 938-948.

[24] A. Kossiakoff, F.O. Rice, Thermal Decomposition of Hydrocarbons, Resonance Stabilization and Isomerization of Free Radicals, Journal of the American Chemical Society, 65 (1943) 590-595.

[25] F.O. Rice, The Thermal Decomposition of Organic Compounds from the Standpoint of Free Radicals. I. Saturated Hydrocarbons, Journal of the American Chemical Society, 53 (1931) 1959-1972.

[26] F.O. Rice, K.F. Herzfeld, The Thermal Decomposition of Organic Compounds from the Standpoint of Free Radicals. VI. The Mechanism of Some Chain Reactions, Journal of the American Chemical Society, 56 (1934) 284-289.

[27] R. Van de Vijver, N.M. Vandewiele, P.L. Bhoorasingh, B.L. Slakman, F. Seyedzadeh Khanshan, H.-H. Carstensen, M.-F. Reyniers, G.B. Marin, R.H. West, K.M. Van Geem, Automatic mechanism and kinetic model generation for gas-phase and solution-phase processes: a perspective on best practices, recent advances, and future challenges, International Journal of Chemical Kinetics, submitted (2014).

[28] M.K. Sabbe, F. De Vleeschouwer, M.F. Reyniers, M. Waroquier, G.B. Marin, First Principles Based Group Additive Values for the Gas Phase Standard Entropy and Heat Capacity of Hydrocarbons and Hydrocarbon Radicals, J. Phys. Chem. A, 112 (2008) 12235-12251.

[29] M.K. Sabbe, M. Saeys, M.F. Reyniers, G.B. Marin, V. Van Speybroeck, M. Waroquier, Group additive values for the gas phase standard enthalpy of formation of hydrocarbons and hydrocarbon radicals, J. Phys. Chem. A, 109 (2005) 7466-7480.

[30] F.R. Menter, Two-equation eddy-viscosity turbulence models for engineering applications, Aiaa J., 32 (1994) 1598-1605.

[31] H.S. Wilf, Mathematics for the physical sciences, Wiley, 1962.

[32] G.H. Golub, J.H. Welsch, Calculation of Gauss quadrature rules, Mathematics of Computation, 23 (1969) 221-&.

[33] A. Passalacqua, eigenSolver, 2012.

[34] B.S. Garbow, EISPACK — A package of matrix eigensystem routines, Computer Physics Communications, 7 (1974) 179-184.

[35] L. Liang, J.G. Stevens, J.T. Farrell, A Dynamic Multi-Zone Partitioning Scheme for Solving Detailed Chemical Kinetics in Reactive Flow Computations, Combustion Science and Technology, 181 (2009) 1345-1371.

[36] F. Perini, High-dimensional, unsupervised cell clustering for computationally efficient engine simulations with detailed combustion chemistry, Fuel, 106 (2013) 344-356.

[37] Y. Shi, R.P. Hessel, R.D. Reitz, An adaptive multi-grid chemistry (AMC) model for efficient simulation of HCCI and DI engine combustion, Combustion Theory and Modelling, 13 (2009) 83-104.

[38] K.M. Van Geem, M.F. Reyniers, G.B. Marin, Two severity indices for scale-up of steam cracking coils, Industrial & Engineering Chemistry Research, 44 (2005) 3402-3411.

[39] L. Redjem-Saad, M. Ould-Rouiss, G. Lauriat, Direct numerical simulation of turbulent heat transfer in pipe flows: Effect of Prandtl number, International Journal of Heat and Fluid Flow, 28 (2007) 847-861.

[40] S.V. Patankar, C.H. Liu, E.M. Sparrow, Fully developed flow and heat-transfer in ducts having streamwise-periodic variations of cross-sectional area, Journal of Heat Transfer-Transactions of the Asme, 99 (1977) 180-186.

[41] D.J. Van Cauwenberge, C.M. Schietekat, J. Floré, K.M. Van Geem, G.B. Marin, CFD-based design of 3D pyrolysis reactors: RANS vs. LES, Chemical Engineering Journal, accepted (2015).

[42] G.R. Newman, B.E. Launder, J.L. Lumley, Modeling the behavior of homogeneous scalar turbulence, Journal of Fluid Mechanics, 111 (1981) 217-232.

[43] S.E. Elghobashi, B.E. Launder, Turbulent time scales and the dissipation rate of temperature variance in the thermal mixing layer, Physics of Fluids, 26 (1983) 2415-2419.

[44] S.V. Patankar, V.S. Pratap, D.B. Spalding, Prediction of turbulent-flow in curved pipes, Journal of Fluid Mechanics, 67 (1975) 583-595.

[45] K. Sudo, M. Sumida, H. Hibara, Experimental investigation on turbulent flow through a circular-sectioned 180 degrees bend, Exp. Fluids, 28 (2000) 51-57.

[46] H. Sugiyama, D. Hitomi, Numerical analysis of developing turbulent flow in a 180° bend tube by an algebraic Reynolds stress model, International Journal for Numerical Methods in Fluids, 47 (2005) 1431-1449.

[47] G.J. Heynderickx, G.G. Cornelis, G.F. Froment, Circumferential tube skin temperature profiles in thermal cracking coils, AIChE Journal, 38 (1992) 1905-1912.

[48] G.J. Heynderickx, G.F. Froment, Simulation and comparison of the run length of an ethane cracking furnace with reactor tubes of circular and elliptical cross sections, Industrial & Engineering Chemistry Research, 37 (1998) 914-922.

Chapter 6:

Catalytic coating for reduced coke

formation

Abstract

A novel catalytic coating that converts coke to carbon oxides by reaction with steam was developed. Several coating formulations were tested in a jet stirred reactor setup and the best performing formulation was further evaluated in a pilot plant setup. Application of the coating during steam cracking of ethane at industrially relevant conditions resulted in a reduction of the asymptotic coking rate by 76 %. The coating activity remained constant over several coking/decoking cycles. Scanning electron microscope and energy diffractive X-ray analyses showed good adhesion of the coating to the base alloy even after several coking/decoking cycles. Coupled furnace-reactor run length simulations of an industrial ethane cracking unit were performed and resulted in an increase of the run length by a factor of six. However, the simulated CO_2 yield is higher than the design value of a typical caustic tower.

6.1 Introduction

Coke formation on the inner wall of the tubular reactors of steam cracking units has a negative impact on the economics of the steam cracking process. As coke is formed, the cross-sectional area of the reactor is reduced, resulting in a higher pressure drop over the reactor. This higher pressure drop results in a change in product selectivities as bimolecular reactions – often leading to the formation of aromatics – are favored over monomolecular reactions. Furthermore, the highly insulative coke layer hampers the heat transfer from the furnace to the reactors. To operate at a constant cracking severity over time, the fuel flow rate to the furnace burners has to be increased to compensate for this extra conductive heat transfer resistance. Consequently the reactor tube metal temperature rises over time. When the maximum tube metal temperature

(TMT) reaches the metallurgically maximum allowable temperature, typically 1360-1380 K, or the reactor pressure drop exceeds a predefined maximum value, operation is halted for about 48 hours and the reactors are decoked using steam or - more commonly - a steam/air mixture. As this decoking operation limits the yearly production capacity and has high operating costs, many technologies to reduce coke formation have been developed and installed commercially over the last decades. These technologies can be roughly divided into three groups: three-dimensional (3D) reactor technologies, feed additives and surface technologies. In 3D reactor technologies, the reactor tube geometry is altered from the conventional bare, straight tube to a more complex geometry to enhance convective heat transfer and/or increase heat transfer area. For example finned tubes [1-3], ribbed [4] or partially ribbed [5] tubes and swirl flow tubes [3] have been investigated. All these technologies lead to an increased pressure drop compared to conventional bare tubes and hence affect the ethene selectivity [6]. The second category is one of the most widely applied techniques to reduce coke formation. For some additives a combination of pretreatment and continuous addition is applied, while for others only continuous addition is beneficial. Sulfur-containing compounds are the most commonly applied group of additives [7-15]. The role of sulfur additives on diminishing carbon monoxide formation is well established, but their effect on coke formation is debated [16]. Besides sulfur-containing additives, components with phosphorus [16-18] and silicon [7, 19] have also been investigated. The present work belongs to the third category of surface technologies such as high performance alloys and coatings. Steam cracking reactors are typically made out of heat-resistant Fe-Ni-Cr alloys which resist coke formation by an oxide layer of chromia [20, 21]. Often aluminum and manganese are added to enhance the coking resistance of the alloys by forming a protective alumina or a

manganese chromite ($MnCr_2O_4$) spinel layer respectively [20, 21]. Alternatively, a thin layer of a coating can be deposited on the reactor base alloy surface. Distinction can be made between barrier coatings that passivate the inner wall and catalytic coatings [22] that convert coke to carbon oxides. A barrier coating pacifies the base alloy by covering the catalytically active sites, eliminating catalytic coke formation. However, the non-catalytic coke formation through a free-radical mechanism is not prevented. In contrast, catalytic coatings eliminate the base alloy catalytic coke formation by covering the original active sites and provide catalytic sites for converting radically formed coke to carbon oxides and hydrogen by reaction with steam via gasification reactions. Hence, a positive catalytic activity is added besides the elimination of the negative catalytic activity of the base alloy.

Several authors have investigated the application of barrier coatings in steam cracking reactors. Zychlinski et al. [23] tested the performance of the AlcroPlex[®] coating in an electrobalance setup. AlcroPlex[®] is an Al/Si barrier coating that is applied in a two-step chemical vapor deposition process. This coating decreases the total coke deposition up to 90 % when cracking ethane and up to 80 % when cracking naphtha compared to a reference HP 40 material. Ganser et al. [24] described the application of AlcroPlex[®] in an industrial ethane cracker. The run length of the furnace was doubled from 30 days to more than 60 days after installation of coated tubes. In addition, lower CO formation was measured and decoking operation was accomplished in less than half the normal time. After one year of installation, metallurgical analyses were performed on the coated reactor tubes. No carburization of the tubes was seen and the coating seemed essentially unchanged.

NOVA Chemicals and Kubota have developed a technology - commercialized as ANK 400 - to reduce both catalytically and radically formed coke [25, 26]. The heat resistant base alloy is separated from the process gas with a micron-sized inert manganese chromium oxide ANK 400 spinel. Application of fresh ANK 400 tubes in two ethane cracking furnaces resulted in an increase of the run length from 33 to more than 400 days. Subsequent runs had a duration of around 175 days. Westaim Surface Engineered Products developed another barrier coating, called CoatAlloy [27-29]. CoatAlloy consists of an engineered surface, an enrichment pool and diffusion barriers coated on the bulk alloy. In the original patent [30], the intermediary diffusion barrier is an aluminum-containing coating deposited directly onto the bulk alloy substrate prior to deposition of the enrichment pool. The enrichment pool is a MCrAlX material in which M is nickel, cobalt, iron or a mixture thereof and X is yttrium, hafnium, zirconium, lanthanum or a combination thereof. This enrichment pool and the bulk alloy are heat-treated to metallurgically bond the coating and to form a multiphasic microstructure. The overlay coating is then aluminized by depositing a layer of aluminum and oxidizing the resulting coating to form an alumina surface layer. Between 1995 and 2001 several improvements have been made to the technology resulting in an increased operating limit from 1293 K (Original CoatAlloy^{TM}) to 1333 K (CoatAlloy^{TM} - 1060) and 1373 K (CoatAlloy^{TM} - 1100) [29]. By 2001, CoatAlloy coatings were installed in 25 furnaces globally and typically resulted in a decrease in coking rate by about 90 % [29].

Besides the inert barrier coatings, several catalytic coatings have also been developed. The so-called Catalyzed-Assisted Manufacture of Olefins (CAMOL) coating was developed by

Quantiam Technologies and NOVA Chemicals from 2001 to 2008 and is since 2011 commercialized by BASF Qtech [22, 31]. Two families of coatings have been developed; one manganese and one tungsten based [32]. As such two products are commercially available: the Low-Catalytic Gasifier (LCG) and the High-Catalytic Gasifier (HCG) [33]. The LCG can be used for ethane-propane cracking, while the HCG coating targets at heavier feedstocks cracking such as naphthas. The coatings have been installed in an industrial naphtha cracking furnace. After three years in operation, it was found that modified start up procedures are required in order to reactivate the catalytic sites [33]. A small amount of HCG was coated on the reactors' outlet tubes. Before application of the coating, the furnace was typically limited by high outlet TMT's. However, with the help of this small amount of HCG, the furnace became pressure drop limited instead [33]. This shows that only a small amount of HCG can gasify a significant amount of coke. A sample taken from a reactor after 14 months of service showed minor damage to the coating which could be repaired after an oxidation procedure [33].

SK-corporation developed a method of on-line coating the reactor inner walls with a catalytic film, called PY-COAT [34]. The method comprises three steps of vapor depositing: a solution of a metal alkoxide and a chromic compound to form a buffer layer on the inner walls; a metal alkoxide as a barrier on the buffer layer and finally an alkali metal/alkaline earth metal compound alone or mixed with metal alkoxides as a decoking layer on the barrier. Application in a Millisecond naphtha cracking furnace more than doubled the run length.

In the following, a new catalytic coating, called YieldUp, is presented. The coating is based upon a family of ceramic catalysts having doped perovskite structures that are capable of converting coke to carbon oxides and hydrogen. The performance of different formulations of this coating

was probed in a jet stirred reactor (JSR) setup. The optimal coating formulation was further tested in a pilot plant setup. Finally, the application of the coating when scaling the JSR and pilot plant data to an industrial ethane cracker was simulated.

6.2 Experimental section

6.2.1 Coating

YieldUp consists of an engineered synthetic ceramic [35, 36]. When exposed to high temperature steam, water molecules are chemisorbed and deprotonated, resulting in the formation of highly reactive oxygen atoms that react with deposited coke to carbon oxides. A family of YieldUp catalyst materials has been developed that provides a wide range of anti-coking activities as described below. The ceramic coating was applied to the JSR coupons by forming an aqueous slurry of catalyst microparticles and other additives and dip-coating the coupons, followed by a high-temperature sintering step. The same slurry formulation was used to coat the inner surface of the reactor tubes used in the pilot plant experiments. A typical coating thickness ranges from 20 to 50 µm.

6.2.2 Jet stirred reactor

As the jet stirred reactor setup has been extensively described by Muñoz Gandarillas et al. [20, 21], only a brief description is given here. The setup consists out of three parts: a feed section, a reactor section and an analysis section. The feed section controls the mass flow rates of gases and water by thermal mass flow controllers, vaporizes water to steam in an evaporator, mixes the steam with the hydrocarbon feedstock and heats the mixture to the reactor inlet temperature of 903 K. The reaction section is a jet stirred reactor made out of quartz. Inside the reactor, a small,

flat coupon is suspended from an electrobalance. The coupon mass is tracked over time and increases as coke deposits on the coupon. In the analysis section, the reactor effluent is first quenched to prevent further cracking. Afterwards, the reactor effluent composition is measured with two gas chromatographs (GC) using nitrogen as internal standard: a refinery gas analyzer dedicated to the analysis of components with less than 5 carbon atoms and a TRACE^{TM} Ultra GC detecting hydrocarbons ranging from methane to naphthalene.

6.2.3 **Experimental procedures and conditions in the jet stirred reactor**

Similar operating procedures and conditions were used as described by Muñoz Gandarillas et al. [20] and hence, only a brief description is given here. The experiments consisted of three cycles of a 6 h cracking step and a decoking step and one cycle of a 12 h pre-oxidation step and a 2 h cracking step. Afterwards, the coupons were removed for Scanning electron microscope (SEM) and energy dispersive X-ray (EDX) analyses. Before the first cycle, a pre-oxidation step is performed. In the pre-oxidation step, the coupon is oxidized in the reactor to have a surface state similar to the start-of-run surface state of an industrial reactor. First, the reactor temperature is raised from room temperature to 1023 K under a constant $6.7 \cdot 10^{-3}$ Nl s^{-1} nitrogen flow. Afterwards, the feed is switched to air to oxidize the coupon. No presulfidation of the coupon was performed. After 12 h of oxidation, the feed is switched back to nitrogen and the reactor temperature is increased to 1283 K. During heating, $11.0 \cdot 10^{-6}$ kg s^{-1} of a water/dimethyl disulfide (DMDS) solution and 0.0275 Nl s^{-1} ethane are send to the evaporators and vented in order to get a steady evaporation and mixing. DMDS was dissolved in water to have a continuous addition of $50 \cdot 10^{-6}$ kg DMDS/kg ethane which is common practice in industrial crackers to limit

the formation of carbon oxides. Once the set reactor temperature is reached, the cracking mixture is sent to the reactor. The reactor temperature is controlled throughout the cracking runs at 1159 K, a value that is reached 5 min after introduction of the cracking mixture in the reactor. After the 6 or 2 h of cracking, the reactor temperature is set to 1173 K and the flow rate of ethane and steam is set to zero, leaving only nitrogen to purge the reactor. Once this temperature is reached, the reactor is cooled down to 1023 K with a steam flow rate of $6.7 \cdot 10^{-6}$ kg s^{-1}. Once that temperature is reached, a mixture of air ($8.3 \cdot 10^{-3}$ Nl/s) and nitrogen ($8.3 \cdot 10^{-3}$ Nl/s) is fed to the reactor. During the decoking step, the reactor is heated to 1173 K using a heating ramp of 300 K/h. As soon as the reactor reaches 1173 K, the air flow is maintained, but the nitrogen flow is switched off to mimic industrial decoking practice. These conditions are kept for 15 minutes and then the feed to the reactor is switched back to nitrogen ($6.7 \cdot 10^{-3}$ Nl/s) only. In the fourth cycle, i.e. after 2 h of cracking, the coupon was not decoked, but removed from the reactor for analysis after cooling down the reactor to room temperature with a nitrogen flow rate of $6.7 \cdot 10^{-3}$ Nl/s.

6.2.4 **Pilot plant setup**

A schematic representation of the pilot plant is shown in Figure 6-1. Since the main parts of this unit, the analytical equipment and the calibration procedure have been described previously by Wang et al. [8], Dhuyvetter et al. [10] Van Geem et al. [37], Pyl et al. [38, 39] and Dijkmans et al. [40] , only a short description is given here. Similar to the JSR setup, the pilot plant setup has three main sections; the feed section, the reaction section and the analysis section. In the feed section, the flow rate of the different feedstocks to the reactor is controlled by CORI-FLOW$^{®}$ pumps. Ethane, air and nitrogen are fed directly from the gas bottle, while demineralized water is fed from an intermediate storage vessel. The reactor is mounted in a furnace of about 4 m long,

0.7 m wide and 2.6 m high. The furnace is wall fired with ninety premixed gas burners distributed over the two side walls. The furnace is divided into seven separate cells by means of brick walls inside the furnace. The seven cells can be fired independently to set a temperature profile along the reactor axial coordinate. Twenty thermocouples and eight manometers along the reactor measure the temperature and pressure of the process gas. The reaction section of the reactor tube, i.e. where the process gas temperature is above 823 K, is about 12 m long and has an internal diameter of 9 mm. Just downstream the furnace, a sample is taken for the on-line C_5^+ analysis. Next, the effluent is cooled in a double pipe heat exchanger using oil as coolant. The condensate and tars are removed from the oil cooler effluent with a knock-out vessel and a cyclone. A fraction of the gaseous effluent of the cyclone is withdrawn for on-line C_4^- analysis, while the rest is sent directly to the flare. Nitrogen is added before the C_4^- analysis to be used as internal standard. The reactor outlet pressure is regulated by a control valve. As steam is not measured on any gas chromatograph and as it cannot be considered an inert because of the high carbon oxides and hydrogen yields, normalization was performed based on the carbon balance instead of the total mass balance.
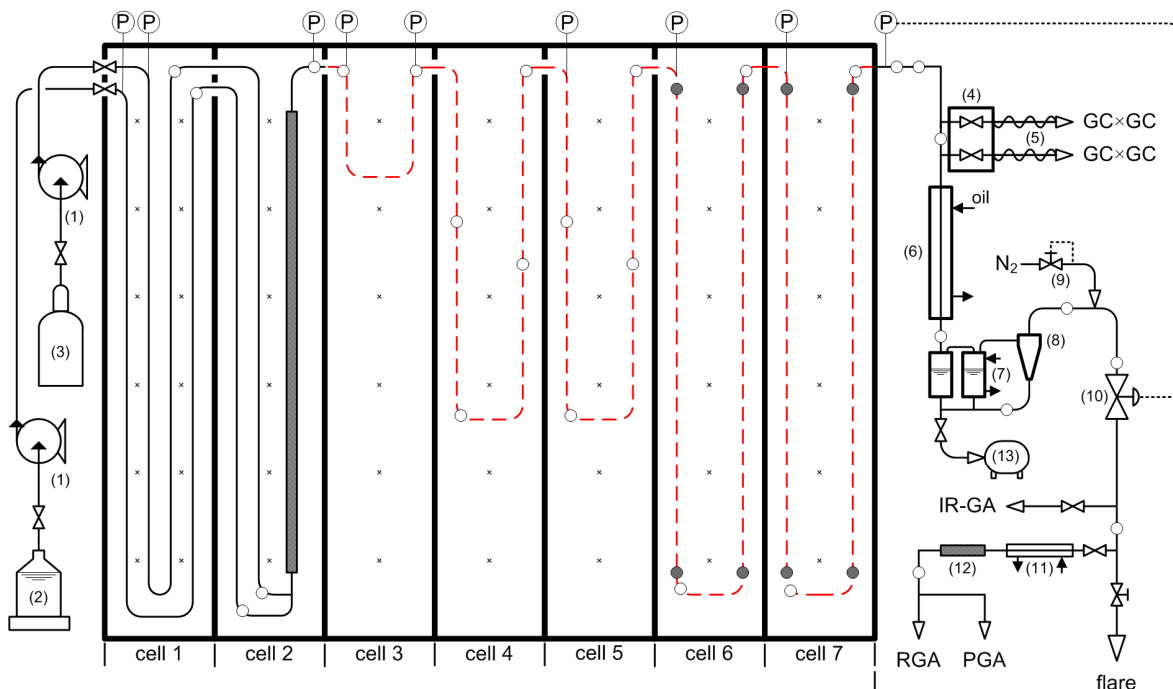
Figure 6-1: Schematic overview [37] of the pilot plant setup indicating the process gas temperature (○), reactor outer wall temperature (●) and process gas pressure (P) measurements (1: Mass flow controllers, 2: demineralized water reservoir, 3: gas bottles, 4: sampling oven at 300°C, 5: heated transfer lines at 300°C, 6: oil cooled heat exchanger, 7: water cooled condenser, 8: cyclone, 9: nitrogen internal standard addition, 10: outlet pressure control valve, 11: water cooled heat exchanger, 12: gypsum dryer).

6.2.5 **Experimental procedures and conditions in the pilot plant setup**

The experiments carried out in the pilot plant consisted of the same three main steps as the JSR experiments; pre-oxidation, cracking and decoking. The process conditions of all three step are summarized in Table 6-1. Prior to a cracking experiment, the reactor was pre-oxidized with a steam/air mixture. After 2 hours of pre-oxidation, nitrogen is fed to the reactor and the desired cracking temperature profile is set. Once the temperature profile is reached, the flow rates of steam, ethane and nitrogen are set. Upon the introduction of hydrocarbons, the process gas

temperature decreases by about 20 K due to the endothermic cracking reactions. After about 20 minutes the set temperature profile is again reached. In the experiments where continuous DMDS addition was applied, the DMDS was added in the water feed barrel to provide the desired concentration. The tubing connecting the water barrel to the reactor was treated with Restek's Sulfinert® coating to avoid adsorption of DMDS on the tubing inner walls. After 6 hours of cracking, the flow rate of the cracking mixture is set to zero, nitrogen is fed to the reactor and the temperatures of cell 4 to 7 are set to 1023 K. Once this new temperature profile is reached, a steam/air mixture is used to decoke the reactor. During decoking, the CO and CO_2 concentrations in the reactor effluent are continuously measured by means of an infrared meter. From these values and the measured effluent flow rate, the coke burned from the reactor wall is determined. When the molar CO_2 concentration of the effluent drops below 1 mol %, the temperatures of cell 4 to 7 are increased to 1073 K. When the concentration of CO_2 in the effluent is lower than 0.1 mol %, the nitrogen flow is stopped and only air is used. Furthermore, a filter is installed in the condensers after the reactor, where entrained coke is collected. After each experiment, this collected coke is dried and weighed. The reported coke values are the sum of burned and entrained coke. In total six pilot plant experiments were performed, referred to as INC, YieldUp, NO S, PRES, DIL1 and DIL2. In the INC experiment an uncoated Incoloy 800HT reactor was used. In all other experiments, the inner wall of the reactor was coated with YieldUp1 from cell 3 to 7 as indicated by the red, dashed line in Figure 6-1. Although the same temperature profile shown in Table 6-1 was used in all experiments, the mass flow rates were altered to study the effect of dilution and DMDS addition on the coating performance. The process conditions of all experiments are summarized in Table 6-3. INC and YieldUp serve as the reference cases using an

uncoated and coated reactor respectively. In these experiments, ethane was cracked at a flow rate of $8.333 \cdot 10^{-4}$ kg/s, a steam dilution of 0.385 kg steam/kg ethane and a continuous sulfur addition of $50 \cdot 10^{-6}$ kg DMDS/kg ethane. In experiment NO S, the effect of DMDS addition was tested by not adding any DMDS. It is noted that this experiment was performed first not to influence the results by the memory effect of sulfur on the coil from previous experiments as reported by Tong et al. [41]. In experiment PRES, the effect of DMDS presulfiding was assessed. Presulfiding was performed after pre-oxidation using a $750 \cdot 10^{-6}$ kg DMDS/kg water mixture at a flow rate of $1.111 \cdot 10^{-3}$ kg/s for 1 hour. In DIL1, the effect of lower steam partial pressure was investigated. The steam mass flow rate was halved to $0.161 \cdot 10^{-3}$ kg/s and nitrogen was added to provide the same molar dilution. In DIL2, the effect of lower total dilution was investigated by reducing the dilution to 0.1925 kg steam/kg ethane. To maintain the same total molar inlet flow rate, the ethane and steam flow rate were scaled to $1.036 \cdot 10^{-3}$ and $0.199 \cdot 10^{-3}$ kg/s respectively.

Table 6-1: Process conditions of the pre-oxidation, pre-sulfidation, cracking and decoking step during a pilot plant experiment.

	Pre-oxidation	Pre-sulfidation		Cracking		Decoking			
		Pre-start	Start	Pre-start	Start*	Pre-start	Start	CO_2<1vol%	CO_2<0.1vol%
Mass flow rate [g/s]									
Steam	0.278	1.111	1.111	0.0	0.321	0.280	0.280	0.280	0.0
Air	0.278	0.0	0.0	0.0	0.0	0.0	0.230	0.230	0.230
Ethane	0.0	0.0	0.0	0.0	0.833	0.0	0.0	0.0	0.0
Nitrogen	0.0	0.0	0.0	0.833	0.0	0.230	0.0	0.0	0.0
Dimethyl disulfide	0.0	0.0	$8.333 \cdot 10^{-4}$	0.0	$4.165 \cdot 10^{-5}$	0.0	0.0	0.0	0.0
Temperature profile [K]									
COT cell 1	773	773		773		773	773	773	773
COT cell 2	823	773		823		823	823	823	823
COT cell 3	1073	903		1023		1023	1023	1023	1023
COT cell 4	1073	1023		1063		1073	1073	1123	1123
COT cell 5	1073	1093		1093		1073	1073	1123	1123
COT cell 6	1073	1133		1113		1073	1073	1123	1123
COT cell 7	1073	1143		1128		1073	1073	1123	1123

*Flow rates of YieldUp and INC experiment, for other experiments see Table 6-3.

6.3 Experimental results and discussion

6.3.1 **Jet stirred reactor**

6.3.1.1 Product yields and coking rates

The effect of applying the YieldUp catalytic coating on product yields and coke formation was assessed in the JSR setup. To this end three coupons coated with a different YieldUp formulation were tested and compared to a reference Incoloy 800HT coupon. The process conditions, product yields and coking results are shown in Table 6-2. The conversion of ethane amounted to about 70 wt% and the yields of ethene and propene were about 50.5 wt% and 0.78 wt% respectively. The yields of hydrogen and carbon oxides increased by application of the YieldUp1 formulation. The yields of other components are not influenced by the coating as differences are within the experimental error. The amount of coke deposited on the coupon was significantly decreased in all cycles by application of all coating formulations compared to the reference Incoloy 800HT alloy. For the first cycle coke reductions of 87, 74 and 73 % were obtained compared to the Incoloy 800HT alloy for the YieldUp1, YieldUp2 and YieldUp3 formulation respectively. The lower amount of deposited coke results in higher carbon oxides and hydrogen yields in the YieldUp1 experiment as part of the coke formed on the coating is gasified. This holds to a lesser extent for YieldUp2 and YieldUp3 as for these coating formulations less coke if gasified.

Table 6-2: Process conditions, product yields and coking results of ethane cracking in the JSR.

Coupons	Incoloy 800HT	YieldUp1	YieldUp2	YieldUp3
Temperature [K]	1159	1159	1159	1159
Ethane flow rate [kg/s]	$3.63 \cdot 10^{-6}$	$3.63 \cdot 10^{-6}$	$3.63 \cdot 10^{-6}$	$3.63 \cdot 10^{-6}$
Steam flow rate [kg/s]	$11.0 \cdot 10^{-6}$	$11.0 \cdot 10^{-6}$	$11.0 \cdot 10^{-6}$	$11.0 \cdot 10^{-6}$
Dilution [kg/kg]	0.33	0.33	0.33	0.33
Conversion [wt%]	69.34	70.33	69.44	69.47
Mass of coke [10^{-6} kg / 6h]				
1st cycle	39.0	5.0	10.0	10.2
2nd cycle	42.5	6.5	12.0	11.3
3rd cycle	45.0	9.0	17.2	12.6
$R_{c,init.}$ [10^{-6} kg /s/m²]				
1st cycle	22.4	2.0	5.3	5.8
2nd cycle	19.2	2.3	7.2	5.80
3rd cycle	19.1	2.4	10.2	7.70
4th cycle	19.10	4.1	5.3	5.20
$R_{c,asym.}$ [10^{-6} kg/s/m²]				
1st cycle	4.0	0.9	1.0	1.1
2nd cycle	6.1	1.2	1.9	1.5
3rd cycle	7.0	1.7	2.2	1.8
Product Yields [wt% dry]*				
H_2	4.28	4.37	4.22	4.21
CO	0.05	0.93	0.07	0.06
CO_2	0.02	0.19	0.02	0.02
CH_4	7.06	7.12	7.18	7.1
C_2H_6	30.66	29.67	30.56	30.53
C_2H_4	50.53	50.64	50.67	50.53
C_3H_8	0.11	0.11	0.12	0.11
C_3H_6	0.75	0.78	0.81	0.80
C_2H_2	1.28	1.41	1.41	1.46
$1,3-C_4H_6$	1.11	1.13	1.03	1.03
Benzene	2.42	2.37	2.34	2.33

* Product yields averaged over all cycles. Asymptotic carbon oxides and hydrogen yields reported.

The total amount of coke deposited in these 6 hours experiments depends on the respective contribution of the initial, catalytic coke formation rate and the asymptotic, free-radical coke formation rate. However, in industrial units the run length is almost solely determined by the asymptotic coke formation rate. The initial and asymptotic coking rates are depicted in Figure 6-2A and B respectively. The initial coking rate is calculated as the average coking rate between minute 15 and 30 of the cracking experiment. The first 15 min are excluded because the mass signal has to stabilize after the introduction of the cracking mixture in the reactor. The asymptotic coke formation rate is calculated as the average coking rate over the last cracking hour, when the rate stays constant over time. As the fourth cracking run only lasted 2 h, no asymptotic coking rate is reported for this cycle. The initial coking rates of all YieldUp formulations are significantly lower than for the reference Incoloy 800HT alloy. YieldUp1 performs best, while YieldUp2 and YieldUp3 show a similar initial coking rate. The initial coking rates of the coated coupons remain more or less stable over subsequent cycles, besides a small increase in the third cycle for YieldUp2 and YieldUp3. Also in the asymptotic regime, application of any of the tested YieldUp formulations is seen to reduce the coking rate. Again the YieldUp1 formulation has the best performance, showing a reduction of the asymptotic coking rate by 73, 75 and 74 % compared to the reference coupon for the 1st, 2nd and 3rd cycle respectively. This stable reduction in coking rate over multiple cycles shows that the coating retains its catalytic activity over different coking/decoking cycles.
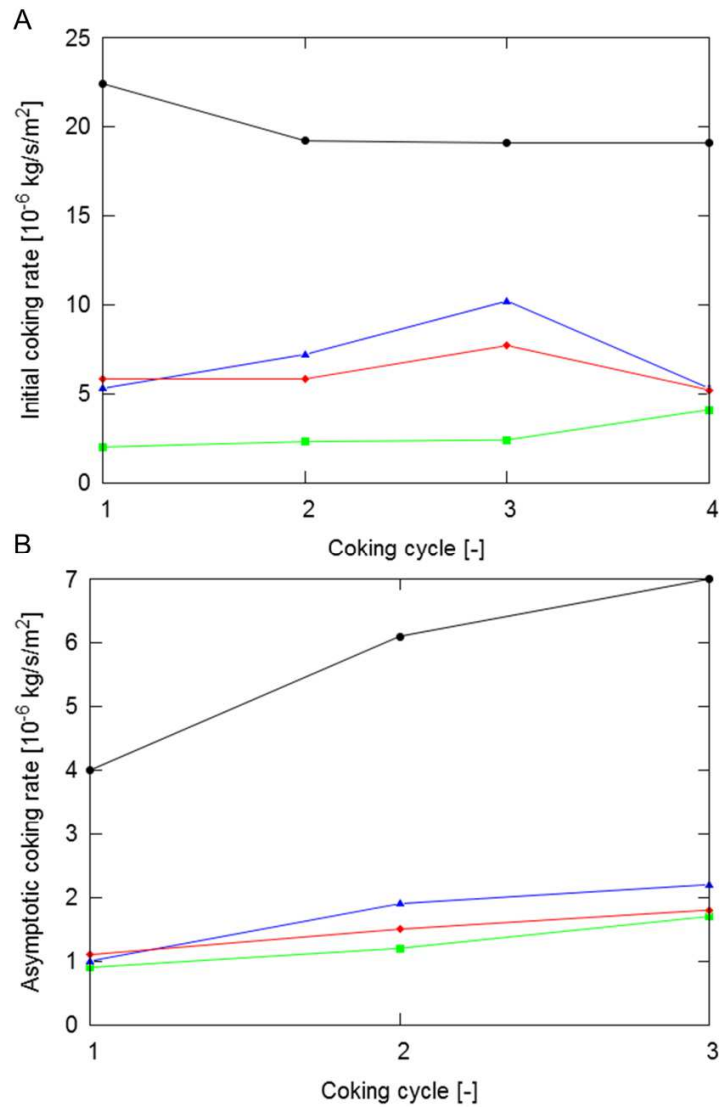
Figure 6-2: Initial coking rate [10^{-6} kg/m²/s] (A) and asymptotic coking rate [10^{-6} kg/m²/s] (B) as a function of coking cycle [-]: ●— - Incoloy 800HT; ■— - YieldUp1; ▲— - YieldUp2; ◆— - YieldUp3.

6.3.1.2   SEM and EDX analyses

Scanning electron microscope (SEM) analysis of the top surface and cross-sectional energy dispersive X-ray (EDX) line scans and element mappings have been performed on the coked coupons after the 4th coking cycle. All analyses were performed as described by Muñoz Gandarillas et al.[20].

A top view of the coked YieldUp1, YieldUp2 and YieldUp3 coupon after the fourth cycle of ethane cracking is shown in Figure 6-3A, B and C respectively. Multiple cracks are seen in the surface of the YieldUp1 coupon. This coupon had the least amount of coke deposited after 2 hours of cracking. Hence, the surface morphology of the coked sample retains many characteristics of the catalytic coating underneath because of the low coke deposition. The surface of the YieldUp2 coupon looks distinctly different with a clear coke layer covering the coating. The YieldUp3 surface shows characteristics of both YieldUp1 and YieldUp2. The amount of coke deposited is also intermediary between the two other coatings. The surface exhibits some cracks in the coke layer, fewer in number, but larger than in the YieldUp1 sample.
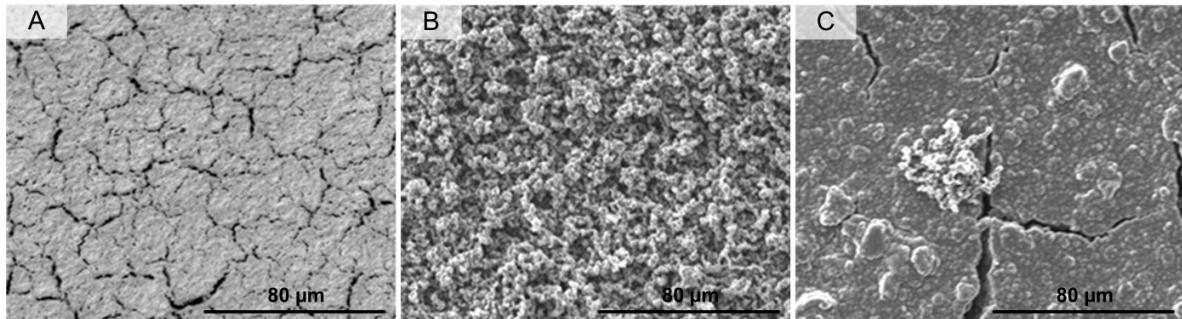
Figure 6-3: SEM images of coked surface after the fourth cracking cycle: 750×, 10 kV of: YieldUp1 (A), YieldUp2 (B) and YieldUp3 (C).

Cross-sectional cuts were made of all three coked, coated coupons and investigated with SEM, EDX line scans and elemental mappings. The cross-sectional SEM images of the three coupons are shown in Figure 6-4. Five segments can be distinguished in all three coupons; the bulk alloy, an oxide layer, the catalytic coating, the coke layer and the resin embedment used during the analysis. The oxide layer was partly present before dip-coating the coupons, but also stems from the sintering step in the manufacturing process. This step aims at increasing the adhesion of the coating to the alloy by allowing atoms to diffuse between the layers at high temperature.
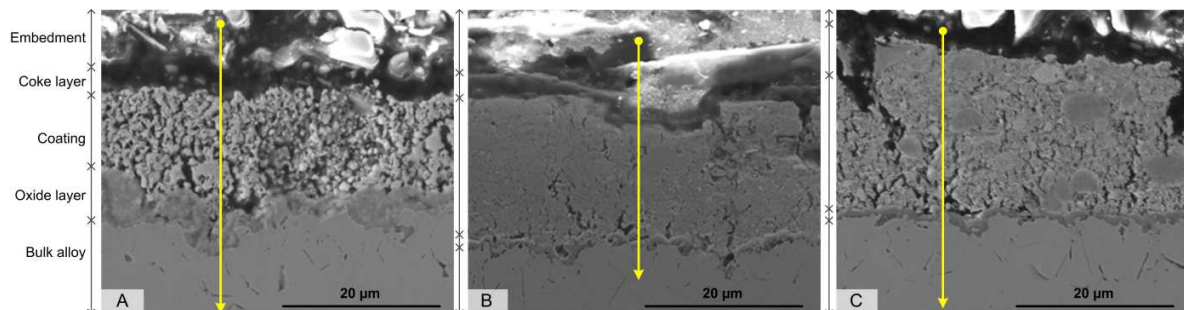
Figure 6-4: Cross sections of coked coupons of YieldUp1 (A), YieldUp2 (B) and YieldUp3 (C), arrows indicate path of EDX line scan analyses.

From Figure 6-4, the thickness and structure of the different layers can be analyzed. The YieldUp1 coating is approximately 15 µm thick and is very porous. This high surface area explains its superior activity compared to the two other coating formulations. The thickness of the oxide layer varies between 2 and 8 µm. The coke layer thickness is below 1 µm. No clear voids are seen in-between the coating, the oxide layer and the base alloy. This indicates the good adhesion between the different layers after several coking/decoking cycles and even after the thermal stresses from cooling down the coupon to room temperature. The YieldUp2 coating is 30 µm thick. The coating is less porous than YieldUp1, which can explain the lower coke gasification activity. Again the different layers are still well attached showing the stable adhesion of the coating on the bulk alloy. The oxide layer of YieldUp2 is significantly thinner, only about 2-4 µm. The thickness of the catalytic layer of YieldUp3 is about 25 µm. Some dense particles can be seen in this layer surrounded by a more porous phase. Two large cracks are seen in the catalytic layer. The left crack almost reaches the oxide layer and spalling of the coating seems imminent after more cycles. As the YieldUp3 formulation was made using a different method

than YieldUp1 and YieldUp2, this method seems inferior concerning coating adhesion. The oxide layer is similar to the layer on YieldUp2, i.e. about 2-4 µm thick.

The arrows in Figure 6-4 indicate the path of the EDX line scans. The line scan results are shown in Figure 6-5, Figure 6-6 and Figure 6-7 for YieldUp1, YieldUp2 and YieldUp3 respectively. The line scans clearly show the coating elements, i.e. barium, cerium, zirconium and oxygen, in the coating layer. The oxide layer shows some typical features of an high-alloyed centrifugal cast Ni-Cr-Fe alloy: a high presence of chromium, manganese and oxygen indicating a $MnCr_2O_4$-spinel, the presence of Si, indicating SiO_2 and an overall low presence of iron and nickel. The oxide layer also contains elements of the coating which assures a good adhesion between the coating and the oxide layer. The presence of sulfur was assessed because of the continuous addition of DMDS during cracking, but the sulfur content was found to be negligible and is therefore not shown. In all coupons, negligible presence of nickel and iron is found in the catalytic coating, showing that the oxide layer works as an efficient diffusion barrier for these elements.
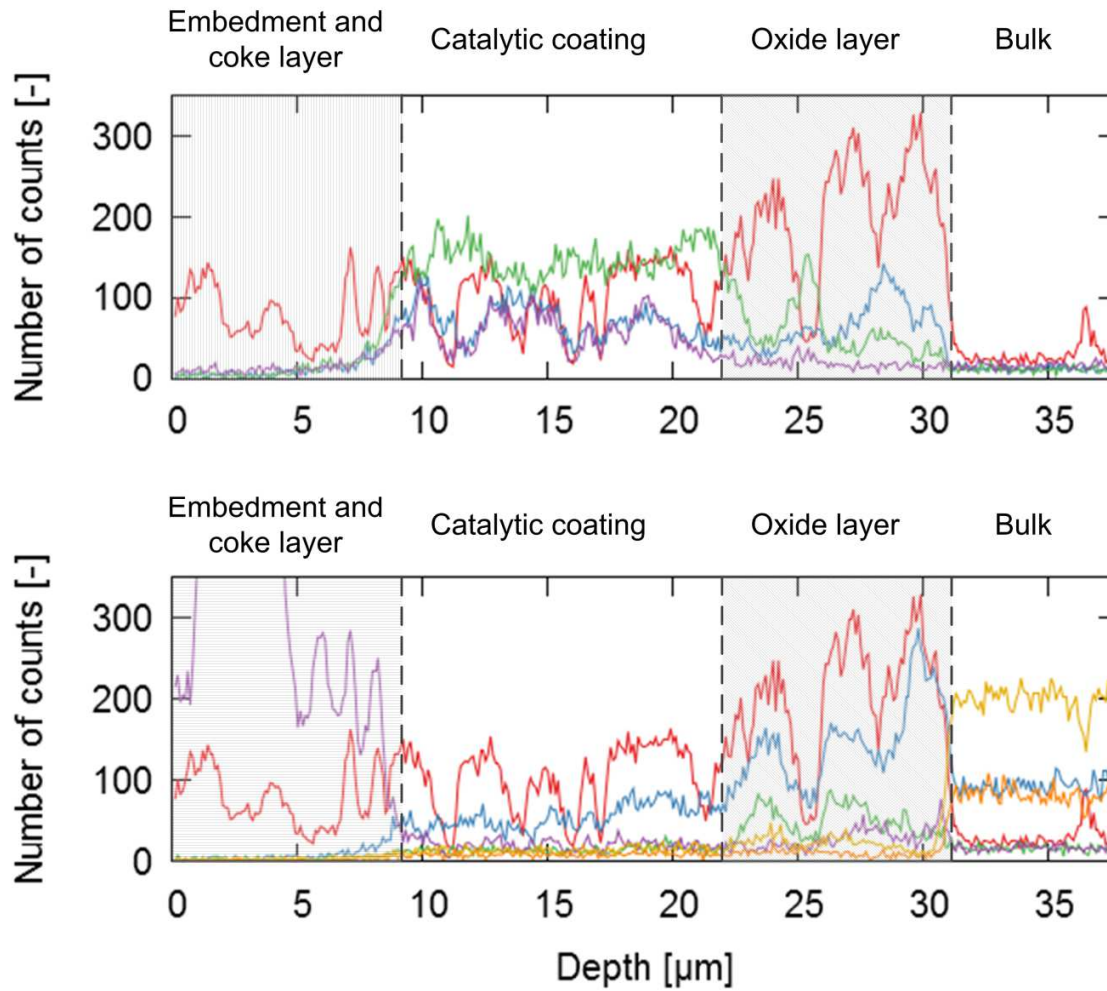
Figure 6-5: EDX line scan analysis of coked YieldUp1 coupon at 15 kV: coating elements (top): ———— - O; ———— - Ba; ———— - Ce; ———— - Zr; and base alloy elements (bottom): ———— - O; ———— - Cr; ———— - Mn; ———— - Si; ———— - Ni; ———— - Fe.
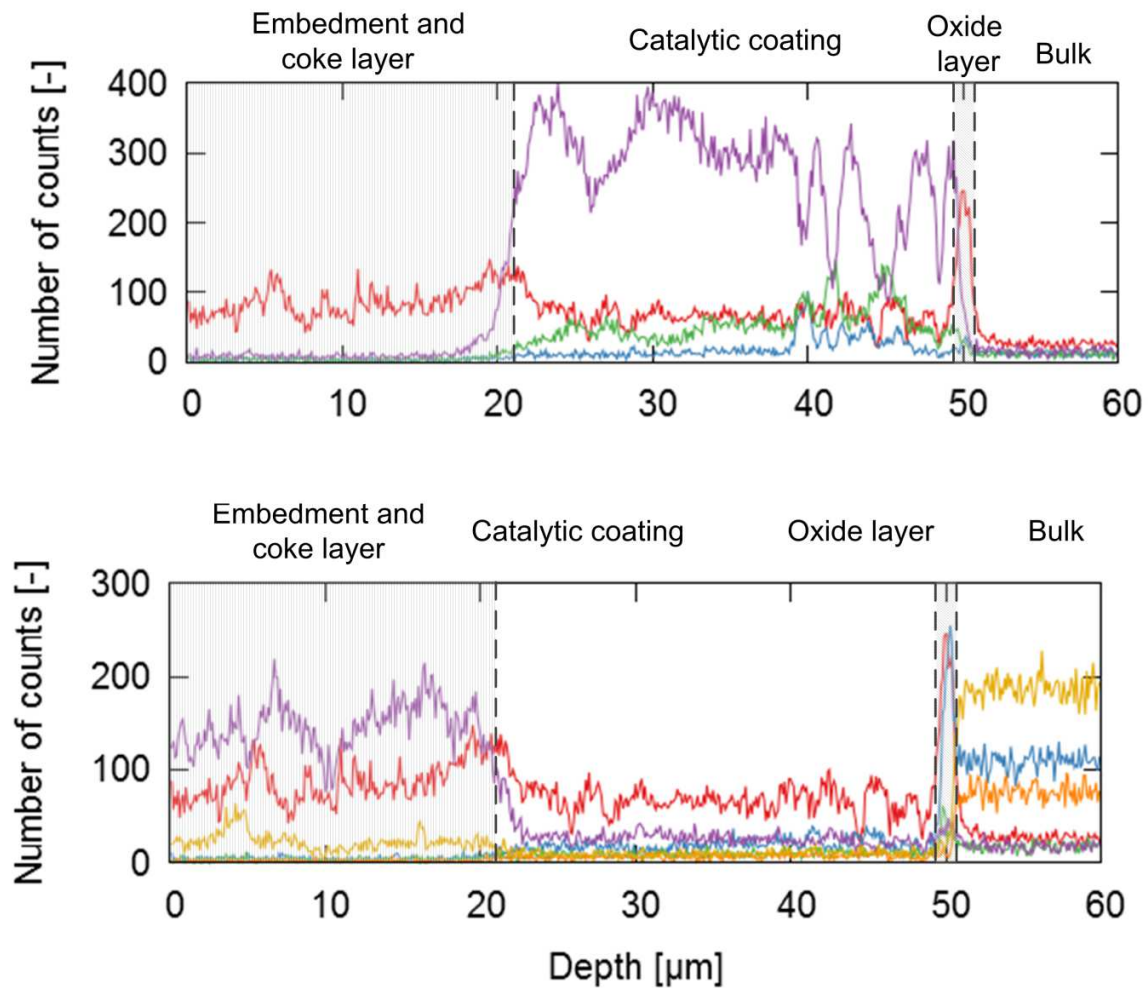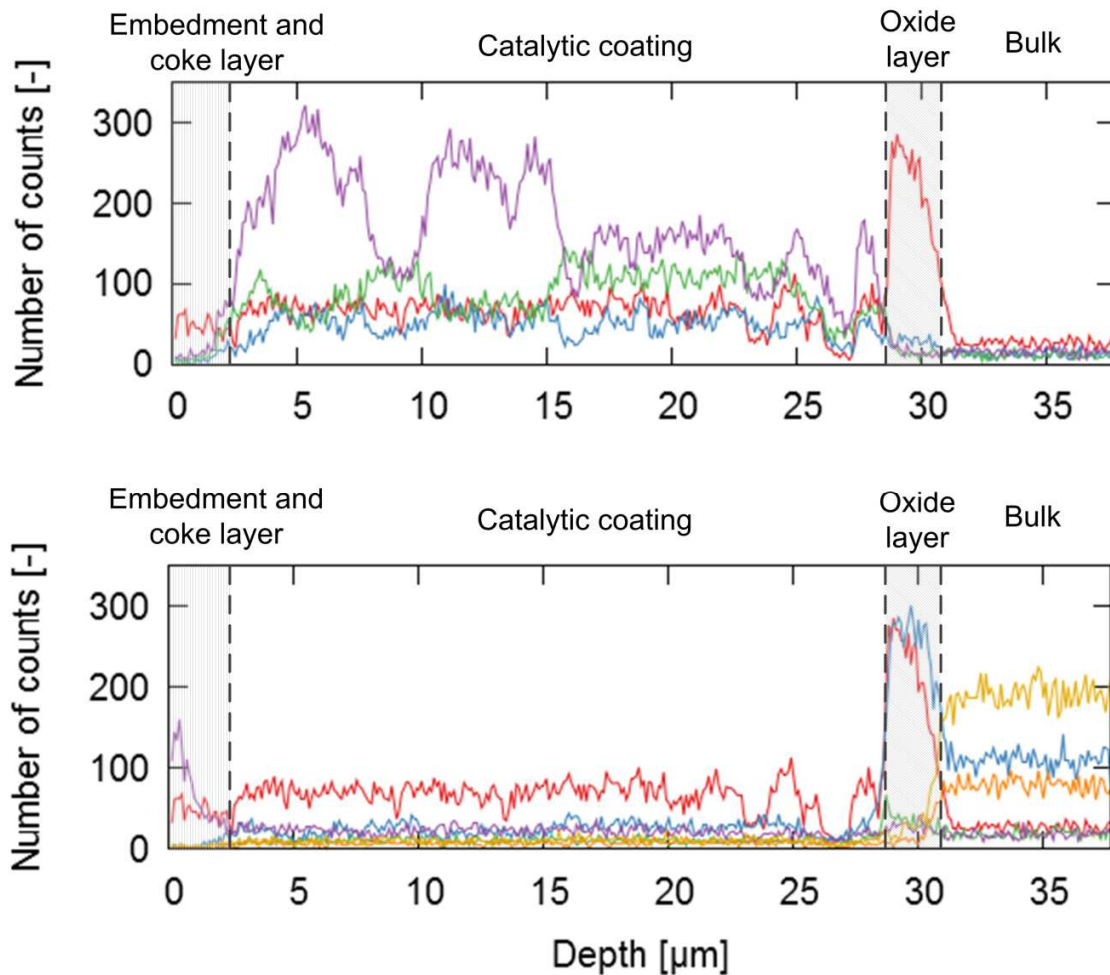
Figure 6-6: EDX line scan analysis of coked YieldUp2 coupon at 15 kV: coating elements (top): ———— - O; ———— - Ba; ———— - Ce; ———— - Zr; and base alloy elements (bottom): ———— - O; ———— - Cr; ———— - Mn; ———— - Si; ———— - Ni; ———— -Fe.

Figure 6-7: EDX line scan analysis of coked YieldUp3 coupon at 15 kV: coating elements (top): ———— **- O;** ———— **- Ba;** ———— **- Ce;** ———— **- Zr; and base alloy elements (bottom):** ———— **- O;** ———— **- Cr;** ———— **- Mn;** ———— **- Si;** ———— **- Ni;** ———— **- Fe.**

The elemental mappings of all three coupons are shown in Figure 6-8. The element mappings of YieldUp1 in Figure 6-8 show that barium, cerium and oxygen are uniformly distributed over the coating, while agglomerates of high zirconium concentration exist. Some carbon is present in the coating pores showing that the entire surface area of the coating is used for coke gasification. The

oxygen and chromium mappings show that the oxide layer covers the base alloy fully. The oxide layer acts as a good diffusion barrier as no iron and nickel are detected above the oxide layer. In the YieldUp2 formulation, more zirconium was used as also seen in the elemental mappings. Both barium and zirconium are quite uniformly dispersed over the layer, while local spots with high cerium concentration exist. The presence of carbon is lower due to the lower porosity of the coating compared to YieldUp1. Although the oxide layer is much thinner than the YieldUp1 coating, it fully covers the base alloy and prevents nickel and iron from diffusing upwards. From the zirconium mapping, it is seen that the dense phase of the YieldUp3 coating mainly consists of zirconium and lacks cerium. Again the cracks and pores are filled with carbon. The oxide layer is less continuous than with YieldUp1 and YieldUp2 as some interruptions of low oxygen content exist. Nonetheless, low iron and nickel presence is detected above the oxide layer.
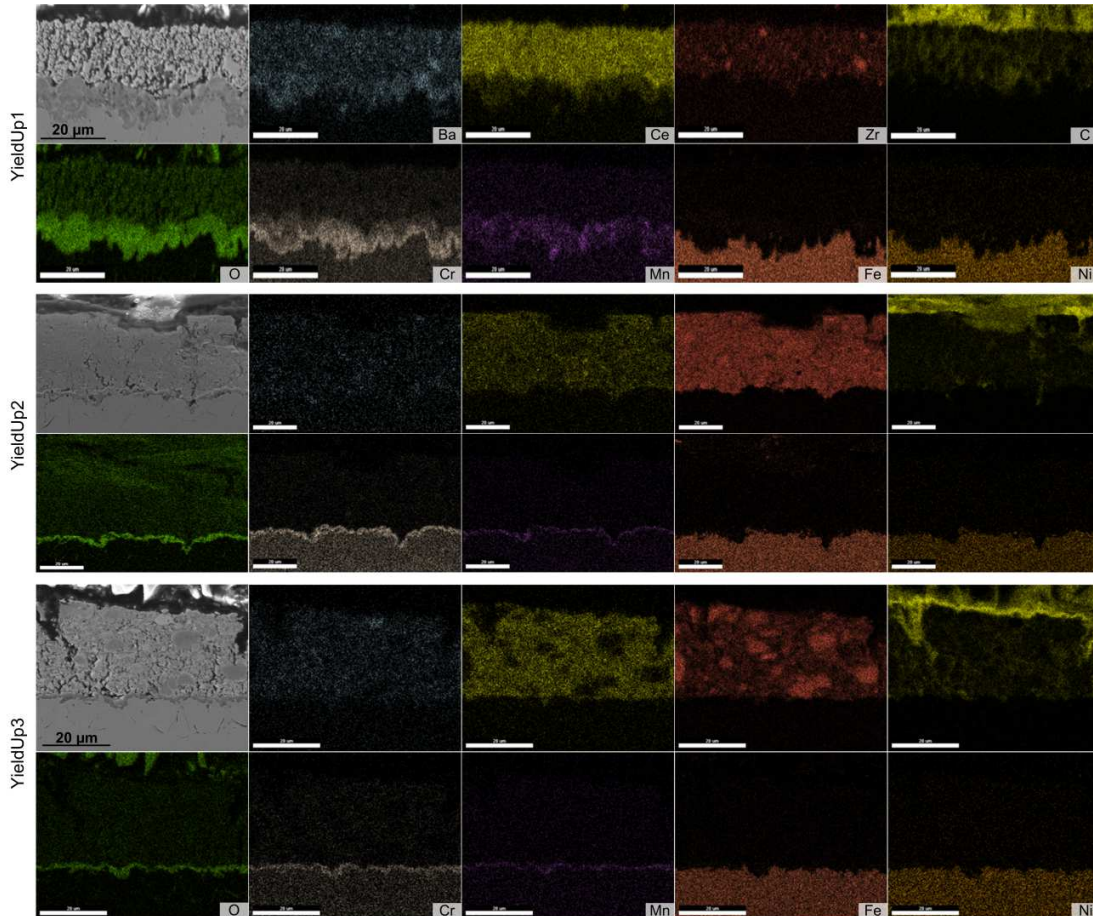
Figure 6-8: Element mappings of cross sections of coked coupons of YieldUp1 (top), YieldUp2 (middle) and YieldUp3 (bottom).

6.3.2 **Pilot plant setup**

As YieldUp1 showed the best coking resistance and a good adhesion to the base alloy during the JSR experiments, this formulation was further tested in a pilot plant setup for steam cracking. As depicted in Figure 6-1, the YieldUp1 coating was applied on the reactor inner wall from cell 3 to cell 7. Six experiments were performed evaluating the effect of sulfur addition and dilution on coking rate and product yields. The results of the pilot experiments are summarized in Table 6-3.

Table 6-3: Summary of coke and yield data of pilot plant ethane experiments.

Experiment	INC	YieldUp1	NO S	PRES	DIL1	DIL2
Process conditions						
Reactor	Incoloy	YieldUp1	YieldUp1	YieldUp1	YieldUp1	YieldUp1
Feed [10^{-3} kg/s]	0.833	0.833	0.833	0.833	0.833	1.036
H_2O flow rate [10^{-3} kg/s]	0.321	0.321	0.321	0.321	0.161	0.199
N_2 flow rate [10^{-3} kg/s]	0.000	0.000	0.000	0.000	0.249	0.000
S addition [10^{-6} kg S/ kg ethane]	50	50	0	50	50	50
H_2O/HC ratio [10^{-3} kg/s]	0.385	0.385	0.385	0.385	0.193	0.193
(H_2O+N_2)/ethane ratio [kg/kg]	0.385	0.385	0.385	0.385	0.492	0.193
(H_2O+N_2)/ethane ratio [mol/mol]	0.642	0.642	0.642	0.642	0.642	0.321
COT [K]	1128.15	1128.15	1128.15	1128.15	1128.15	1128.15
COP [bar abs]	1.7	1.7	1.7	1.7	1.7	1.7
Yields*						
$\sum$C4- [wt%]	98.9	102.4	104.7	102.6	101.2	100.8
Ethene selectivity [wt%/wt%]	80.3	80.0	78.2	79.7	79.8	80.1
Ethane conversion [wt%]	63.9	63.2	63.9	64.0	63.4	61.5
H_2	4.20	4.54	4.88	4.52	4.24	4.04
CH_4	3.72	3.48	3.65	3.58	3.67	3.59
C_2H_6	36.10	36.79	36.13	35.98	36.62	38.50
C_2H_4	51.33	50.57	49.97	51.03	50.55	49.26
1,3-C_4H_6	1.40	1.31	1.20	1.33	1.41	1.38
CO	0.01	1.75	3.72	2.03	1.65	0.99
CO_2	0.02	2.19	3.61	2.44	1.02	0.98
Net coke deposited [g coke/6h]	18.5	4.4	2.1	3.3	3.9	6.1
Gasified coke [g C/6h]	1.8	242.4	464.3	276.9	177.5	154.8
% C to coke and COx [%]	0.02	3.37	6.45	3.85	2.46	1.73

* Average over 9-13 effluent analyses per experiment. Asymptotic carbon oxides and hydrogen yields reported.

Comparing experiment INC and YieldUp1, it is seen that the amount of coke deposited was reduced 76 % by application of the YieldUp1 coating compared to the Incoloy 800HT reactor. This value corresponds well to the measured decrease of the asymptotic coking rate during the JSR experiments. Consequently, the effluent contained more hydrogen, CO and CO_2 than during the INC experiment as more coke was gasified. The increase in hydrogen and carbon oxide yields by application of the YieldUp1 coating is much higher in the pilot plant experiments than in the JSR experiments due to the higher surface-to-volume ratio of the pilot plant reactor: 5.1 m^{-1} and 444.4 m^{-1} for the JSR and pilot reactor respectively. Taking into account the small difference in conversion between the INC and YieldUp1 experiment and the experimental errors, the yield of other components is not significantly influenced by the coating. From the carbon oxides yields, the amount of coke gasified by the coating can be calculated. As seen from Table 6-3, 1.8 g of coke is gasified in the INC reference experiment, while 242.4 g of coke is gasified in the YieldUp1 experiment. Hence, 0.02 and 3.37 % of all carbon fed to the reactor is converted to coke or carbon oxides in the INC and YieldUp1 experiment respectively. This consideration shows that the coating gasifies more than the amount of coke that is normally formed on a reference alloy. This could be caused by the high surface roughness of the coating resulting in a higher coke deposition rate or the coating converting gaseous hydrocarbons to carbon oxides. It is clear that this coating formulation is too active and that more research is needed into tuning the coating activity.

The absence of continuous DMDS addition was evaluated in experiment NO S. The influence on hydrocarbon species yields is minor. The increase in CO and CO_2 yield is much more apparent;

CO increases from 1.8 to 3.7 wt% and CO_2 from 2.2 to 3.6 wt% compared to experiment YieldUp1. Hence, continuous DMDS addition can mitigate CO and CO_2 production when the coating is applied. In agreement with previous works [8, 9], the coking rate decreased without the addition of DMDS. Presulfidization of the coil with a steam/DMDS solution prior to the continuous DMDS addition was evaluated in experiment PRES. Presulfidization before continuous DMDS addition shows a coke tendency that is slightly higher than to solely continuous DMDS addition, resulting in lower carbon oxides yields. Finally, the effect of lowering the dilution was evaluated in two experiments: DIL1 and DIL2. In experiment DIL1 the steam mass flow rate was halved and nitrogen was added to remain at the same total molar flow rate to cancel out the effect of reduced hydrocarbon partial pressure on the product yields. As DMDS was continuously added, comparison is made to the YieldUp1 experiment. The yields of CO and CO_2 were lower; CO dropped from 1.8 to 1.7 wt% and CO_2 from 2.4 to 1.0 wt%. The low dilution experiment DIL1 shows a coking rate similar to YieldUp1. Hence, it seems enough water is present to convert coke to carbon oxides as in experiment YieldUp1. In experiment DIL2 the steam dilution was also halved to 0.1925 g steam/g ethane. However, no nitrogen was added in this experiment. To maintain a similar conversion, the flow rates of ethane and steam were scaled to have the same molar flow rate as in experiment YieldUp1. Lower ethane conversion and resulting lower olefin yields were measured. The CO and CO_2 yields decreased to 0.99 and 0.98 wt% respectively. In experiment DIL2 a higher coking rate was measured compared to YieldUp1. Higher coke formation is expected due to higher hydrocarbons partial pressure and the coating converting less coke to CO and CO_2 due to the lower steam partial pressure. However, comparing with the INC experiment, a decrease in coking rate by 67 % is still obtained while

increasing the ethane throughput by 24 %. This experiment shows that besides obtaining longer run lengths, also higher production capacity can be obtained by application of the coating.

6.4 Simulation of an industrial ethane steam cracking unit

6.4.1 Furnace and reactor model

The reactor simulations were performed using the in-house developed COILSIM1D program. This program applies the plug flow assumption and solves the resulting one-dimensional continuity, momentum and energy equations. As COILSIM1D has been described in detail by Van Geem et al. [42] and Pyl et al. [38], only the modifications made to model the effect of the coating on product yields and coking rate are discussed here.

As by application of the coating the hydrogen and carbon oxides yields are strongly influenced, the effect of coking and gasification reactions on the product yields is explicitly modeled. The net amount of coke deposited depends on two terms; coke formation and subsequent coke gasification. Coke formation is modeled using the coke model of Plehiers [43] which uses ethene and propene as coke precursors. Gasification was modeled using the following reactions:

$$C + H_2O \rightarrow CO + H_2$$

$$C + 2H_2O \rightarrow CO_2 + 2H_2$$
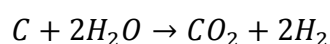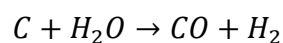
Two sets of Arrhenius parameters for the gas-solid reactions were used to model the coated and the uncoated reactor respectively. For the uncoated reactor case, the original model parameters of the model of Plehiers were used. The activation energy of the gasification reactions was taken

from Bennet and Price [44] while the pre-exponential factors were fitted to the carbon oxide yields during pilot plant experiment INC. For the coated reactor case, the pre-exponential factors of the coke-forming reactions of the Plehiers model were fitted to the coking rate of the pilot experiment YieldUp. The pre-exponential factors can be different by application of the coating as the surface roughness is different from the reference alloy surface roughness. The original activation energies were used as the activation energy is independent of the reactor inner wall material. Indeed, the asymptotic coking rate is modeled where the active sites are radical sites of the coke layer. The activation energies of the gasification reactions were determined from a thermo gravimetric analysis based on the results of Wang et al. [35]. The obtained activation energy for gasification on the coating is 196.343 kJ/mol which is as expected significantly lower than the value of 238.290 kJ/mol reported by Bennet and Price [44] without catalytic activity. The reactions and kinetics for the coke gasification are rather global and approximate. Further improvement of the simulation results is possible by implementation of a single-event microkinetic model. This was considered outside the scope of this work as it requires additional experiments to elucidate the occurring elementary reactions and to quantify the accompanying kinetic and thermodynamic parameters.

By including gas-solid reactions, the right-hand side of the transport equation of species j has two terms describing the gas-phase and gas-solid reactions respectively:

$$\frac{dF_j}{\Omega dz} = \left(\sum_{i=1}^{nreac_f} \alpha_{i,j} r_{f,i} \right) + a_v \left(\sum_{k=1}^{nreac_s} \alpha_{k,j} r_{s,k} \right) \tag{6.1}$$

with a_v the surface area of the coke layer in an axial increment dz:

$$a_v = \frac{4\pi(d_{int} - 2d_C)dz}{\pi(d_{int} - 2d_C)^2 dz} = \frac{4}{(d_i - 2d_C)} \tag{6.2}$$

where d_C is a function of axial position and time. It is obvious from (6.1) that the influence of the gasification reactions on the yield of carbon oxides and hydrogen decreases as the reactor surface-to-volume ratio decreases.

For simulation of the heat transfer in the furnace, the in-house developed FURNACE code was used which applies the method of Hottel and Sarofim [45] further improved by Vercammen and Froment [46]. In this method the furnace enclosure is divided into a number of discrete surface areas and volumes that are assumed to be isothermal and to have uniform radiative properties. For each zone an energy balance is constructed and from the resulting set of equations the unknown heat fluxes and temperatures are calculated. For an elaborate discussion reference is made to previous works [43, 47-51].

Two coupled furnace-reactor run length simulations were performed according to the procedures of Plehiers et al. [43] and Heynderickx et al. [51]. Figure 6-9 shows a flow sheet of the calculation procedure of a coupled FURNACE-COILSIM1D run length simulation. As coking reactions are much slower than the gas-phase cracking reactions, pseudo-steady state is assumed, i.e. the run time is increased in a stepwise manner using a predefined time step. A time interval of 125 hours was seen to be sufficient for the considered furnace. Every time step a coupled furnace-reactor simulation is performed. The insert in Figure 6-9 shows the calculation procedure of such a coupled simulation. A coupled simulation starts with reactor simulations based on an initial guess of the heat flux profiles. These reactor simulations return new estimates for the external tube metal temperature profiles. With these updated boundary conditions, a furnace

simulation is performed, returning updated heat flux profiles to the reactors. Next, the updated heat flux profiles are used to perform new reactor simulations. This iterative approach is repeated until convergence is reached, i.e. when all furnace zone and surface temperatures change less than a threshold value of 1 K. During every time step the fuel flow rate is adjusted in an outer iteration loop to match the user-specified conversion. Once the desired conversion is obtained in time step t, the coke growth during this time step is added to the existing coke layer and a new time step is initialized. This is repeated until the user-specified maximum allowable tube metal temperature or maximum reactor pressure drop is exceeded in any reactor in the furnace.
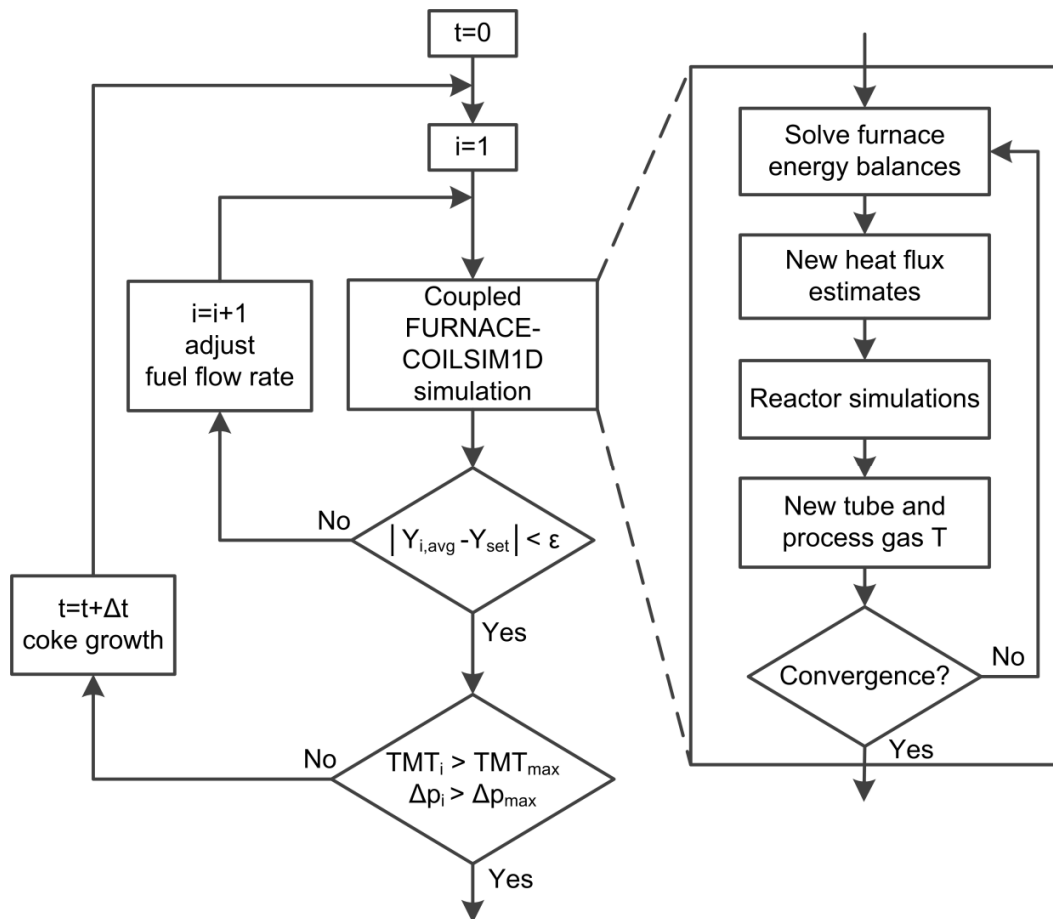
Figure 6-9: Calculation procedure of a coupled FURNACE-COILSIM1D run length simulation.

6.4.2 **Description of the industrial unit**

Figure 6-10 shows a top view of half of the rectangular furnace. Ethane is cracked in four serpentine reactors of eight passes suspended side by side in the center of the furnace. The reactors have a larger diameter in the two last passes compared to the first six. The process gas enters the reactors at both end sides and in the middle of the furnace and flows downwards. As the furnace is symmetrical, only the depicted half is simulated. The maximum allowable tube

metal temperature for the reactor alloy is 1343 K. If this temperature is exceeded, production is halted to decoke. The characteristics of the furnace, reactors and material properties are summarized in Table 6-4. In each side wall 64 radiation burners are placed. The total fuel gas flow rate for the 128 burners is adjusted over time to maintain the ethane conversion at 65 %. The air excess is 2 % compared to the stoichiometric air requirement for complete combustion. The burner cup temperature and the temperature of the flue gas entering the furnace are calculated using the method developed by Plehiers [48]. The composition of the flue gas is derived from the stoichiometry of the combustion reactions. The composition of the feed and the operating conditions of the reactor are listed in Table 6-5.

Table 6-4: Details of the simulated industrial unit.

Furnace		
Length	9.304	m
Height	13.450	m
Depth	2.100	m
Thickness refractory material	0.230	m
Thickness insulation material	0.050	m
Number of burners	128	-
Reactors		
Number of reactors	4	-
Type	serpentine coils	-
# passes	8	-
Total length	100.960	m
Internal diameter		
pass 1-6	0.124	m
pass 7-8	0.136	m
External diameter		
pass 1-6	0.140	m
pass 7-8	0.153	m
Tube wall thickness	0.008	m

Table 6-5: Feedstock composition and operating conditions of the reactor coils.

Composition of the feed		
Ethane	100.0	wt%
Reactor operating conditions		
Total hydrocarbon flow	3.889	kg s^{-1}
Inlet temperature	873.15	K
COP	182385	Pa abs
Steam dilution	0.35	kg steam/kg ethane
Ethane conversion	65	wt%
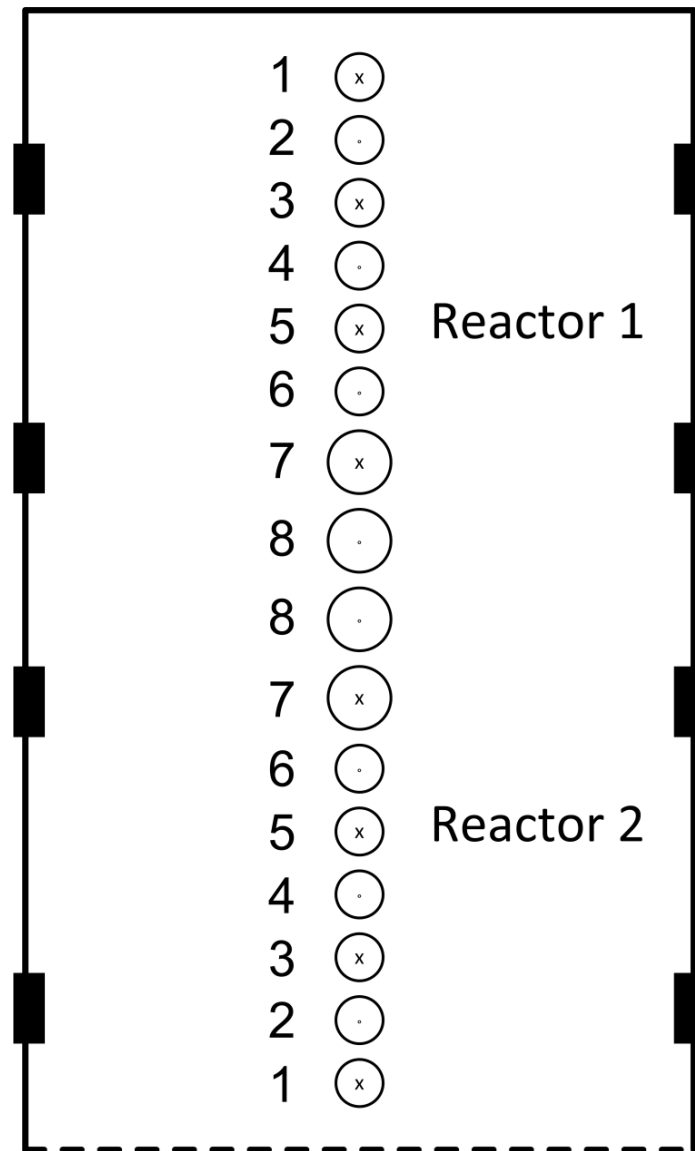
Figure 6-10: Top view of half of the furnace: ■ - burner location; ⊗ - pass with downward flowing process gas; ◯ - pass with upward flowing process gas; —— - refractory wall, ▬ ▬ - symmetry plane.

6.4.3 **Simulation results**

The maximum external tube metal temperature as a function of runtime is shown in Figure 6-11. The maximum allowable temperature of 1343 K is surpassed after 42 and 260 days for the uncoated and coated case respectively. An increase in runlength by more than 525 % can be obtained by application of the coating. Assuming 24h for a decoking operation of the furnace, 8.5 and 1.4 cracking/decoking cycles are possible within 1 year of operation. Hence, by application of the coating 8.5 – 1.4 = 7.1 extra days of production are available per year. Moreover the lower energy input needed on a yearly basis due to a reduction of the number of decoking operations will influence the cracker economics beneficially.
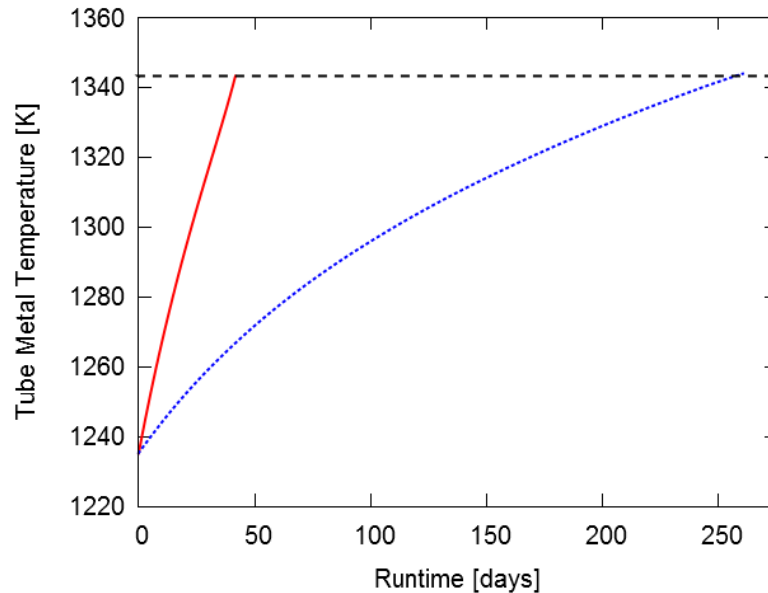
Figure 6-11: Maximum external tube metal temperature [K] as a function of runtime [days]: ▬▬▬ **-**
uncoated and ┄┄┄┄ **- coated case**

Table 6-6 summarizes the main results and process conditions at start-of-run (SOR) and end-of-run (EOR). The carbon monoxide yield increases from 13 ppmw to 216 ppmw by application of the coating. The carbon dioxide yield increases from 13 ppmw to 344 ppmw. This increase in carbon oxide yields is significantly less than in the pilot plant experiments due to the lower surface-area-to-volume ratio in industrial reactors compared to the pilot plant reactor. Typical maximum allowable yields for downstream units are about 1000-2000 ppmw and 150-200 ppmw for CO and CO_2 respectively. Hence, the carbon dioxide yield is too high and a less active coating should be applied to comply carbon dioxide specifications. More research is thus needed towards elucidating the occurring elementary reactions on the coating to further tune the coating activity.

Table 6-6: Simulation results* for the uncoated and coated case at start-of-run (SOR) and end-of-run (EOR) conditions.

	Uncoated		Coated	
	SOR	**EOR**	**SOR**	**EOR**
Coil-inlet pressure [kPa abs]	307	367	307	363
Coil-outlet-temperature [K]	1127	1131	1127	1129.88
Residence time [s]	0.67	0.69	0.67	0.72
Maximum tube temperature [K]	1235	1343	1235	1344
Maximum coke thickness [mm]	0.0	13.9	0.0	17.4
Ethane conversion [%]	65.8	65.8	65.8	65.8
Runlength [days]	42		260	
Yields [wt%]				
H_2	3.75	3.68	3.75	3.67
CH_4	5.43	6.00	5.44	6.24
CO	0.001	0.001	0.02	0.02
CO_2	0.001	0.001	0.03	0.03
C_2H_2	0.39	0.37	0.27	0.34
C_2H_4	51.39	50.48	51.38	49.95
C_2H_6	34.22	34.21	34.17	34.22
C_3H_6	1.04	1.15	1.04	1.19
C_3H_8	0.19	0.21	0.19	0.21
$1,3\text{-}C_4H_6$	1.52	1.57	1.53	1.61
$n\text{-}C_4H_{10}$	0.44	0.44	0.44	0.45
Benzene	0.58	0.71	0.58	0.80

*All reactor-related results are averaged over the two reactors.

From Table 6-6, it is seen that the ethene selectivity decreases more severely over the runlength in the coated case compared to the uncoated case. The process gas pressure as a function of reactor axial position is shown in Figure 6-12A. The total reactor pressure drop is similar for the coated and uncoated cases at EOR conditions. However, a larger pressure drop occurs at the end of the reactor in the coated case. As ethene concentration is high towards the end of the reactor,

more ethene is converted by bimolecular reactions in the coated case compared to the uncoated case. This higher pressure drop at the end of the reactor is caused by the thicker coke layer as evidenced by Figure 6-12B. In the coated case relatively more coke is formed towards the end of the reactor as the coke/gas interface temperature is higher here. The activation energy of the gasification reactions is lower than the activation energy of the coking reactions, leading to a relatively higher net coke deposition at higher temperatures, i.e. at the end of the reactor. The higher loss in ethene selectivity over the runlength could be solved by applying a coating activity profile along the reactor axial position, e.g. a more active coating in the last two passes.
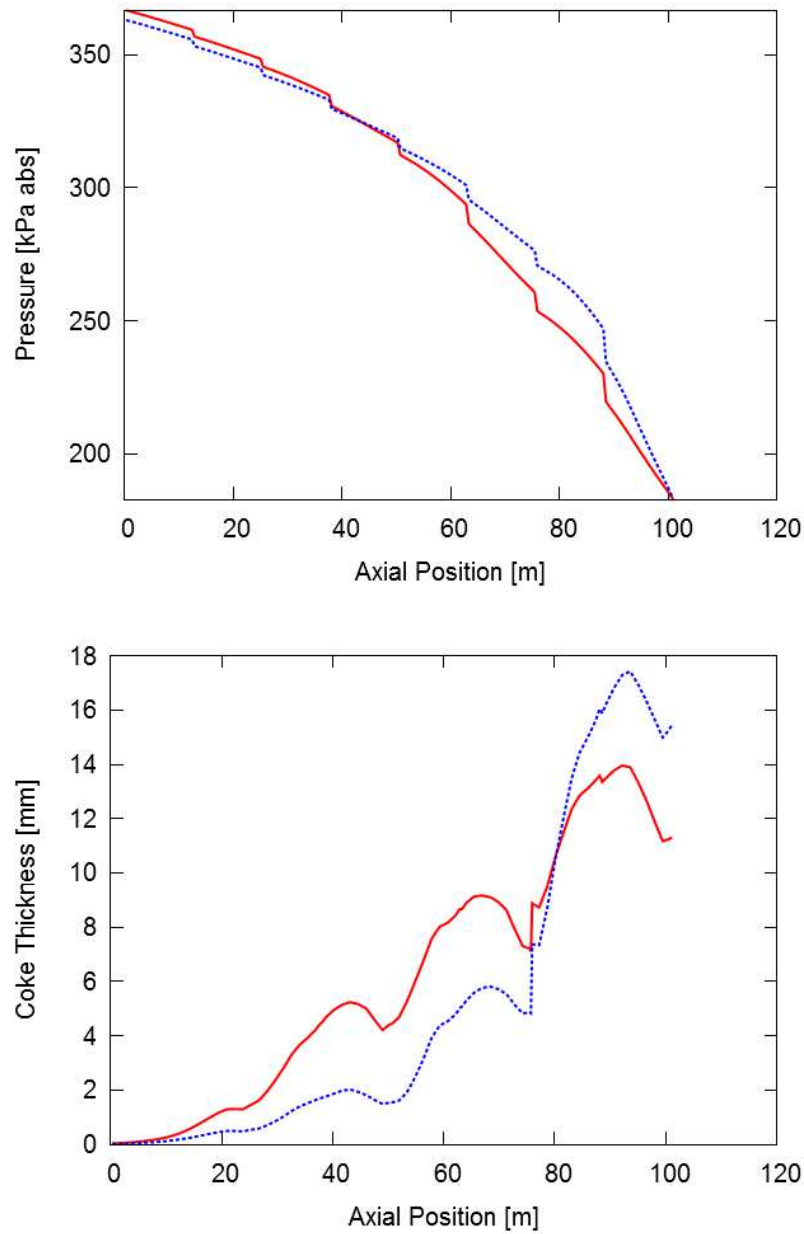
Figure 6-12: Pressure [kPa abs] (A) and coke thickness [mm] (B) at end-of-run conditions as a function of reactor axial position [m] : ────── **- uncoated and** ∙∙∙∙∙∙∙∙∙∙ **- coated case.**

6.5 Conclusions

A novel catalytic coating, called YieldUp, that gasifies coke to carbon oxides by reaction with steam, was developed for application on the inner wall of steam cracking reactors. Three coating formulations were tested in a jet-stirred reactor setup and subsequently analyzed with SEM and EDX. All three formulations showed drastically reduced coking rates over multiple coking/decoking cycles compared to a reference alloy. SEM analyses of the coked coupons showed that for two coating formulations, the coating stays well attached to the base alloy over multiple coking/decoking cycles. The best performing formulation in terms of coking resistance was further tested in a pilot plant setup. Coke formation was reduced by 76 % compared to the reference alloy reactor. Experiments at lower dilution showed that an increase of throughput by more than 24 % can be combined with a coke reduction by 67 %. Application of the coating resulted in increased hydrogen and carbon oxide yields by gasification of coke. Further scale up was assessed by simulation of an industrial ethane cracker. Application of the coating resulted in an increase of the simulated run length increase by 525 % while the CO and CO_2 yields are limited to 216 ppmw and 344 ppmw respectively. These findings show that the new coating can effectively reduce coke formation and prolong run length. The CO_2 yield is higher than the typical design value of downstream units. Hence, more research is needed towards elucidating the reactions occurring on the coating to further tune the coating activity.

References

[1] J.J. De Saegher, T. Detemmerman, G.F. Froment, Three dimensional simulation of high severity internally finned cracking coils for olefins production, Revue De L'Institut Français Du Pétrole, 51 (1996) 245-260.

[2] T. Detemmerman, G.F. Froment, Three dimensional coupled simulation of furnaces and reactor tubes for the thermal cracking of hydrocarbons, Revue De L'Institut Français Du Pétrole, 53 (1998) 181-194.

[3] C.M. Schietekat, M.W.M. van Goethem, K.M. Van Geem, G.B. Marin, Swirl flow tube reactor technology: An experimental and computational fluid dynamics study, Chemical Engineering Journal, 238 (2014) 56-65.

[4] T. Torigoe, K. Hamada, M. Furuta, M. Sakashita, K. Otsubo, M. Tomita, Mixing element radiant tube (MERT) improves cracking furnace performance, 11th Ethylene Producers' Conference, Houston, TX, 1999.

[5] M. Györffy, M. Hineno, K. Hashimoto, S.-H. Park, M.-S. You, MERT performance and technology update, 21st Ethylene Producers' Conference, Tampa, FL, 2009.

[6] C.M. Schietekat, D.J. Van Cauwenberge, K.M. Van Geem, G.B. Marin, Computational fluid dynamics-based design of finned steam cracking reactors, AIChE Journal, 60 (2014) 794-808.

[7] J. Wang, M.-F. Reyniers, K.M. Van Geem, G.B. Marin, Influence of silicon and silicon/sulfur-containing additives on coke formation during steam cracking of hydrocarbons, Industrial & Engineering Chemistry Research, 47 (2008) 1468-1482.

[8] J. Wang, M.-F. Reyniers, G.B. Marin, Influence of dimethyl disulfide on coke formation during steam cracking of hydrocarbons, Industrial & Engineering Chemistry Research, 46 (2007) 4134-4148.

[9] M.-F. Reyniers, G.F. Froment, Influence of metal-surface and sulfur addition on coke deposition in the thermal-cracking of hydrocarbons, Industrial & Engineering Chemistry Research, 34 (1995) 773-785.

[10] I. Dhuyvetter, M.-F. Reyniers, G.F. Froment, G.B. Marin, D. Viennet, The influence of dimethyl disulfide on naphtha steam cracking, Industrial & Engineering Chemistry Research, 40 (2001) 4353-4362.

[11] M. Bajus, V. Vesely, J. Baxa, P.A. Leclercq, J.A. Rijks, Steam cracking of hydrocarbons: 5. Effect of thiophene on reaction-kinetics and coking, Industrial & Engineering Chemistry Product Research and Development, 20 (1981) 741-745.

[12] M. Bajus, V. Vesely, Pyrolysis of hydrocarbons in the presence of elemental sulfur, Collection of Czechoslovak Chemical Communications, 45 (1980) 238-254.

[13] M. Bajus, J. Baxa, P.A. Leclercq, J.A. Rijks, Steam cracking of hydrocarbons: 6. Effect of dibenzyl sulfide and dibenzyl disulfide on reaction-kinetics and coking, Industrial & Engineering Chemistry Product Research and Development, 22 (1983) 335-343.

[14] M. Bajus, J. Baxa, Coke formation during the pyrolysis of hydrocarbons in the presence of sulfur-compounds, Collection of Czechoslovak Chemical Communications, 50 (1985) 2903-2909.

[15] D. Depeyre, C. Filcoteaux, B. Blouri, J.G. Ossebi, Pure norma-nonane steam cracking and the influence of sulfur-compounds, Industrial & Engineering Chemistry Process Design and Development, 24 (1985) 920-924.

[16] J. Wang, M.-F. Reyniers, G.B. Marin, The influence of phosphorus containing compounds on steam cracking of n-hexane, Journal of Analytical and Applied Pyrolysis, 77 (2006) 133-148.

[17] S. Vaish, D. Kunzru, Triphenyl phosphite as a coke inhibitor during naphtha pyrolysis, Industrial & Engineering Chemistry Research, 28 (1989) 1293-1299.

[18] K.K. Ghosh, D. Kunzru, Reduction of coke formation during naphtha pyrolysis using triethyl phosphite, Industrial & Engineering Chemistry Research, 27 (1988) 559-565.

[19] D.E. Brown, J.T.K. Clark, A.I. Foster, J.J. McCarroll, M.L. Sims, Inhibition of coke formation in ethylene steam cracking, Acs Symposium Series, 202 (1982) 23-43.

[20] A.E. Munoz Gandarillas, K.M. Van Geem, M.-F. Reyniers, G.B. Marin, Influence of the Reactor Material Composition on Coke Formation during Ethane Steam Cracking, Industrial & Engineering Chemistry Research, 53 (2014) 6358-6371.

[21] A.E. Muñoz Gandarillas, K.M. Van Geem, M.-F. Reyniers, G.B. Marin, Coking Resistance of Specialized Coil Materials during Steam Cracking of Sulfur-Free Naphtha, Industrial & Engineering Chemistry Research, 53 (2014) 13644-13655.

[22] S. Petrone, Y. Chen, R. Deuis, L. Benum, R. Saunders, C. Wong, Catalyzed-assisted manufacture of olefins (CAMOL): Realizing novel operational benefits from furnace coil surfaces, 20th Ethylene Producers' Conference, New Orleans, LA, 2008.

[23] W. Zychlinski, K.A. Wynns, B. Ganser, Characterization of material samples for coking behavior of HP40 material both coated and uncoated using naphtha and ethane feedstock, Materials and Corrosion-Werkstoffe Und Korrosion, 53 (2002) 30-36.

[24] B. Ganser, K.A. Wynns, A. Kurlekar, Operational experience with diffusion coatings on steam cracker tubes, Materials and Corrosion, 50 (1999) 700-705.

[25] L. Benum, Achieving longer furnace runs at NOVA Chemicals, 2002 AIChE Spring Meeting, New Orleans, LA, 2002.

[26] M. Györffy, L. Benum, L. Sakamoto, Increased run length and furnace performance with Kubota and NOVA Chemicals' ANK 400 anticoking technology; data from current installations as well as technologyimprovements for higher thermal stability and decoking robustness, 2006 AIChE National Meeting, Orlando, FL, 2006.

[27] S. Petrone, R. Manyam, A. Wysiekierski, K. Tzatzov, Y. Chen, A "carbon-like" coating to improved coking resistance in pyrolysis furnaces, 10th Annual Ethylene Producers' Conference, New Orleans, LA, 1998.

[28] M. Bergeron, E. Maharajh, T. McCall, A low coking environment for pyrolysis furnace - CoatAlloy, 11th Annual Ethylene Producers' Conference, Houston, TX, 1999.

[29] T. Redmond, A. Bailey, Y. Chen, G. Fisher, R. Miller, Performance of Coatalloy coating systems in ethylene pyrolysis furnaces using different feedstocks, 12th Annual Ethylene Producers' Conference, Atlanta, GA, 2000.

[30] S. Petrone, R. Mandyam, A. Wysiekierski, Surface alloyed high temperature alloys, S.E.P. Corp., (1997).

[31] S. Petrone, R. Deuis, P. Unwin, Catalyzed-assisted manufactur of olefins (CAMOL): Year-(4) update on commercial furnace installations, 22th Ethylene Producers's Conference San Antonio, TX, 2010.

[32] S. Petrone, R. Deuis, F. Kong, Y. Chen, Catalytic surfaces and coatings for the manufacture of petrochemicals, B. Corporation, (2013).

[33] S. Rech, Catalyzed-Assisted Manufacture of Olefins (CAMOL™): Updated for Use in Naphtha Service, http://www.basf-qtech.com/, 2013.

[34] SK-Corporation, Coke Inhibition Technologies - Commercial Experience: F. SK Corporation - PY-COAT, 13th Ethylene Producers' Conference, Houston, TX, 2001.

[35] S. Wang, W. Peng, Q.D. Fu, Z., Z. Wu, C. Lin, Y. Gu, X. Zhang, L.B. Kool, Method and reactor for cracking hydrocarbon, (2011).

[36] S. Wang, W. Peng, Q. Fu, Z. Deng, Z. Wu, C. Lin, Y. Gu, X. Zhang, L.B. Kool, Cracking hydrocarbons in a reactor with an inner surface comprising perovskite material to reduce the build-up of coke deposits, G.E. Company, (2011).

[37] K.M. Van Geem, S.P. Pyl, M.-F. Reyniers, J. Vercammen, J. Beens, G.B. Marin, On-line analysis of complex hydrocarbon mixtures using comprehensive two-dimensional gas chromatography, Journal of Chromatography A, 1217 (2010) 6623-6633.

[38] S.P. Pyl, C.M. Schietekat, M.-F. Reyniers, R. Abhari, G.B. Marin, K.M. Van Geem, Biomass to olefins: Cracking of renewable naphtha, Chemical Engineering Journal, 176 (2011) 178-187.

[39] S.P. Pyl, T. Dijkmans, J.M. Antonykutty, M.F. Reyniers, A. Harlin, K.M. Van Geem, G.B. Marin, Wood-derived olefins by steam cracking of hydrodeoxygenated tall oils, Bioresource Technology, 126 (2012) 48-55.

[40] T. Dijkmans, S.P. Pyl, M.-F. Reyniers, R. Abhari, K.M. Van Geem, G.B. Marin, Production of bio-ethene and propene: alternatives for bulk chemicals and polymers, Green Chemistry, 15 (2013) 3064-3076.

[41] Y. Tong, M.K. Poindexter, C.T. Rowe, Inhibition of coke formation in pyrolysis furnaces, Abstracts of Papers of the American Chemical Society, 210 (1995) 92.

[42] K.M. Van Geem, M.F. Reyniers, G.B. Marin, Challenges of modeling steam cracking of heavy feedstocks, Oil & Gas Science and Technology - Revue d'IFP Energies Nouvelles, 63 (2008) 79-94.

[43] P.M. Plehiers, G.C. Reyniers, G.F. Froment, Simulation of the run length of an ethane cracking furnace, Industrial & Engineering Chemistry Research, 29 (1990) 636-641.

[44] M.J. Bennett, J.B. Price, A physical and chemical examination of an ethylene steam cracker coke and of the underlying pyrolysis tube, J Mater Sci, 16 (1981) 170-188.

[45] H.C. Hottel, A. Sarofim, Radiative Heat Transfer, McGraw-Hill, New York, 1967.

[46] H.A.J. Vercammen, G.F. Froment, An improved zone method using monte-carlo techniques for the simulation of radiation in industrial furnaces, International Journal of Heat and Mass Transfer, 23 (1980) 329-337.

[47] M.V.R. Rao, P.M. Plehiers, G.F. Froment, The coupled simulatoin of heat-transfer and reaction in a pyrolysis furnace, Chemical Engineering Science, 43 (1988) 1223-1229.

[48] P.M. Plehiers, G.F. Froment, Firebox simulation of olefin units, Chemical Engineering Communications, 80 (1989) 81-99.

[49] G.J. Heynderickx, M. Nozawa, Banded gas and nongray surface radiation models for high-emissivity coatings, AIChE Journal, 51 (2005) 2721-2736.

[50] G.J. Heynderickx, M. Nozawa, High-emissivity coatings on reactor tubes and furnace walls in steam cracking furnaces, Chemical Engineering Science, 59 (2004) 5657-5662.

[51] G.J. Heynderickx, G.F. Froment, Simulation and comparison of the run length of an ethane cracking furnace with reactor tubes of circular and elliptical cross sections, Industrial & Engineering Chemistry Research, 37 (1998) 914-922.

Chapter 7: Conclusions and perspectives

The subject of this work was the development of tools for the simulation and design of steam cracking reactors. More specifically, the application of computational fluid dynamics for the design of steam cracking reactors and the evaluation of three dimensional reactor technologies to enhance heat transfer was the main focus.

7.1 Conclusions

In Chapter 2, a recent three-dimensional reactor technology for steam cracking reactors, the so-called Swirl Flow Tube® (SFT®) reactor technology was evaluated experimentally and numerically with computational fluid dynamics simulations. The experiments showed that application of a SFT® results in an increase of the heat transfer coefficient by a factor of 1.2 to 1.5 compared to a straight tube. The penalty paid in the pressure drop increase is moderate compared to other 3D technologies and only amounts to 1.4 to 2.2 depending on the Reynolds number and the SFT® geometric parameters. A computational fluid dynamics model was adopted that showed satisfactory agreement to the experimental results. The simulation results allow attributing the increased heat transfer and pressure drop to a higher wall shear stress. The experimental and simulation results confirm the potential for the application of the SFT technology in steam cracking furnaces because of the lower average wall temperatures at the cost of a moderate pressure drop increase. More general, these simulations show that non-reactive CFD simulations validated with a rather simple experimental setup can be used to assess the

potential of a three-dimensional reactor technology and to study the effect of geometric parameters on pressure drop and heat transfer.

In Chapter 3, three-dimensional CFD simulations were performed in which the detailed free-radical chemistry was for the first time accounted for. The start-of-run external tube metal temperatures could be reduced by up to 50 K when applying optimal fin parameters compared to conventionally used bare tubes. Implementation of a validated coking model for light feedstocks showed that coking rates are reduced up to 50%. However, the increased friction and inner surface area lead to a factor 1.22 to 1.66 of pressure drop increase, causing minor but significant shifts in light olefin selectivity. For the optimized helicoidally finned reactor the ethene selectivity decreased, while propene and 1,3-butadiene selectivity increased with a similar amount.

In Chapter 4, a methodology was developed to use detailed single-event microkinetic reaction networks in computational fluid dynamics simulations of steam cracking reactors by on the fly application of the pseudo-steady state assumption. Depending on the reaction network size, a speedup factor from 7 to 54 was obtained compared to the standard FLUENT routines. The methodology was applied to the simulation of an industrial propane cracking reactor comparing a conventional bare reactor and a helicoidally finned reactor. The difference in product selectivities are caused by a combination of the increase in cross-sectional temperature uniformity and an increase in pressure drop. Comparison of the 3D simulation results to 1D plug flow reactor simulation results shows that a significant error is made by neglecting the increased reaction rates in the laminar film near the reactor inner wall. Therefore the 1D plug flow reactor model COILSIM1D was extended to account for the non-uniform radial temperature profile. Doing so, the heat input, COT and TMT simulated with the 1D model are closer to the corresponding

values in the 3D simulations. However, the effect of the reactor geometry on product selectivities is only well captured for a few products by the 1D model. This consideration shows the necessity of highly detailed 3D simulations upon evaluation of the application of a 3D reactor design for a specific cracker.

In Chapter 5, a code was developed for the three-dimensional simulation of steam cracking reactors based on the free, open-source CFD software package OpenFOAM®. The code incorporates the methodology of applying PSSA to the radicals discussed in Chapter 4. Furthermore, the effect of turbulent temperature fluctuations on the reaction rates is accounted for by a probability density function for temperature. To this end, an extra continuity equation for the temperature variance is solved. The effect of turbulence-chemistry interaction on product yields under typical steam cracking conditions was seen to be limited to about 0.1 wt%. To further reduce the computational time, a dynamic zoning method was implemented. Cells with a similar thermochemical state are grouped into zones based on two features and the rates of formation are calculated based on the zonal averages. These are then mapped back to the individual cells of the grid on which the continuity equations are solved. The code was then successfully applied to the simulation of an industrial butane cracking reactor.

In Chapter 6, a catalytic coating for reduced coke formation, called YieldUp, was tested experimentally and the scale-up to an industrial unit was simulated. Three different formulations of the coating were tested in a jet-stirred reactor setup and showed reduced coking rates over multiple coking/decoking cycles compared to a reference alloy. The most coking rate-reducing coating was further tested in a pilot plant setup. The overall coke formation was reduced by 76% compared to a reference alloy reactor. Scale up was assessed by simulation of an industrial ethane cracking reactor. Application of the coating resulted in a simulated increase of the reactor

runlength by 525 % while the CO and CO_2 yields were 216 ppmw and 344 ppmw respectively. This relatively high CO_2 yield can be higher than the specifications of downstream units depending on the design of the caustic tower. Hence further research towards tuning the coating activity is necessary.

7.2 Perspectives

Computational Fluid Dynamics simulations of industrial steam cracking reactors are challenging because of the widely varying length scales. On the one hand, the size of industrial reactors is large, i.e. the reactor lengths range from 10 to 100 m. On the other hand, wall-resolved, low-Reynolds treatment of the near wall region is recommended for the accurate simulation of the effect of three-dimensional technologies altering the inner surface of the reactors. This results in a thickness of the first cell near the inner wall in the µm range. These grid requirements yield meshes of 10^7-10^8 cells. Adopting detailed chemistry calculations on these meshes results in an almost intractable number of algebraic equations that need to be solved. Therefore, to reduce computational time, only simulations with Reynolds-Averaged Navier-Stokes (RANS)-based turbulence models were performed in this work. In this approach, all turbulent length scales are modeled with a turbulence model and only ensemble averaged flow variables are computed. RANS models usually perform well in standard flows such as channel flows, but often fail to correctly predict flow separations. Such flow separations are to be expected in some 3D reactor technologies, such as the Mixing Element Radiant Tubes (MERT) patented by Kubota[®]. On the contrary, Large Eddy Simulation (LES) directly calculate the largest, most energetic vortical structures and model the smaller-scale eddies. Large Eddy Simulations undoubtedly show an unseen potential for modeling turbulent flows and recent advances in computational power have

transformed it in an accessible tool for academics and an option available in most commercial CFD programs. However, the application of LES to wall-bounded turbulent flows is challenging as the ratio of turbulent length scales in the tube core to the length scales in the inner layer is very large, requiring excessively fine grids. The grid requirements for LES scale with the Reynolds number to the power of 1.8. Current computational capabilities limit the application of LES to flows at a Reynolds number of 60,000-100,000. Hence, it is clear that the simulation of most industrial reactors operating at Reynolds numbers from 100,000-200,000 is currently out of range. To avoid the use of fine grids near the wall in high-Reynolds number LES, the near wall flow behavior is often represented with a wall model. In that case, the no-slip boundary condition is replaced by a wall-stress model in the first grid cell near the wall. The combination of such a wall model does even not necessarily lead to correct mean-velocity profiles due to the so-called log-layer mismatch [1]. As the turbulence induced by three-dimensional reactor technologies originates from the wall, the application of wall models in LES for these reactors should be done carefully by comparison to wall-resolved LES. Another way to limit the computational cost of LES is by applying stream wise periodic boundary conditions and by isolating the fluctuating components from the mean stream wise gradient [2-4]. Although this methodology shows several limitations, e.g. the effect of return bends and manifolds present in real steam cracking reactors cannot be taken into account, it is a perfect tool for the comparison of the pressure drop and heat transfer increase caused by different three-dimensional reactor geometries and geometric parameter studies. The application of stream wise periodic LES to fully developed pipe flow has been performed in several works [2, 4]. Extension of this methodology to reactive flows is less straightforward because the species concentrations cannot be treated easily as periodic scalars. Hence, modifications to the non-reactive methodology are necessary to take into account the

effect of molar expansion, density decrease by temperature increase and the effect of residence time distribution on species concentrations.

In the reactive CFD simulations of the present work, chemistry calculations were implemented by using a segregated solver, i.e. all continuity equations, including energy and species transport equations are solved consequently. This methodology was largely possible as the stiffness from the system is removed by application of the pseudo-steady state assumption. However, using a coupled method can be an attractive approach. Two main approaches have been investigated for the solution of stiff, large systems of partial differential equations; fully coupled algorithms and algorithms based on operator splitting methods. The main advantage of fully coupled algorithms is that all or some, e.g. species and energy, equations are solved simultaneously and that the interactions between these equations are taken into account together. However, the size of the resulting matrix for the algebraic solver can pose prohibitive memory requirements when detailed chemistry is implemented. In operator splitting, the equations are broken down in several sub-equations modeling part of the physics involved [5]. For reactive flow, the chemical reaction processes can be conveniently separated from the transport processes. The main advantages of operator splitting methods is that the memory-intensive matrix operations of fully coupled algorithms are avoided and that the best numerical method to solve each sub-equation can be chosen. The main disadvantage is that the separate algorithms can be very complex and differ from term to term. Moreover, to solve each sub-equation a time-marching over the so-called operator splitting time is done. This makes that solvers based on the operator splitting method are inherently transient solvers. Nonetheless, operator splitting can be applied to steady-state problems by using a larger value for the operator splitting time, i.e. larger CFL number, which

does not guarantee a correct transient solution but ultimately leads to an accurate steady-state solution. The application of operator splitting introduces an error in the solution, called the splitting error that increases with increasing CFL number and can pertain in the steady-state solution. Hence, the possible shorter simulation time of an operator splitting-based method will depend on the balance between the increased convergence rate as the chemical reaction sub-equations are typically solved coupled with an ordinary differential equation solver and the value of the CFL number to guarantee a stable convergence towards the steady state solution. The latter can require very small time steps caused by the high Reynolds number in steam cracking reactors.

In the performed CFD simulations of industrial reactors, a heat flux profile that only depends on the reactor axial coordinate was applied. However, also azimuthally or circumferentially non-uniformities in the heat flux exist due to the existence of two sides on the cracking tubes, i.e. a fire-side directed towards the side walls and burners and a shadow-side directed towards other reactor tubes. Obtaining these detailed heat flux profiles requires a coupled furnace-reactor simulation, with both the furnace and reactor simulated in 3D. The most straightforward way seems to be the development of a furnace simulation code based on the OpenFOAM® program also used in Chapter 5 as an appropriate solver is available, i.e. edcSimpleFOAM based on the eddy dissipation concept (EDC) model [6, 7]. The EDC model is often used to account for turbulence–chemistry interactions in combustion simulations. The model is based on a general reactor concept for the calculation of the average net species production rates in turbulent reactive flows. Combustion takes place in regions associated with the smallest turbulence structures, the so-called fine-structures [8]. Every computational cell is considered to be

composed of a reactive space, namely the fine-structures and the surrounding fluid that is inert. The reactive space is modeled as a Perfectly Stirred Reactor exchanging mass and energy with the surrounding inert fluid. By coupling this furnace code with the three-dimensional reactor solver, the effect on product yields and coking of shadow effects could for the first time be quantified. Additionally, the performed CFD simulations of steam cracking reactors are for start-of-run conditions, i.e. with no coke layer on the inner wall of the reactor. The effect of the growing coke layer on the fluid dynamics can be accounted for by dynamic meshing or adaptive mesh refinement. Indeed, the non-uniform coke formation can influence the performance of three-dimensional reactor technologies along the runlength.

In Chapter 6, the performance of a catalytic coating to reduce coke formation was studied experimentally and numerically. Although the coating showed a significant coke reduction compared to a reference alloy over several cracking/decoking cycles, further research is necessary to come to a more mature, commercial technology. First, the effect of temperature on the coating activity should be investigated further. Indeed, in industrial crackers process conditions are often altered depending on the feedstock. Secondly, the focus of the performed experimental program on both the Jet-Stirred Reactor (JSR) and the pilot plant setup was on ethane cracking and a similar experimental program should be performed with naphtha. Indeed, for the cracking of ethane adequate coke-reducing alloys exist [9], while a similarly mature and performing technology for naphtha cracking is still lacking. Finally, experiments dedicated at unraveling the occurring elementary reactions on the coating should be performed. This would allow improving the current modeling effort of the coating which can lead to further optimization

of the coating formulation and will improve the accuracy of the simulated scale-up to industrial

reactors.

References

[1] P. Wu, J. Meyers, A constraint for the subgrid-scale stresses in the logarithmic region of high Reynolds number turbulent boundary layers: A solution to the log-layer mismatch problem, Physics of Fluids, 25 (2013).

[2] L. Redjem-Saad, M. Ould-Rouiss, G. Lauriat, Direct numerical simulation of turbulent heat transfer in pipe flows: Effect of Prandtl number, International Journal of Heat and Fluid Flow, 28 (2007) 847-861.

[3] D.J. Van Cauwenberge, C.M. Schietekat, J. Floré, K.M. Van Geem, G.B. Marin, CFD-based design of 3D pyrolysis reactors: RANS vs. LES, Chemical Engineering Journal, accepted (2015).

[4] S.V. Patankar, C.H. Liu, E.M. Sparrow, Fully developed flow and heat-transfer in ducts having streamwise-periodic variations of cross-sectional area, Journal of Heat Transfer-Transactions of the Asme, 99 (1977) 180-186.

[5] E. Baudrez, G.J. Heynderickx, G.B. Marin, Steady-state simulation of Fluid Catalytic Cracking riser reactors using a decoupled solution method with feedback of the cracking reactions on the flow, Chemical Engineering Research & Design, 88 (2010) 290-303.

[6] E. Ghasemi, S. Soleimani, C.X. Lin, RANS simulation of methane-air burner using local extinction approach within eddy dissipation concept by OpenFOAM, International Communications in Heat and Mass Transfer, 54 (2014) 96-102.

[7] B. Lilleberg, D. Christ, I.S. Ertesvag, K.E. Rian, R. Kneer, Numerical Simulation with an Extinction Database for Use with the Eddy Dissipation Concept for Turbulent Combustion, Flow Turbulence and Combustion, 91 (2013) 319-346.

[8] G.D. Stefanidis, B. Merci, G.J. Heynderickx, G.B. Marin, CFD simulations of steam cracking furnaces using detailed combustion mechanisms, Computers & Chemical Engineering, 30 (2006) 635-649.

[9] M. Györffy, L. Benum, L. Sakamoto, Increased run length and furnace performance with Kubota and NOVA Chemicals' ANK 400 anticoking technology; data from current installations as well as technologyimprovements for higher thermal stability and decoking robustness, 2006 AIChE National Meeting, Orlando, FL, 2006.

Appendix A: Validation reduced kinetic models

In the various chapters of this work, several reduced kinetic models are used. In this appendix, validation of the applicability of these reduced models is shown by comparison to the results obtained with their respective complete equivalents. As 3D simulations with the complete kinetic models are impossible because of the high computational load, comparison is made through 1D simulations using the Reaction Design's CHEMKIN[®] [1] plug flow reactor model which has a proprietary modified version of the DASPK solver [2] to numerically solve the set of stiff ordinary differential equations.

A.1 Propane kinetic model of Chapter 3

This kinetic model was obtained by restricting the β-network of the single-event microkinetic CRACKSIM mechanism [3] to the molecules and radicals relevant to propane cracking and all reactions between these species. The full model contains 135 species and 1053 reactions. The reduced model contains 13 molecules, 13 radicals and 206 reactions. A plug flow reactor simulations was performed using the temperature and pressure profile shown in Figure A-1 which are similar to the profiles of the three-dimensional reactor simulations.
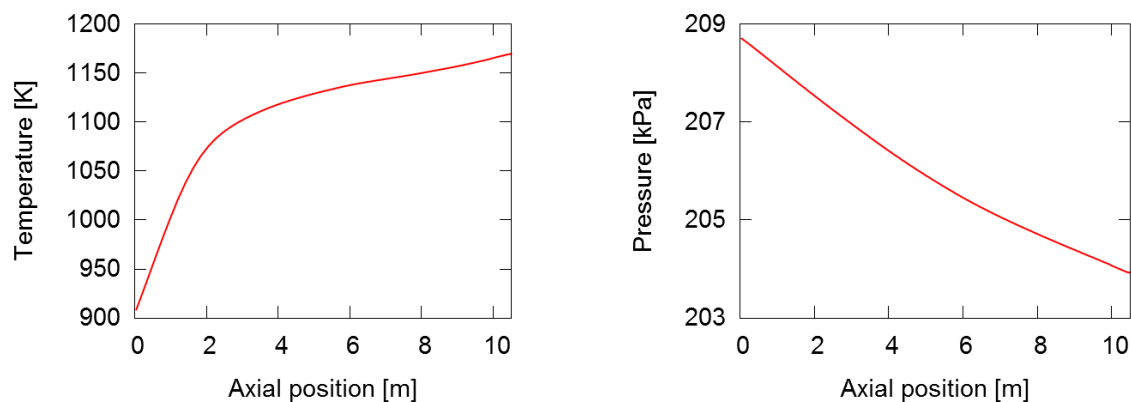
Figure A-1: Temperature [K] (left) and pressure [kPa] (right) as a function of axial position [m].

Figure A-2 compares the yields obtained using the reduced model and the complete kinetic model. Given the small size of the kinetic model and not tuning any kinetic or thermodynamic parameter of the occurring reactions, a good agreement is obtained. The agreement for the most abundant species, i.e. propane, ethene, propene and methane is good. For most species, the yield using the reduced kinetic model is slightly higher as some components having a considerable yield with the full model, e.g. benzene and toluene, are not accounted for in the reduced model.
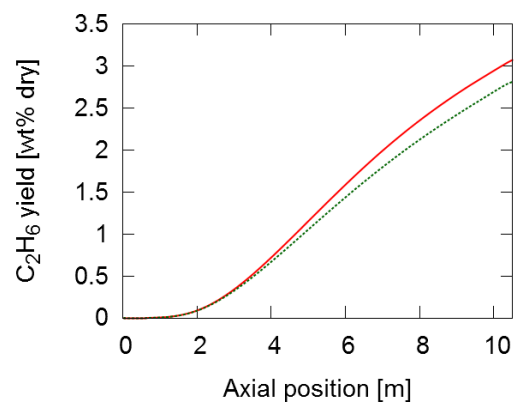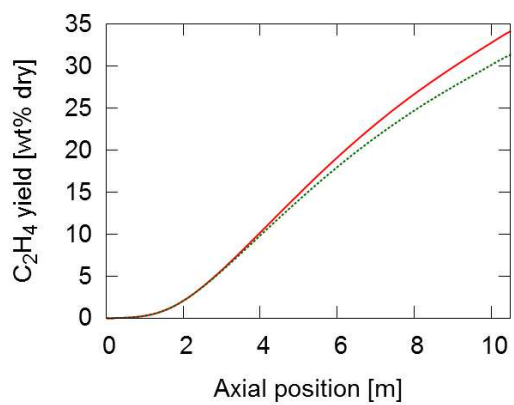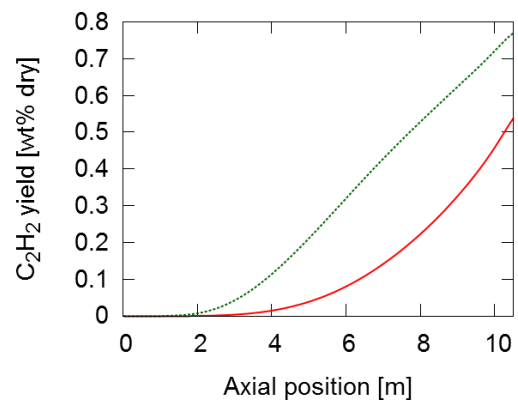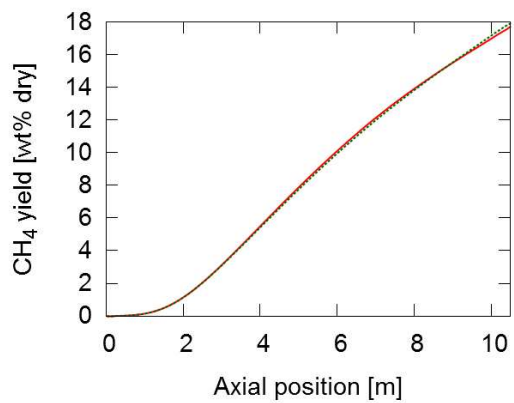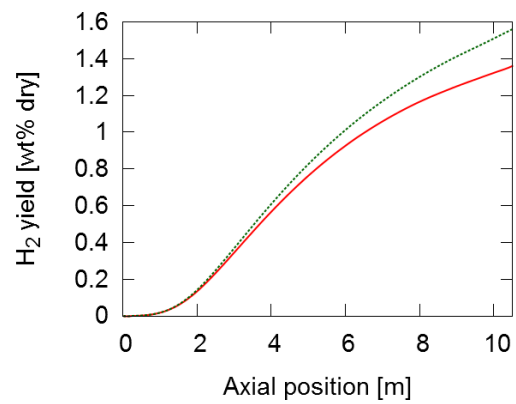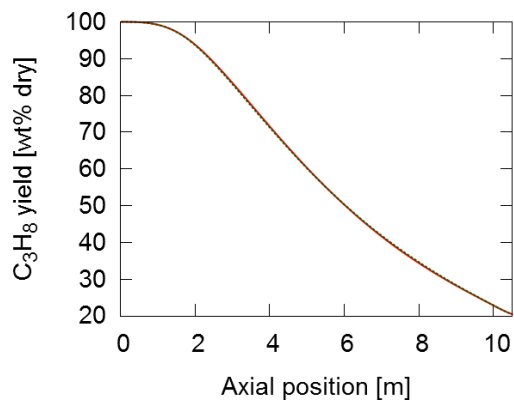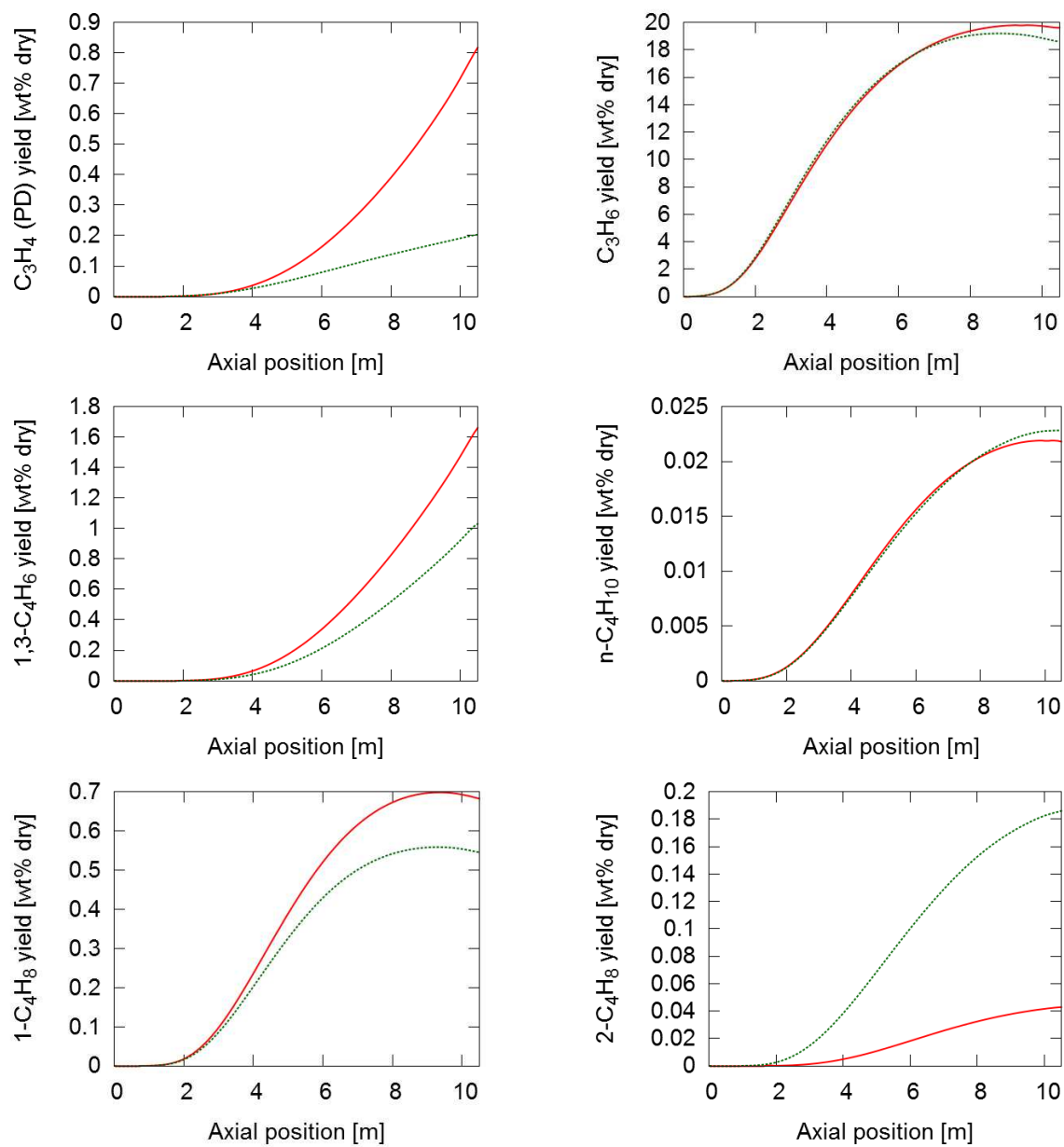
Figure A-2: Yields [wt% dry] as a function of axial position [m]: ———— **- Reduced model;** - - - - - - **- Full model.**

A.2 Propane kinetic model of Chapter 4

The reduced network used in the simulations of the industrial propane cracking reactor was obtained from the full network of Dijkmans et al. [4] by removal of all species and reactions irrelevant for propane cracking. Important to note is than no kinetic parameters were adjusted to improve the agreement between the reduced and the full network. To assess the validity of the reduction for propane crackiing, 14 isothermal plug flow simulations were performed with both the reduced and the full network at a temperature range from 873 to 1173 K covering the entire propane conversion range.

Figure A-3 A shows that a good agreement is obtained for the conversion as a function of reactor temperature. Also for the hydrogen, methane and ethene yield shown in Figure A-3 A, B and C respectively, a good agreement between the reduced and the full network is seen.
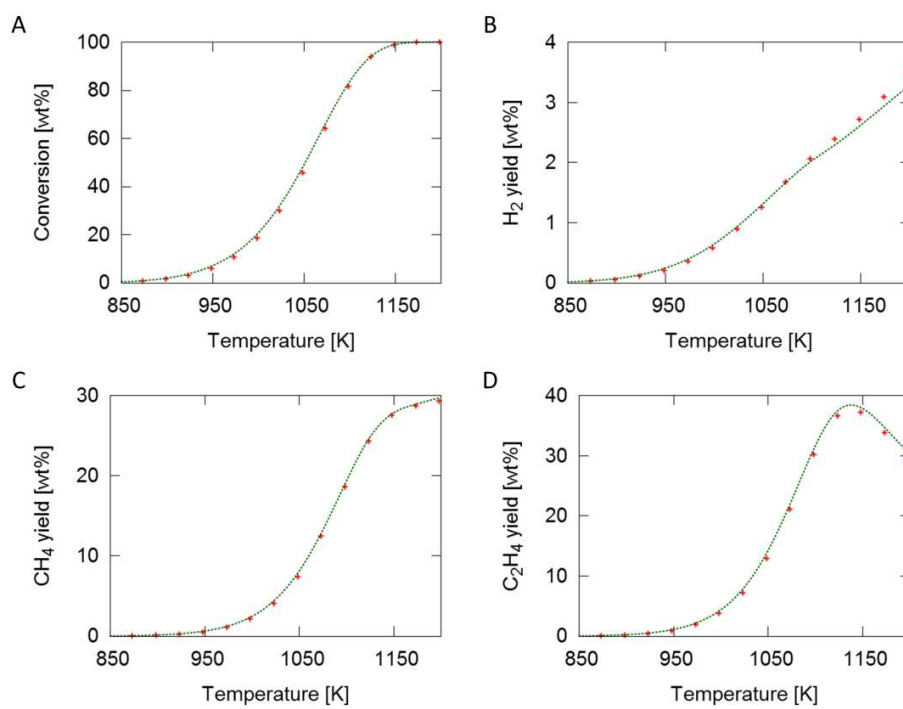
Figure A-3: Conversion (A), hydrogen yield (B), methane yield (C) and ethene yield (D) [wt%] as a function of temperature [K]: + - full network, ----- - reduced network.

Figure A-4 shows the yields of propene and C4-(di)olefins. The maximum around 1075 K is slightly overpredicted by the reduced model but overall a satisfactory accuracy is obtained.
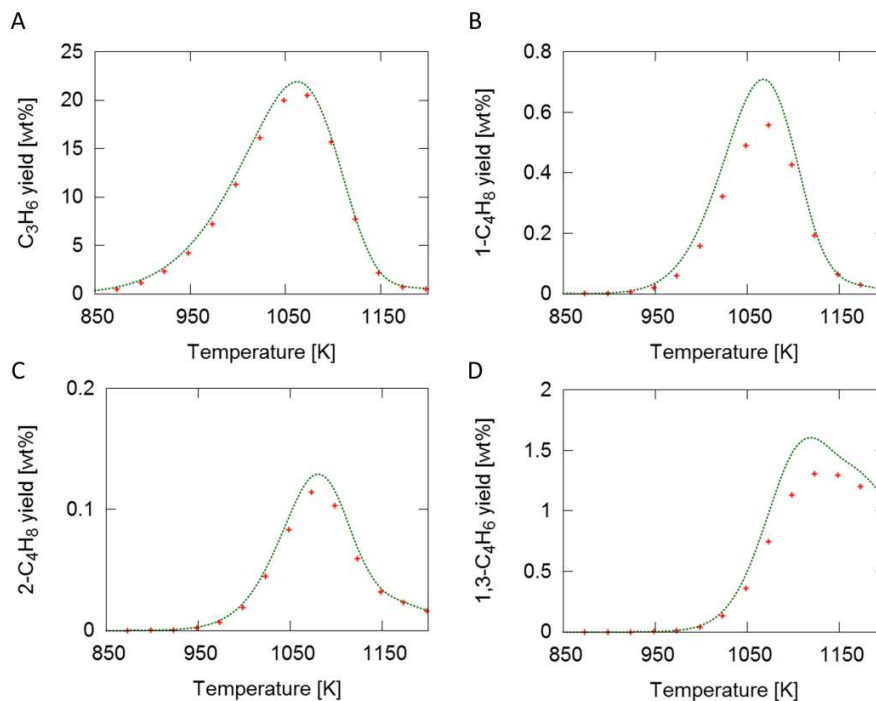

Figure A-4: Propene (A), 1-butene yield (B), 2-butene yield (C) and 1,3-butadiene yield (D) [wt%] as a function of temperature [K]: +- full network, ····· - reduced network.

Figure A-5 shows the yields of 1,3-cyclopentadiene and the most abundant aromatic species, i.e. benzene, toluene and naphthalene. The agreement for 1,3-cyclopentadiene is good. Above 1150 K, the yield of benzene is significantly underpredicted while the toluene and naphthalene yields are overpredicted. It is noted that these cracking severities is not reached in the performed 3D simulations. Indeed, the benzene, toluene and naphthalene yields in the simulated industrial propane cracker are around 2.4, 0.4 and 0.8 wt% respectively. The agreement between the reduced and the full network at these cracking severities is good.
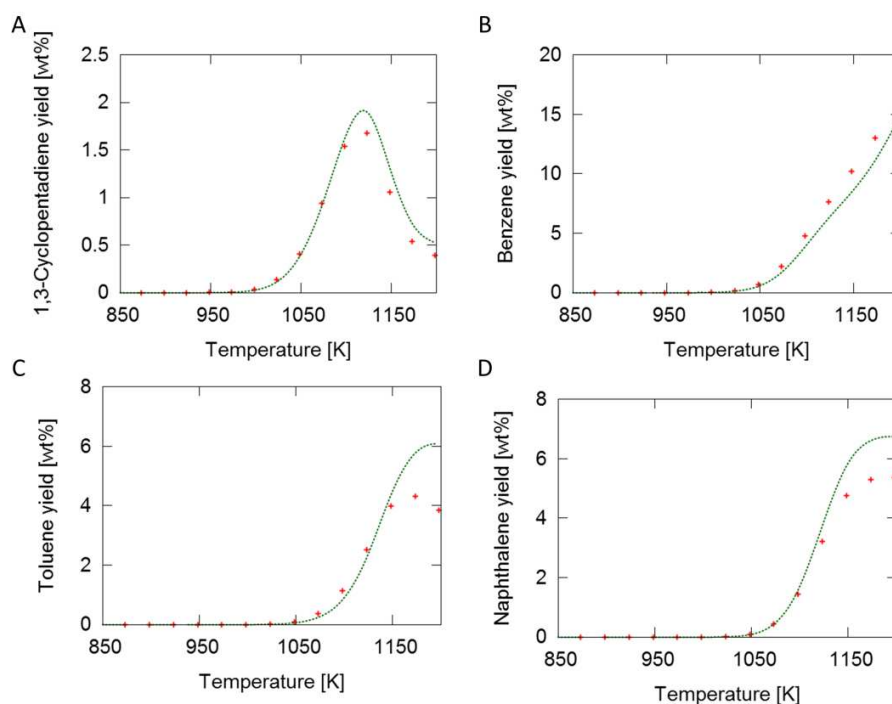
Figure A-5: 1,3-cyclopentadiene (A), benzene yield (B), toluene yield (C) and naphthalene yield (D) [wt%] as a function of temperature [K]: + - full network, ····· - reduced network.

A.3 Butane kinetic model of Chapter 5

The single event micro-kinetic model adopted in the simulations of the butane-cracking U-coil was obtained by reducing the network of Van de Vijver et al. [5] to its main species and corresponding reactions. The full model contains 195 species and 14551 reactions while the reduced model only contains 20 species and 149 reactions. Both models were used to simulate a set of seven pilot plant experiments over a range of relevant process conditions shown in Table 1.

Table 1: Experimental conditions of butane-cracking pilot plant experiments.

Coil outlet temperature (K)	820-860
Coil outlet pressure (Pa)	1.59-2.01
n-Butane inlet flow rate (mol/s)	15
Steam dilution (kg$_{steam}$/kg$_{hydrocarbons}$)	0.699-0.846
Space time (s)	0.36-0.47

Figure A-6 A and B show a parity plot for the full and reduced mechanism respectively. The agreement between the full model and the simulated data is satisfactory with most yields within less than 10% relative error. Only the propene yield is overestimated in all experiments. Also for the reduced mechanism a satisfactory agreement is obtained with most yields simulated within less than 10% relative error from the experimental value.
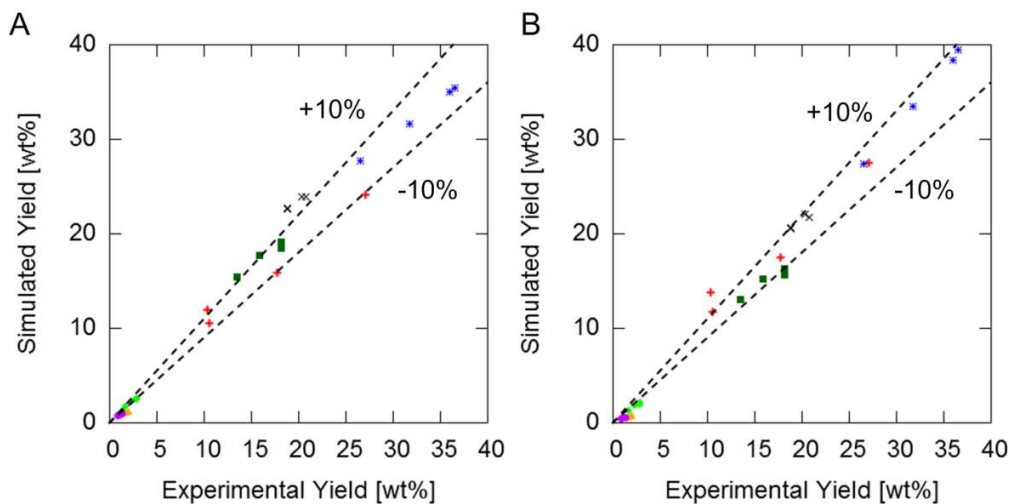

Figure A-6: Parity plot of yields for full (left) and reduced (right) network: ✚ - butane, ✳ - ethene, ■ - methane, ✕ - propene, ▲ -1-butene, ◆ -1,3-butadiene, ● -hydrogen, dashed lines indicate -10% and +10%.

References

[1] R.J. Kee, F.M. Rupley, J.A. Miller, M.E. Coltrin, J.F. Grcar, E. Meeks, H.K. Moffat, G. Lutz, A.E. Dixon-Lewis, M.D. Smooke, J. Warnatz, G.H. Evans, R.S. Larson, R.E. Mitchell, L.R. Petzhold, W.C. Reynolds, M. Caracotsios, W.E. Stewart, P. Glarborg, C. Wang, O. Adigun, W.G. Houf, C.P. Chou, S.F. Miller, P. Ho, D.J. Young, CHEMKIN Release 4.1.1, Reaction Design, Inc., San Diego, CA, USA, 2007.

[2] S. Li, L. Petzold, Design of New DASPK for Sensitivity Analysis, UCSB Technical report., (1999).

[3] K.M. Van Geem, Single Event Microkinetic Model for Steam Cracking of Hydrocarbons, Chemische Proceskunde en Technische Chemie, Ugent, 2005-2006.

[4] T. Dijkmans, S.P. Pyl, M.-F. Reyniers, R. Abhari, K.M. Van Geem, G.B. Marin, Production of bio-ethene and propene: alternatives for bulk chemicals and polymers, Green Chemistry, 15 (2013) 3064-3076.

[5] R. Van de Vijver, N.M. Vandewiele, P.L. Bhoorasingh, B.L. Slakman, F. Seyedzadeh Khanshan, H.-H. Carstensen, M.-F. Reyniers, G.B. Marin, R.H. West, K.M. Van Geem, Automatic mechanism and kinetic model generation for gas-phase and solution-phase processes: a perspective on best practices, recent advances, and future challenges, International Journal of Chemical Kinetics, submitted (2014).

Appendix B: Grid independence

This appendix shows the results of the grid independence study of the parametric study and the reactive simulations of Chapter 3. A grid independence study was performed on the pressure drop simulations of the tubes adopted by Albano et al. [1]. The results of the study are summarized in Figure B-1. At a mesh density of approximately 6.10^5 and 3.10^5 cells/meter for the fluid grid independence is obtained as the pressure drop changes less than 0.1% with further refinement of the mesh. Grid sizes in wall units for grid independence were seen to be $(R\Delta\theta^+, \Delta y^+, \Delta z^+) = (0, 0.8\text{-}50, 333)$. These values were used as upper limits for all grids.
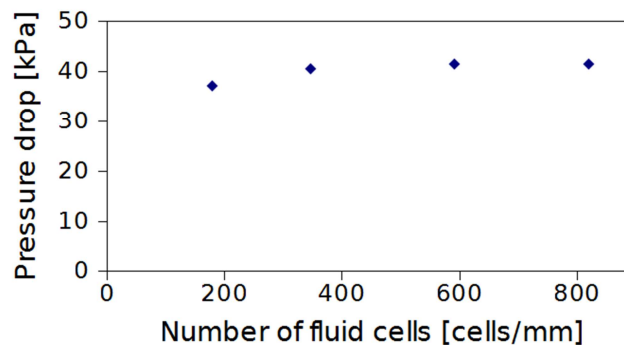

Figure B-1: Pressure drop [kPa] as a function of number of fluid cells [cells/mm].

The grid used in the reactive simulation of the SmallFins reactor was further refined based on the temperature gradient of the converged solution to assure grid independence of the product yields. With this refined mesh, 100 additional iterations were carried out. No changes in the results are simulated by grid refinement when the yields are rounded to 2 digits as shown in Table 1.

Table 1: Comparison adopted and refined mesh simulation results for the SmallFins reactor.

	SmallFins	SmallFins Refined
Number of cells [-]	11,919,896	13,715,473
Coil-outlet-temperature [K]	1192.7	1192.7
Pressure drop [kPa]	48.42	48.42
Pressure drop ratio [-]	1.66	1.66
Propane conversion [-]	85.16	85.17
P/E ratio [wt%/wt%]	0.485	0.485
Residence time [s]	0.163	0.163
Product Yields [wt%]		
H_2	1.49	1.49
CH_4	19.25	19.25
C_2H_2	0.98	0.98
C_2H_4	38.11	38.12
C_2H_6	3.46	3.46
C_3H_4	1.22	1.22
C_3H_6	18.47	18.47
C_3H_8	14.84	14.83
$1,3-C_4H_6$	1.53	1.53
$1-C_4H_8$	0.56	0.56
$2-C_4H_8$	0.03	0.03
$n-C_4H_{10}$	0.02	0.02
Valuable light olefins*	58.11	58.11
Product Selectivity [-]		
H_2	1.75	1.75
CH_4	22.61	22.61
C_2H_2	1.15	1.15
C_2H_4	44.75	44.76
C_2H_6	4.07	4.07
C_3H_4	1.43	1.43
C_3H_6	21.69	21.69
$1,3-C_4H_6$	1.79	1.79
$1-C_4H_8$	0.65	0.65
$2-C_4H_8$	0.03	0.03
$n-C_4H_{10}$	0.02	0.02
Valuable light olefins*	68.24	68.25

[1] J.V. Albano, K.M. Sundaram, M.J. Maddock, Applications of Extended Surfaces in Pyrolysis Coils, Energy Progress, 8 (1988) 160-168.

Appendix C: Averaging procedures

In the following all adopted procedures for averaging the three-dimensional simulation data are discussed for temperature. Note that similar procedures are applied to the other variables (e.g. pressure, coking rate, species concentrations,...).

- Mixing cup average over a cross-section area as a function of axial position

This procedure is illustrated in Figure C-1. The mixing cup averaged temperature over a cross section T_{avg} at axial position z_1 is defined as:

$$T_{avg} = \frac{1}{\phi_{m,tot}} \int_0^{r_{max}} \int_0^{2\pi} \phi_m(r,\theta,z_1) \ T(r,\theta,z_1) \, dr d\theta$$

(1)

with ϕ_m the mass flow rate, T the temperature, r the radial coordinate, θ the azimuthal coordinate, r_{max} the maximum inner radius and $\phi_{m,tot}$ the total mass flow rate = $\int_0^{r_{max}} \int_0^{2\pi} \phi_m(r,\theta,z_1) \, dr d\theta$. From the simulation results, this mixing cup averaged temperature is obtained by numerical integration over all faces i of the cross section at an axial position z_1:

$$T_{avg} = \frac{1}{\phi_{m,tot}} \sum_{i=1}^{nface} \phi_{m,i} \, T_i$$

(2)

with T_i the temperature of face i, $\phi_{m,i}$ the flow through face i, $nface$ the number of faces

in the cross-section and $\phi_{m,tot} = \sum_{i=1}^{nface} \phi_{m,i}$.
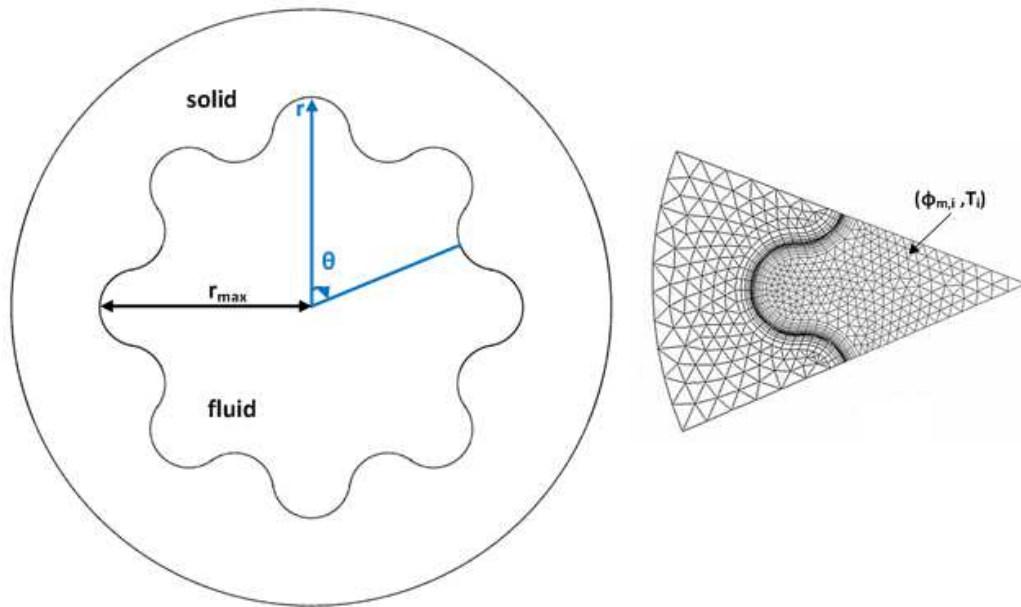

Figure C-1: Illustration of calculation of the mixing cup averaged temperature over a cross-section: a) entire cross section; b) grid of simulated 1/8 of a cross section.

- Azimuthally area-average over a perimeter as a function of axial position

This procedure is illustrated in Figure C-2 and adopted for the calculation of average

values at the reactor inner wall at a fixed axial position z_1. The azimuthally area-averaged

temperature over a perimeter at axial position z_1 is defined as:

$$T_{az} = \frac{1}{\Omega_{in}} \int_0^{2\pi} \Omega(\theta, z_1)\, T(\theta, z_1)\, d\theta \tag{3}$$

with T the temperature and Ω_{in} the inner perimeter and θ the azimuthal coordinate. From the simulation results, this azimuthally area-averaged temperature is obtained by numerical integration over all faces i at the tube inner wall at a certain axial position:

$$T_{az} = \frac{1}{\Omega_{in}} \sum_{i=1}^{nface} \Omega_i\, T_i \tag{4}$$

with T_i the temperature of face i, Ω_i the length of surface i, $nface$ the number of faces at the inner wall in the cross-section, Ω_{tot} the total inner perimeter and θ the azimuthal coordinate.
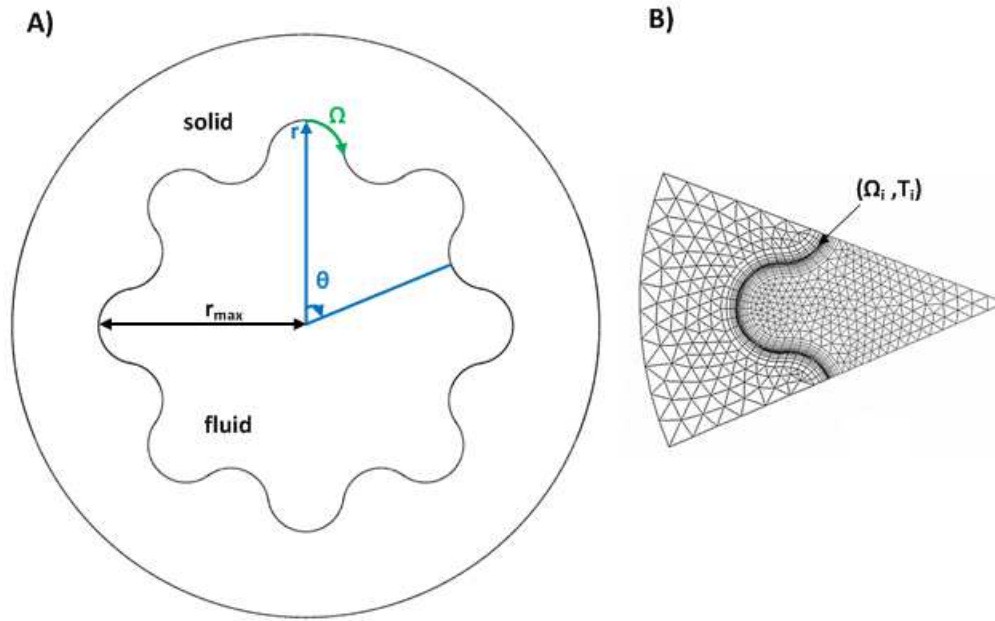
Figure C-2: Illustration of calculation of the azimuthally area-averaged temperature over a cross-section: a) entire cross section; b) grid of simulated 1/8 of a cross section.

- Azimuthally mixing cup average as function of radial position

This procedure is illustrated in Figure C-3. The mixing cup averaged temperature at a certain radial position r_1 at axial position z_1 is defined as:

$$T_{az} = \frac{1}{\phi_{m,r_1}} \int_0^{2\pi} \phi_m(r_1, \theta, z_1) T(r_1, \theta, z_1) \, d\theta \tag{5}$$

with ϕ_m the mass flow rate, T the temperature, θ the azimuthal coordinate and $\phi_{m,tot}$ the total mass flow rate at radial position $r_1 = \int_0^{2\pi} \phi_m(r_1, \theta, z_1) \, d\theta$.

From the simulation results, this mixing cup averaged temperature at a certain radial position r_1 at axial position z_1 is obtained by numerical integration over all faces i of the cross section at axial position at axial position z_1 over a certain interval around the radial position r_1:

$$T_{rad} = \frac{1}{\phi_{m,tot}} \sum_{i=1}^{nface} \phi_{m,i} \; T_i \; , \forall i : r_1 - \frac{\Delta r}{2} < r_i < r_1 + \frac{\Delta r}{2} \tag{6}$$

with T_i the temperature of face i, $\phi_{m,i}$ the flow through face i, $nface$ the number of faces in the cross-section, Δr the interval width, r_i radial coordinate of center of face i and $\phi_{m,tot} = \sum_{i=1}^{nface} \phi_{m,i}, \forall i : r_1 - \frac{\Delta r}{2} < r_i < r_1 + \frac{\Delta r}{2}$. The azimuthally mixing cup averaged values are plotted along the normalized radial position $r_{1,norm}$ calculated as $r_{1,norm} = {r_1}/{r_{max}}$
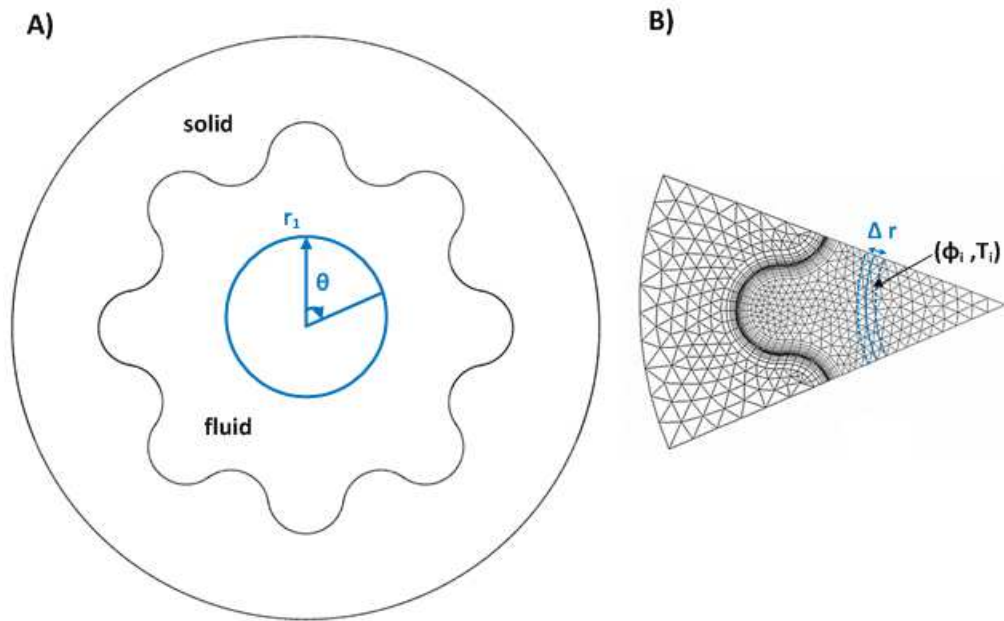
Figure C-3: Illustration of calculation of the azimuthally mixing cup averaged temperature as a function of radial position: a) entire cross section; b) grid of simulated 1/8 of a cross section.